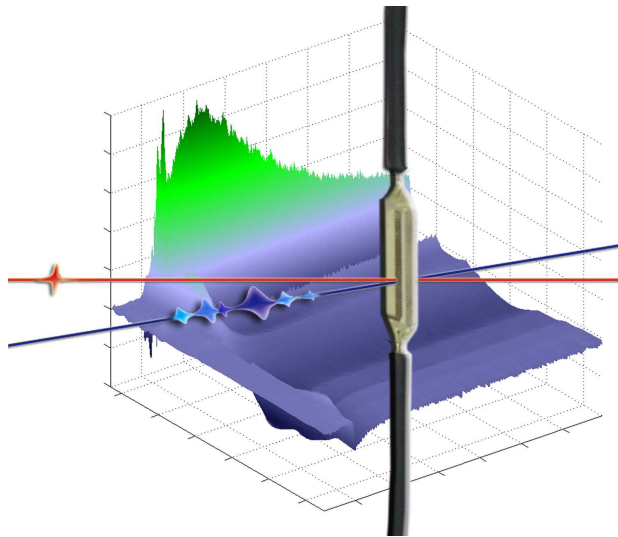


# Adaptive Femtosekunden-Quantenkontrolle komplexer Moleküle in kondensierter Phase



Dissertation zur Erlangung des  
naturwissenschaftlichen Doktorgrades der Bayerischen  
Julius-Maximilians-Universität  
Würzburg

vorgelegt von  
Gerhard Sebastian Vogt  
aus Köln

Juni 2006

Eingereicht am: 1. Juni 2006  
bei der Fakultät für Physik und Astronomie

1. Gutachter: Prof. Dr. G. Gerber  
2. Gutachter: Prof. Dr. V. Dyakonov  
der Dissertation

1. Prüfer: Prof. Dr. G. Gerber  
2. Prüfer: Prof. Dr. V. Dyakonov  
3. Prüfer: Prof. Dr. H. Hinrichsen  
im Promotionskolloquium

Tag des Promotionskolloquium: 14. September 2006

# List of Publications

Parts of this work have been published in the following references:

T. Brixner, C. Dietl, G. Krampert, P. Niklaus, E. Papastathopoulos, T. Pfeifer, R. Selle, G. Vogt, D. Walter, C. Winterfeldt and G. Gerber,  
*Adaptive femtosecond quantum control*,  
In F. Krausz, G. Korn, P. Corkum and I. A. Walmsley (Eds.), *Ultrafast Optics IV*,  
Volume 95 of *Springer Series in Optical Sciences*, pp.119–128, Springer, Berlin (2004).

G. Vogt, G. Krampert, P. Niklaus, and G. Gerber,  
*Optimal Control of Photoisomerisation*,  
Phys. Rev. Lett **94**, 068305-1–068305-4 (2005).

G. Vogt, G. Krampert, P. Niklaus, and G. Gerber,  
*Teaching lasers to twist molecules*,  
In T. Kobayashi, T. Okada, T. Kobayashi, K. A. Nelson and S. DeSilvestri (Eds.),  
*Ultrafast Phenomena XIV*,  
Volume XX of *Springer Series in Chemical Physics*, Springer, Berlin (2005).

P. Nuernberger, G. Vogt, R. Selle, S. Fechner, T. Brixner, and G. Gerber,  
*Generation of Femtosecond pulse sequences in the ultraviolet by spectral phase modulation*  
In J. T. Sheridan, and F. Wyrowski (Eds.), *Photon Management II*,  
Proceedings of SPIE 6187, No. 22, pp.151-162 (2006)

P. Nuernberger, G. Vogt, G. Gerber, R. Improta, and F. Santoro,  
*Femtosecond study on the isomerization dynamics of NK88: I. Ground state dynamics after photoexcitation*  
J. Chem. Phys. **125**, 044512-1–044512-10 (2006).

G. Vogt, P. Nuernberger, G. Gerber, R. Improta, and F. Santoro,  
*Femtosecond study on the isomerization dynamics of NK88: II. Excited state dynamics*  
J. Chem. Phys. **125**, 044513-1–044513-11 (2006).

P. Nuernberger, G. Krampert, T. Brixner, G. Vogt,  
*Rotation–translation device for condensed-phase spectroscopy with small sample volumes*

Rev. Sci. Instrum. **77**, 083113-1–083113-6 (2006).

G. Vogt, P. Nuernberger, R. Selle, F. Dimler, T. Brixner, and G. Gerber,  
*Analysis of femtosecond quantum control mechanisms with colored double pulses*  
Phys. Rev. A **74**, 033413-1–033413-8 (2006).

G. Vogt, P. Nuernberger, T. Brixner, and G. Gerber,  
*Reverse control in bacteriorhodopsin by pump and shaped dump femtosecond laser pulses*

Submitted to Chem. Phys. Lett.

P. Nuernberger, G. Vogt, T. Brixner, and G. Gerber,  
*Femtosecond Pump–shaped-dump–probe study of retinal in Bacteriorhodopsin*,  
In R. J. D. Miller, A. M. Weiner, P. Corkum, and D. M. Jonas (Eds.), Submitted  
to *Ultrafast Phenomena XV, Springer Series in Chemical Physics*, Springer, Berlin  
(2007).

P. Nuernberger, G. Vogt, T. Brixner, P. Marquetand, V. Engel, and G. Gerber,  
*Investigation of wave packet dynamics with shaped-dump pulses*  
In preparation.

G. Vogt, P. Nuernberger, T. Brixner, and G. Gerber,  
*Femtosecond quantum control in the condensed phase*  
In press, Phys. Chem. Chem. Phys.

# Contents

|  |           |
|--|-----------|
| <b>List of Publications</b>  | <b>i</b>  |
| <b>Introduction</b>  | <b>1</b>  |
| <b>1 Methods</b>   | <b>5</b>  |
| 1.1 Electronic transitions in molecules . . . . .                      | 6         |
| 1.2 Transient absorption spectroscopy . . . . .                        | 7         |
| 1.3 Fluorescence upconversion . . . . .                                | 8         |
| 1.4 Influence of polarization: Anisotropy measurements . . . . .       | 11        |
| 1.5 Spectroscopic signals in a simple model . . . . .                  | 14        |
| 1.6 Mathematical description within the rate-equation theory . . . . . | 17        |
| 1.7 Basic sketch for optimal control . . . . .                         | 21        |
| 1.7.1 Ultrashort laser pulses in optimal control schemes . . . . .     | 21        |
| 1.7.2 Concepts for optimal control . . . . .                           | 23        |
| 1.8 Spectroscopic methods for liquid phase feedback signals . . . . .  | 28        |
| 1.9 Mathematical description of double pulse generation . . . . .      | 31        |
| <b>2 Technological concepts</b>  | <b>39</b> |
| 2.1 Laser system . . . . .   | 39        |
| 2.2 Extension to other wavelengths regions . . . . .                   | 41        |
| 2.3 Self-phase modulation and white-light generation . . . . .         | 44        |
| 2.4 Pulse shaper . . . . .   | 47        |
| 2.5 Shaping pulses in the UV region . . . . .                          | 49        |
| 2.6 Pulse characterization methods . . . . .                           | 51        |
| 2.6.1 Self referencing technique - FROG . . . . .                      | 52        |

|          |  |            |
|----------|--|------------|
| 2.6.2    | Characterization of complex UV-Pulses XFROG . . . . .                    | 54         |
| <b>3</b> | <b>Reaction dynamics at conical intersections</b>                        | <b>57</b>  |
| 3.1      | Beyond the Born Oppenheimer approximation . . . . .                      | 57         |
| 3.2      | Isomerization as an example for conical intersections . . . . .          | 61         |
| 3.3      | Geometrical rearrangement reactions . . . . .                            | 63         |
| 3.3.1    | Isomerization in a simple system . . . . .                               | 64         |
| 3.3.2    | Isomerization in a large biological system . . . . .                     | 69         |
| 3.4      | Schemes for optimal control in the vicinity of conical intersections . . | 71         |
| <b>4</b> | <b>NK88 - a simple cyanine dye</b>                                       | <b>75</b>  |
| 4.1      | Experimental details for the spectroscopy experiments . . . . .          | 76         |
| 4.2      | Computational details . . . . .  | 77         |
| 4.3      | Study of the excited state dynamics . . . . .                            | 78         |
| 4.3.1    | Results of the experiments . . . . .                                     | 78         |
| 4.3.2    | Results of the computations . . . . .                                    | 84         |
| 4.3.3    | Assessing the excited-state dynamics from the experimental data          | 86         |
| 4.3.4    | Interpreting the excited state dynamics . . . . .                        | 91         |
| 4.4      | Ground state dynamics after photoexcitation . . . . .                    | 94         |
| 4.4.1    | Results of the experiments . . . . .                                     | 95         |
| 4.4.2    | Results of the computations . . . . .                                    | 98         |
| 4.4.3    | discussion . . . . .   | 100        |
| 4.5      | Optimal control of the photoisomerization efficiency . . . . .           | 107        |
| 4.5.1    | Experimental details . . . . .   | 107        |
| 4.5.2    | Feedback signal and single-parameter control schemes . . . .             | 108        |
| 4.5.3    | Multiparameter control . . . . .   | 112        |
| 4.6      | Effects of the fluorescence efficiency on the isomerization . . . . .    | 115        |
| 4.6.1    | Experimental details . . . . .   | 116        |
| 4.6.2    | Results and Discussion . . . . .   | 116        |
| 4.7      | Conclusion . . . . .   | 120        |
| <b>5</b> | <b>Bacteriorhodopsin - an important isomerization in nature</b>          | <b>121</b> |
| 5.1      | Dynamics and spectroscopic signals . . . . .                             | 124        |

|          |  |            |
|----------|--|------------|
| 5.2      | Reducing the isomerization yield by active control schemes . . . . .         | 130        |
| 5.2.1    | Experimental details . . . . .   | 130        |
| 5.2.2    | Reverse control by pump–shaped-dump–probe scheme . . . . .                   | 130        |
| 5.2.3    | The pump–dump–repump–probe scheme . . . . .                                  | 136        |
| 5.3      | Reducing the isomerization yield by shaping the excitation pulse . . . . .   | 138        |
| 5.4      | Experimental details . . . . .   | 139        |
| 5.5      | Results and Discussion . . . . .   | 140        |
| 5.6      | Conclusion . . . . .   | 143        |
| <b>6</b> | <b>Analysis of femtosecond quantum control mechanisms with double pulses</b> | <b>145</b> |
| 6.1      | Characterization of the double-pulse generation method . . . . .             | 146        |
| 6.2      | The effect of spectral modulation on the fluorescence efficiency of NK88     | 149        |
| 6.3      | Adequacy of fitness landscapes for interpretation of control mechanisms      | 152        |
| 6.3.1    | Details of the experimental setup . . . . .                                  | 152        |
| 6.3.2    | Results and Discussion . . . . .   | 152        |
| 6.4      | Analysis of the intrapulse dumping mechanism . . . . .                       | 156        |
| 6.5      | Conclusion . . . . .   | 159        |
|          | <b>Summary and outlook</b>   | <b>161</b> |
|          | <b>Zusammenfassung und Ausblick</b>  | <b>165</b> |
|          | <b>Appendix</b>  | <b>171</b> |
| <b>A</b> |  | <b>171</b> |
| A.1      | The coherent artifact . . . . .  | 171        |
| A.2      | Short-time anisotropy measurements on NK88 . . . . .                         | 173        |
| A.3      | Wave packet dynamics of $I_3^-$ and photodissociation . . . . .              | 175        |
| A.4      | Rotation–translation device for spectroscopy with small sample volumes       | 179        |
| A.4.1    | Design of the sample holder and experimental setup . . . . .                 | 180        |
| A.4.2    | Experimental characterization . . . . .                                      | 183        |
| A.5      | Calculated double-pulse pulse shapes . . . . .                               | 187        |
|          | <b>Literaturverzeichnis</b>  | <b>187</b> |





# Introduction

Chemical reactions play an essential role in many parts of our life. As a direct consequence, there has always been the desire to be able to influence the outcome of chemical processes. In the field of chemistry a large variety of different methods have been developed to produce new substances. As the number of required products increased steadily, in many cases very complicated methods were necessary to synthesize the desired substances. With these complex syntheses methods, the borders of traditional chemistry have often been touched.

A new alternative approach, called adaptive femtosecond quantum control, became accessible by the invention of ultrafast lasers [1]. In this new and fast developing field of laser chemistry, sophisticated shaped laser pulses drive a molecular reaction into the desired product channels. This can circumvent the use of many difficult reaction steps until a substance is finally produced. It may even allow the generation of molecules or molecular geometries which have not been accessible before.

The fundamentals of adaptive femtosecond quantum control were most intensively investigated in the gas phase [2–5]. Nevertheless, due to the high particle density and the fact that many reactions require a condensed environment, the liquid phase is a preferred medium for chemical reactions. Already first prototype experiments based on simple reactions have shown that the concept of femtosecond quantum control is also applicable for solvated molecules [6–9].

A very interesting class of reactions is the rearrangement of the molecular structure, called isomerization. Many physical and chemical properties, such as the absorption spectra, depend on the given molecular geometry. Changing the arrangement of the atoms in space with light can then trigger important subsequent processes. Because of the effects and applications, isomerization reactions are of vital importance to many processes in the field of physics, chemistry, and biology. For example the first step of vision within the human eye is initiated by an ultrafast isomerization.

In many cases, isomerization reactions can be initiated by irradiation with light. The liquid phase in turn is important to obtain high product yields and is often required for certain reactions. Thus it is interesting to investigate adaptive femtosecond quantum control applied to geometrical rearrangement reactions of complex molecules in a condensed medium.

With adaptive femtosecond quantum control, laser pulse shapes can be designed, that drive reactions into the desired direction. The success of the concept of adaptive femtosecond quantum control is based upon the fact that complete knowledge of the structure and dynamics of a molecule is not required in order to determine the optimal laser pulse shapes. If a complete theoretical simulation of the system would be possible, the laser pulse shape could be calculated. However, in general such a simulation can not be accomplished for realistic molecules and solvent interactions. For the experimental realization of adaptive femtosecond quantum control, only a feedback signal that monitors the outcome of a reaction is needed. In a closed-loop approach the laser pulse shape which optimally fulfills the control objective can be iteratively acquired. The additional optimization of certain very basic laser parameters, such as wavelength, intensity or polarization and the choice of suitable conditions for the reactants can increase the product yield.

However, in the context of adaptive femtosecond quantum control, the experimental characterization of the molecular reaction is not dispensable. In order to monitor the reaction yield by a feedback signal, it is necessary to determine adequate spectroscopic signals of the reactants. The information about the reaction dynamics is also important for the characterization and interpretation of the control mechanism. Since the decisive reaction steps often take place on a femtosecond to picosecond time scale, one has to set up suitable methods to be sensitive to this time regime. Furthermore, pulse characterization methods are indispensable as well to understand the control mechanism. With the knowledge of the dynamics and the control mechanisms for a specific system, in an iterative process new techniques can be developed, that are specially adapted to the given problem.

This thesis mainly deals with the study and optimization of geometrical rearrangement of two molecular systems: the isomerization reaction of a medium-size molecule from the family of the cyanine dyes in the liquid phase and the isomerization of the very complex biological system of retinal within the protein bacteriorhodopsin. The methods and concepts for monitoring and controlling such complex systems are presented in the first two chapters. More specific information about isomerization and possible control methods in the context of geometrical rearrangement reactions are given in Chapter 3.

The first part of Chapter 4 presents the investigation of the molecular dynamics of the cyanine molecule in different solvents using various spectroscopic methods. A conclusive scheme of the dynamics was found in collaboration with F. Santoro and R. Imbrota performing quantum dynamical calculations. On the basis of this information, the potential of the method of adaptive femtosecond quantum control for molecules in condensed matter is demonstrated for this medium-size molecule in the liquid phase. The required feedback signals can be measured by transient absorption spectroscopy. In this spectroscopic technique, the system is excited with a pump pulse and the dynamics can be interrogated by a temporally delayed probe pulse. After excitation with

---

light, the isomerization efficiency, i.e. the relative yield of the educt to the product isomers, can be both enhanced and reduced by specifically designed pump laser pulses. Finally the effect of the enhancement of the radiative decay channel on the isomerization efficiency is analyzed.

Chapter 5 deals with the biomolecular system bacteriorhodopsin. Adaptive femtosecond quantum control is first applied to directly shape the pump laser pulse. This experiment shows that a reduction of the isomerization yield and therewith the isomerization efficiency is possible. Motivated by different theoretical calculations, a new pump–shaped-dump–probe scheme for influencing the molecular dynamics is developed. The shaped-dump pulse can influence the dynamics at times, when the decisive reaction step occurs. This scheme allows for the control of molecular systems, as demonstrated for the biomolecular system bacteriorhodopsin, and it additionally provides information on the wave-packet evolution.

In Chapter 6, a further developed method is presented that can facilitate the analysis of control mechanisms of adaptively determined optimal laser pulse shapes and provide an insight into the reaction mechanism. This method makes use of fitness-landscapes, in which the system’s response for parametrized pulse shapes is systematically measured. By scanning the pulse separation and the relative amplitude of colored double pulses, pump-dump scenarios can be realized, which often play an important role. The concept is first characterized by experiments whose outcome is theoretically simulated. It is then demonstrated in an experiment on the excitation efficiency of a large dye molecule in solution, i.e. the amount of excited molecules for differently shaped laser pulses in relation to their pulse energy. Finally the isomerization process of the biomolecular system bacteriorhodopsin is illuminated using colored double-pulse control-landscapes. These different experiments show the capability of colored double-pulse fitness-landscapes to investigate reaction dynamics and to identify the mechanism of adaptively determined laser pulse shapes.



# Chapter 1

## Methods

Many basic processes of molecular dynamics take place on a femtosecond time scale. By attaining the femtosecond time resolution, it became possible in principle to monitor and understand the fundamental processes ruling the molecular dynamics. Depending on the given problem, different methods are suitable and necessary to investigate the aspects of such reactions. With rising complexity of the investigated systems one method alone often does not deliver enough information to understand the whole dynamics. Therefore different experimental methods, all illuminating the undergoing dynamics from different views, are necessary for a hopefully complete picture of the molecular processes.

Besides only monitoring reactions a very compelling task is to take influence on the development of the undergoing dynamics. There are many different methods to reach this goal by means of shaping an exciting laser field. These can be summarized under the term optimal control. In recent years a method labeled “adaptive femtosecond quantum control” has been shown to be capable to automatically find solutions that fulfill a given control task. To understand the control mechanism of adaptively determined optimal control fields, a complete analysis of the molecular dynamics is necessary. Beside this, different experimental methods, based upon systematic scans of physical meaningful pulse shapes can help to unmask the way, the reaction is controlled by a certain pulse shape.

This chapter presents suitable methods for investigating the molecular dynamics, in medium and large systems, either in the liquid phase or embedded in a protein matrix. Subsequently, the basic possibilities of controlling molecular reactions by influencing the exciting laser field are discussed. Furthermore the theoretical basis for a scheme for reducing the problem of complexity is presented.

## 1.1 Electronic transitions in molecules

An electronic transition is the promotion of an electron from an occupied orbital to an unoccupied orbital by the absorption of a photon. The most prominent electronic transition is the excitation from the ground state into the first excited state. Beside this of course the inverse is also possible as well as transitions to even higher lying states. These electronic transitions and the observation and manipulation of the following molecular dynamics will be the key subject of this thesis.

Electronic transitions are located in the visible and in the ultraviolet wavelength region (see Figure 1.1). Depending on the excitation wavelength, transitions between different kinds of orbitals can be induced. Especially at shorter wavelengths, excitation into higher excited states takes place.

In polyatomic molecules, the electronic states are depending on the degrees of freedom of the molecule. Thus the excited states are characterized by potential (hyper)surfaces which contain the potential energy as well as the averaged kinetic energy of the electron. It has been shown that often only certain degrees of freedom are relevant. Therefore the potential energy surfaces can be simplified to be dependent on a certain number of relevant reaction coordinates. Many examples for these potential energy surfaces can be found in this thesis.

The molecular dynamics after excitation can be described by the Schrödinger equation:

$$i\hbar \frac{d}{dt} |\psi_t\rangle = [H - \mu \vec{E}(t)] |\psi_t\rangle \quad (1.1)$$

$H$  is the Hamilton-operator of the system,  $\mu$  the transition dipole moment,  $E(t)$  the electric field at time  $t$  and  $|\psi_t\rangle$  the wave function of the system. In the case of

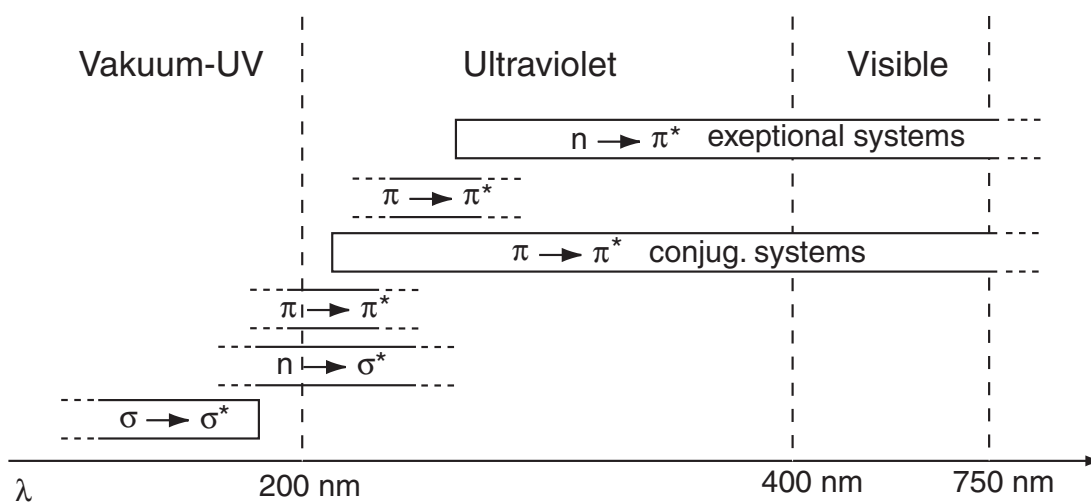


Figure 1.1: Areas of absorption for different kinds of transitions. The molecular orbitals are termed after the nomenclature of Kasha [10].

dissolved molecules, as it is the matter in this work, the interaction with the solvent has to be considered in the Hamilton operator.

The spectrum of sufficiently short femtosecond laser pulses can cover multiple vibrational levels of the molecule, which can then be coherently excited. This superposition will then result in a wave packet. The temporal evolution of the wave packet is depending on the potential surfaces and can be experimentally monitored (see Sections 1.2 and A.3).

## 1.2 Transient absorption spectroscopy

A molecular reaction starts at an educt state and finally ends in the product state. While proceeding from the one to the other state, different intermediates can be reached. Therefore during the reaction, different physical properties vary with time. The change of these properties can characterize the different steps of the reaction and can be used to monitor the dynamics of the system.

To monitor the change of the desired physical properties connected with the reaction, generally one measures the signal of an subensemble. This is especially true for solvated systems. The members of this subensemble must all start with the reaction at the same time, while the remaining molecules only cause a constant background signal. The effect, that initiates the reaction, must be short compared to the time scale on which the reaction takes place. Thermal heating, the common way to initiate a reaction in traditional chemistry can thus not be used. As seen in the previous section many reactions can be initiated by irradiation with light of the proper wavelength. With the invention of ultrashort laser pulses in the femtosecond regime it is for example possible to fulfill the above stated requirements for exciting molecules in a time window, that is short compared to the duration of the reaction.

Since these dynamics often take place on a femtosecond time scale, the temporal change of the physical properties can not be recorded in a direct way. The fastest photodiodes have a time resolution of still about 20 ps and even streak cameras are limited to about 400 fs [11].

To overcome this limitation, one can use a second ultrashort laser pulse (called probe pulse), whose time duration is shorter than the reaction dynamics. The intensity of the probe-pulse depends on the absorption coefficient of the sample to the time of the interaction. By changing the time delay between excitation and the second probe pulse one can thus measure the change of the dynamics with time, if the absorption coefficient in the monitored wavelength region is sufficiently effected by the reaction. The excitation event is often labeled as pump event, the second interaction as probe event.

As already stated in the introduction to this chapter and as one will see in Chapters 4, 5 and 6 the temporal evolution of the absorption can yield a lot of valuable infor-

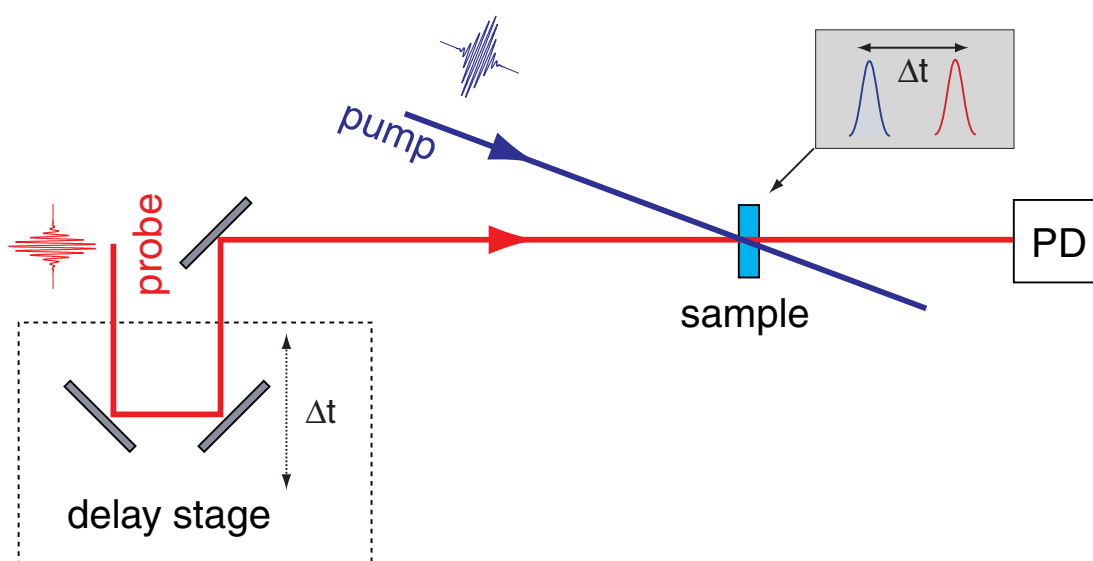


Figure 1.2: Basic setup for a transient absorption experiment. The pump and the probe pulses are spatially overlapped in the sample. The pump pulse excites a certain amount of molecules and the probe pulse monitors the temporal change of their absorption coefficient and therewith the reaction dynamics. To achieve this, the time delay between the two pulses can be varied by a delay line. The modulated probe pulse is then recorded with a photodiode.

mation and already show many features of the dynamics. It should be mentioned that there are cases that need other methods, e.g. if different states have the same absorption properties. Some of these methods will be discussed in the next sections.

A simple scheme for a pump-probe setup that is also the basis for the pump-probe experiments in this work is shown in Figure 1.2. An ultrashort pump pulse is used to excite a certain amount of molecules. An also ultrashort probe pulse can be temporally delayed by changing its propagation length. After interaction of the probe pulse with the molecules the pulse energy is monitored by a photodiode. With the help of wavelength selection different states can be selectively monitored. This kind of spectroscopy is called transient absorption spectroscopy.

### 1.3 Fluorescence upconversion

The fluorescence can provide a lot of valuable information about a reaction. If a molecular system is excited to a higher lying excited state very often fluorescent states are accessed before finally reaching the product state. The steady-state fluorescence spectrum can already provide a good insight into the reaction mechanism. More information can naturally be obtained by the time resolved fluorescence. This can be achieved by different methods. The easiest way is within a transient absorption experiment. If



a fluorescent state is populated the population can be stimulated down to a lower state with the help a probe photon of the proper wavelength. The monitored probe-pulse intensity is thus increased. This method has the big disadvantage that very often in the same wavelength region, where fluorescence is prominent, also absorption takes place. These different signals form a resulting signal which can be very difficult to interpret.

To overcome this disadvantage a different method must be used to measure the fluorescence separated from the absorption signals. Therefore the probe-interaction step, that ensures a femtosecond time resolution, must be transferred to a place where no absorption of the molecules interferes with the fluorescence signal.

To ensure the desired time resolution so called nonlinear effects in special crystals are used. There are a big variety of nonlinear effects in crystals which are summarized in Section 2.2. In the case of monitoring the fluorescence in a time resolved way, one can make use of the effect of sum- or difference-frequency mixing of two pulses. If certain conditions are ensured, two pulses with the central frequencies  $\omega_1$  and  $\omega_2$  can produce a signal at  $\omega_3 = |\omega_1 \pm \omega_2|$ . These conditions are important in the method of fluorescence upconversion. Namely they are spatial and temporal overlap, correct polarization of the two incoming pulses at  $\omega_1$  and  $\omega_2$ , transparency of the crystal at all involved frequencies and correct angle of the crystal axis concerning the electric field vector of the incoming pulses at a fixed crystal temperature. If one of these conditions is not met perfectly it affects the intensity of the produced pulse at  $\omega_3$ . If one of the two pulses is much shorter than the other, the intensity of the signal pulse at a fixed time delay between the two source pulses is mainly effected of the temporal pulse structure of the longer pulse. By changing the time delay between the two source pulses the temporal profile of the longer one can be mapped out. The nature of the underlying nonlinear process is not important for this measurement. Whether sum- or difference-frequency mixing is used only depends on the signal quality that the processes can provide.

In the case of fluorescence upconversion the emitted fluorescence by the excited molecules is used as the longer source pulse. A second pulse, that should be as short as possible, is overlapped in a nonlinear crystal with the fluorescence. This pulse is called gate-pulse. If all conditions are fulfilled for a sum- or difference-frequency signal, the temporal profile of the fluorescence can be measured by monitoring the sum- or difference-frequency signal depending on the time delay between the two source pulses. This method is termed fluorescence upconversion.

Since the fluorescence signal is often already very low in intensity, the upconverted signal is even lower. This is especially the case if competing non-fluorescent paths exist, as it is the case in the molecules which are investigated in this work. Therefore special care must be taken in suppressing the pump and gate-light. The fluorescence is normally red-shifted concerning the pump-wavelength. Due to this, the pump light can be sufficiently suppressed with an appropriate filter without effecting the fluorescence too much. Special care should be taken in such a configuration, because in principle, it is possible that the pump beam causes fluorescence in the filter, that can cause a

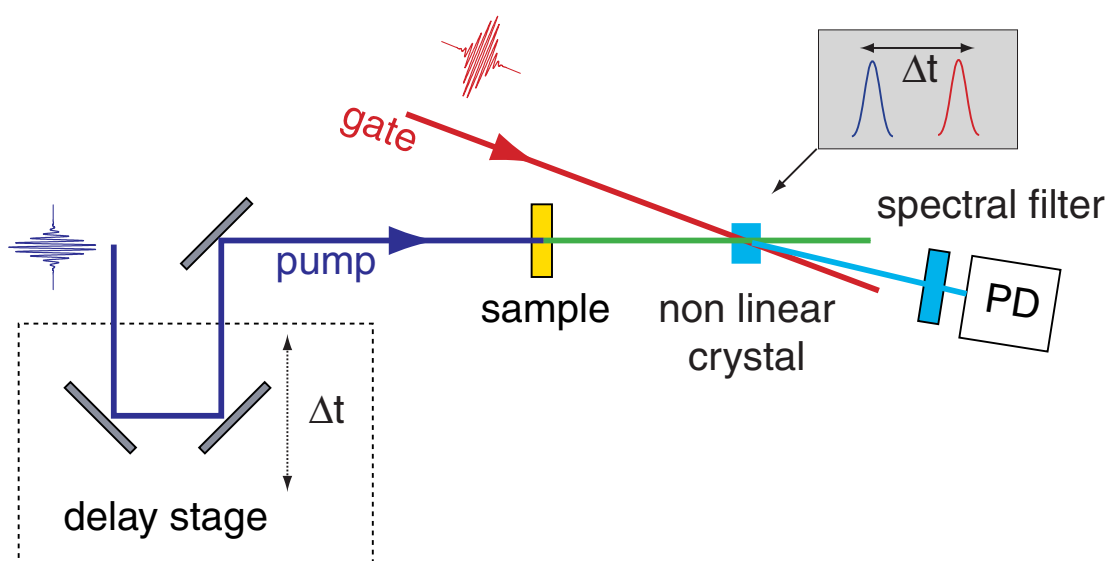


Figure 1.3: Schematic setup for a fluorescence upconversion experiment. The molecules in the sample are excited by the pump pulse. Their fluorescence is frequency mixed in a nonlinear crystal with a gate pulse, whose pulse duration is shorter than the time of the underlying dynamics, that cause the fluorescence. The time delay between the fluorescence and the gate pulse can be varied by a delay line. The frequency-mixed signal can be further filtered in the frequency domain and then recorded by a photodiode.

misleading signal. By replacing the molecule with the solvent only, this effect can be ruled out.

By changing the orientation of the axis of the up-converting crystal, the wavelength of the fluorescence can be very effectively selected, since the acceptance bandwidth for either sum- or difference-frequency is quite narrow for a thick crystal. The frequency-resolution can even be enhanced by appropriate filters or by the use of a monochromator or spectrometer. In Figure 1.3 a standard fluorescence upconversion setup is presented. By using spherical mirrors in an improved light collecting geometry, the solid angle for collecting the fluorescence light can be increased [12, 13]. Furthermore in a very specialized setup, even an entire fluorescence band in a broad range of  $10,000 \text{ cm}^{-1}$  can be upconverted without readjusting optical elements. This allows measurements of the fluorescence by upconversion with a single pump-gate scan.

Stimulated emission and fluorescence upconversion, although being quite different in the way they are acquired, are trying to measure the same effect. The similarity of both signals has been repeatedly emphasized in the literature [14]. Differences in the dynamics can occur in the case where the pump and the probe pulse in the stimulated emission experiment temporally overlap.

Therefore the fluorescence upconversion experiment gives very valuable informa-

tion about excited state dynamics since it only probes the fluorescence and thus can help separating the stimulated emission contribution from the absorption contribution in transient absorption experiments in the very common case of overlapping bands.

## 1.4 Influence of polarization: Anisotropy measurements

Up to now, all methods have been discussed, without having a special focus on the polarization of the laser pulses. When exciting and probing with linearly polarized pulses, one can expect an influence of the polarization on the resulting signal [15–19].

Beside some exceptions like the  $C_{60}$  molecule, most chromophores absorb light in a preferred direction. In a simple model, molecules having their dipole axis parallel to the electric field vector of the pump pulse are preferentially excited. Thus the sample is anisotropic after the excitation act. Of course the same effect is valid for the probe pulse. In the case that the dipole moment changes its orientation during the time between the pump and the probe act, for example because of a geometrical rearrangement of the molecular structure, this will cause an additional modulation of the probe signal. Moreover, on a longer time scale, the initially anisotropic subensemble will become isotropic due to its brownian motion. This effect is called rotational diffusion [16, 20, 21].

For example probing a population that does not decay, in a pump-probe geometry, in which the probe polarization is parallel to the pump polarization, will nevertheless result in an exponentially decaying signal on top of a constant offset. At time zero, the subensemble of excited molecules is highly anisotropic. The probability for absorbing a second photon is then proportional to the square of the scalar product of the transition moment  $\vec{M}(t)$  and the electric field vector  $\vec{E}$ . This means that the absorption is proportional to  $\cos^2(\theta(t))$  with  $\theta$  being the angle between  $\vec{M}(t)$  and  $\vec{E}$ . In this simple model system lets assume that the transition moment involved in the pump step is parallel with the one in the probe step. Then, because the probe pulse was chosen to have its polarization parallel to the polarization of the pump pulse, the preselected subensemble has its transition moment parallel to the probe electric field vector. This causes  $\theta$  to be close to zero for most of the molecules and therefore  $\cos^2(\theta)$  close to its highest value. Therefore, the modulation of the probe is very efficient.

After the excitation act, brownian motion takes place and the initially preselected subensemble changes its anisotropy and becomes more isotropic. The average value of  $\cos^2(\theta)$  for the subensemble gets lower until reaching asymptotically the value for the isotropic case.

The situation for the method of fluorescence upconversion is identical. The pump step will cause a preselection. Because this ensemble is anisotropic, the fluorescence is anisotropic as well. The upconverting crystal acts as a polarization analyzer due to its phase matching conditions.

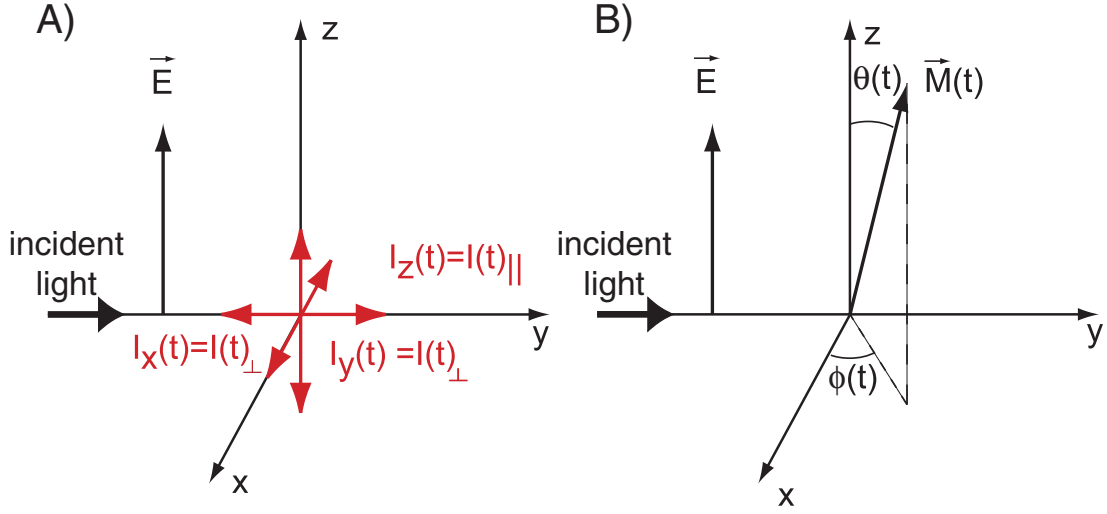


Figure 1.4: Definitions and relations for describing the anisotropy A) Definitions and relations between the fluorescence intensity components  $I_i(t)$ , for a sample placed at the origin of the coordinate system.  $\vec{E}$  is the electric field vector of the linear polarized incident light B) Characterization of the orientation of the transition moment  $\vec{M}(t)$ .

To describe these effects the term anisotropy is introduced. In a cartesian coordinate system lets the incident electric field vector of linear polarized light be in the  $z$  direction (see Figure 1.4). For the example of fluorescence, the components of the fluorescence intensity that are parallel and perpendicular to the electric field vector are denoted as  $I_z(t) = I_{\parallel}$  and  $I_x(t) = I_y(t) = I_{\perp}(t)$ . These individual components can for example be measured with the help of spectral filters to suppress the pump light and polarization filters. The total intensity  $I(t)$  is thus

$$I(t) = I_x(t) + I_y(t) + I_z(t) = I_{\parallel}(t) + 2I_{\perp}(t). \quad (1.2)$$

With these relations two definitions are formulated in common literature. The polarization ratio  $p(t)$ :

$$p(t) = \frac{I_{\parallel}(t) - I_{\perp}(t)}{I_{\parallel}(t) + I_{\perp}(t)} \quad (1.3)$$

and the anisotropy  $r(t)$ :

$$r(t) = \frac{I_{\parallel}(t) - I_{\perp}(t)}{I_{\parallel}(t) + 2I_{\perp}(t)}. \quad (1.4)$$

As seen from Equation 1.2, the anisotropy  $r(t)$  is the quotient from the difference of the  $I_{\parallel}(t)$  and  $I_{\perp}(t)$  to the total fluorescence intensity, while the polarization ratio  $p$  sets the same difference in relation to the fluorescence intensity in direction of the

observation. These two definitions are connected via the direct relation

$$r(t) = \frac{2p(t)}{3 - p(t)} \quad (1.5)$$

between anisotropy  $r(t)$  and polarization ratio  $p(t)$ . However, in newer literature generally the anisotropy  $r(t)$  is discussed.

As already stated in the beginning the transition moment varies with time. The orientation of the transition moment  $\vec{M}(t)$  can be characterized by the angle  $\theta(t)$  with the z-axis and the angle  $\phi(t)$  with x-axis. The components of the transition moment for a particular molecule along the three axes are then  $\vec{M}(t) \cos \alpha_i(t)$  with  $\alpha_i(t)$  being the angles between the transition moment and the three axis  $i=x,y,z$ .

Because there is no phase relation between the elementary emissions, the contribution of each molecule to each intensity component is proportional to the square of the corresponding transition moment. For a complete ensemble of molecules summation over all N molecules give the expression:

$$I_i(t) = const \cdot M^2 \sum_{j=1}^N \cos^2(\alpha_{ij}(t)) = const \cdot M^2 N \overline{\cos^2(\alpha_i(t))} \quad (1.6)$$

for  $i=x,y,z$ . The bar characterizes the ensemble average over the N molecules at the time t.

The sum of the three average values of  $\overline{\cos^2(\alpha_i(t))}$  must be equal to unity in the defined coordinate system,  $\overline{\cos^2(\alpha_x)} + \overline{\cos^2(\alpha_y)} + \overline{\cos^2(\alpha_z)} = 1$ . Because of the axial symmetry around the z-axis,  $\overline{\cos^2(\alpha_x(t))} = \overline{\cos^2(\alpha_y(t))}$  holds. Therefore the expression  $\overline{\cos^2(\alpha_z(t))} = \overline{\cos^2(\theta(t))} = 1 - 2\overline{\cos^2(\alpha_x(t))}$  is obtained. Then the anisotropy can be given by

$$r(t) = \frac{I_{\parallel}(t) - I_{\perp}(t)}{I(t)} = \frac{I_z(t) - I_y(t)}{I_x(t) + I_y(t) + I_z(t)} \quad (1.7)$$

$$= \frac{\overline{\cos^2(\theta(t))} - \overline{\cos^2(\alpha_x(t))}}{\overline{\cos^2(\alpha_x(t))} + \overline{\cos^2(\alpha_y(t))} + \overline{\cos^2(\theta(t))}} \quad (1.8)$$

$$= \frac{\overline{\cos^2(\theta(t))} - \frac{\overline{\cos^2(\theta(t))} - 1}{2}}{\overline{\cos^2(\alpha_x(t))} + \overline{\cos^2(\alpha_x(t))} - (1 - 2\overline{\cos^2(\alpha_x(t))})} \quad (1.9)$$

$$= \frac{3\overline{\cos^2(\theta(t))} - 1}{2} \quad (1.10)$$

These results are important for understanding the change of the anisotropy with time which means the change of the orientation of the transition moment. From this behaviour, important conclusions for molecular dynamics can be drawn.

To hold the results of these methods simple, it is desirable to separate the influence of the change of the population and the change of the orientation of the transition moment on the probe signal. To probe only the change of the population the anisotropy

has to be equal zero.

The information of the change of the population can be reconstructed from the signals  $I_{\perp}(t)$  and  $I_{\parallel}(t)$  [19]:

$$I_{MA}(t) = \frac{1}{3}(I_{\parallel}(t) + 2 \cdot I_{\perp}(t)) \quad (1.11)$$

The sum  $I_{\parallel}(t) + 2 \cdot I_{\perp}(t)$  is, as shown in the beginning, the total fluorescence intensity. This of course is independent of the direction of the transition moment. Instead of this method also probing under an angle of  $54.7^{\circ}$  eliminates the effect of the direction of the transition moment on the probe signal [19]. This angle is known as the “magic angle” in the literature [19, 22–24]. Therefore the anisotropy  $r(t)$  measures the evolution of the direction of the transition moment, while pump-probe or fluorescence upconversion spectroscopy under magic angle condition measures the change of the population. Using the Equation 1.11 for measuring a signal, free of the influence of the transition moment direction, has the experimental disadvantage, that two signals have to be measured instead of only one, as in the case of a magic angle measurement.

If more than one state contributes to the anisotropy signal, then the anisotropy is the superposition of the anisotropy of each state weighted with the normalized intensity:

$$r(t) = \sum_i \frac{I_i(t)}{I_{total}(t)} r_i(t) \quad (1.12)$$

with  $I_{total}(t) = \sum_i I_i(t)$  and  $I_i(t)$  is the individual intensity of each contributing state. This is called the “additivity law of anisotropies” [16, 18].

The law of additivity has especially consequences in pump-probe anisotropy experiments. There the anisotropy is weighted by the individual contributions to the transient absorption signal. These contributions can now be both positive and negative, for absorption band on the one hand and bleach or stimulated emission on the other hand (see Section 1.5). Therefore  $I_{total}(t)$  can become zero and thus  $r(t)$  for the complete signal infinite [18, 19, 22, 24].

Nevertheless, the individual anisotropies do not become infinite. In contrast to this, in the above used picture, it can easily be shown, that the values of  $r(t)$  must be in the interval of  $[-0.2, 0.4]$  [16]. Under special geometrical conditions and in the coherent regime, the anisotropy can exceed these values [15, 25].

## 1.5 Spectroscopic signals in a simple model

To describe the molecular dynamics adequately, it is necessary to know the potential energy surfaces in dependence of all relevant coordinates. In the case that these potential energy surfaces are known, one should be able to identify and explain all

spectroscopic signals. Unfortunately especially in the liquid phase one can not directly measure the potential energy surfaces.

Another possibility is to calculate them with *ab initio* methods. With increasing complexity of the system, naturally these calculations become more difficult. Especially in the case of solvated molecules the influence of the solvent must also be taken into account. Despite these difficulties, many calculations of the potential energy surfaces of even very complex molecules have been published (e.g. [26–29]). Most often these calculations only deal with the ground state and the first excited state.

In many cases, if the potential energy surfaces are not perfectly known, one can use a reduced model. In this reduced model, different areas on the potential energy surface, on which at least a part of the population is trapped for a longer time, are reduced to a fixed state. In the evolution of the molecular dynamics after excitation, these states become populated and depopulated. This model suffers from the fact that many effects, connected with the shape of the potential energy surface such as wave packet motion can not be explained. Therefore especially effects taking place in the first few 100 femtoseconds, may not be explainable in this model. On longer time scales, this model becomes more exact. Despite these shortcomings the model can even be helpful explaining signals in the short time region, since the effect of wave packet motion for example is often superposed on the signal, caused by the decay of the population [30–33]. In a model, where both contributions are fitted, they can thus be separated from each other [34–37].

In Figure 1.5 the potential energy surfaces for a model molecule are shown. There are many molecules showing a similar behaviour as in the presented example, although in most cases it is necessary to introduce at least a second coordinate to explain all signals. But for simplicity, in this chapter this simplified example will be used. The first excited surface shows a small barrier, as it is the case for example in stilben, the plant photoreceptor phytochrome or in the green fluorescence protein [38–41]. This barrier divides the surface into an energetically higher and a lower lying part which can be symbolized by two different states. In common literature the region on the excited surface, to where the wave packet is initially excited is called Franck-Condon region (FC). In the sample molecule, similar to many real cases, this FC region shall lie in that way that the higher lying state gets first populated. This state shall not be a fluorescent state, therefore with a certain decay time the lower lying part of the excited state gets populated. From there a decay to the ground state shall be possible by emitting a photon.

These simple population dynamics can be represented by the three-state model in Figure 1.5 B. The different states are connected to each other, and the population transfer is characterized by decay- and rise times of the different signals. This model has the advantage, that the shape of the different spectroscopic signals due to the change of the population in the different states can be easily calculated as will be presented in the next section. It has been shown that many features of the underlying dynamics can be explained with the help of such reduced models. However, the interpretation on the basis of such models must be handled with care, since effects such as solvent shift can

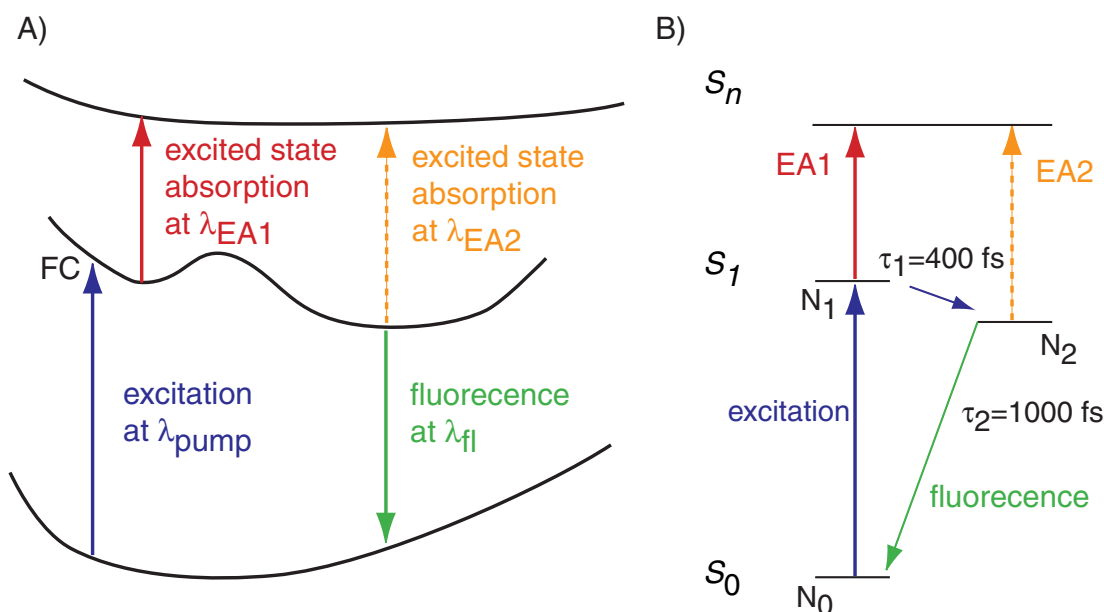


Figure 1.5: A) Potential energy surfaces for a model molecule. The ground state  $S_0$  is barrierless, while the excited state forms a small barrier. After excitation a wave packet is formed at the Franck-Condon region (FC). This wave packet is first trapped in the minimum before the barrier, from where no fluorescence shall take place. From the second minimum, the ground state can be accessed by emitting a photon. Excited state absorption can take place from both minima on the first excited surface  $S_1$ , but at slightly different wavelengths  $\lambda_{\text{EA1}}$  and  $\lambda_{\text{EA2}}$ . B) Reduced model of the same molecule. Areas on the energy surfaces, where the population gets trapped are characterized by a state  $i$  with the population  $N_i$ . The population gets transferred from the ground state  $S_0$  to the first state on the  $S_1$  surface. From there the population decays with  $\tau_1$  to the second state. This state can be depopulated with the decay time  $\tau_2$ .

for example produce similar signals as two different states. A careful analysis over a broad spectral range is necessary to rule out such effects.

Here, it is also very likely, that the initially prepared wave packet oscillates in the first minimum. If the time resolution is sufficiently high, it is possible to see these oscillations on top of the signal, caused by the population decay [30–33, 42]. Since the oscillatory behaviour superposes on the decay signal, it can be included into the model, as mentioned above.

In a pump-probe experiment, there are several different effects, modulating the probe pulse and reflecting the undergoing molecular dynamics. As already explained in Section 1.2 the absorption coefficient of the molecule after excitation varies with time thus reflecting the dynamics. In the case here for example the molecule can be excited onto the first excited state by an ultrashort pulse at the wavelength  $\lambda_{\text{pump}}$ . After the pump pulse has passed the sample, a certain amount of molecules is transferred into the first excited state. Until these molecules do not have repopulated the ground



state again, they will not absorb at  $\lambda_{pump}$ , except another even higher lying state is accessible with this energy from the excited state. If this is not the case the probe signal at  $\lambda_{pump}$  is enhanced due to the missing absorption by the excited molecules. This is called "pump-depletion" or simply only "bleach". This bleach signal thus reflects the repopulation of the ground state.

The decay to the ground state itself takes place in the given case by fluorescence. This can either be monitored by fluorescence upconversion or in a pump-probe experiment by stimulated emission. These signals therefore reflect the dynamics on the excited state.

From the first excited state surface, other even higher lying states are very often accessible. Since a higher lying region is present and a lower lying one on the first excited surface, it is possible, that with the wavelength  $\lambda_{EA2}$  a certain higher lying excited state by only one of the two regions can be accessed. This is called excited state absorption. If both regions on the first excited surface absorb at  $\lambda_{EA}$  the individual signals superpose to a resulting signal.

Beside the discussed signals, whose shape can be calculated by the rate-equation theory in the next section, there is the signal of hot ground state absorption, that will naturally occur in a molecular system like the given one. After being excited to the  $S_1$  surface and the following decay back to the  $S_0$  ground state, the molecule will be in a vibrational hot configuration which is called hot ground state. Since the hot ground state configuration is nevertheless not too different from the ground state itself, its absorption band is basically similar, but broadened and red-shifted. While the vibrational cooling takes place, the absorption band of the hot ground state gets more and more the shape of the steady state absorption spectrum of the molecule [43–45].

Besides the hot ground state absorption which will occur in the presented molecule, there can even be additional effects causing absorption signals in a real molecule. After excitation, different photoproducts can be reached, either already on the excited state or after the decay to the ground state. These photoproducts will also exhibit hot ground state absorption and in the case that they are still in an excited state, they can also contribute to the fluorescence spectrum [46,47]. Very prominent products are dissociation products and the resulting further reactions [48–53] and geometrical rearrangements, as for example ring-opening [54–57] or *cis-trans* isomerization [37, 52, 58–69]. In addition to these signals, there can also occur solvated electron absorption and the absorption of different ionized species [70–73], as well as shift because of the interactions with the solvent [74].

## 1.6 Mathematical description within the rate-equation theory

The temporal change of the population in the different states in the reduced model in Section 1.5 can be calculated by the rate-equation theory. The ground state population

$N_{01}$  gets transferred by an ultrashort pump-pulse into the first excited state. The effect of the temporal width of the pump-pulse is discussed at the end of the section. The initial population in the first state decays with the decay time  $\tau_1$  to the second state. The inverse of the decay time is labeled rate  $k_i = \frac{1}{\tau_i}$  and gives the name to this kind of mathematical description. The second state gets populated with  $\tau_1$  and depopulated with  $\tau_2$ . This time is finally the rise time with that the ground state gets repopulated. For this sequence one can formulate a set of differential equations:

$$\frac{dN_1(t)}{dt} = -\frac{1}{\tau_1}N_1(t) \quad (1.13)$$

$$\frac{dN_2(t)}{dt} = -\frac{1}{\tau_2}N_2(t) + \frac{1}{\tau_1}N_1(t) \quad (1.14)$$

$$\frac{dN_0(t)}{dt} = \frac{1}{\tau_2}N_1(t) \quad (1.15)$$

These differential equations can be easily solved:

$$N_1(t) = N_{01} \exp\left(-\frac{t}{\tau_1}\right) \quad (1.16)$$

$$N_2(t) = \frac{\tau_2}{\tau_2 - \tau_1} \left( \exp\left(-\frac{t}{\tau_1}\right) - N_{01} \exp\left(-\frac{t}{\tau_1}\right) \right) \quad (1.17)$$

$$N_0(t) = \frac{\tau_2}{\tau_2 - \tau_1} \left( 1 - \exp\left(-\frac{t}{\tau_2}\right) \right) - \frac{\tau_1}{\tau_2 - \tau_1} \left( 1 - N_{01} \exp\left(-\frac{t}{\tau_1}\right) \right) \quad (1.18)$$

The population in the different states can be monitored in a pump-probe experiment on different ways, by pump-depletion, excited state absorption and stimulated emission in the given case. The population of the first state on the excited surface before the barrier can be visualized by the excited state absorption at the probe-wavelength  $\lambda_{probe} = \lambda_{EA1}$ . Since the second state after the barrier does fluoresce, the population  $N_2(t)$  of this state can be monitored by two ways, either by stimulated emission at  $\lambda_{probe} = \lambda_{fl}$  or by excited state absorption at  $\lambda_{probe} = \lambda_{EA2}$ . Finally the repopulation of the  $S_0$ -ground state can be seen in the pump-depletion signal at  $\lambda_{probe} = \lambda_{pump}$ .

The temporal evolution of three of these signals are shown in Figure 1.6 in the first column. Stimulated emission and pump depletion have a negative absorption signal, because the probe intensity is enhanced due to the processes at the corresponding wavelengths. The change of the populations is shown in the second column.

In real molecules the discussed effects will not occur at a certain wavelength, but in a broad spectral band. The pump depletion is in the whole spectral region present, where the steady state absorption spectrum of the excited state is different from zero. Also the excited state absorption presents itself often as very broad bands, since the higher lying excited states are quite dense. Therefore the absorption bands of the different states often overlap, giving a broad band of excited state absorption with several

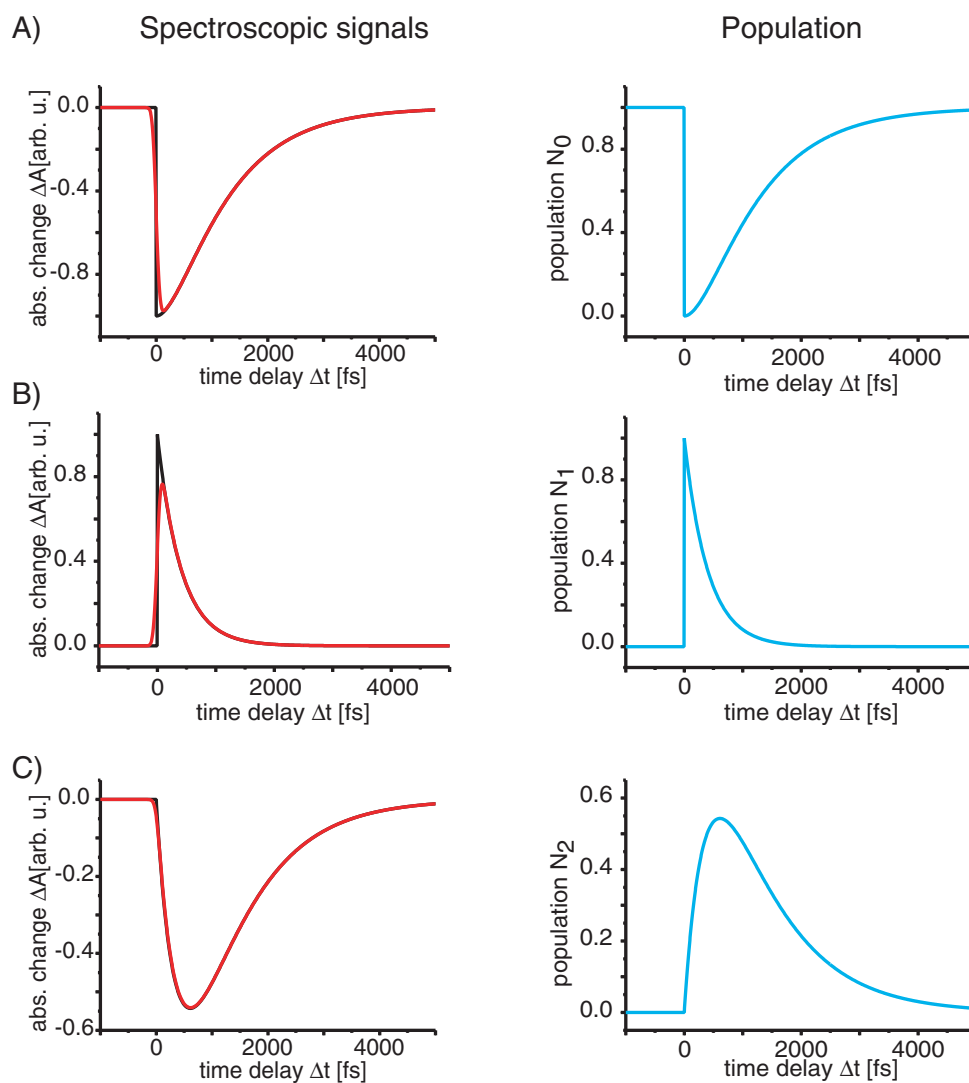


Figure 1.6: The plots of the first column show different spectroscopic pump-probe signals, that can be expected from the model, presented in Figure 1.5. With each of the spectroscopic signals, the temporal evolution of the population of one of the three states can be monitored. Black lines represent the calculated pump-probe signals for delta-function like pulses, while the red lines consider the influence of a Gaussian-shaped response function with FWHM=120 fs. The populations are given in the second column and are the result of the rate-equation model for the situation, described in Figure 1.5. A) Left: Pump depletion at  $\lambda_{probe} = \lambda_{pump}$ , right: Temporal evolution of the ground state population  $N_0(t)$ . B) Left: Excited state absorption at  $\lambda_{probe} = \lambda_{EA1}$ , right: Temporal evolution of the ground state population  $N_1(t)$ . C) Left: Stimulated emission at  $\lambda_{probe} = \lambda_{f1}$ , right: Temporal evolution of the ground state population  $N_2(t)$ .

maxima [59, 75]. The fluorescence band itself is on the red side with respect to the pump-wavelength. If different fluorescent states are present, the fluorescence as well can exhibit different maxima and thus cover a broad range in the spectrum.

All these bands can now overlap and superpose to a signal of very complicated shape. Additionally there will also be the contributions of hot-ground state absorption, the absorption of different products, solvated electrons, ionized species and effects due to solvent interactions, that can make the understanding of the pump-probe traces quite difficult. Methods, such as fluorescence upconversion (see Section 1.3) which can measure one of these contributions in absence of the others, can highly improve the interpretation of such pump-probe traces.

Up to now, all curves have been calculated for delta-function like pulses. The influence of a pulse with a certain pulse shape can be included into the signal by the convolution of the temporal behavior of the molecule  $f(t)$  and the response function  $g(t)$ .

$$S(\tau_d) = \int_{-\infty}^{\infty} g(t - \tau_d) f(t) dt \quad (1.19)$$

In this equation,  $S(\tau_d)$  denotes the measured signal, as it is the result from a real experiment. Here one can assume that the pulses are Gaussian-shaped and thus the response function is as well:

$$g(t) = \frac{2\sqrt{\ln(2)}}{FWHM\sqrt{\pi}} \exp\left(-4\ln(2)\frac{t^2}{FWHM^2}\right) \quad (1.20)$$

FWHM denotes the width of the response function at the half of its maximum amplitude. The convolution of the calculated signals for the model molecule with a response function of a FWHM of 120 fs are shown in Figure 1.6 as red lines. This value is chosen in that way that the dynamics can still be easily realized also in the convoluted case. As one can see from Figure 1.6A, if the time scale on which the molecular dynamics takes place is in the order of the FWHM of the response function, the experimental signal gets washed out. But if the response function is known, the dynamics can still be identified. With a very good experimental setup, dynamics taking place on a time scale much shorter than the time scale of laser pulse duration can be identified with a very accurate treatment of the measured signals [76].

Very often at least a part of the dynamics lasts much longer than the pulse duration. In these cases a delta-function is taken as response function. Already in the case of the ground state repopulation dynamics in Figure 1.6C the difference of the experimental signal (red lines) and the pure solution of the rate equations which is equivalent to the convolution with a delta-function, is negligible. In such cases the response function can be neglected.

## 1.7 Basic sketch for optimal control

There are many ways in controlling molecular reactions. For example, in conventional chemistry parameters such as temperature, pressure or concentration are changed to influence the outcome of a reaction. Another possibility is the formation of more stable products, with the help of catalysts.

The use of laser sources, in particular those, delivering ultrashort pulses, opens a different access to control molecular reactions. These methods are often summarized in the expression “optimal control”.

### 1.7.1 Ultrashort laser pulses in optimal control schemes

Some of the methods, summarized in the expression “optimal control“, base upon effects due to spectral phase of the electric light field. In the given case it is sufficient to look at linear polarized laser beams, since in the discussed experiments only electric fields of linear polarization are used. The electric field has a spatial and a temporal dependence. Many effects can be theoretically described by only considering the temporal dependence. To hold the description simple,  $\vec{E}(x, y, z, t)$  is reduced to  $E(t)$ . The spectral electric field can then be defined as

$$E(\omega) = |E_0(\omega)| e^{-i\phi(\omega)} \quad (1.21)$$

In this equation  $|E_0(\omega)|$  is the spectral amplitude and  $\phi(\omega)$  the spectral phase. The temporal electric field  $E(t)$  can be calculated by the inverse Fourier transformation of the spectral field:

$$E(t) = \frac{1}{\sqrt{2\pi}} \int_{-\infty}^{\infty} E(\omega) e^{i\omega t} d\omega \quad (1.22)$$

and the spectral electric field  $E(\omega)$  by the Fourier transform of the temporal field vice versa:

$$E(\omega) = \frac{1}{\sqrt{2\pi}} \int_{-\infty}^{\infty} E(t) e^{-i\omega t} dt \quad (1.23)$$

Because the temporal electric field  $E(t)$  is real, for the spectral electric field the relation  $E(\omega) = E^*(-\omega)$  is valid [77]. Therefore the values for positive frequencies are sufficient for a complete characterization of the spectral electric field.

$$E^+(\omega) = |E(\omega)| e^{i\phi(\omega)} = \begin{cases} E(\omega) & \text{for } \omega \geq 0, \\ 0 & \text{for } \omega < 0, \end{cases} \quad (1.24)$$

and

$$E(\omega) = E^+(\omega) + E^-(\omega) \quad (1.25)$$

The temporal electric field can be written as

$$E(t) = \frac{1}{2} |A(t)| e^{i\phi(t)} + c.c. = E^+(t) + E^-(t) \quad (1.26)$$

$E^+(t)$  can be derived from  $E^+(\omega)$  by inverse Fourier transformation.

In most cases of experimental relevance the spectral amplitude is centered around a carrier frequency  $\omega_0$  and non-negligible values for the spectral intensity are only expected in a small interval  $\Delta\omega$  around this carrier frequency. The spectral phase in 1.26 can thus be developed in a Taylor series around  $\omega_0$  if it does not change significantly with the frequency  $\omega$ :

$$\begin{aligned} \phi(\omega) = & \phi(\omega_0) + \left[ \frac{d\phi}{d\omega} \right]_{\omega_0} (\omega - \omega_0) + \frac{1}{2} \left[ \frac{d^2\phi}{d\omega^2} \right]_{\omega_0} (\omega - \omega_0)^2 + \\ & \frac{1}{6} \left[ \frac{d^3\phi}{d\omega^3} \right]_{\omega_0} (\omega - \omega_0)^3 + \dots \end{aligned} \quad (1.27)$$

The first coefficient describes a constant phase and is in the context of this work unimportant. The second one is antiproportional to the group velocity. This coefficient is responsible for a shift in time, as one can see by an inverse Fourier transformation. The third one is the derivative of the second one and therefore also called ‘‘group velocity dispersion’’ (GVD, sometimes also called ‘‘group delay dispersion’’ GDD). This shows the change of the group velocity with the frequency. The other terms are called after their order (‘‘Third Order Dispersion’’, TOD, ‘‘Forth Order Dispersion’’, FOD, ...). Especially the third, but also the forth and the fifth coefficient are often used as a single control parameter in control experiments, because of their physical relevance to many processes.

In the same way the temporal phase in 1.21 can be written as

$$\phi(t) = \phi(t=0) + \left[ \frac{d\phi}{dt} \right]_{t=0} t + \frac{1}{2} \left[ \frac{d^2\phi}{dt^2} \right]_{t=0} t^2 + \frac{1}{6} \left[ \frac{d^3\phi}{dt^3} \right]_{t=0} t^3 + \dots \quad (1.28)$$

The first coefficient again describes a constant phase, while the second symbolizes a shift in the frequency domain. The third coefficient shows the change of the frequency with the time. If the time-dependent frequency increases monotonously the pulse is called up-chirped and the third coefficient is different from zero. The pulse starts with red frequencies and sweeps to blue ones. In the acoustic analogue, this produces a characteristic noise, from which the name ‘‘chirp’’ is taken. In the case that the time-dependent frequency decreases monotonously the pulse is called down-chirped. The other coefficients are named ‘‘second order chirp’’, ‘‘third order chirp’’, ... . In the case that the phase is constant the pulse is called bandwidth limited. This pulse has the shortest time duration for a given spectrum. The fact that a linear spectral phase shifts the laser pulse in time gets especially relevant for time-dependent feedback signals as will be shown in Chapters 4, 5, and 6.

Due to the fact that the linear coefficient is only responsible for a temporal or spectral shift respectively, very often the “time-dependent phase”  $\varphi(t)$  is introduced:

$$\varphi(t) = \phi(t) - \omega_0 t \quad (1.29)$$

The time-dependent instantaneous frequency  $\omega(t)$  then becomes:

$$\omega(t) = \frac{d\phi}{dt} = \omega_0 + \frac{d\varphi}{dt} \quad (1.30)$$

With this definition  $E^+(t)$  can be written as

$$E^+(t) = \frac{1}{2}A(t)e^{i\varphi(t)}e^{i\omega_0 t} = \frac{1}{2}\tilde{A}(t)e^{i\omega_0 t} \quad (1.31)$$

with  $\tilde{A}(t)$  as the complex field envelope.

In experimental measurements the pulse energy is an important parameter. The pulse energy can be calculated by integration of the temporal pulse intensity over the spatial and temporal coordinates. The temporal intensity can be obtained by averaging over one optical cycle of the laser field:

$$I(t) = \varepsilon_0 cn \frac{1}{T} \int_{t-T/2}^{t+T/2} E^2(t') dt' \cong 2\varepsilon_0 cn \tilde{A}(t)\tilde{A}^*(t) \quad (1.32)$$

And analogue for the spectral intensity:

$$I(\omega) \cong 2\varepsilon_0 cn |E(\omega)|^2 \quad (1.33)$$

## 1.7.2 Concepts for optimal control

The control of molecular reactions has been traditionally achieved by conventional chemistry. The growing understanding of the molecular structure and the invention of the laser seemed to open a new possibility to control reactions. The idea was to deposit enough energy in a molecular bond by irradiation of light of a certain wavelength until it breaks [78]. The conceptual problem is the ultrafast redistribution of the energy throughout the whole molecule [79, 80]. Because of the coupling of the individual vibrational modes, the irradiated energy is redistributed and therefore the selective breaking of bonds is not possible.

Beside this conceptual problem for selective bond breakage, different excitation wavelengths can nevertheless influence the outcome of a chemical reaction [60]. First, tuning the excitation wavelength more and more into the absorption maximum will cause the simple control effect of a higher number of excited molecules. Of course this trivial effect will cause a higher product yield, but this mechanism does not influence

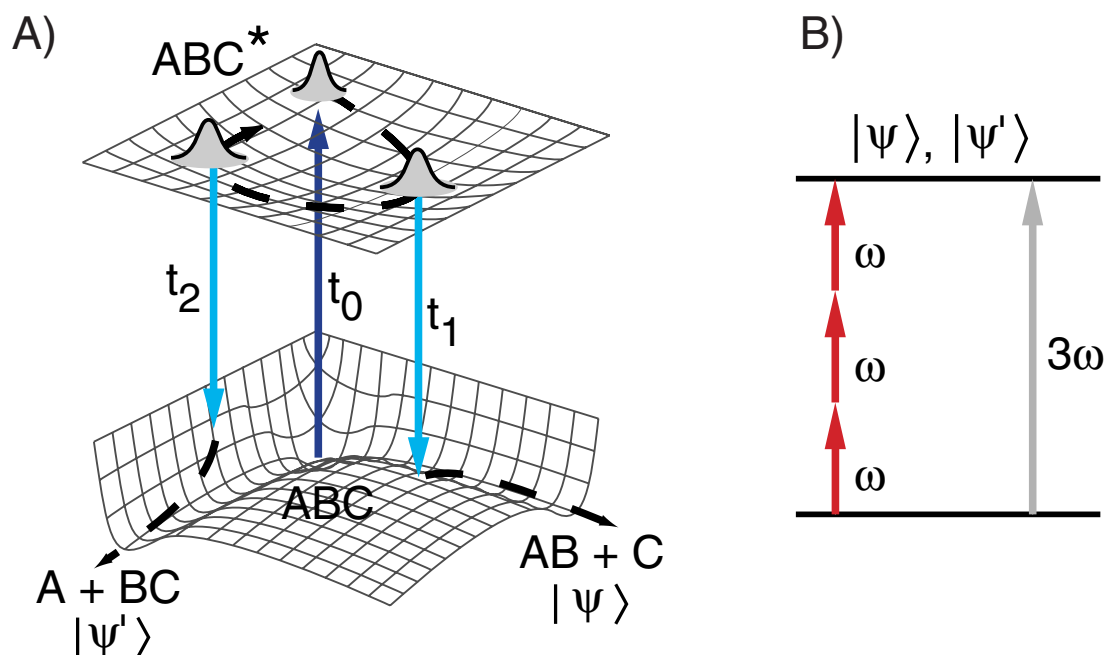


Figure 1.7: A) Sketch of the Tannor-Kosloff-Rice scheme [85–88]. By an ultrashort pump-pulse, a wave packet is created on the first excited surface. With the help of a second pulse of the proper wavelength and time delay in respect to the excitation event, the wave packet can be dumped into the desired product channel. B) Sketch of the Brumer-Shapiro scheme [89–94]. The initial and the final state are for example coupled by a single and a three photon transition. The population of the final state can be controlled by varying the relative phase between the two transitions.

the reaction directly. Beside this effect, different excitation wavelengths correspond to different Franck-Condon regions (see Section 1.1). The initial wave packet starts on different spots on the potential energy surface or even on a different surface. These changed starting values will influence the evolution of the wave packet and thus the final outcome of the reaction.

A similar single control parameter can be the intensity. Entering a high intensity regime, the shape of the potential energy surface will depend on the intensity of the laser field [81–84]. The modification of the potential energy surfaces will influence the evolution of the population. This can then effect the yield of the expected products.

These methods and other single control schemes for influencing chemical reaction are still very limited. The possibilities of modifying the evolution of a reaction are restricted to a few cases, in which the wave packet can effectively be influenced in the desired way. A more global method, that does not only work in a few single cases must be able to control the evolution of the reaction in a more general way and additionally take the processes of the redistribution of the excitation energy into account.

One way in this direction is the so called pump-dump or in some cases pump-



repump scheme, first introduced by Tannor, Kosloff and Rice [85–88] (see Figure 1.7A). In the first case, an ultrafast pump-pulse will create a wave packet on the excited surface, where it will evolve within time. After some time delay a second pulse can dump the wave packet to a lower potential energy surface. The wave packet will be transferred to a certain spot which can correspond to the desired product. This point depends on the choice of the parameters, connected with the dumping process. Beside the time delay between the two pulses the wavelength of both the pump and the dump pulse must be chosen to fit to the energy difference between the different spots on the potential energy surfaces. Not only the dumping of the wave packet, but also the excitation to an even higher lying potential energy surface is possible. There it will also evolve for some time and then decay back to lower lying potential energy surfaces and finally to some product state. It has been shown, that by this way, the dynamics can be modified as well [95].

Normally the wave packet tends to spread very fast. This causes the Franck-Condon overlap to become very poor in most cases and thus the control via a pump-dump mechanism is often very difficult. Applying different chirps to the excitation laser pulse have shown to influence the spreading of wave packets. Revivals of wave packets can thus be influenced [32, 96, 97]. Even more complex phase functions are able to reduce the effect of wave packet-spreading at a certain point in time and thus making the concepts of pump-dump schemes even more efficient [98].

Beside these complex variants of the Tannor-Kosloff-Rice scheme, there are different methods for controlling molecular dynamics based on the interference of different paths. Brumer and Shapiro proposed in 1986 a scheme based on this concept that was first experimentally realized in 1989 on atoms and later on also on small and medium size molecules [89–94](see Figure 1.7B). In this approach, the ground state is coupled to degenerate final states via two multiphoton transitions of different order, eg. a single photon with the frequency  $3\omega$  transition and a three photon transition at  $\omega$ . By tuning the relative phase between the  $\omega$  and the  $3\omega$  pump-pulse, constructive and destructive interference between population of the two degenerate final states can occur.

This intuitive scheme can now be extended to all the paths, that can be accessed by the different frequencies within an ultrashort laser pulse. A very interesting example in this context is the coherent control of the two-photon excitation of Cs-atoms by the group of Y. Silberberg [99, 100]. They showed both theoretically and experimentally, that certain dark pulses do not excite the system at all, while other pulses induce transition as effectively as transform limited pulses. These pulses have in contrast to the transform limited pulse a greatly reduced amplitude.

There is as well the chance that different competing paths exist, on which a certain point on a potential energy surface can be reached. Because of this a splitting of the initial wave packet and the interference at a different spot can cause an influence on the reaction dynamics [26].

The term optimal control covers a very broad spectrum of very different control mechanisms. The necessary control fields often have a very complicated structure.

These control fields can now in principle be theoretically calculated. Calculating an electric control field bears the problem of having a proper knowledge of the molecular Hamiltonian. The group of A. Rice has shown, that increasing the complexity of a molecular system changes the calculated control field [101]. They performed their calculation on the quite small, only three atoms spanning system HCN exhibiting the isomerization reaction  $\text{HCN} \rightarrow \text{CNH}$ . With increased complexity of the model, the complexity of the control field increases as well, while it is still possible to guide the reaction to the desired goal. They conclude that reducing the complexity of the calculations for the optimal electric control fields is not likely to be useful for the design of control fields, used for actively controlling reactions of polyatomic molecules.

Beside the difficulty in calculating the necessary pulse shapes, there is the question of their robustness under real experimental conditions. In most cases it will be very likely that the conditions under which the experiment is performed and the pulse shapes have been calculated will differ from each other. Beside parameters like temperature and pressure which may have small variations, the initial laser pulse normally does not have a Gaussian spectrum as generally assumed in the theory. Additionally its pulse duration and carrier frequency often shifts within an experimental period. This will probably need to correct the calculated pulse shapes at least a little bit. Such corrections will probably not be possible during the experiment, since the necessary calculations are very time-consuming.

Already in 1992, J. Rabitz has proposed a scheme to overcome these difficulties [1]. In this case, the problem is not separated into the steps of acquiring the Hamiltonian or respectively the mechanism of the reaction and then calculating the necessary electric control field which will modify the outcome of a reaction. In contrast to this, the Rabitz-scheme uses the experimental outcome of a reaction to guide the search for the desired electric control field. With the help of the experimental outcome, the effectiveness of an applied control field can be estimated. Different control fields are tested on the problem and with this information, new control fields can be calculated. These electric control fields have the potential to be better adapted to the given problem [102].

The problem of calculating better adapted pulse shapes can be done with the help of a learning algorithm. By this method, the control objective can be iteratively obtained. The remaining problem of generating shaped pulses has been solved with the help of a so called pulse shaper [103–105]. The working principle is explained in Section 2.4.

There are different algorithms, that can solve the problem of finding the pulse shape, that fulfills the control objective best. There are for example the method of testing all possibilities, Monte-Carlo simulations, simulated annealing or evolutionary algorithms. All this methods have their advantages and disadvantages which are discussed in [106]. Good results could be achieved by using evolutionary algorithms. These algorithms imitate the evolutionary process in nature. Transferred to the given problem, a certain number of random pulse shapes (individuals) is tested and form a first

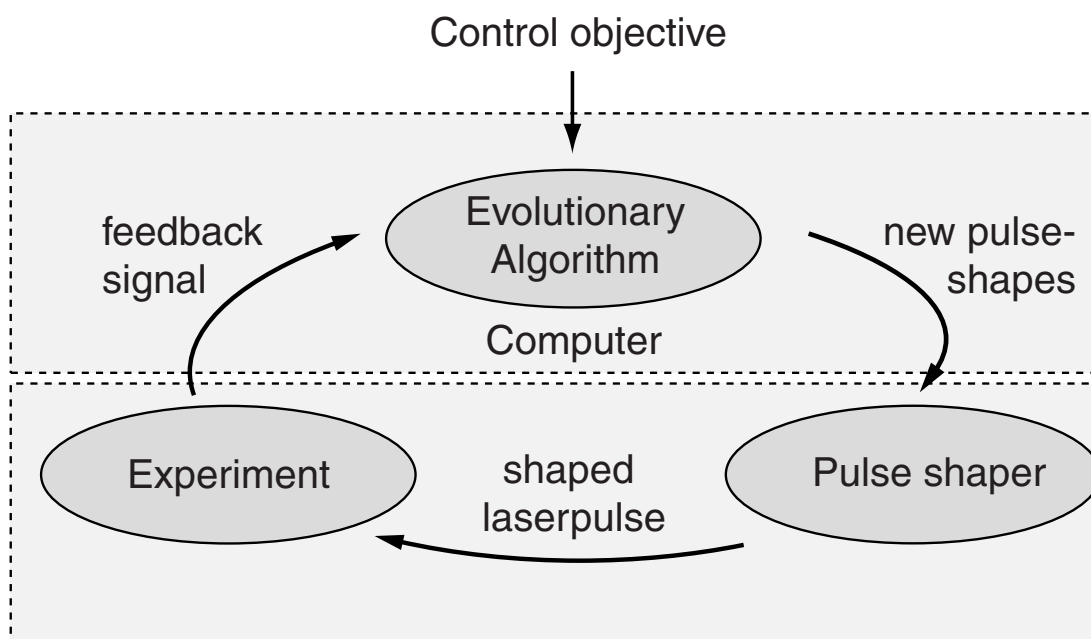


Figure 1.8: Scheme for adaptive femtosecond quantum control. A random first generation of laser pulse shapes will be experimentally tested onto the desired system according to a given control objective. Based on these experimental results, an evolutionary algorithm calculates a new generation of pulse shapes which have the potential to be better adapted to the given problem. By this method, the control objective can be iteratively obtained.

generation. Based on the effectiveness (fitness) of the different individuals, they survive, get crossed over or mutated. Depending on the representation of the pulse shape parameters and the formation of the next generation, these algorithms can be divided into the two subgroups of evolutionary strategies and genetic algorithms. The algorithm used in this work combines aspects of both. The exact realization is summarized in [106–108].

The described concept is called closed-loop learning control and has been successfully applied to many different molecular problems. These include for example the optimization of the excitation efficiency [6–8, 109], dissociation processes in the gas phase [2–5], energy transfer in large biomolecular molecules [9], selective excitation of different vibrational modes [110, 111] and the control of the geometrical rearrangement in the liquid phase [112].

After successfully having performed a closed-loop learning control experiment, it is necessary to measure the pulse shape and to calculate the electric field. A natural question that arises at this point, is how the control mechanism works. As described in the beginning, there are many different mechanisms that can influence a reaction. If not special care is taken (see Section 1.9) the learning algorithm can find pulse shapes based on any possible control mechanism, as well as pulse shapes that are a combina-

tion of all and even including features that are not necessary. Comparison with theory can help to understand the control mechanism [113, 114]. In some cases the control mechanism can be directly seen in the control fields in the context of the investigated problem. Of course basic, information about the process from other measurements must be available.

The control of different isotopes in  $K_2$  has been shown to depend to a big part on a shift in the excitation wavelength [115]. The manipulation of photodissociation reactions of small molecules in the gas phase was identified to happen by pulse sequences using the characteristic oscillation period of the molecule [116]. For the control of vibrational dynamics, double pulses have shown to form a good solution [110, 117]. Although in the latter experiment the algorithm used a reduced parameterization in which the parameters of a multipulse sequence were optimized, such a multipulse structure would also be evident from the result of an unrestricted optimization. Beside these cases it is often very difficult to directly access the control mechanism from the pulse shape. Therefore other methods are necessary to obtain the desired information from the measured pulse shape. These experimental methods are introduced in Section 1.9.

## 1.8 Spectroscopic methods for liquid phase feedback signals

As described in the previous section, an adequate feedback signal is essential for performing adaptive femtosecond quantum control experiments. This feedback signal has to provide the information about the effect of a shaped laser pulse on the system. With the help of this information, the learning algorithm can determine new better adapted pulse shapes by an iterative procedure. This method requires a high amount of tested individual pulse shapes. Using a full 128 pixels basis to define the spectral phase in which each pixel can be varied independently a lower limit for the necessary amount of pulse shapes will be about 1500. This limit arises from the experience of many experiments in our laboratory. Laser system instabilities will make it difficult to perform optimizations over more than 12 hours. Therefore the information about the response of the system on a pulse shape has to be recorded in less than a minute, although a more realistic upper level will be 10 s or less.

Every feedback method which can provide the necessary information within at least a minute can be used to guide the learning algorithm. The most suitable detection method strongly depends on the system under investigation. The most important control experiments in this thesis deal with the control of reactions in the liquid phase. Therefore the detection method to monitor the photoproduct concentrations has to be applicable in the liquid environment. Many chemical analysis methods such as chromatography are very sensitive to certain photoproducts, but they cannot fulfill the time limitation condition. Moreover, several chemical analysis techniques furthermore have the disadvantage that the affected sample volume has to be transported to a

different place where detection occurs. Such a complex procedure will most likely lower the accuracy of the information and therefore should not be used if possible.

In many adaptive femtosecond quantum control experiments on photodissociation of molecules in the gas phase, mass spectrometry was very successfully employed to identify the reaction products [2–5]. Liquid phase samples including complex biomolecules can in principle also be investigated by mass spectrometry techniques, such as electrospray ionization mass spectrometry or laser spray mass spectrometry [118–120]. However, this work will mainly deal with the control and investigation of the light-induced change of the atomic arrangement within molecules. The reaction products thus have different geometrical configurations, but identical atomic compositions and therefore cannot be detected by mass spectrometry methods.

In general, there are several optical methods which are capable to identify different photoproducts including isomers. If the photoproducts fluoresce at different frequencies, the amount of emitted light is proportional to the amount of photoproducts [7,47]. In order to fluoresce, the photoproducts have to be still in an excited state or must be excited with a second laser pulse. In many cases, the fluorescence spectra of different products strongly overlap. Thus, fluorescence is often a reliable tool for the identification of isomers, with the exception of situations where their fluorescence spectrum strongly overlap.

The Raman spectra of most molecules and even of isomers of the same molecule generally differ from each other and can thus be used to identify them. Different methods have been developed to record Raman spectra of molecules using cw-lasers, such as linear Raman spectroscopy, induced Raman spectroscopy or CARS (coherent anti-Stokes Raman spectroscopy). For a review on these methods, see Reference [11]. Linear Raman spectroscopy has the disadvantage of a low signal-to-noise ratio in comparison to the non-linear techniques, such as induced Raman spectroscopy or CARS. Otherwise, the setups which are necessary for the non-linear techniques are much more complicated.

In certain cases, such as for example in ultrafast switching processes as it is the topic of this thesis, it may be necessary to monitor concentrations of short-living products. Then the detection method has to possess a sufficient time resolution, which can be provided by several optical methods. The temporal evolution of vibrational modes can be monitored by CARS based on ultrafast lasers. Unfortunately the spectral resolution suffers strongly in time resolved CARS, which results in much broader Raman-lines compared to those in CW-Raman spectra. Ingenious modifications, often including pulse shaping methods, can help to improve the spectral resolution [121–129]. This can make it difficult to distinguish between the Raman spectra of different isomers. Also, the high intensities lead to a nonresonant Raman contributions, obscuring the desired resonant Raman lines. Up to now several single and multiparameter control schemes have been applied to Raman experiments [111, 121, 129–135]. It has been shown that it is possible to selectively excite certain modes and to influence the decay time of them. However, the low spectral resolution and the experimental difficulties limit the usefulness of time-resolved CARS for monitoring photoproducts.

There are several methods based on transient grating effects, that can provide information about a molecular reaction and the resulting reaction products (see for example Reference [77] and Reference [136]). Degenerate four-wave mixing (DFWM) has proven to be capable to serve as feedback signal for adaptive multiparameter control of vibrational dynamics [110, 117] of a molecule in the gas phase. Also single parameter control of a gas phase dissociation reaction could be monitored using DFWM as detection method [136]. DFWM can also be applied to solvated systems as for example shown in Reference [137]. For performing DFWM, at least three laser pulses are necessary. Using a fourth pump laser pulse provides the possibility to have an excitation wavelength different from the probe wavelength. This increases the complexity of the setup. Furthermore, the measurement of different states with DFWM makes it necessary to tune the wavelengths of the three DFWM pulses. Therefore it is very difficult to directly probe multiple reaction products with this technique.

With transient absorption spectroscopy (see Section 1.2), multiple reaction products which have different absorption spectra can be easily detect. The absorption spectra of molecules generally differ from each other in the infrared region, which make transient absorption spectroscopy by probing in this wavelength region an ideal method to provide a feedback signal to guide a control [138]. Also in the ultraviolet and visible wavelength regions, the photoproducts can have different absorption bands. Since it is experimentally much easier to perform experiments with laser pulses in the visible regime, using a feedback signal in the visible will facilitate the experiment. In order to perform transient absorption spectroscopy, only two laser pulses are required, which reduces noise introduced by vibrations of the optical elements and allows a fast alignment of the setup. The disadvantage of transient absorption spectroscopy in comparison to DFWM is the heterodyne measurement. The signal is a small modulation imposed on the probe intensity. It can be extracted by a difference measurement, which limits the repetition rate but increases the signal-to-noise ratio slightly.

With fluorescence upconversion spectroscopy (see Section 1.3), the time-resolved fluorescence of a molecule can be measured. If the population of a certain transition state has to be monitored, fluorescence upconversion can serve as feedback signal. However in many cases, the fluorescence spectra of molecules are very broad and therefore it is often difficult to distinguish between different photoproducts on the basis of their fluorescence. Furthermore, the method requires more experimental endeavors in comparison to probing stimulated emission by transient absorption spectroscopy, which is feasible more easily

In this thesis, experiments on the control of isomerization reaction are presented (see Chapters 4 and 5). It will turn out that an ultrafast measurement technique is required to monitor the product isomer yield. This feedback signal will be provided by transient absorption spectroscopy in the visible wavelength region. Because signals

at multiple wavelengths have to be recorded, transient absorption spectroscopy is the ideal feedback for the control of an isomerization reaction.

In Chapter 6 and in Chapter 4, Section 4.6, experiments are presented for which much simpler feedback signals are sufficient, which are the third harmonic generation yield in the first and the molecular fluorescence in the second case.

## 1.9 Mathematical description of double pulse generation

In the previous section, it could be seen that there are often many possible control mechanisms to a given problem. Some of these control mechanisms have a coherent nature and base on the interference of different paths, some of them base on non-coherent effects such as changing the excitation yield by drifting the central wavelength of the excitation pulse to the absorption maximum of the system.

Adaptive femtosecond quantum control experiments based on a feedback signal opens the possibility to find the optimal solution for a given problem under the given circumstances (see Section 1.7). In this adaptive approach, different solutions for a given problem can be combined, because the combination is often an even better solution than the individual ones only. In addition to this, the optimal solution can contain meaningless parts that do not help solving the given problem, but do not negatively affect the found solutions either. These parts make it often very difficult to understand a solution, that is found in an adaptive femtosecond quantum control experiment.

There are several different approaches by different groups to encounter this problem. Already the very first adaptive femtosecond quantum control experiment by K. Wilson used in principle a special attempt to simplify their solution [6]. They reduced the space of the possible solutions, by parameterizing the basis. The solution has been described by a very limited set of parameters. This bears both advantages and disadvantages. If the parameters are chosen well according to the given problem, the optimal solution has the chance of containing no misleading information. If the parameters have furthermore a physical meaning, it is well possible, that the found solution can be easily understood. Of course the price to pay is that initial knowledge about the given problem normally has to be present to find an adequate set of parameters. In addition to this, one can not be sure to have found the best possible of all solutions, since the solution space is restricted. The last disadvantage can be diminished by additional optimal control experiments without any restrictions on the parameter space. The fittest individual of this optimization can then be compared with the outcome of the fittest individual in the restricted case.

This concept of changed basis sets has been used by M. Motzkus [9,110] and largely improved by the group of T. Weinacht [139–141]. They introduced additional penalty functions to further suppress the occurrence of unimportant parts in the solution for a given optimization problem. This method improves largely the possibility of getting

the physical meaning out of such an optimal control solution.

A crucial question is the choice of the correct basis for the given problem. This issue has been tried to be solved by a concept known from statistics, called principal component analysis [142]. In this approach, the different generations of an optimization are analyzed by the calculation of a covariance matrix (see [142]). The eigenvector corresponding to the largest eigenvalues of this matrix are correlated with the fitness most. This set of eigenvectors serves as a new better basis and the basis can even be reduced since the eigenvectors for small eigenvalues should be of less significance. This method bears the problem that a covariance matrix based on the outcome of an evolutionary algorithm does often not contain enough information to yield a good new basis. The analysis of a large number of different covariance matrices is necessary to get a good new basis.

The attempts for understanding the outcome of an adaptive femtosecond control experiment, as performed by the groups of K. Wilson or T. Weinacht, are basically based on the reduction of the space of solutions and parameterizing it to a small number of parameters. For an accurate treatment many successful optimizations with many different basis sets and many penalty functions have to be performed. To find the correct values for each penalty function, several successful optimizations are necessary. For complicated setups with complex molecules and interaction with the environment as it will be the topic in this thesis, a high number of optimal control experiments is difficult to perform, since every single optimal control experiment will take many hours. Including the necessary preparations before the control experiment and the additional measurements after it, in the case of bacteriorhodopsin one single control experiment takes on average twelve hours. Therefore the presented attempt is not usable in this case.

To overcome this problem, the test measurements must be possible to be performed with high accuracy in a short time. Therefore the idea is not to parameterize the space of solutions for the optimal control experiment, but to perform a sufficient high number of additional experiments in which different parameters of physical meaning are scanned continuously. The accessible subspace of solutions by this method is quite small in comparison with all the possibilities, that can be accessed in a free optimal control experiment. But because the parameters are chosen with a physical meaning, the tested subspace has a high relevance and a good chance of showing an interesting behaviour.

This method has been used to investigate reaction mechanisms long before the first adaptive femtosecond quantum control experiments [32, 143–145]. Single parameters, such as chirp, excitation wavelength or excitation energy have proven to have a high influence on many reactions. In possible control experiments for many reactions, such single control parameters can be included in the optimal control solution. Comparing the optimal solution with different individual solutions, that also partly solve the given problem, can help identifying the meaningful part in the optimal solution and separating it from the misleading information.



The method of scanning different parameters furthermore has the advantage of being reproducible. In the case that the parameter set is complete enough, this method can be similarly valuable as the method of reducing the basis set of a control experiment. Of course a much higher subspace can be addressed by the method of the reduced basis set for the optimization. But there is as well the chance that the global maximum is not found, depending on the learning algorithm. In the case of a parameter scan, often many values can be interpolated and do not need to be measured. Therefore a parameter scan can contain a similar amount of information as being addressed by a restricted closed-loop experiment. In the closed-loop experiment in principle every possible pulse shape can be addressed. However, many of those pulse shapes will have no significant difference or are completely meaningless in the context of the control objective. These cases can be excluded in a parameter scan.

In the context of scanning different parameters, the group of T. Baumert has applied different sinusoidal phase-functions in the frequency domain on an Autler-Townes state-doubled problem [84]. This problem has been shown to be extremely sensitive to the given parameterization. Adapting different sinusoidal phase-functions on a laser-pulse in the frequency domain results in pulse trains of different amplitude and distance in the time domain. The experiment has shown, that the space of possible solutions is very complex, showing multiple local maxima and minima.

In this work, a scheme for testing pump-dump like processes is presented. Many reactions have been shown to be sensitive to such pulse shapes as shown in Section 1.7. These pump-dump like processes are performed by two pulses, the first one prepares the molecule in a certain state, the second influences the excited molecule after some time in a desired way. The outcome depends on the time delay between the two pulses, the central frequency and the amplitude of the pulses. Since in an optimal control experiment the solution can easily be optimized for these parameters, a systematic scan of these would yield a lot of valuable information.

Other experiments have shown that the absolute phase difference between two pulses can have influence on the reaction [110, 117]. Therefore scanning the difference of the absolute phase between the two pulses is also a very interesting control parameter.

Double pulses can be generated by applying a special spectral phase to a bandwidth limited laser pulse. As seen in Section 1.7.1, a linear spectral phase shifts the pulse in the time domain. Intuitively a colored double pulse can be created by applying a triangular spectral phase which shifts a part of the spectrum forward and the other part backward in time [146]:

$$\phi(\omega) = \text{Sign}(\omega - (\omega_0 + \delta\omega)) \frac{\Delta\tau}{2} (\omega - (\omega_0 + \delta\omega)) \quad (1.34)$$

In this equation is  $\frac{\Delta\tau}{2}$  the spectral phase slope and  $(\omega_0 + \delta\omega)$  the point at which the spectrum is broken and shifted either forward or backward in time. Thus  $\Delta\tau$  determines the pulse delay between the two pulses and the spectral breakpoint  $\omega_0 - \delta\omega$  the spectral

width and the amplitude of the sub-pulses.

The spectral amplitude  $|E(\omega)|$  of the laser pulse can be assumed to be Gaussian

$$|E(\omega)| = E_0 e^{-\frac{(\omega - \omega_0)^2}{\sigma^2}} \quad (1.35)$$

In this equation,  $\sigma$  is the half width at 1/e. If Equations 1.34 and 1.35 are inserted in Equation 1.21 one gets the spectral electric field for this definitions which can be transformed into the time domain by the inverse Fourier transformation 1.22:

$$E(t) = \frac{E_0 \sigma}{2\sqrt{2}} e^{-i\omega_0 t} \left( e^{-\frac{(\frac{\Delta\tau}{2} + t)^2 \sigma^2}{4}} \left( 1 - i \operatorname{Erfi} \left( \frac{1}{2} \left( \frac{\Delta\tau}{2} + t \right) \sigma \right) \right) + e^{-\frac{(\frac{\Delta\tau}{2} - t)^2 \sigma^2}{4}} \left( 1 - i \operatorname{Erfi} \left( \frac{1}{2} \left( \frac{\Delta\tau}{2} - t \right) \sigma \right) \right) \right) \quad (1.36)$$

with the antisymmetric *Erfi* function defined by

$$\operatorname{Erfi}(x) = 2\pi^{-\frac{1}{2}} \int_0^x e^{(y^2)} dy. \quad (1.37)$$

If the spectral breakpoint  $\omega_0 + \delta\omega$  is set to the carrier-frequency, one gets two pulses, whose amplitudes are equal. In this case Equation 1.36 can be decomposed in a sum of two electric field  $E(t) = E_1(t) + E_2(t)$  with

$$E_{1,2}(t) = \frac{E_0 \sigma}{2\sqrt{2}} e^{-i\omega_0 t} \left( e^{-\frac{(\frac{\Delta\tau}{2} \pm t)^2 \sigma^2}{4}} \left( 1 - i \operatorname{Erfi} \left( \frac{1}{2} \left( \frac{\Delta\tau}{2} \pm t \right) \sigma \right) \right) \right) \quad (1.38)$$

In this representation, one can easily see, that the temporal electric field is composed of two individual pulses centered around  $\pm \frac{\Delta\tau}{2}$ .

With the two parameters  $\Delta\tau$  and  $(\omega_0 + \delta\omega)$ , double pulses with a desired distance and a defined amplitude ratio can be created. Two illustrative examples for a double pulse distance of 1000 fs and identical amplitudes in the first case and different in the second are shown in Figure 1.9A and B.

By scanning the two parameters time delay and breakpoint and applying the resulting pulse shapes to a problem, sensitive to the this parameterization, a two dimensional control map can be measured. With the help of this control map, the dependence of the given problem on the double pulse distance, color and amplitude ratio can be directly visualized.

As mentioned before, it could be very interesting to investigate the effect of the phase difference between the two individual pulses. Therefore the effect of a phase step on the temporal pulse shape is investigated first. Again a Gaussian spectral amplitude  $|E(\omega)|$  is assumed for the laser pulses (see Equation 1.35). In this case the spectral phase has the form:

$$\phi(\omega) = A \cdot \operatorname{UnitStep}(\omega - (\omega_0 + \delta\omega)) \quad (1.39)$$

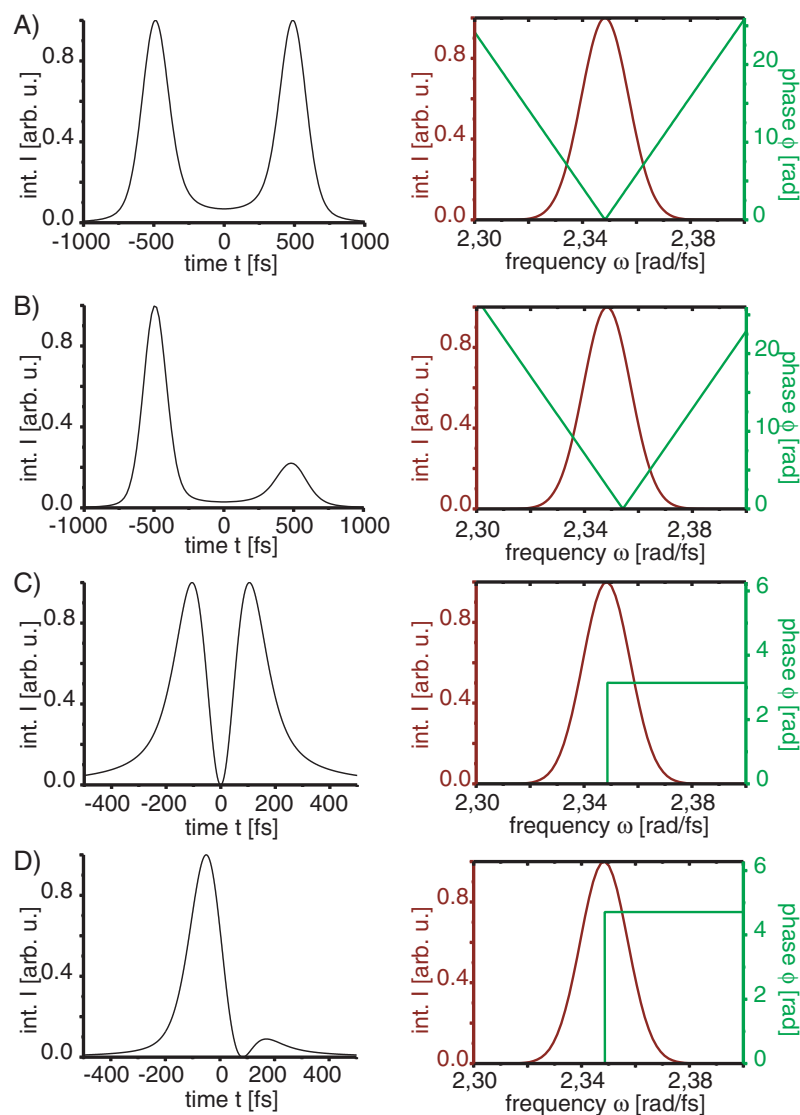


Figure 1.9: A), C), D) Plots of the analytical solutions for different spectral phase functions. The first column presents the calculated temporal amplitude profiles, the second column the assumed spectral amplitude profile and spectral phase. A) Triangular spectral phase for a slope of 1000 fs and for a breakpoint at  $\omega_0 + \delta\omega = 2.348 \text{ rad/fs}$ . B) Numerical solution for the case of a triangular phase with the same slope as in A) but for a breakpoint  $(\omega_0 - \delta\omega) = 2.354 \text{ rad/fs}$ . In plots C) and D) the spectral phase describes a step-function with  $A = \pi$  in the first case and  $A = 3/2\pi$  in the second. In all cases, the spectral width at 1/e of the maximal amplitude is  $\sigma = 0.017 \text{ rad/fs}$  and the carrier-frequency is  $\omega_0 = 2.348 \text{ rad/fs}$ .

UnitStep(x) is the step function with 0 for  $x < 0$  and 1 for  $x \geq 0$ .  $A$  is the amplitude

factor for the phase step. For the case of  $\sigma = 1$  and  $\delta\omega = 0$ , an easy expression for the temporal electric field can be obtained by the inverse Fourier transformation:

$$E(t) = e^{-i\omega_0 t} \frac{\sigma e^{\frac{\sigma^2 t^2}{4}} E_0 (1 + e^{iA} + i(-1 + e^{iA}) \text{Erfi}(-\frac{\sigma t}{2}))}{2\sqrt{2}}. \quad (1.40)$$

This simple spectral phase function already has a big influence on the temporal shape of the laser pulse as can be seen from the two examples in Figure 1.9C and D.

To investigate the combined effect of the phase step and the triangular phase, a program has been written, that integrated parts of the numerical package LAB2 in the computer code [147]. With the help of this numerical package the effect of different phases can be simulated under experimental conditions. Changes of the spectral phase can be applied by a pulse shaper. As will be discussed in Section 2.4, this experimental tool has certain limitations. If the desired pulse shape gets closer to these limitations, the experimental results will include more artifacts. The simulated pulse shapes in this chapter are still in a region, where the experimental artifacts are very small. Still they are included in the calculations.

The first two rows in Figure 1.10 show three example pulses for different triangular phases and different phase steps in the temporal and in the spectral region. A more complete table can be found in the Appendix A.5, since it will become necessary for the understanding of the experimental results presented in Chapter 6. The pulse parameters are chosen similar to our the experimental possibilities, a carrier-frequency of  $\omega_0 = 2.348 \text{ rad/fs}$  and a pulse duration of 80 fs. The breakpoint  $\omega_0 - \delta\omega$  is for all cases set to 0. The first column shows the bandwidth limited case. The second the result for the small value of  $\Delta\tau = -150 \text{ fs}$  and a phase step of  $3/2\pi$  identical the case in Figure 1.9D. Since  $\Delta\tau$  is nearly twice the value of the pulse duration, the effect of the triangular phase slope is already visible. This effect causes two pulses of equal amplitude. The additional phase step of  $A = 3/2\pi$  is responsible of the difference of the two amplitudes. For values of  $\Delta\tau$  being larger than 500 fs, the modulation of the amplitudes due to the phase step becomes very small.

Most experiments in this work are not performed at the central frequency  $\omega_0 = 2.348 \text{ rad/fs}$  but at the frequency of the second harmonic ( $\omega_0 = 4.7 \text{ rad/fs}$ ). This can be achieved by frequency doubling in a nonlinear crystal (see Section 2.2). Since this effect is proportional to the square of the fundamental intensity, the effects of the different amplitudes gets enhanced. This can be very well seen in the third row of Figure 1.10. Due to the additional squaring of the intensity by the second harmonic process, the different pulse shapes can have different pulse energies.

The simulation of scanning the triangular phase slope  $\frac{\Delta\tau}{2}$  and the phase step  $A$  for the breakpoint  $\omega_0 - \delta\omega$  at the carrier frequency and frequency doubling the resulting pulse will produce in the contour plot for the pulse energy. For better comparison with the experimental data, this contour plot is shown in Chapter 6, Figure 6.2B. For convenience the wavelength is chosen as parameter for the breakpoint instead of the frequency. The second harmonic of the fundamental laser pulse is very easily accessible

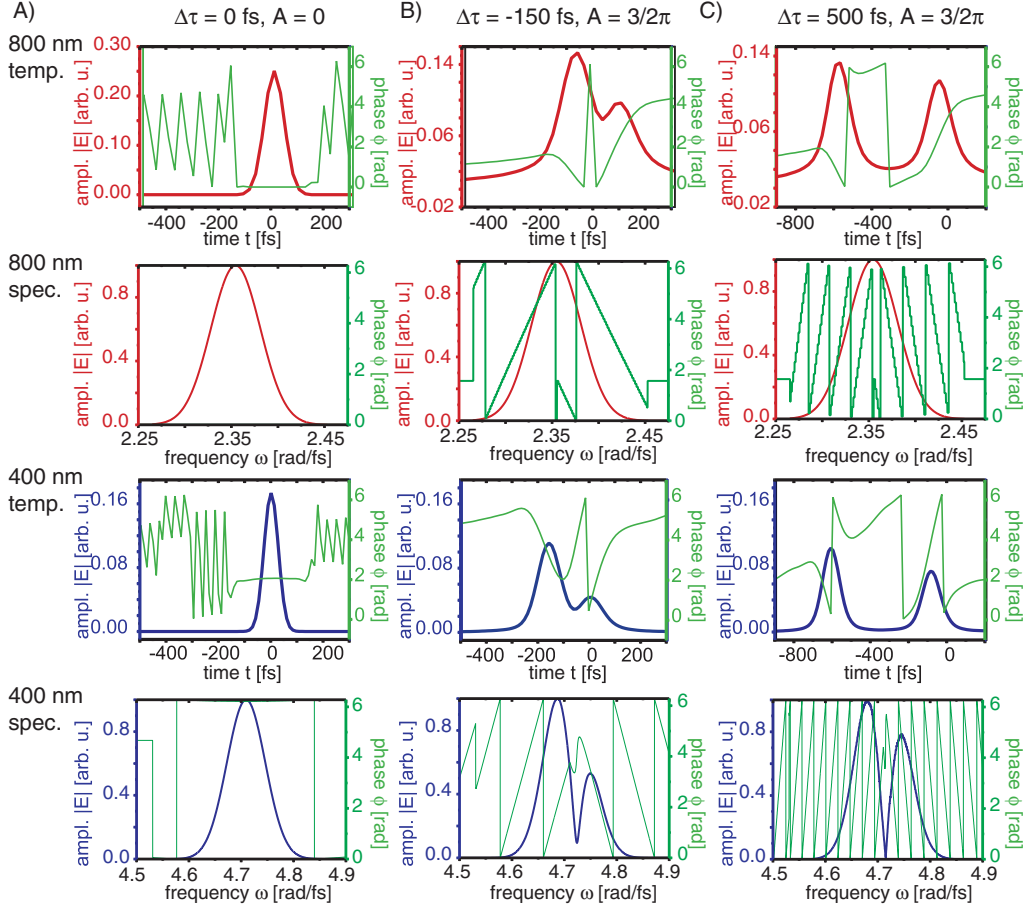


Figure 1.10: Spectral and temporal pulse amplitude profiles and phase functions for different spectral phases, calculated with a program that integrated parts of the numerical package LAB2 into the programming code [147]. For all pulse shapes a carrier frequency of  $\omega_0 = 2.348$  rad/fs and a pulse width of 80 fs are assumed. The different rows show the spectral and temporal representation of the electric field for the fundamental pulse in the first two rows and for the second harmonic in a BBO (Beta Barium Borate) crystal with a thickness of  $100 \mu\text{m}$  in the last two rows. The numerical calculations include the experimental artifacts that will result from the pulse shaper and the crystal. The second harmonic generation is assumed to take place in a non-depleted regime. The column A) shows the different representations for a bandwidth limited pulse, the next column B) for a double triangular phase slope of  $-150$  fs and a phase step of  $A = 3/2\pi$ . In the case of column C) the double triangular phase slope is chosen to be  $-500$  fs and  $A = 3/2\pi$ . A more complete table can be found in the Appendix A.5.

in an experiment and can thus be useful for comparing the theory with the experiment.

Scanning the triangular phase slope  $\frac{\Delta\tau}{2}$  and the phase step  $A$  at a fixed breakpoint  $\lambda_0 - \delta\lambda$  thus results in a big variety of different pulses. In the case  $A=0$  only colored

double pulses are produced. In contrast, in the case that  $A$  is unequal to zero the double pulses are additionally modulated in their amplitude and exhibit a spectral phase step. This results in a map of a high number of different pulse shapes, that can cause pump-dump like processes.

Scanning the triangular phase slope  $\frac{\Delta\tau}{2}$  and the break point  $\lambda_0 - \delta\lambda$  for the phase step  $A=0$  and frequency doubling the resulting pulse will result in the contour plot for the pulse energy shown again for better comparison with the experiments in Chapter 6 Figure 6.3B. Also in this case, the frequency doubling process will cause different pulse energies for the different spectral phases. The lowest energy is expected for double pulses of the same height due to the squaring process by the second harmonic generation. If the breakpoint  $\lambda_0 - \delta\lambda$  is very different from the central wavelength  $\lambda_0$  the pulse gets only shifted in time, and therefore no difference compared to zero spectral phase will be the result.

Due to the second harmonic process, the spectrum of the pulse is highly modulated and in most cases not Gaussian anymore (see the tables in Appendix A.5 and Figure 1.10). This has to be considered if this parameterization scheme is used including frequency doubling. Simulations including effects due to the excitation with spectrally different pump-pulses are necessary to understand the outcome of the experiment. Such simulations are demonstrated in Chapter 6.2.

# Chapter 2

## Technological concepts

The main ideas and necessary methods for the experiments in the context of this work have been presented in Chapter 1. This chapter describes the technological details, essential to perform the desired experiments. A main topic of this thesis is the use of spectrally shaped femtosecond laser pulses in various ways. The technological concept for generating laser pulses and shaping their spectral phase is described in the beginning of this chapter. These laser pulses can then be used in the experiments. Therefore most often wavelengths other than those available by the pure laser system itself are needed. These can be obtained by using different nonlinear effects. By passing several optical elements and in many cases a nonlinear crystal, the phase-shaped laser pulses change their properties. Therefore a characterization of the pulse shape close to the experiment is needed for pulses of different central wavelengths. The methods for characterization of the pulse shape, that are employed in this thesis, are outlined at the end of the chapter.

### 2.1 Laser system

The main component of the whole setup is the laser system. This laser system has been partly rebuilt during this work, mainly to increase its pointing stability and to decrease the fluctuations of the pulse energy both on a short and on a long time scale. Therefore, the beam traveling distance between the different components is decreased to a minimum. Different components such as mirror holders and posts have been replaced by more stable versions. Newly available beamsplitters with better characteristics allow for a higher throughput and a broader spectrum. New solid-state pump laser sources greatly reduce the pulse-to-pulse fluctuations. In the context of the rebuilding of the laser system, all optical components on the laser table got rearranged to guarantee the best performance.

The rebuilt laser system now produces ultrashort laser pulses at a central wavelength of 800 nm, a repetition rate of 1 kHz, a pulse duration of 80 fs and a pulse energy

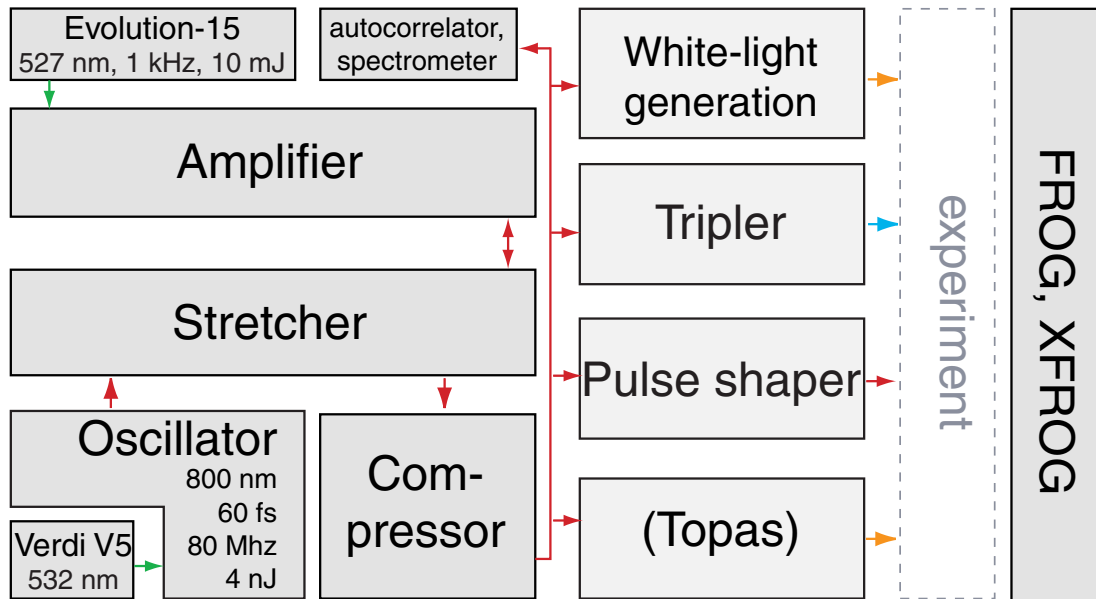


Figure 2.1: Scheme of the arrangement of the basic components of the laser system. The ultrashort pulses from the oscillator are stretched to 120 ps in the stretcher to avoid damage in the succeeding components. The stretched pulses are amplified in the following component by a factor of  $10^6$  and afterward temporally compressed to 80 fs. The resulting pulse has a central wavelength of 800 nm, a pulse energy of 0.7 mJ at a repetition rate of 1 kHz. Additionally the diagnostic tools, the pulse shaper and the different possibilities for converting light into different frequency regions are shown as well as their integration into the experiment. These additional components as far as necessary for the experiments will be introduced in this chapter.

of 0.7 mJ. Briefly, the homebuilt oscillator is pumped by a solid-state diode-pumped frequency-doubled Nd:Vanadate laser from Coherent Inc. (model: Verdi V-5) [148]. By using the Kerr-lens mode-locking effect in a Ti:sapphire crystal, the oscillator produces pulses at central wavelength of 800 nm, a pulse duration of about 60 fs and a pulse energy of 4 nJ at a repetition rate of 90 MHz [149]. This pulse energy is in most cases not high enough to perform the desired experiments. Therefore the pulse are amplified based on the principle of chirped pulse amplification [150]. The pulses from the oscillator get stretched in the so called stretcher to a pulse duration of 120 ps by introducing positive chirp. This is necessary to reduce the peak intensity of the pulses, in order to prevent damage in the succeeding components, especially within the regenerative amplifier. The amplifier itself consists of a Ti:sapphire resonator, which is pumped by a Nd:YLF laser (model: Evolution-15, manufactured by Coherent) working at 10 W, 527 nm and at a repetition rate of 1 kHz [151]. The Nd:YLF laser itself is pumped by an AlGaAs laser diode. One of the stretched oscillator pulses is selected each millisecond by a Pockels-cell and is amplified by a factor of  $10^6$  in the regenerative amplifier. After being amplified the pulse is switched out by the same Pockels-cell.



The pulses are then recompressed in the compressor to a pulse duration of 80 fs.

This setup is shown as a sketch in Figure 2.1. Additionally the diagnostic tools, the pulse shaper and the different possibilities for converting light into different frequency regions are shown as well as their integration into the experiment. These additional components as far as necessary for the experiments will be introduced in this chapter.

## 2.2 Extension to other wavelengths regions

Nonlinear effects are widely used throughout this work. Most important examples are the white-light generation and the sum-frequency mixing. Ultrashort laser pulses are combined with very high intensities and thus with very high field strengths. In this case the polarization  $\vec{P}$  does not scale linearly with  $\vec{E}$  anymore, but higher orders must be taken into account:

$$\vec{P}(\omega) = \epsilon_0 \chi^{(1)}(\omega) \vec{E}(\omega) + \vec{P}^{NL}(\omega) \quad (2.1)$$

$$= \epsilon_0 \left[ \chi^{(1)}(\omega) \vec{E}(\omega) + (\chi^{(2)} \vec{E}(\omega)) \vec{E}(\omega) \right. \\ \left. + ((\chi^{(3)} \vec{E}(\omega)) \vec{E}(\omega)) \vec{E}(\omega) + \dots \right] \quad (2.2)$$

The quantities  $\chi^{(n)}$  are called “nonlinear optical susceptibilities of  $n^{th}$  order”, which are themselves tensors of the order  $n+1$ . For the most general case the magnetic terms in  $\vec{H}$  and mixing terms of  $\vec{H}$  and  $\vec{E}$  must as well be included in Equation 2.1, which are important for the Faraday effect. However, the magnetic terms and mixing terms shall not be considered in the following.

The polarization is the origin for a new electric field strength, whose frequency is in the linear case the same as the one of the fundamental field. Because of the nonlinear part, there is also the chance for new field strengths at different frequencies. This effect can be used for the generation of electric fields at new frequencies, which can be already seen for the term connected with the second order of the nonlinear optical susceptibility. For the simplest case, the electric field can be assumed to be linearly polarized and propagating in the z-direction as a plane wave:

$$\vec{E}(z,t) = \frac{1}{2} \vec{A}(z,t) e^{i(\omega t - k_0 z)} + c.c. \quad (2.3)$$

In this simple case the product of  $\vec{E} \cdot \vec{E}$  yields:

$$\vec{E}^2(z,t) = \frac{1}{4} \vec{A}^2(z,t) e^{i2\omega t - 2kz} + \vec{A}(z,t) \vec{A}^*(z,t) + c.c. \quad (2.4)$$

If  $\chi^{(2)}$  is different from zero a new electric field strength at  $2\omega$  is created in addition to the linear term which causes the field strength at the carrier frequency of the

fundamental beam. Furthermore there is a non-oscillating contribution, which is called “optical rectification”. The voltage cause by this constant field can be experimentally measured [152].

The intensity connected with these new electric fields is strongly dependent on the properties of the material in which they are generated. The most important ones are the transparency, the value of the nonlinearity and since most often crystals are used, the angle of the crystal axis with respect to the electric field. But also external parameters such as the temperature have a high influence on the efficiency.

Starting point for the description of the various effects due to the interaction of the electric field with matter is the wave equation, which can be derived from the Maxwell equations:

$$\left[ \nabla \times (\nabla \times) + \frac{1}{c_0^2} \frac{\partial^2}{\partial t^2} \right] \vec{E}(\vec{r}, t) = -\mu_0 \frac{\partial^2}{\partial t^2} \vec{P}(\vec{r}, t) \quad (2.5)$$

The previous assumption of the simplification of the arbitrary propagation direction allows us to replace  $\nabla \times \nabla \times \vec{E}$  by  $-\partial^2 \vec{E} / \partial z^2$ .

To calculate the electric fields for the very important case of second harmonic generation (SHG), several assumptions have to be made. As most often in problems similar to the second harmonic generation the slowly varying envelope approximation is used. This is valid for all laser pulses, except the shortest. It holds if the laser pulse is significantly longer than an optical cycle (about 2 fs for visible light), what is fulfilled in the experiments in this thesis. The electric field can then be written as a product of a fast varying carrier wave and a slowly varying envelope function. Furthermore, the second order derivatives in Equation 2.5 of the slowly varying envelopes can be neglected since the measure of its change is the derivative. Also the group velocity dispersion and the higher order dispersion are assumed to be of minor influence. In addition, depletion of the fundamental beam is assumed to be of minor importance, so that the terms connected with this effect can be neglected. Then in the case of Type I second harmonic generation, where the fundamental beam propagates either as ordinary or as extraordinary beam, producing an extraordinary or an ordinary wave, the wave-equation can be formulated for the fundamental [77] and the second harmonic beam:

$$\left( \frac{\partial}{\partial z} + \frac{1}{v} \frac{\partial}{\partial t} \right) \tilde{A}_1 = -i\chi^{(2)} \frac{\omega_1^2}{2c^2 k_1} \tilde{A}_1^* \tilde{A}_2 e^{i\Delta k z} \quad (2.6)$$

$$\left( \frac{\partial}{\partial z} + \frac{1}{v} \frac{\partial}{\partial t} \right) \tilde{A}_2 = -i\chi^{(2)} \frac{\omega_1^2}{2c^2 k_1} \tilde{A}_1^2 e^{i\Delta k z} \quad (2.7)$$

The subscript 1 denotes the fundamental field, while the subscript 2 denotes the generated second harmonic field.

For the generation of new field strengths, the conservation of energy requires

$$\omega_2 = 2\omega_1 \quad (2.8)$$

Of course, the momentum-conservation also has to be fulfilled

$$\Delta k = 2k_1 - k_2 \quad (2.9)$$

This relation is called the “phase-matching condition” for the second harmonic generation and  $\Delta k$  the “phase-mismatch” and expresses the momentum-conservation. If the interaction length  $l$  is finite, the momentum-conservation only needs to be fulfilled with an uncertainty of  $1/l$  which is expressed by the phase matching condition 2.9 [153]. The highest efficiency for the second harmonic process is expected, if the momentum conservation is fulfilled, what means that the phase-mismatch  $\Delta k$  is equal zero. Because of the energy conservation (Equation 2.8) and  $k_i = \frac{\omega_i n(\omega_i)}{c_0}$ , Equation 2.9 can be written as

$$\Delta k = 0 = 2 \frac{\omega_1 n(\omega_1)}{c_0} - \frac{\omega_2 n(\omega_2)}{c_0} = \frac{2}{c_0} \omega_1 [n(\omega_1) - n(\omega_2)] \quad (2.10)$$

This relation is not fulfilled for general cases, because ordinary materials do not show anormal dispersion in their transparent regions ( $n(\omega_1) > n(\omega_2)$ ). A possibility to solve this problem is provided by negative uniaxial crystals, for which  $n_{e0}(\omega_i) < n_o(\omega_i)$  is valid.  $n_o$  describes the “ordinary” and  $n_{e0}$  the “extraordinary index of refraction”. The coordinate system shall now be defined in that way, that the optical axis of the nonlinear crystal is identical with the z-axis. The fundamental beam is assumed to lie in the xz-plane and have the angle  $\vartheta$  with the optical axis. The ordinary index of refraction is independent from  $\vartheta$ , while the behaviour of extraordinary index of refraction can be described by [154]:

$$n_e(\vartheta, \omega) = \frac{n_o(\omega)^2 n_{e0}(\omega)^2}{n_o(\omega) \sin^2 \vartheta + n_{e0}(\omega)^2 \cos^2 \vartheta} \quad (2.11)$$

In the case of type I SHG with  $n(\omega_1) = n_o(\omega_1)$  and  $n(\omega_2) = n_e(\omega_2)$  Equation 2.11 can be inserted into 2.10 to calculate the angle  $\vartheta$  at which the phase-matching condition is equal to zero and the second harmonic generation process has the highest yield.

Beside the above explained method to ensure  $\Delta k = 0$ , it is possible to fulfill this condition with the help of the temperature dependence of the refractive index. By this, the angle  $\theta = 90^\circ$  is possible, at which the acceptance is the highest and the misalignment of crystal is less critical. This scheme of temperature phase matching is for example employed in the pump lasers.

The coupled differential Equations 2.6 and 2.7 can be solved for the case of exact phase matching at the carrier frequency and small conversion efficiency (below few tens of percent [77]). The differential equations are then solved by [77, 155]

$$\tilde{A}_2(\omega_2) \propto \int \tilde{A}_1(\omega_1) \tilde{A}_1(\omega_2 - \omega_1) d\omega_1 \quad (2.12)$$

The temporal complex field envelope can be calculated by

$$\tilde{A}_2(t) \propto \tilde{A}_1(t)^2 \quad (2.13)$$

The temporal field of the second harmonic is therefore similar in its structure to the one of the fundamental beam. In contrast to this, the spectral field can be significantly changed due to the convolution in Equation 2.12. This will be discussed in more detail at the end of Section 2.4.

The fundamental beam and the second harmonic have different group velocities. In thick crystals this “group-velocity mismatch” results in a temporal broadening. If the crystal is thin enough, the inverse effect can be observed. Because of the quadratic dependence in Equation 2.13, the second harmonic pulse is shorter than the fundamental pulse. Under certain conditions, the effect of the group-velocity mismatch can also lead to a pulse-shortening, if the temporally leading edge of the second harmonic pulse is always at such a position, that it is influenced by the undepleted part of the fundamental pulse. Then the leading edge will be more amplified than the trailing one, what results in a pulse profile with a reduced full width at the half of its maximum [77, 153].

### 2.3 Self-phase modulation and white-light generation

To get a bright spectrum of information about a molecular reaction it is essential to probe the dynamics at different energies. As pointed out in Section 1.2, in the case of pump-probe spectroscopy, this can be realized by using different wavelengths, for both pump and probe. Since the pump pulse needs to be of a significant intensity in contrast to the probe pulse, different mechanisms for generating light of different wavelengths can be used for either the one or the other.

High intensities can be generated by frequency doubling (see previous Section 2.2), frequency mixing or amplification of a seed beam of low intensity but of a desired wavelength. Difference- or sum-frequency mixing is very similar in its description to the above mentioned case of second harmonic generation [77, 153, 155]. A very prominent case which will also be used in the XFROG (cross-correlation Frequency Resolved Optical Gating, see Section 2.6.2), is the sum-frequency mixing between the fundamental and its second harmonic. This procedure then results in the third harmonic of the fundamental, which is in the given case at 266 nm. Amplification of seed beams is realized in the various kinds of optical parametric amplifiers (OPAs). The generation of the seed pulse varies from case to case. Very prominent representatives are the NOPA (Non-collinear Optical Parametric Amplifier) [156–159] and the TOPAS (Traveling wave Optical Parametric Amplifier of Superfluorescence) [160, 161].

These methods provide pulses at different wavelengths and high energy, have the disadvantage that they are often accompanied by a complicated setup, except in the case of second harmonic generation. For probing the dynamics, high intensities are normally not necessary, even not desired. A different mechanism, white-light generation can produce a necessary spectrum for probing the molecular dynamics.

A white-light continuum can generally be produced by focusing a laser beam of sufficient intensity into a transparent medium. The properties of the generated white-light depend on the properties of the medium, the focal parameters and the seed laser.

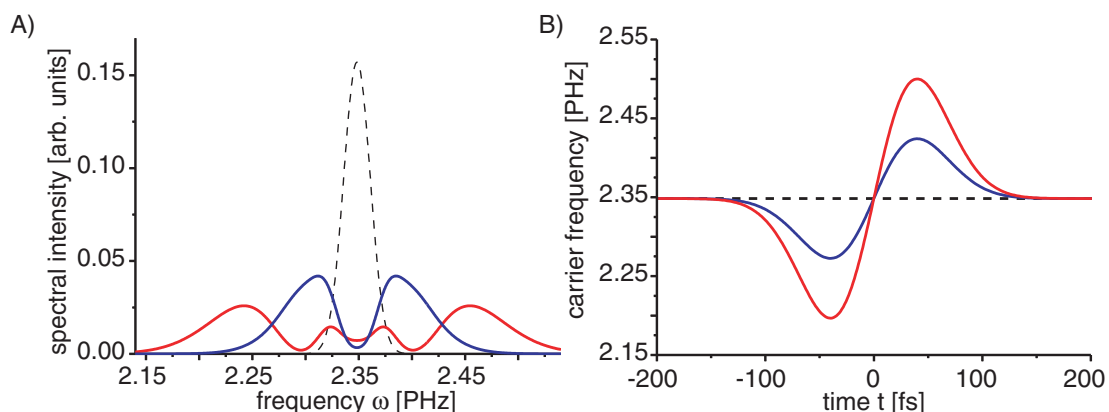


Figure 2.2: Effect of self-phase modulation in a medium with a non-vanishing  $\chi^{(3)}$  nonlinearity on the spectrum A) and on the time-dependent instantaneous frequency B) of an ultrashort laser pulse. The dashed black line shows the spectrum or respectively the time-dependent instantaneous frequency of the pulse before traveling through the medium. The blue line shows the same properties for a Gaussian intensity profile  $I_0(t)$  after passing the medium. The red line shows the effect for the same profile but with twice the amplitude. The same result can be obtained by holding the amplitude constant but doubling the length of the nonlinear medium.

The main origin of the white-light generation is the effect of self-phase modulation. The refractive index does not only depend on the frequency, but also on the intensity of the light passing through the medium [77, 154]. Therefore, the refractive index can be separated into a linear part  $n_0$  and a nonlinear part  $n_2$ , which is affected by the susceptibility of the third order  $\chi^{(3)}$ :

$$n(I) = n_0 + \frac{3\chi^{(3)}}{8n_0}I(t) = n_0 + n_2I(t). \quad (2.14)$$

Because the phase velocity of light in matter is connected via  $c = \frac{c_0}{n(I)}$  with the refractive index, the phase velocity itself depends on the intensity. The speed of light is part of the equation of the wave vector  $k = \omega_0/c$ . By this and Equations 1.29 and 1.32, the equation of the time dependent phase  $\phi(t)$  can be written as:

$$\begin{aligned} \phi(t) &= \varphi(t) + \omega_0 t - kz = \varphi(t) + \omega_0 t - \frac{\omega_0 n(I)}{c_0} z \\ &\sim \varphi(t) + \omega_0 t - \frac{\omega_0 (n_0 + \frac{3\chi^{(3)}}{8n_0} \tilde{A}^2(t))}{c_0} z. \end{aligned} \quad (2.15)$$

To simplify the description, a flat initial phase with an absolute value of zero is assumed. Because the intensity varies with time, an ultrashort laser pulse modulates its own time-dependent phase when traveling through a medium with non-vanishing  $\chi^{(3)}$ .

The modulation mainly depends on the length of the medium, of the temporal intensity profile and the nonlinearity. The resulting spectral field can be calculated by the inverse Fourier transformation from the temporal field including the self-modulated phase. For an initially Gaussian pulse, the result is shown for several different amplitudes in Figure 2.2A. The same picture can be obtained by holding the amplitude of the Gaussian pulse constant and vary the length of the nonlinear medium or vary the nonlinearity. For comparison the spectrum of the input beam is shown as well.

The time-dependent instantaneous frequency can be calculated by using Equations 1.30 and 2.15:

$$\omega(t) = \omega_0 - \frac{\omega_0 n(I)}{c_0} z \quad (2.16)$$

In the case of a Gaussian amplitude profile, the instantaneous frequency will first start at smaller frequency compared to the carrier frequency of the original pulse and then move to higher frequencies. This situation is shown in Figure 2.2B for different amplitudes of a Gaussian profile.

Beside the broadening of the spectrum the pulse is also temporally elongated. Due to the broad spectrum the pulse could now be recompressed to an even smaller pulse duration than before.

These simple calculations can only be applied to pulses with several cycles of the electric field, because the nonlinear refractive index  $n_2$  does not instantaneously follow the intensity profile. For the case of ultrashort pulses in the few-cycle regime, this fact must be considered.

Unfortunately, in many cases the experimentally recorded spectra, especially those that are important for generating a stable and broad continuum, can not be solely explained by self-phase modulation. There are several other processes influencing the generation of new frequencies. Due to the modulation of the refractive index with the intensity, the speed of light is as well modulated, which causes the pulse center to travel with a different velocity than the trailing and leading edge of the pulse. This effect is called “self-steepening”. The exact behaviour can be calculated [77,162] and the effect measured as well in the case of propagation through optical glass fibers [163]. The calculations are rather complex but intuitively one can understand that the temporal pulse shape is drastically changed by this effect. Since the time domain is directly connected with the frequency domain via the Fourier transformation the spectrum is modulated as well as a result of the temporal modulation. Since the temporal pulse profile is asymmetric, the  $E(\omega)$  also shows an asymmetric behaviour.

A further interesting effect arises, because of the “self-focusing” effects of the laser pulse in a medium, whose refractive index is depending on the intensity. The non-uniform intensity distribution of the laser pulse across the beam profile results in a transverse variation of the index of refraction. This can lead to a focusing effect depending on the way in which the refractive index change takes place. If the pulse starts to focus, the region near the pulse center undergoes the most self-phase-modulation. The resulting dispersion causes the highest modulated fraction to flow away from the

pulse center due to the different speed of light. This results in a splitting of the initially Gaussian pulse in two pulses. Again this modulation of the temporal pulse shape causes a modulation in the spectral region. This effect of pulse splitting can be treated numerically [77, 164].

Despite these mentioned effects, there are, depending on the medium in which the white-light is generated, many other nonlinear effects influencing the spectrum. These are for example parametric four-photon mixing, Raman scattering and multiphoton-excitation [77, 165]. Molecular resonances of course will naturally also complicate the process, although for normal applications, white-light is not generated close to resonances.

The maximum spectral broadening is of special practical interest and has been proven to be strongly material dependent. In the case of white-light generation in solids, it has been shown that the width of the producible spectrum is proportional to the energy gap of the material that is used. Nevertheless, there is no material that could provide the needed spectral broadening necessary to perform the desired experiments. This disadvantage can be overcome by changing the wavelength of the pump-light for the white-light generation.

Due to the white-light generation process and the resulting dispersion, the pulse is no longer bandwidth-limited. The white-light continuum can be regarded as a chirped pulse, whose spectral components can be treated independently [76]. This causes the individual part of the probe pulse to have a different time-zero with respect to the pump-pulse (see also Section A.1).

## 2.4 Pulse shaper

For the concepts of influencing molecular dynamics with lasers as presented in Section 1.7.2, it is necessary to be able to modify the laser pulse in a general way. Beside these general concepts, many control approaches are based on temporally spaced pulse sequences with temporal distances of few tens of femtoseconds. Unfortunately it is quite difficult to experimentally shape an ultrashort pulse directly in the time domain.

But since the description of ultrashort laser pulses in the time domain is connected by the inverse Fourier transformation with the description in the frequency domain (see Section 1.7.1), shaping of an ultrashort laser pulse can be achieved either in the one or in the other.

There are several different methods for shaping ultrashort laser pulses. Nearly all of them are based on a so called  $4f$ -setup. The incoming laser beam gets dispersed by a grating. The dispersed beam is then collimated by a lens with a focal length  $f$ . The grating itself is positioned in the focal plane of this lens. In that way, the individual frequency components will be focused into the focal plane of the lens, which is also called "Fourier plane". This setup works in principle like a Fourier transformation. A second lens of a focal length  $f$  and a second grating in the same distance from

the Fourier plane as in the first case works like an inverse Fourier transformation. In an ideal case and without any further components, a laser pulse leaves this geometry without any modification. This setup is called “zero-dispersion compressor” [166].

The spectrally dispersed pulse can now be modified in the Fourier plane by spatial light modulators (SLM). There are several different variations of SLMs, which can spectrally shape ultrashort laser pulses.

An example for such SLMs is the acousto-optical modulator [167, 168], which uses diffraction by an acoustic wave, that can be externally controlled. The diffracted part of the pulse is modulated according to the acoustic wave.

A second variant modulates the spectral phase by elongation or shortening of the optical path between the different frequency components. This can be achieved by deformable mirrors, deformed by either small piezo-motors or electrostatically by small electrodes [169–171]. The mirror can be constructed with the help of a membrane causing a smooth phase function or with a microarray of small individual mirrors.

An exotic possibility modulates the optic path by rotating very small glass plates, which are located in the Fourier-plane [172]. Thus the spectral phase gets modulated as well.

The oldest dynamical concept is based on a liquid crystal display [103, 104]. It consists of a certain number of glass plates, that are coated with indium-tin oxide (ITO). To each of these glass plates an electric AC-voltage can be individually applied. In the case of no voltage, the long-stretched liquid-crystal molecules of the display are oriented perpendicular to the beam propagation. In the case of the presence of a suitable AC-voltage, the orientation of the molecules changes. This modulates the refractive index for light along the corresponding axis. The change of the refractive index causes a change of the wavelength of the light passing through the pixel, if the polarization of the light is chosen correspondingly to the orientation of the liquid crystals. This results in a different phase according to the applied voltage with respect to the case without any voltages applied to the pixel. In this way, the phase of the individual spectral components and thus the spectral phase can be modified with respect to the given resolution provided by the numbers of pixel of the liquid crystal display.

In a slightly modified geometry with the help of two polarizers, the pulse shaper based on a SLM does not modulate the spectral phase but the amplitude. Using a double-layered liquid crystal display, it is also possible to shape the two polarizations or both amplitude and phase at the same time [105]. In principle, by combining these different possibilities, for both polarizations the phase and amplitude can be shaped.

All the different possibilities for modifying the spectral phase have their advantages and disadvantages which are discussed in the given references. In this work a liquid crystal based pulse shaper is used, that does modify the spectral phase of an ultrashort laser pulse. Figure 2.3 shows the design of the pulse shaper. Since the laser beam



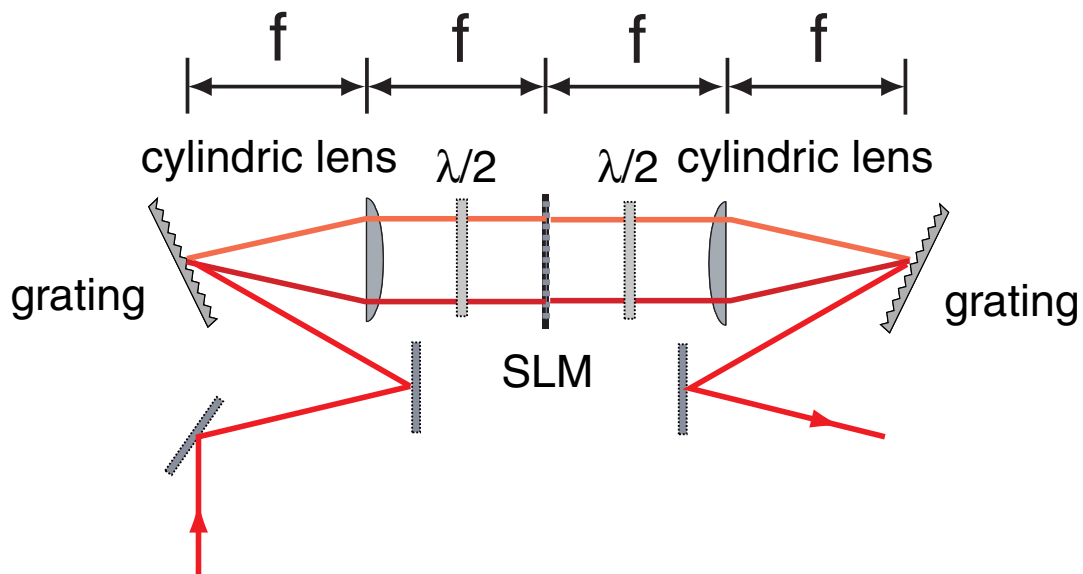


Figure 2.3: The pulse shaper used in this work consists of a zero-dispersion compressor and a spatial light modulator (SLM). The first grating disperses the incoming laser pulse. The dispersed light is then collimated by a cylindrical lens. The different frequency components of the incoming light can thus be easily modulated in its spectral phase with the help of a liquid crystal display, that is placed in the focal plane. The setup is continued symmetrically to the focal plane. Because the used liquid crystal display can only modulate s-polarized light, but the laser beam is generally p-polarized, two  $\lambda/2$ -waveplates are used to rotate the polarization before and after the liquid crystal display. With this setup it is possible to shape the spectral phase of the incoming laser pulse.

is commonly p-polarized, but in the case of the liquid crystal display used for the experiments in this thesis can only modulate s-polarized light, two  $\lambda/2$  waveplates are needed before and after the SLM. Cylindrical lenses care for an optimal use of the full height of the pixels to reduce the chance of damaging the display due to a high intensity. The voltage can in principle be varied in 4096 steps (12 bit), but for a phase between 0 and  $2\pi$  a region is optimal that can be covered by 2000 steps. Since the display consists of 128 pixels, this results in  $2000^{128}$  possible pulse shapes if all pixels contribute to the modulation of the phase.

## 2.5 Shaping pulses in the UV region

During this work, shaped pulses at wavelengths around 400 nm are required for many experiments. This wavelength regime has the big advantage to be more or less easily accessible by frequency-doubling of the Ti:Sapphire fundamental pulse. Pulse shaping

in this wavelength regime can be done in various ways. The simplest way is the direct shaping of the 400 nm laser pulse. This has been reported for acousto-optical pulse shapers [173], as well as for micromirror devices [169]. The last case shows, that the concept can in principle be adapted for every kind of deformable mirror in the case, that a suitable coating that reflects the desired wavelengths is available for the device. All these mentioned devices have either the problem that they only exist in a prototype variant, as for the micromirror, or they exhibit other disadvantages, like a low throughput or a restricted number of possible pulse shapes.

The available liquid crystal displays have the big disadvantage that its transmittance only reach down to 450 nm. Direct shaping of the 400 nm pulse is thus not possible. Therefore the laser pulse must be converted to the desired regime after the shaping process. In principle this is possible on two ways, either by frequency doubling or by sum frequency mixing with an unshaped laser pulse (see Section 2.2 and [174, 175]). The latter variant has the disadvantage that the resulting energy of the 400 nm shaped laser pulse is rather low. To guarantee complicated temporal pulse structures, the unshaped pulse has to span the time window that is needed for the temporal structures. This makes it necessary to have a temporally very long unshaped pulse with a small peak intensity. Therefore the sum-frequency signal of the long unshaped and the shaped pulse will be quite low in its intensity.

The second variant is based on direct frequency doubling of the modulated pulse [174]. On the one hand, this ensures a high intensity of the 400 nm beam, which is often desired in the experiment. But on the other hand one has to keep in mind that the intensity is lower for temporally stretched pulses than for pulses close to the bandwidth-limit (see Equations 2.12 and 2.13). This will also be the case in the first variant of mixing the shaped pulse with an unshaped one, since the unshaped pulse necessarily will have a Gaussian shape and therefore will be of different intensity at different times. However, the degree of the modulation in the intensity will not be that significant compared to the second case of direct second harmonic generation but as stated above its total yield generally will be much smaller.

As already seen in the plots in Section 1.9 and A.5, the spectrum of the second harmonic of the fundamental can significantly differ from the initial Gaussian shape of the 800 nm fundamental pulse. In the easy, but very often used case of a sinusoidal spectral phase, the second harmonic spectrum can be analytically calculated. A pulse with a spectral sinusoidal phase structure

$$E_1(\omega) \sim e^{-\left(\frac{\omega_1 - \omega_0}{\sigma}\right)^2} e^{i\Phi \cos(\Delta t(\omega_1 - \omega_0))} \quad (2.17)$$

will result in a train of pulses with a temporal separation of  $\Delta t$ .  $\Phi$  is the modulation amplitude and  $\omega_0$  the carrier frequency. Inserting Equation 2.17 into the definition for the second harmonic, Equation 2.12, will result in a term, that is essentially proportional to the sum over all Bessel functions multiplied by an exponential function that decreases with  $n\Delta t\sigma$ , where  $n$  is the index of the sum [174]. For ultrashort pulses with a large value of  $\sigma$  and a pulse train with a large temporal pulse separation  $\Delta t$ , this

expression can be reduced to the term containing only the zero-order Bessel function  $J_0$  [174]:

$$E_2(\omega_2) \sim e^{-\frac{1}{2}\left(\frac{\omega_2-\omega_0}{\sigma}\right)^2} J_0\left(2\Phi\cos\left(\frac{1}{2}\Delta t\omega_2\right)\right) \quad (2.18)$$

As one can see the second harmonic spectrum is clearly modulated. Modulation of phase and amplitude opens up a big space of physically significant pulse shapes compared to the case of phase-only modulation. Amplitude modulation has shown to sometimes have a significant influence on the control objective [115]. Also the second harmonic of the double pulses result in a highly modulated spectrum (see plots in Section 1.9 and A.5). As will be demonstrated in Chapter 6, this modulation is for example mainly responsible for the fluorescence yield for a medium-size molecule from the family of the cyanines. Simulations of the effect of the modulated spectrum with respect to the control objective are therefore desirable (see Section 6.2).

## 2.6 Pulse characterization methods

After a successful control experiment, it is necessary to characterize the pulse shape, that fulfills the control objective. In analogue to this sequence the last section in this chapter concerning the technological methods will deal with the pulse characterization. Several different methods have been developed for characterizing the pulse shape of an ultrashort laser pulse. Among them are FROG (“Frequency Resolved Optical Gating”) [176–178], SI (“Spectral Interferometry”) [179], SPIDER (“Spectral Phase Interferometry for Direct Electric Field Reconstruction”) [180–186], STRUT (“Spectrally and Temporally Resolved Upconversion Technique”) [187, 188] and others. Many of these techniques exists in different variants to compensate for certain disadvantages that each method naturally has.

Here it is desired to characterize ultrashort laser pulses in a temporal regime from 80 fs up to several picoseconds both at 400 nm and 800 nm. Techniques as SPIDER can not characterize both short pulses and long pulses without a modification of the hardware. The standard variant of FROG, based on second harmonic generation for example can not characterize wavelengths at 400 nm. But as a big advantage, it is self-referencing. This means that neither initial information about the pulse is needed nor that a known reference pulse is used to measure the unknown pulse. In contrast techniques such as the SI need a well characterized reference pulse.

To overcome these disadvantages, a combined FROG and XFROG is constructed. The FROG is capable to characterize the 800 nm pulse by correlating the unknown pulse with itself. This characterization works best, if the pulse is not too complicated. The XFROG technique is an extension of the FROG technique. The XFROG technique uses a known pulse for the correlation with the unknown pulse. Because this pulse can be of a different wavelength, this has the advantage that also pulses at a central wavelength of 400 nm can be characterized by this technique. In the case of

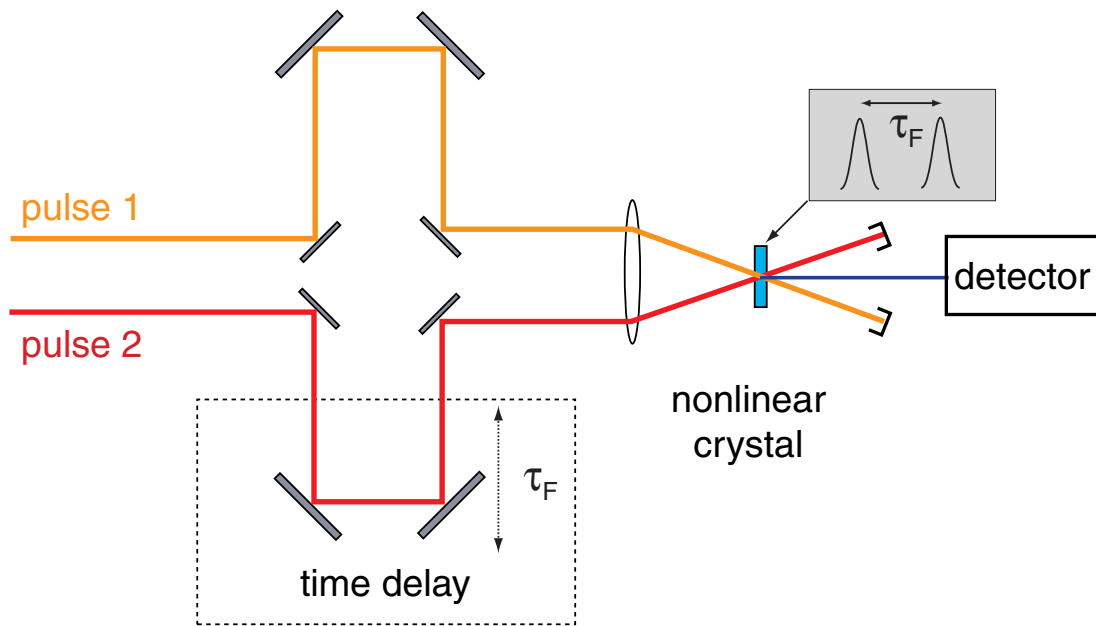


Figure 2.4: Three of the pulse characterization methods, autocorrelator, FROG and XFROG, used throughout this work base on the scheme presented in this picture with slight variations. Two pulses, which can be temporally delayed relative each other, are spatially overlapped in a nonlinear crystal. The resulting sum-frequency signal can then be detected in dependence on the temporal delay. The three methods for pulse characterization differ in the input pulses and the detection method. In the case of the autocorrelation, the pulse 1 and 2 are identical copies and only the cooperative signal is detected. Therefore a complete characterization of the field is not possible, except in special cases. It is possible to get the complete information if not the pulse energy but the spectrum is recorded. This variant is called FROG. If the two input pulses are not identical replica, but a known reference pulse is used for one of the two pulses, the setup is called XFROG. The advantages and disadvantages of the different methods are explained in the text.

the experiments in this theses, the necessary known reference pulse is a fraction of the unshaped 800 nm pulse that can be characterized by FROG. Therefore both methods are very well suited for the characterization of both 400 nm and the 800 nm pulses.

### 2.6.1 Self referencing technique - FROG

A very common technique for online characterization of pulses is the autocorrelator. Two pulses become spatially overlapped in a nonlinear crystal, for example in a non-collinear geometry (see Figure 2.4). That means that the two pulses do not travel parallel but have a certain angle relative to each other. With the help of a delay stage, the one pulse can be delayed with respect to the other. Then, the resulting intensity

of the mixing process in dependence of the time delay  $\tau_F$  is detected and forms the autocorrelation signal:

$$A_k(\tau_F) = \int_{-\infty}^{\infty} I_t(t)I_r(t - \tau_F)dt. \quad (2.19)$$

This autocorrelation function is both symmetric and real which can be seen from the correlation theorem:

$$A_k(\omega) = \sqrt{2\pi}I(\omega)I(\omega)^* \quad (2.20)$$

The Fourier transformation of the autocorrelation is proportional to the spectral intensity. Because of this, only few information can be drawn out of the measurement of the autocorrelation function.

An infinite set of symmetric and asymmetric functions can have the same autocorrelation function. In the case of unmodulated pulses it can be assumed that the pulse shape is Gaussian or  $\text{sech}^2$ -like. With this assumption the pulse duration  $\tau_P$  can be obtained from the autocorrelation measurement, which is connected with the FWHM of the autocorrelation over the relation  $\tau_{ak} = \sqrt{2}\tau_P$ .

This information is very helpful to monitor the laser during an experiment but can not give the necessary information about a pulse shape as necessary after a control experiment. A small modification of the setup can yield much more information. Instead of monitoring only the pulse energy, the whole spectrum in dependence of the delay is recorded. This geometry is then called FROG and the measured signal FROG trace. This measurable FROG trace can be written as the square of the electric field:

$$I_{FROG}(\omega, \tau_F) = |E_{sig}(\omega, \tau_F)|^2 = \left| \int_{-\infty}^{\infty} \frac{1}{\sqrt{2\pi}} E_{sig}(t, \tau_F) e^{-i\omega t} dt \right|^2 \quad (2.21)$$

If  $E_{sig}(t, \tau_F)$  is known, the field can be obtained more or less straight forward. The signal field is composed of

$$E_{sig}(t, \tau_F) = \frac{1}{4}A(t)A(t - \tau_F)e^{i[\phi(t)+\phi(t-\tau_F)]} \quad (2.22)$$

$A(t)e^{i\phi}$  is now of interest, which can be obtained by integrating  $E_{sig}(t, \tau_F)$  over  $\tau_F$ . This is identical to the Fourier transformation for the new variable  $\Omega$ , in the case that this variable is set to zero:

$$E_{sig}(t, \Omega) = \int_{-\infty}^{\infty} \frac{1}{\sqrt{2\pi}} E_{sig}(t, \tau_F) e^{-i\Omega\tau_F} d\tau_F \quad (2.23)$$

$$E_{sig}(t, \Omega = 0) = \int_{-\infty}^{\infty} \frac{1}{\sqrt{2\pi}} E_{sig}(t, \tau_F) d\tau_F \quad (2.24)$$

By inserting Equation 2.22 in Equation 2.24 and substituting  $\tau_F \rightarrow \tau'_F = t - \tau_F$ , it is possible to calculate the desired field  $A(t)e^{i\phi}$  :

$$E_{sig}(t, \Omega = 0) = A(t)e^{i\phi(t)} \int_{-\infty}^{\infty} \frac{1}{\sqrt{2\pi}} A(t - \tau_F) e^{i\phi(t - \tau_F)} d\tau_F \quad (2.25)$$

$$= A(t)e^{i\phi(t)} \int_{-\infty}^{\infty} \frac{1}{\sqrt{2\pi}} A(\tau'_F) e^{i\phi(\tau'_F)} d\tau'_F \quad (2.26)$$

$$\propto A(t)e^{i\phi(t)} \quad (2.27)$$

The difficulty is now to obtain the electric signal field  $E_{sig}(t, \tau_F)$ . There are different algorithms to fulfill this task, which generally start from a random pulse shape and then calculate the FROG trace via Equation 2.21. The result is then compared with the measured data and a FROG-error is calculated and iteratively minimized, which expresses the similarity between the calculated and the measured field. For this retrieval a commercial software is used in the laboratory (FROG version 3 from Femtosoft Technologies [189]).

## 2.6.2 Characterization of complex UV-Pulses XFROG

The difference between the FROG and the XFROG technique lies only in the nature of the input beams. While in the case of the FROG technique the two beams are identical, the XFROG technique uses a reference beam which is different from the one, which shall be characterized. The retrieval of the electric signal field is identical to the FROG case and the electric field to be characterized can be obtained from the retrieved signal field in a similar manner. In the XFROG case, in which the sum-frequency generation is used,  $E_{sig}(t, \tau_F)$  is written as:

$$E_{sig}(t, \tau_F) = \frac{1}{4} A(t) A_{ref}(t - \tau_F) e^{i[\phi(t) + \phi_{ref}(t - \tau_F)]} \quad (2.28)$$

By inserting this equation into 2.24 again the relation 2.25 is obtained.

The XFROG method was successfully used to characterize very weak pulses [190, 191]. Beside this the technique has the very appealing advantage that the two spectra of the involved pulses do not have to overlap. This makes it possible to characterize pulses both in the UV (for example by difference-frequency mixing as in Reference [192]) as well as in the IR (for example by the sum-frequency of the unknown pulse with an adequate reference pulse as in Reference [193]).

A second advantage is the possibility of an intuitive understanding of the pulse shape from the XFROG trace for many cases, as it is not so easy for the case of the FROG trace. This can be very well visualized by Figure 2.5, where the FROG and XFROG

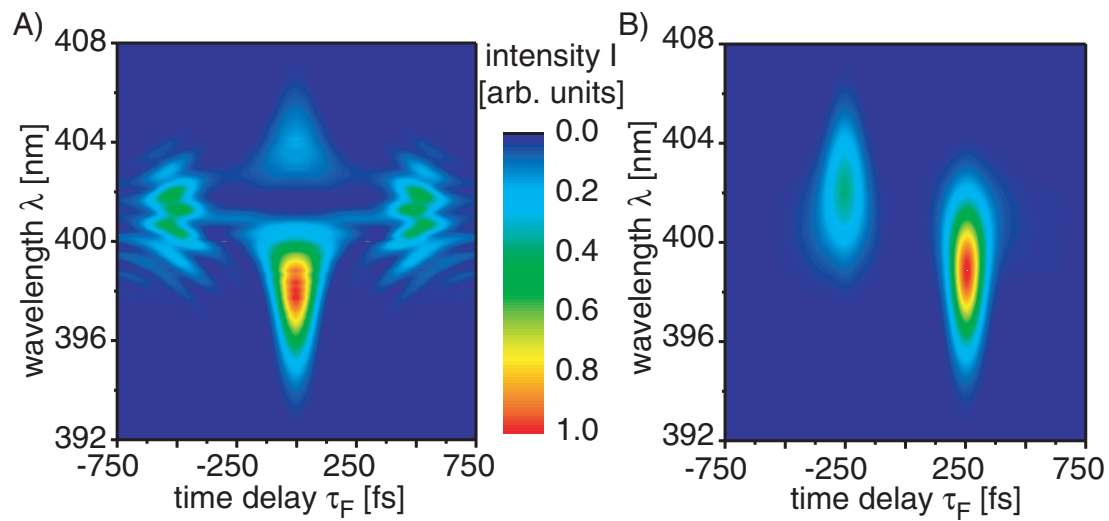


Figure 2.5: FROG trace A) and XFROG trace B) of a pulse with a spectral phase, causing double pulses in the temporal regime. The individual pulses have a distance of 500 fs and have different carrier frequencies. Additionally the amplitude differs slightly. With the definitions of Section 1.9, the phase structure can be characterized by a phase slope of 500 fs, no phase step and with a breakpoint at 803 nm for a central wavelength of 800 nm. The pulse structure can be very easily realized from the XFROG trace of this shaped pulse with an unshaped Gaussian pulse of a central wavelength of 800 nm and a FWHM of 15 nm, while interpretation of the FROG trace is not that intuitive.

trace for a sample pulse is shown. In this case it is a double pulse generated by a triangular spectral phase with a slope of 500 fs and a break point, that is shifted by three nanometers according to the carrier wavelength. In the temporal regime this results in two individual pulses, at different carrier frequencies and different amplitudes with a distance of 500 fs (for more information see Section 1.9). This structure can very well be realized in the XFROG trace of the shaped pulse with a Gaussian-like unshaped pulse at a central wavelength of 800 nm at a FWHM of 15 nm. As a consequence of the correlation, the pulse structures of the original pulse are blurred. In the FROG case the reference pulse is the shaped pulse itself, which produces a much more complex signal.





# Chapter 3

## Reaction dynamics at conical intersections

The first part of this chapter mainly introduces the theoretical concepts for molecular dynamics in the vicinity of conical intersections. These are expected to play an essential role in many systems in which an ultrafast reaction is accompanied by a radiationless decay to the ground state. The isomerization reactions which this thesis deals with, belong to this type of reaction. To understand the early time dynamics of such reactions, theoretical simulations greatly help understanding the experimental data. Therefore, the second part of the chapter presents the theoretical findings which are of general importance to understand the experimental results in the following chapters. Additionally, the present state of research concerning the molecules used in the experiments, is also shortly summarized.

Beside the investigation of reaction mechanisms, this thesis mainly deals with their control. The fundamental control mechanisms have already been introduced in Chapter 1. However, the actual control mechanism for a given problem can be complicated. Both the nature of the control problem, as well as the excitation field must be considered. Employing pulses at wavelengths which lead to an excitation to higher lying potential energy surfaces enables different control mechanisms, compared to the use of wavelengths for direct excitation to the first excited energy surface. At the end of this chapter, concepts for the optimal control of photoisomerization reactions are presented. These cover excitation to higher lying states, active and passive control mechanisms for examples relevant to the reaction types investigated in this work.

### 3.1 Beyond the Born Oppenheimer approximation

One of the most important concepts for the theoretical calculation of molecular dynamics is the Born-Oppenheimer adiabatic approximation and has therefore found entrance into many textbooks [14]. To summarize briefly, this approximation allows to calcu-

late the dynamical processes in two steps. First the Schrödinger-equation is solved for the case of fixed nuclei. In the second step the exact eigenstates of the system are expanded in the fixed nuclei states. Inserting this ansatz into the Schrödinger equation for the complete system results in a system of coupled differential equations. In the case of the Born-Oppenheimer approximation, the parts of the equations that are responsible for the coupling (coupling terms) are omitted. This can be justified by considering the kinetic energy operator as a small perturbation of the electronic motion. The nuclear motion can thus be thought of as if it were proceeding on the potential energy surface of a given electronic state.

Many molecular dynamics are well characterized by the Born-Oppenheimer approximation. Nevertheless, it is well known that neglecting the coupling terms is not justified in general [194–200]. This is for example the case if the spacing of the electronic eigenvalues is small compared to the typical spacing associated with the nuclear motion. In this case the residual coupling via the nuclear kinetic energy operator causes transitions between the adiabatic electronic states [194]. Such behaviour has very early been considered by F. Hund in 1927 and theoretically described in the following years by J. von Neumann and E. Wigner as well as by E. Teller [201–203].

The crossing of potential energy surfaces has long been thought as a relatively uncommon occurrence. But with the experimental progress concerning the molecular dynamics, it became clear that many chemical reactions are accompanied by electronic relaxation all the way to the ground state. In addition the time scale of many reactions only spans a few picoseconds, making an efficient decay mechanism to the ground state necessary.

The invention of efficient computers has largely influenced and stimulated the field of theoretical modeling of molecular dynamics. Since the 1980s many molecular systems of increasing complexity have been investigated. These investigations have shown that the crossing of potential energy surfaces are not uncommon occurrences, but in contrast very often found.

The question under which conditions such crossings occur can be easily answered [202, 203]. It is supposed that the correct electronic eigenfunctions for all energy levels are known, except for the two potential curves which are expected to cross. For these, two arbitrary wave-functions  $\psi_1$  and  $\psi_2$  are chosen in that way that they form a complete orthogonal basis. The corresponding eigenvalues  $E_1(\vec{R})$  and  $E_2(\vec{R})$  have to be eigenvalues of the matrix

$$H(\vec{R}) = \begin{pmatrix} H_{11}(\vec{R}) & H_{12}(\vec{R}) \\ H_{21}(\vec{R}) & H_{22}(\vec{R}) \end{pmatrix}. \quad (3.1)$$

In this equation  $\vec{R}$  describes coordinates of the nuclei and the individual matrix entries are given by

$$H_{kl}(\vec{R}) = \langle \psi_k | H(\vec{R}) | \psi_l \rangle. \quad (3.2)$$

The eigenvalues can now be easily determined with the help of the characteristic polynomial:

$$\det H(\vec{R}) = \begin{vmatrix} H_{11}(\vec{R}) - E(\vec{R}) & H_{12}(\vec{R}) \\ H_{21}(\vec{R}) & H_{22}(\vec{R}) - E(\vec{R}) \end{vmatrix}. \quad (3.3)$$

This results in the eigenvalues  $E_{1,2}(\vec{R})$ :

$$E_{1,2}(\vec{R}) = \frac{H_{11}(\vec{R}) + H_{22}(\vec{R})}{2} \pm \sqrt{\left(\frac{H_{11}(\vec{R}) - H_{22}(\vec{R})}{2}\right)^2 + H_{21}(\vec{R})H_{12}(\vec{R})}. \quad (3.4)$$

Since  $H(\vec{R})$  is Hermitean, the relation  $H_{21}(\vec{R}) = H_{12}(\vec{R})^*$  is valid. If there should be a crossing of the potential energy surfaces, the two eigenvalues  $E_{1,2}$  have to be degenerated. Obviously this makes it necessary that the squareroot in Equation 3.4 vanishes. This is exactly the case if the off-diagonal element  $H_{12}(\vec{R})$  and the difference between the two diagonal elements  $H_{11}(\vec{R}) - H_{22}(\vec{R})$  are equal zero:

$$H_{12}(\vec{R}) = 0 \quad (3.5)$$

$$\text{and } H_{11}(\vec{R}) - H_{22}(\vec{R}) = 0. \quad (3.6)$$

If the off-diagonal elements are complex the number of condition increases by one ( $Re(H_{12}(\vec{R})) = 0$  and  $Im(H_{12}(\vec{R})) = 0$ ). However, most theoretical calculations only use real valued Hamiltonians for describing molecular dynamics at conical intersections. Condition 3.5 is in general not valid in the case of diatomic molecules with eigenfunctions, because the off-diagonal elements are normally not equal zero (non-crossing rule). In the case of molecules with more than two atoms, condition 3.5 can be fulfilled by varying two parameters.

Still this small calculation does not answer the question whether a conical intersection is in the region where the molecular dynamics is actually taking place. It could be well possible that there is a degeneracy of the energy surfaces for a certain molecular system, but at such parameters that the point of the conical intersection does not influence the molecular dynamics. To answer this question, to the best, one has to solve the Hamilton equation and calculate the energy expectation values and the wave packet dynamics after the influence of an electric field that excites a molecule.

The effect of crossing potential energy surfaces can be seen in a simple two-state two-mode model. In this model two nondegenerate electronic states  $\psi_1$  and  $\psi_2$  are coupled by a single vibrational mode  $Q_2$ , the coupling mode. In addition, there is a tuning mode  $Q_1$  that modulates the energy separation. The most simple Hamiltonian resulting in non-adiabatic dynamics for this simple system can be written as follows [14, 194–200]:

$$H(Q_1, Q_2) = H_c(Q_1, Q_2) + H_t(Q_1, Q_2) \quad (3.7)$$

with

$$H_c(Q_1, Q_2) = T_c(Q_1, Q_2) + \sum_{k=1}^2 |\psi_k\rangle \frac{\omega_k}{2} Q_2^2 \langle \psi_k| + |\psi_1\rangle \lambda Q_2 \langle \psi_2| + |\psi_2\rangle \lambda Q_2 \langle \psi_1| \quad (3.8)$$

$$H_t(Q_1, Q_2) = T_t(Q_1, Q_2) + \sum_{k=1}^2 |\psi_k\rangle (E_k + \frac{\omega_k}{2} Q_1^2 + \kappa_k Q_1) \langle \psi_k|. \quad (3.9)$$

$E_1$  and  $E_2$  are the vertical excitation energies at the reference geometry  $Q_1 = 0$ ,  $Q_2 = 0$  of the states  $\psi_1$  and  $\psi_2$ .  $\omega_i$  are the two harmonic vibrational frequencies of the system. The  $\kappa_i$  are essentially the gradients of the electronic excitation energies with respect to  $Q_1$  and are called the intrastate coupling constants. The interstate coupling by the coupling mode can be visualized very well by the matrix elements  $|\psi_1\rangle \lambda Q_2 \langle \psi_2|$  and  $|\psi_2\rangle \lambda Q_2 \langle \psi_1|$ . In these terms  $\lambda$  is the interstate coupling constant. Finally  $T_{kin}(Q_1, Q_2) = T_c(Q_1, Q_2) + T_t(Q_1, Q_2)$  denotes the nuclear kinetic energy operator.

The adiabatic potential energy surfaces can now be obtained as eigenvalues of  $H(Q_1, Q_2) - T_{kin}(Q_1, Q_2)$ , what means diagonalizing the Hamilton operator in the fixed nuclei limit  $T_{kin}(Q_1, Q_2) \rightarrow 0$  [194,196,197,199,204]. This model Hamiltonian or variants of it has been used in several theoretical simulations to describe and investigate the dynamics in the vicinity of conical intersections [194–200]. The resulting adiabatic potential energy surfaces for the given Hamiltonian for the two-state two-mode prototype conical intersection model are shown in figure 3.1. The values for  $\kappa_i$  and  $\lambda$  can be directly obtained from *ab initio* calculation by fitting the given model to the calculated adiabatic surfaces [196]. This projection on a simplified model can help to understand the mechanisms, responsible for the dynamics.

Figure 3.2D-F shows the tuning effect, the dependence of the energy gap on the tuning mode  $Q_1$ . In contrast 3.2A-C shows the effect of the coupling mode for three fixed values of  $Q_1$ . One can see very well that the shape of the lower surface is strongly modulated, having a double minimum character. At a certain value of  $Q_1$  and  $Q_2$  the potential energy surfaces are seen to cross (at  $Q_1 = -0.8571$  and  $Q_2 = 0$ ). From the perspective view in 3.2A and D as well as from Figure 3.1 the elliptic double cone near the point of intersection can be visualized very well.

The dimension of the conical intersection is depending on the number  $n$  of relevant nuclear degrees of freedom. In general, condition 3.5 for the intersection of the potential energy surfaces determines a hypersurface of dimension  $n-2$  in nuclear coordinate

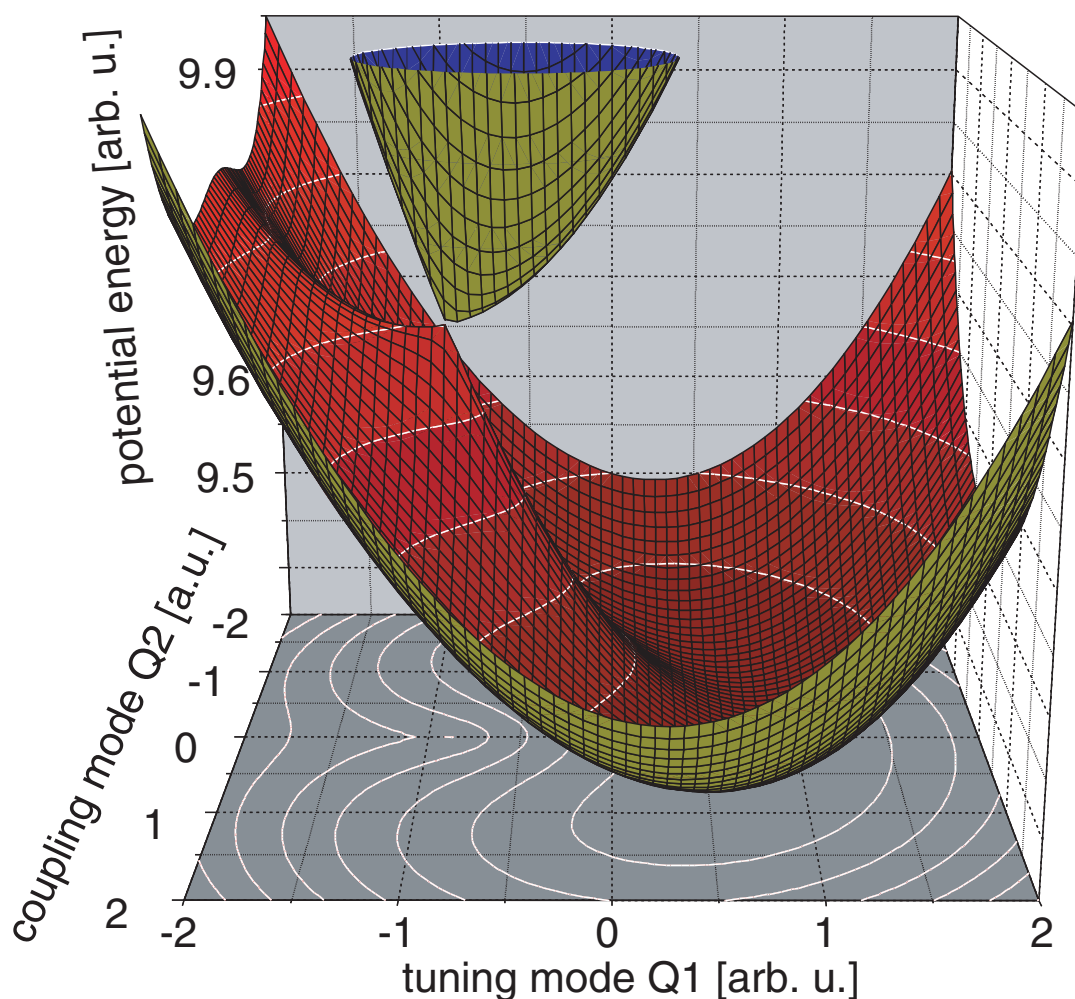


Figure 3.1: Perspective view of the adiabatic potential energy surfaces for the two-state two-mode prototype conical intersection model. The conical shape of the intersection can very well be visualized in this plot. In the given case the values for the model are:  $E_1 = 9.45$ ,  $E_2 = 9.85$ ,  $\kappa_1 = -0.212$ ,  $\kappa_2 = 0.255$ ,  $\omega_1 = 0.258$ ,  $\omega_2 = 0.258$ ,  $\lambda = 0.318$ .

space. By increasing  $n$  beyond the value  $n = 2$ , the isolated points of the intersection become continuous manifolds and thus the coordinate range of close approach of potential energy surfaces increase tremendously [200].

## 3.2 Isomerization as an example for conical intersections

As can be seen in Chapters 4 and 5, at least the isomerization reactions under investigation take place in less than a few picoseconds. Additionally, the isomerization in

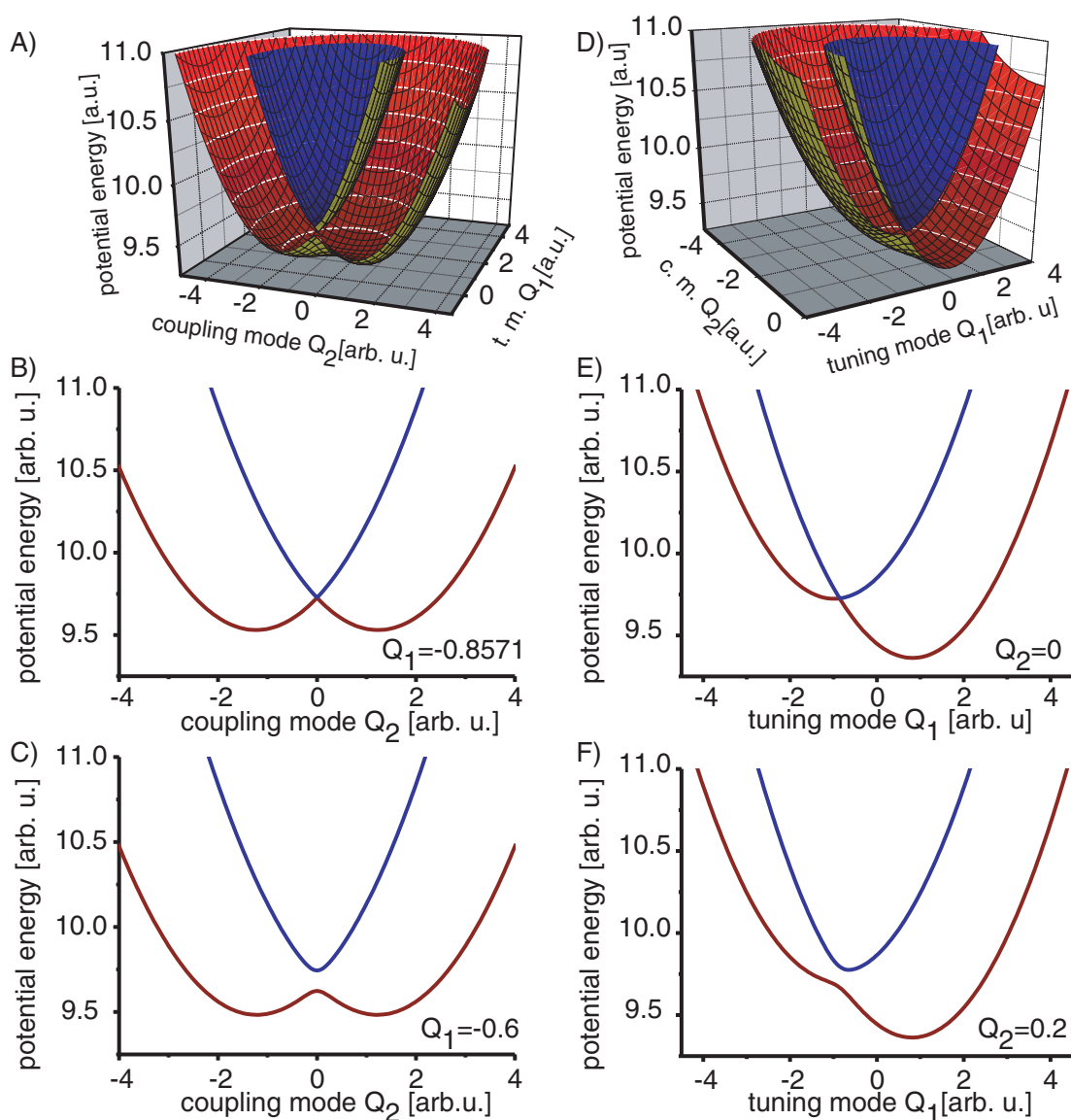


Figure 3.2: Plot D)-F) show the effect of the tuning mode on the adiabatic potential energy surfaces for the two-state two-mode prototype conical intersection model. A)-C) show the effect of the coupling mode. To visualize how the shape of the adiabatic potential energy surfaces are effected, cuts are presented for certain fixed values of  $Q_1$  and  $Q_2$ , respectively. To visualize double-minimum character of the lower surface and the conical shape near the intersection points, perspective cuts along both involved modes are shown in A) and D).

these cases is accompanied by populating the electronic ground state. This makes a fast decay to the  $S_1$  surface necessary.

Isomerization reactions have very early been in the focus of many theoretical publications concerning the dynamics connected with the decay through a conical inter-

section [26–29, 45, 199, 205]. Already by additionally introducing a periodic potential and using more tuning modes in the model-system represented by Equation 3.8, many effects of the isomerization reaction can be very well simulated [199]. By using a model that is better adapted to a realistic molecule, it is now even possible to simulate the experimental observable data. For example S. Hahn and G. Stock have presented calculated pump-probe spectra for the molecule rhodopsin which is related to the molecule bacteriorhodopsin used in this work [14, 27, 205]. They show that it is even possible to simulate pump-probe data which reflects the dynamics in the vicinity of conical intersections.

### 3.3 Geometrical rearrangement reactions

There are several types of reactions accompanied by a rearrangement of the molecular structure. In many cases this rearrangement has the side effect of taking place on relatively long time scales since the molecular structure has to be twisted or changed otherwise. This also often includes a new arrangement of the solvent shell. Thus, for bigger systems such a molecular rearrangement can well take place on a milisecond or even longer time scale. Nevertheless, there are reactions types, involving molecular rearrangement which take place on an ultrafast, femto- or picosecond time scale. These reaction types often work as trigger for a succeeding reaction which then can take place on much longer time scales. This is for example the case in the protein bacteriorhodopsin, in which a smaller molecular part, namely the retinal molecule, is the trigger for the proton-pumping mechanism of the whole molecule (see also Section 3.3.2). By such a mechanism, a molecular rearrangement can be influenced by effects, taking place on an ultrafast time scale (e.g. a complex photochemical switch or folding of a protein) [206].

Processes that take place on an ultrashort time scale and involve a change in the molecular structure are for example ring-opening or isomerization reactions [54, 56, 57]. Due to these effects, these reactions have very important functions in physics, chemistry and nature. For example the process of vision is essentially depending on an ultrafast isomerization of the molecule retinal. The same molecule is also responsible for the survival of the bacteria halobacterium halobium in salt lakes. For these reasons it is of special interest to understand the undergoing molecular dynamics and to investigate possible methods for controlling the reaction mechanism.

Because of this importance to many fields of science, this thesis examines this topic on two different systems: on a small one from the group of cyanine dyes, namely 3,3'-diethyl-2,2'-thiacyanine (NK88) dissolved in methanol and on the very complex biomolecular system bacteriorhodopsin. Some necessary basics to understand the experiments and interpretations concerning the two systems are given in the next section for the smaller system NK88 and in the section thereafter for the more complex system bacteriorhodopsin.

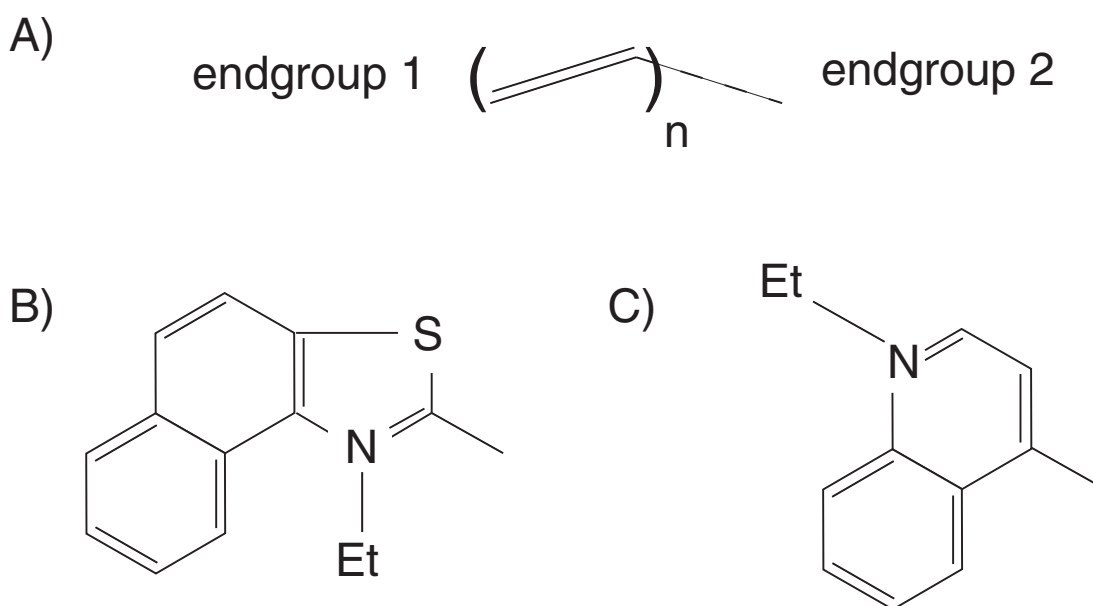


Figure 3.3: Structure of the cyanines. They consist of a polymethine chain of length  $n$  and two endgroups. A) polymethine chain. B) benzothiazolyl (ET: ethyl group) and C) 4-quinolyl endgroup. A methine chain with  $n=0$  and with two endgroups of the first type forms the molecule NK88, while with two endgroups of the second type the molecule 1144C is formed.

### 3.3.1 Isomerization in a simple system

The symmetric cyanines are probably the most widely used class of molecules undergoing photoisomerization. They have an immense variety of applications, for the most part in laser technology as Q-switches, saturable absorbers and laser media [207–210]. Due to their excellent suitability for photosensitization, they can be utilized for everyday technology like photographic materials [211, 212], solar cells [213, 214] or as recording layer in compact discs [215], as well as for diagnostic purposes [216, 217].

The main chromophore of the cyanines is the polymethine chain (see Figure 3.3). According to the length of the chain, the molecule is labeled with the respective Greek prefix. At the two ends of this chain, there can be different endgroups. In the case that the endgroups are identical, the molecule belongs to the group of the symmetric cyanines, in the case that they are different, to the asymmetric cyanines. The properties of these two families differ slightly (see for example [218, 219]). Since this thesis deals with members of the symmetric group, the asymmetric cyanines will not be discussed here. If as endgroups  $NR_2$ , with R being an alkyl group, are used, the molecule belongs to the family of streptocyanine dyes. Members of this family are used in the early theoretical calculations, since they consist of only a few atoms. Unfortunately streptocyanines are not chemically very stable [75]. The stability can nevertheless be



drastically enhanced by using different heterocyclic groups at both ends of the chain. In the case of the molecule used in this work the methine chain consists only of three carbon atoms, from which two of these are members of the endgroup. The endgroups themselves have a benzothiazolyl structure.

While the cyanines with a longer methine chain have been subject of various experimental and theoretical investigations (see [75] for a review), only few information is known about cyanines with a short chain.

The most intensive investigations have been performed by the group of V. Sundström on the system 1,1'-diethyl-4,4'-cyanine(1144C) [59–65]. Their experiments essentially show, that the bond twisting occurs on a sub-picosecond time scale and that the first excited energy surface can be regarded as barrierless. However, despite the similarity of the structures of 1144C and NK88 both the ground state dynamics and the excited state dynamics show significant and interesting differences. This fact makes the investigation of the dynamics of NK88 a very exciting task.

Beside these investigations on short-chained cyanine dyes, already in the seventies the fluorescence lifetime of the molecule NK88 was calculated indirectly from the measured absorption and fluorescence spectra. However, no deeper conclusions on the molecular dynamics could be drawn at that time [220].

A more recent publication [75] mainly deals with the excited state absorption of several cyanine dyes. The group's own sub-picosecond measurements including information from other publications about excited state absorption of different cyanine dyes lead to a rule for predicting the absorption wavelengths of the excited states of the dye molecules. With this rule and from own measurements for the molecule NK88 they predicted the wavelength region (around 390 nm) and the decay time of the excited state absorption (sub-ps regime).

The same publication also succeeded in identifying the spectrum of the photoproducts. The lifetimes of the photoproducts are much longer than the lifetime of the other processes, with the exception of the ground state bleach. Since the ground state bleach has the same shape as the ground state spectrum, the spectrum of the photoproducts can be easily obtained, even without having a sub-picosecond time scale. As disadvantage of this procedure, multiple photoproducts can not be separated, if their decay times are similar.

With the computers becoming more powerful, the group of cyanines have been subject of several theoretical investigations [29, 221]. Especially the dynamics of the short-chained cyanine dyes have very early been simulated theoretically [59, 222]. H. B. Schlegel, M. Olivucci, M. A. Robb, T. Vreven and coworkers mainly focused on the effects on the molecular dynamics resulting from different lengths of the polymethine chain while holding the endgroups identical [29]. A second work by P. A. Hunt and M. A. Robb investigated the effect of different excitation conditions on the isomerization (see Section 3.4).

The third one from F. Santoro and R. Improta directly addresses the dynamical evolution and the potential energy surfaces for cyanines with different endgroups [26].

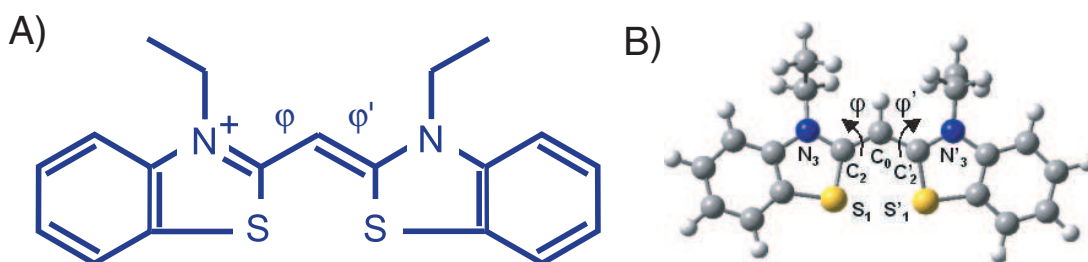


Figure 3.4: A) Schematic drawing of NK88 in its *trans* geometry. B) 3D-Structure of the *trans* isomer of NK88 computed at PBE0/6-31G\* level of theory by F. Santoro and R. Improta (see 4.2). Relevant atomic labels and dihedral angles are indicated .)

These investigations have been influenced by the experiments done within this work, and the discussions motivated different calculations. More specialized calculations to understand the dynamics of the molecule NK88 have been performed in collaboration with the same group [223,224]. These calculations address special issues of the molecular dynamics and most of them are introduced in Chapter 4, where they are necessary to understand the experimental data and to get a picture of the molecular dynamics. However, some of the results are rather basic and therefore introduced in this chapter.

Most of the calculations are carried out for the slightly simpler molecule in which the ethyl groups are replaced with simple H-atoms (HTCY). This has been done for reducing the complexity of the system and thereby reducing the necessary time for the different calculations. Nevertheless, at certain points, where it was necessary for the clearness and the computational effort was acceptable, the calculations have been performed for exactly the molecule this thesis also deals with (NK88).

The calculations have shown that the thermodynamically more stable *trans*-isomer in its ground state has a nearly planar geometry. The two-dimensional structure is given in Figure 3.4. As will be shown in Chapter 4 there are two theoretically possible product isomers, *cis* and *double-cis* (*d-cis*). In contrast to the *trans*-isomer, both the *cis*- and the *d-cis* isomer are turned around one of their C-C bonds and exhibit a significant deviation from planarity (see Figure 4.10).

The simplified molecule HTCY in which the ethyl-groups are substituted by a H-atom has similar structures, but the deviation from planarity is less significant.

After irradiation with light of the proper wavelength, a wave packet is created at the Franck-Condon region (FC) on the first excited surface  $S_1$  (see Section 1.5). From there the wave packet in principle evolves to the conical intersection (CI) and decays back to the ground potential energy surface  $S_0$ . The  $S_0 \rightarrow S_1$  transition has in the case of NK88 and HTCY a nonbonding/nonbonding character [26].

The topology of the first excited surface has proven to be quite complicated and therefore the evolution of the wave packet from the Franck-Condon region to the conical intersection is not trivial. It has been shown that two competing paths exist which

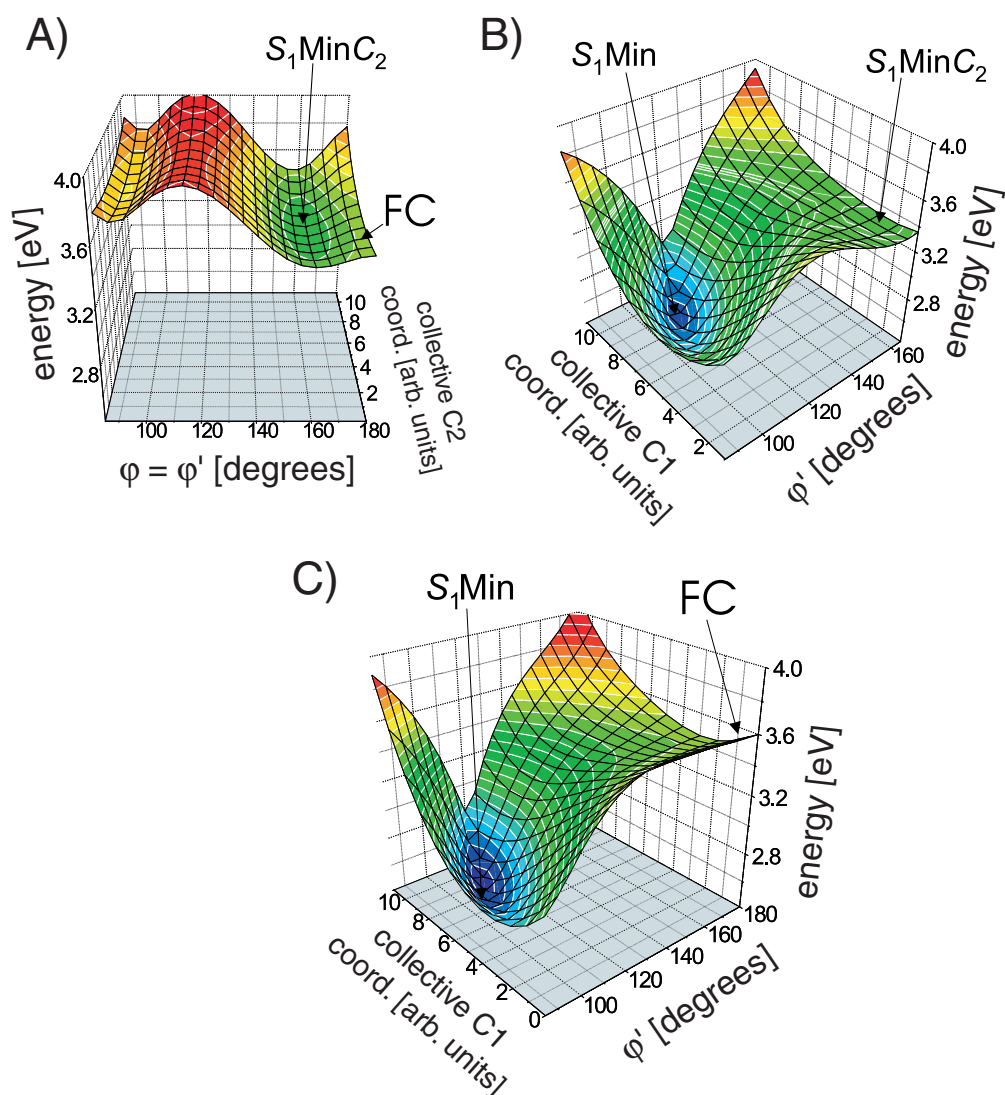


Figure 3.5: Potential energy surfaces for the molecule HTCY along different reaction coordinates (taken from Reference [26]). The evolution from the Franck-Condon region (FC) can proceed on two ways. The first path is represented by the two figures A) and B). It starts at the FC region and then leads to the minimum  $S_1MinC_2$  (A). From there it is necessary to pump energy in asymmetric modes to first reach the minimum  $S_1Min$  and then the conical intersection (B). The second path is display in C). The symmetry is broken at the very beginning and the conical intersection can be directly reached from the FC region over the minimum  $S_1Min$  without passing  $S_1MinC_2$ .

are not too different in their energy. To visualize this behaviour the  $3N-6$  dimensional space needs to be restricted to a two dimensional one. One important coordinate is the torsion  $\varphi'$  around the C-C bond. The other coordinate is defined by linearly interpolating the other internal coordinates between their values at the relevant equilibrium

structures and moving them in a synchronous way. The plot 3.5A shows the potential energy surface in dependence on these two coordinates. Since the molecular structure can be transformed by rotation of  $180^\circ$  into itself, this motion is called  $C_2$  motion in contrast to  $C_1$  motion which stands for a structure which must be rotated by  $360^\circ$  to reproduce itself. From this figure it can be clearly seen that the potential surface exhibits a minimum at an angle of  $\varphi' = 160^\circ$ . This minimum is due to its symmetry labeled as  $S_1MinC_2$ .

In the pure dependency of these coordinates, the conical intersection can not be reached. To get to the conical intersection, it is necessary to pump energy in asymmetric modes (disrotatory motion concerning  $\varphi$  and  $\varphi'$  and asymmetric skeletal mode of the two rings). The potential energy surface in dependence on the angle  $\varphi'$  and these collective asymmetric  $C_1$  modes are shown in Figure 3.5B. This potential energy surface has two minima, a local one which is identical with the above mentioned  $S_1MinC_2$  and a global one, named  $S_1Min$ . The conical intersection CI is not located in the global minimum  $S_1Min$  but at slightly higher energy values. Thus the complete path goes from the FC region to the first minimum  $S_1MinC_2$ , from there to  $S_1Min$  and finally to the conical intersection. This would be the path connected with the lowest energy.

There is also the possibility that the global minimum  $S_1Min$  is reached directly from the FC region if the symmetry between the two rings is broken very early. The according potential energy surface is shown in Figure 3.5C. As one can see from this figure, there is an initial plateau until the angle  $\varphi' = 150^\circ$  is reached, without any barrier. Once the global minimum is reached the situation for the conical intersection is the same as for the first possible path.

The isomerization is accompanied by an intramolecular charge transfer. In the ground state  $S_0$  the charge is almost totally localized on one of the rings. In contrast, in the first excited state, this ring is almost neutral.

The fluorescence has been calculated to mainly arise from the  $S_1MinC_2$  intermediate. Since the minimum  $S_1Min$  is close to conical intersection, fluorescence arising from this area must be at smaller frequencies compared to the excitation frequency, because the distance to the  $S_0$  surface is smaller.

This predicted barrier and competing paths for the molecule NK88 are in strong contrast to the experimental findings for the molecule 1144C which has a more or less barrierless excited surface [59, 61, 62, 65]. This makes an experimental study of the molecular dynamics of NK88 very interesting, but also necessary if the molecule shall be used in a control experiment.

Nevertheless, from the data available, the isomerization dynamics for molecule NK88 is still expected to be on an ultrafast time scale [75, 220], while other chemically realized molecules of the same group have much more delayed dynamics. This behaviour is especially true for cyanines with a long methine chain which have both shown experimentally and theoretically to have a high barrier on the excited surface and therefore very long fluorescence time scales [29, 75]. The barrier finally influences

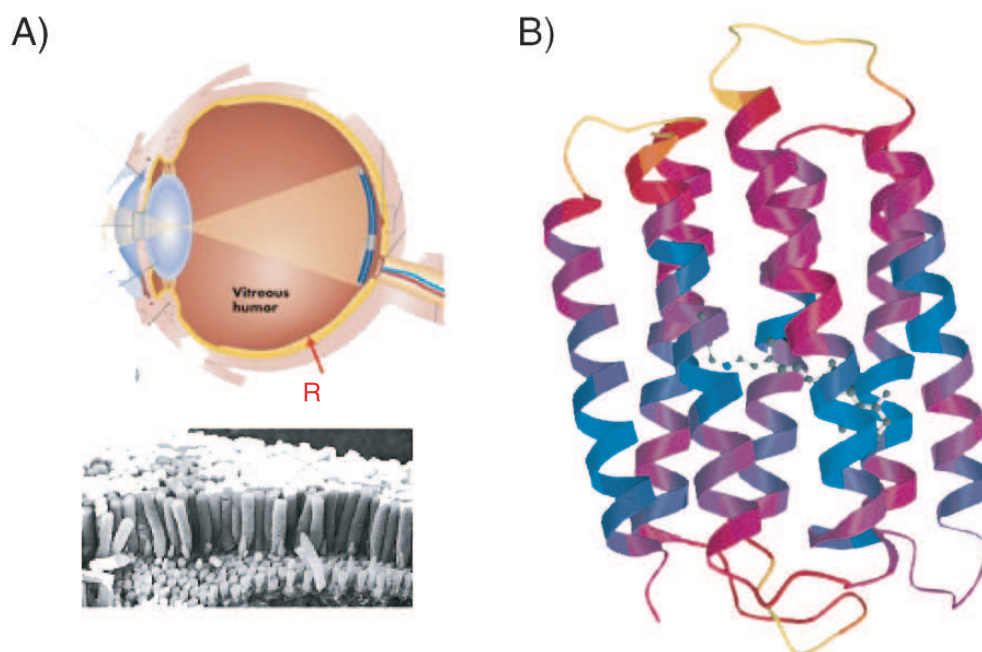


Figure 3.6: Examples of important isomerization reactions of the molecule retinal: A) retina rod cells in the human eye: retinal molecules embedded in the protein rhodopsin. B) the retinal molecule embedded in the protein bacteriorhodopsin (taken from [225]).

the time scales on which the different possible isomers states are populated.

Also the substitution of the sulfur atom in the molecular structure by an oxygen to form oxacyanine or by  $\text{CH}_2$  groups has shown to result in remarkably slower dynamics. In contrast to this, the use of completely different endgroups can result in even faster dynamics. However, all molecules for which information about the excited state is available behave slower than NK88, with the exception of the molecule 1144C. The time scale of the dynamics of this molecule is expected from the available literature data to be comparable with the time scale of NK88.

### 3.3.2 Isomerization in a large biological system

As already pointed out, isomerization is very important for many processes in biological systems. Two very famous examples are shown in Figure 3.6 concerning the molecule retinal, embedded in the protein rhodopsin or in the protein bacteriorhodopsin. Depending on the protein environment the isomerization reaction of the retinal molecule triggers quite different processes. Embedded in rhodopsin, it can be found for example in the human eye and forms the primary step of vision [66]. In bacteriorhodopsin it works as the trigger for a proton pump which is essential for the

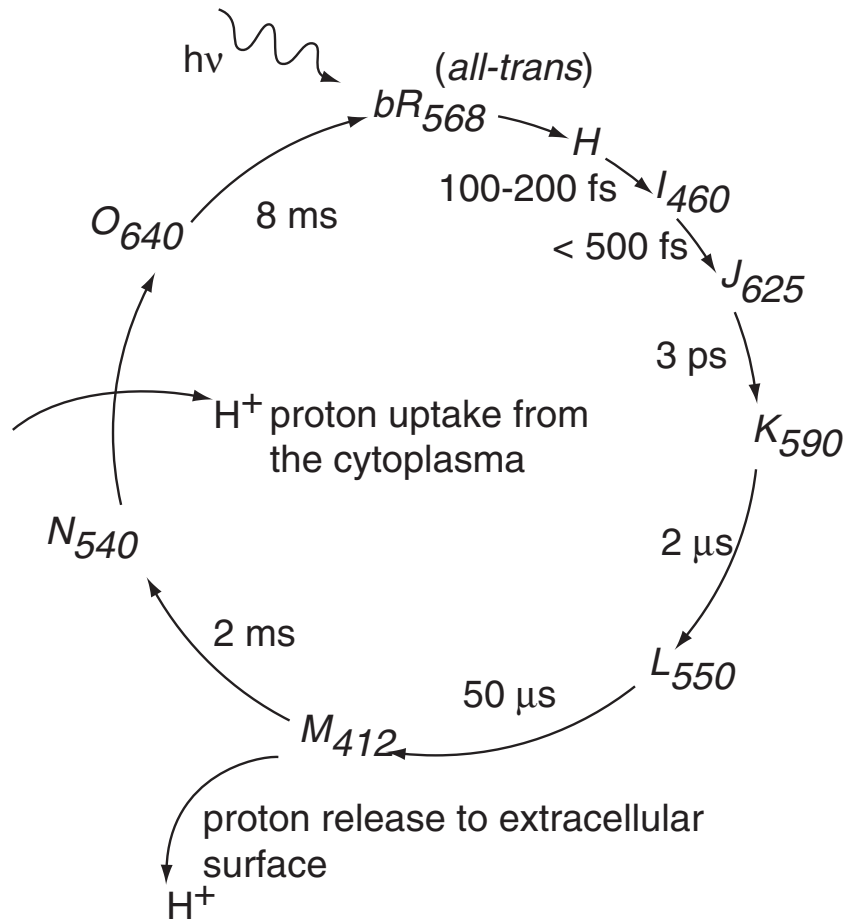


Figure 3.7: This figure shows the complete photocycle of bacteriorhodopsin. As can be seen from the sketch the protein works as a proton pump, whose function is triggered by the initial isomerization of the *all-trans* retinal (BR). The succeeding steps are labeled from  $I_{460}$  to  $O_{640}$ . The central absorption wavelength of the according transition states are given as subscript and the decay times from one state to another are written along the arrows (adapted from [227]).

survival of the bacterium in which bacteriorhodopsin can be found [67–69]. Due to the very specialized function within the biological system, the protein environment is expected to have a large influence on the isomerization reaction itself.

This thesis deals with the membrane protein bacteriorhodopsin which is an integral part of the purple membrane of *Halobacterium halobium*, a bacterium that can be found in salt marshes [67–69]. The chromophore group of this protein is the retinal molecule. In bacteriorhodopsin the photoisomerization of the retinal chromophore is the first step for a proton transport through the bacterium membrane. The proton pump causes a proton gradient which drives the synthesis of adenosine triphosphate [34, 69, 226].

The complete photocycle of bacteriorhodopsin is shown in Figure 3.7 and has been subject to many publications. Experiments carried out with a variety of spectroscopic methods show that different transition states are involved in the photocycle of bacteriorhodopsin:  $bR_{568} \rightarrow H \rightarrow I_{460} \rightarrow J_{625} \rightarrow K_{590} \rightarrow L_{550} \rightarrow M_{412} \rightarrow N_{540} \rightarrow O_{640} \rightarrow bR_{568}$ . The subscript denotes the maximal absorption wavelength at which the respective transition state can be monitored.  $bR_{568}$  denotes the thermodynamically stable ground state of light-adapted bacteriorhodopsin. Roughly, after excitation to the Franck-Condon region ( $H$ ) the  $I_{460}$  transition state is populated in 200 fs. From there, the decay into the  $J_{625}$ -state occurs in less than 500 fs. The  $K_{590}$  state finally has a *13-cis* geometry and is populated in about 3 ps [227].

Since this work only deals with the first steps of the process (steps  $I_{460}$  until  $K_{590}$ , see Figure 3.7) the complex longtime behavior of the protein will not be discussed here (for an overview see [68, 225, 227]). The population of the transition state  $K_{590}$  is required for the following photocycle. If this state is not populated, the following process of proton pumping will not take place. This early time dynamics and the detailed spectroscopic signals, insofar as they are necessary for this thesis, will be discussed more deeply in Chapter 5.

### 3.4 Schemes for optimal control in the vicinity of conical intersections

The fundamental concepts of optimal control schemes are already introduced in Chapter 1. In general the control schemes for different problems are based on one or more aspects of these introduced principles. Nevertheless, the field of theoretical optimal control regarding different control objectives is a topic many groups work on throughout the world. The knowledge of the pure fundamental principles for optimal control alone is not sufficient to regard all problems as solved. Still the interplay of the molecular Hamiltonian with the control field is a very complex problem and it is not necessarily the case that each method can solve the given problem or that a possibility exists to solve it at all. In this context, it is a very interesting question how a given problem can be solved, i.e. how the control field has to be designed and what the underlying control mechanism actually are.

There are several publications that investigate the issue of controlling the isomerization efficiency, what is the aspect this thesis is mainly dealing with [98, 101, 221, 228–233]. In general one can group the different control schemes in passive and active ones [14]. Passive control means that particular wave packets are prepared in the Franck-Condon region by specific tailored pump laser pulses which are then turned off. The wave packets then evolve under the influence of the potential energy surfaces. The term active control means that the laser field remains turned on during the intended reaction. The laser field guides the system from the initial state out of the Franck-Condon region to the final state.

A very exciting computational example concerning passive optimal control of photoisomerization has been performed by M. A. Robb and P. A. Hunt [221]. This study deals with a small cyanine dye (trimethine streptocyanine stCY) which is thus of the same group as the molecule NK88 which is used in this work. For reduction of the computational effort the endgroups are smaller than in the case of the molecule used in this thesis (see Section 3.3).

In many publications, the most probable path for the evolution of a wave packet is estimated by the smallest potential energy. This results in the concept of a conical intersection, viewed as a single spot on the excited surface, having the lowest potential energy. Normally, the conical intersection is not only a spot but in fact a multidimensional surface (see Section 3.1 and [14, 200]).

It has turned out that for the molecule stCY two reaction coordinates are most important (torsion around the central C-C bond and the skeletal stretching). The potential energy surface of the ground state and the first excited state are shown in Figure 3.8 in dependence on these reaction coordinates. In this figure the conical intersection seam is also indicated as well as the minimum energy path trajectory. This trajectory jumps to the ground energy surface at the minimum energy path conical intersection, which is normally only called conical intersection. Depending on the initial conditions at the excitation step, the wave packet does not necessarily need to take the minimum energy path. Thus it does not necessarily get to the ground state surface neither at the same spot as in the minimum energy path nor with the same shape. Naturally, as one can easily take out of Figure 3.8, this will strongly affect whether the trajectory will end up in the left or the right well or in other words, whether the molecule will isomerize or not. If the skeletal stretching is enhanced, this will result in an earlier crossing of the conical intersection seam and thus result in populating preferentially the *trans* well. In contrast, by reducing this skeletal motion and enhancing the torsional motion, an increase of the *cis* isomer yield can be achieved.

A different concept for controlling the *cis-trans* isomerization yield incorporates higher lying states. Since the calculation of higher lying states is very time-consuming and difficult, there are not many theoretical investigations that deal with this topic. Higher lying states generally become more dense and thus the number of conical intersections increase. Excitation into this regime and shaping the wave packet can make advantage of this issue, since many different reaction pathways may now be available.

Most of the theoretically active control schemes in the case of isomerization as control objective work with a shaped excitation step followed by dumping of the population with an also shaped dump pulse [98, 228, 229, 231, 232].

A very complete calculation has been performed on retinal in rhodopsin by Fujimura, Domcke and coworkers [98]. This is a system which is quite similar to the one used in this thesis, but there embedded in the protein bacteriorhodopsin. A similar study has been previously carried out for a simplified model for bacteriorhodopsin with comparable results [228].

As potential energy surfaces for the control study on rhodopsin, the very success-



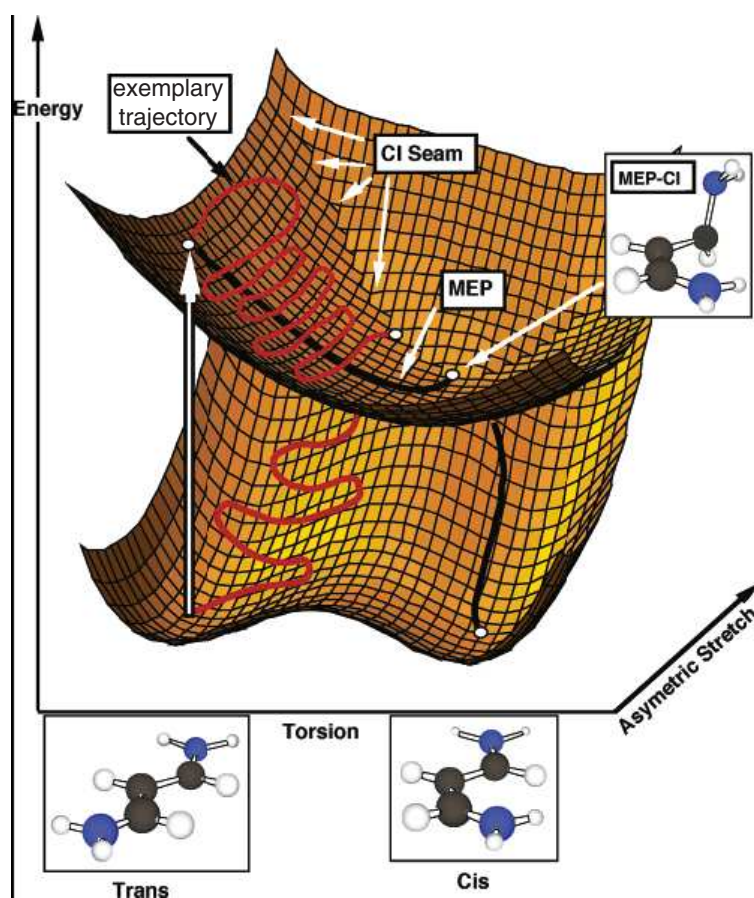


Figure 3.8: Potential energy surfaces of stCY in dependence on the two reaction coordinates on the torsion around the central C-C bond and the skeletal stretching. While the molecules in the left ground state potential well have *trans*-geometry, the molecules in the right well exhibit a *cis*-structure. Also depicted are a minimum energy path trajectory (MEP) and an exemplary trajectory that a wave packet can take after the molecule has been excited from an initial *trans*-configuration. The conical intersection seam (= conical intersection hyperline, see Subsection 3.1) is also shown in the plot. Taken from [221].

ful model from Stock and coworkers is used that simulate the spectral properties and the dynamical behaviour of this molecular system (see [27, 205] and Section 3.2). In their calculations, they have shown that these potential energy surfaces can be well described in dependence on the torsional angle about the C-C bond and an effective coupling mode which corresponds largely to the stretching coordinate of the polyene chain. The calculated pulse structure consists of a shaped excitation pulse which prevents the coupling mode from being excited. This coupling mode is mainly responsible for enhancing dephasing of the wave packet. The less dephased wave packet already ensures a higher product yield. After 400 fs the control field has basically no amplitude

until becoming very intense after 450 fs. This has been identified to be a pump-dump pulse that ensures an even higher yield in the product channel. Since the Franck-Condon factors at this stage are very small, the amplitude of the final feature in the pulse sequence is an order of magnitude larger than the previous pulse structure.

These kinds of electric fields are quite difficult to obtain in a real experiment since the necessary frequency range is quite large. In principle such large spectra can be produced and even shaped, but the experimental effort is high. Therefore a modified variant of this scheme is proposed in Section 5.3 that can at least partly address these described issues.

# Chapter 4

## NK88 - a simple cyanine dye

The relevance of the cyanine dyes both for scientific interest and for technological applications has already been stressed in Section 3.3. Furthermore due to their capability to isomerize, they are well suited for the investigation on the control of geometrical rearrangement reactions.

Very good candidates for this task are the short chained members of the cyanine dyes family, due to their considerably fast isomerization process. Despite the high number of molecules in this subgroup the dynamics of only one member, the molecule 1144C, has been well characterized. Unfortunately this molecule is not so well suited for a possible control experiment, since its absorption maximum does not agree with the wavelength provided by the laser system.

The high relevance of this molecular family paired with the lack of information on the potentially most interesting subgroup for an optimal control experiment motivates a study of the short chained cyanines. Therefore in this chapter the molecular dynamics of a member of the short chained cyanine dye subgroup, namely NK88, is investigated by various spectroscopic methods and in different solvents. These measurements are completed by simulations carried out in a cooperation by F. Santoro and R. Improta. These calculations in comparison with the spectroscopic data are able to give a detailed and reliable description of the overall kinetics. The cooperative investigation on this molecule demonstrate that in a complex problem as given here, the interplay of theory and experiment can yield a much richer description of the molecular processes than one of the fields alone. Because the calculations will greatly increase the understanding of the experimental data, they are also presented in this chapter. The results of these experiments will show remarkable differences in the potential energy surfaces of NK88 in comparison with the molecule 1144C, despite their structural similarities.

On the basis of this data optimal control experiments are performed that show enhancement and suppression of the isomerization efficiency. Single control parameters such as chirp or excitation pulse energy are also compared in their effect on the isomerization process. Finally the effect of optimized fluorescence on the isomerization reaction is investigated in an additional experiment to gather more information about

the influence of the radiative decay channels on the isomerization process.

## 4.1 Experimental details for the spectroscopy experiments

The details of femtosecond laser system and the pulse shaper used in the experiments are presented in Sections 2.1 and 2.4. A fraction of the available pulse energy is used for the pump pulse which is then frequency-doubled in a 400  $\mu\text{m}$  thin lithium triborate (LBO) crystal. In the case of the experiments, using the pulse shaper, the spectral phase of 800 nm beam can be shaped, resulting in phase and amplitude shaped pulses after the frequency doubling process (see Section 2.4).

The pulse energy of the second harmonic generation (SHG) at 400 nm is generally 1.5  $\mu\text{J}$ . In the case of complex pulse shapes, the pulse energy can be significantly smaller compared to that value. The 400 nm pump pulse is then focused by a lens with a focal length of 20 cm into a flow cell where the molecule NK88, dissolved in methanol or ethylene glycol, is constantly exchanged by a peristaltic pump. This way, each laser shot sees a new volume of the solution. The flow cells have a thickness of 200  $\mu\text{m}$  and 2 mm in the cases of methanol and ethylene glycol, respectively. The sample is purchased from Exciton Inc. as cationic dye, namely 3,3'-diethyl-2,2'-thiacyanine iodide, and used without further purification. Absorption spectra are recorded with a Hitachi U-2000 spectrophotometer.

For the probe laser pulse about 50  $\mu\text{J}$  of the 800 nm laser pulse is taken and frequency-double it in a 300  $\mu\text{m}$  thin beta barium borate (BBO) crystal. The resulting 400 nm laser pulse is employed to generate a chirped supercontinuum by focusing it into a sapphire disk. For probe wavelengths above 500 nm, the supercontinuum is generated by leaving out the BBO crystal and focusing the 800 nm beam into the sapphire plate. The white-light probe laser beam is then focused by a lens with a focal length of 15 cm into the sample under an angle of about  $10^\circ$  with respect to the pump laser beam. After passing the sample, the probe pulse is analyzed by a monochromator for detection of different probe-wavelengths from 350 nm to 950 nm. If not otherwise mentioned, the polarizations of pump and probe beam are set to magic angle configurations of  $54.7^\circ$ . The delay between the two pulses can be modified by a computer-controlled delay stage. The dynamics in the measured transient absorption signals are approximated in a single or multiple exponential fitting procedure, as widely used in femtosecond transient spectroscopy [61, 137, 234–241], with rise and decay times taking into account the cross-correlation (200 fs FWHM) of the pump and the white-light probe laser pulses.

A further setup is used for the fluorescence-upconversion experiments. The 800 nm pulse is frequency-doubled in a 400  $\mu\text{m}$  thin LBO crystal, a dichroic mirror then separates the SHG and the fundamental 800 nm laser beams. The 400 nm beam is used as pump pulse, while the 800 nm beam has the function of a gate pulse in the fluorescence

upconversion crystal. A flow cell with a thickness of 2 mm is positioned between two microscope objectives. A 500 nm band-pass filter blocks the remaining pump beam, while the fluorescence proceeds to a further BBO crystal. The fundamental 800 nm light propagates via a computer-controlled delay stage and is focused into the crystal by a lens with focal length of 20 cm under an angle of about  $10^\circ$  with respect to the fluorescence. The angle of the crystal is set to the phase matching condition for the desired wavelength. The sum-frequency signal passes a narrow band-pass filter and the transmitted light is measured with a photomultiplier tube.

## 4.2 Computational details

The calculations in connection with the dynamics of the molecule NK88 have been performed by F. Santorro and R. Improta. Ground state optimization and frequency calculations of minima and transition states (one imaginary frequency) are performed in vacuum at DFT/6-31G(d) level using the PBE0 hybrid functional [242,243]. The transition states are determined according to the STQN method by Schlegel and coworkers [244]. The energies are refined by single-point calculations both at PBE0/6-31+G(d,p) and at MP2/6-311+G(2d,2p) level. Weak dispersive interactions are likely to stabilize the transition structures (vide infra) and MP2 method is known to be more reliable for their treatment [245–248]. Vertical excitation energies are computed by time-dependent DFT (TD-PBE0) at TD-PBE0/6-31+G(d,p)//PBE0/6-31G(d) level. Bulk solvent effects on the ground and the excited states have been taken into account by means of the Polarizable Continuum Model (PCM) [249]. In this model the molecule is embedded in a cavity surrounded by an infinite dielectric, with the dielectric constant of the solvent (for methanol the value 32.64 is used). The cavity of the solute is defined in terms of interlocking spheres centered on non-hydrogen atoms, whose radii are optimized according to the UAHF model [250]. Electrostatic solvation free energies are computed at PCM/PBE0/6-31+G(d,p) level, while for excited states PCM/TD-PBE0/6-31+G(d,p) calculations are performed, according to the procedure outlined in Reference [251]. Thermal contribution to free energy in vacuum are computed from the results of the frequency calculations. All the calculations are performed by the Gaussian03 package [252].

Excited state optimizations are performed both at CIS/6-31G\* level by the Gaussian [252] package and at time dependent DFT (TD-DFT) level by the Turbomole [253] package, utilizing the PBE0 hybrid functional [242, 243] and the dev-SV basis set, whose accuracy is comparable with the standard 6-31G\* one.

## 4.3 Study of the excited state dynamics

Only a few experimental aspects are known about the excited state kinetics of the molecule NK88. Basically only two estimations care about this problem (see Section 3.3). In the seventies, the fluorescence lifetime was calculated from the absorption and fluorescence spectra to be about 1.7 ps [220]. A different group estimated the excited state absorption from own sub-picosecond experiments to be centered around 380 nm and having a life time in the sub-picosecond regime [75]. In contrast there have been several theoretical simulations on this topic, indicating rich excited state dynamics [26, 29, 221].

The dynamics before and directly after the transition back to the ground state are therefore investigated by transient absorption spectroscopy in a wavelength region from 360 nm to 950 nm and in different solvents. To get better access to the excited state dynamics in particular, fluorescence upconversion is as well performed. These results are compared with theoretical simulations to get a conclusive description of the overall kinetics on the first excited surface.

### 4.3.1 Results of the experiments

The absorption spectra for different concentrations are presented in Figure 4.1A for an optical density of 0.1 to 1.1 at the pump-wavelength of 400 nm. The normalized spectra presented in Figure 4.1B show no variation of the absorption characteristics. Figure 4.1C shows the steady-state absorption spectrum of NK88 in methanol at room temperature. It is dominated by the monomer peak at 422 nm and drops significantly before 450 nm. The asymmetry has been attributed to a vibronic shoulder around 406 nm [217]. As a pulse at 400 nm is used, i.e. on the blue side of the absorption spectrum, as pump beam, excitation of several vibronic levels is likely. For the more viscous solvent ethylene glycol, the maximum is shifted by 3 nm to the red. In the following, the focus will be on the transient behavior in methanol, additional measurements in ethylene glycol have been performed for comparison and for further deciphering of the underlying molecular processes.

The overall dynamics are shown in Figure 4.2. Here spectrally resolved pump-probe transients are presented for the first 30 ps for probe wavelengths from 370 nm to 950 nm. In this section the focus will mainly be on the early-time dynamics. The main aspects at early times (seen in Figure 4.2) are the increased absorption around 750 nm and 380 nm, and the decreased absorption between 420 nm and 600 nm and again at around 900 nm. In order to understand the different contributions at these wavelengths, different representative transients are presented and discussed in the following.

The effect of decreased absorption between 420 nm and 600 nm can be well visualized by a transient at a wavelength of 500 nm (see Figure 4.3A). There, only one absorption and one emission process contribute to the total signal as can be seen from

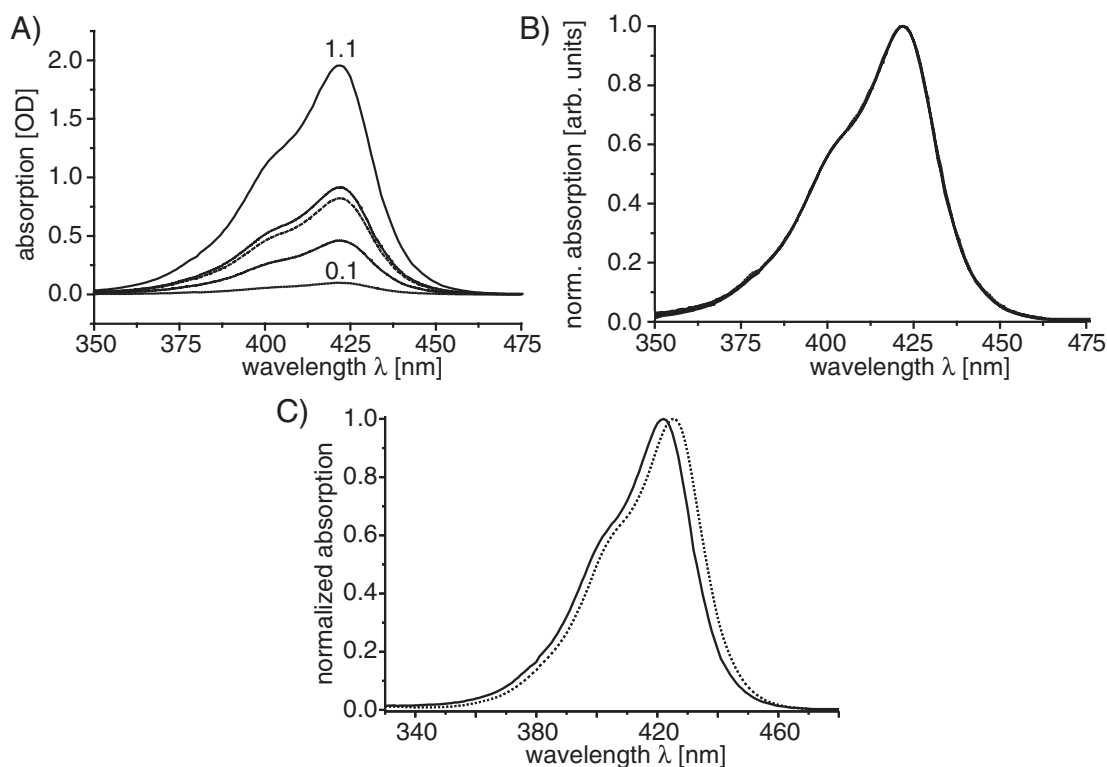


Figure 4.1: A) Steady-state absorption spectrum of NK88 dissolved in methanol at room temperature for different concentrations. B) Normalized spectra for the different concentrations shown above. C) Steady-state absorption spectrum of NK88 dissolved in methanol (solid line) and ethylene glycol (dashed line) at room temperature.

the two curves in Figure 4.3A, which represent a decomposition of the total fit into the two involved processes. The rise time constant with which the emission signal appears is 0.2 ps while the decay time constant with which the emission signal diminishes is 1.9 ps. The absorption contribution rises with 2.2 ps and decays with 11 ps. Fits with a fixed rise time of the absorption contribution yield acceptable results up to rise times of 3 ps.

In order to get a better understanding of the excited-state dynamics we fluorescence upconversion measurements have been performed. The time-resolved fluorescence at 500 nm is shown in Figure 4.3B. This wavelength is close to the maximum of the fluorescence spectrum. The fit to the data associated with 500 nm gives basically a monoexponential decay curve with 1.8 ps. A biexponential model fits the data better, but the second decay contributes only less than 2% with a decay time constant of about 9 ps. Thus, it will not be considered in the following.

The transient absorption at 700 nm shows the temporal behavior of the increased absorption starting around 600 nm until 950 nm. The fit to this data consists of two parts: a fast decay with a time constant of  $\tau=1.4$  ps and an offset. This offset is

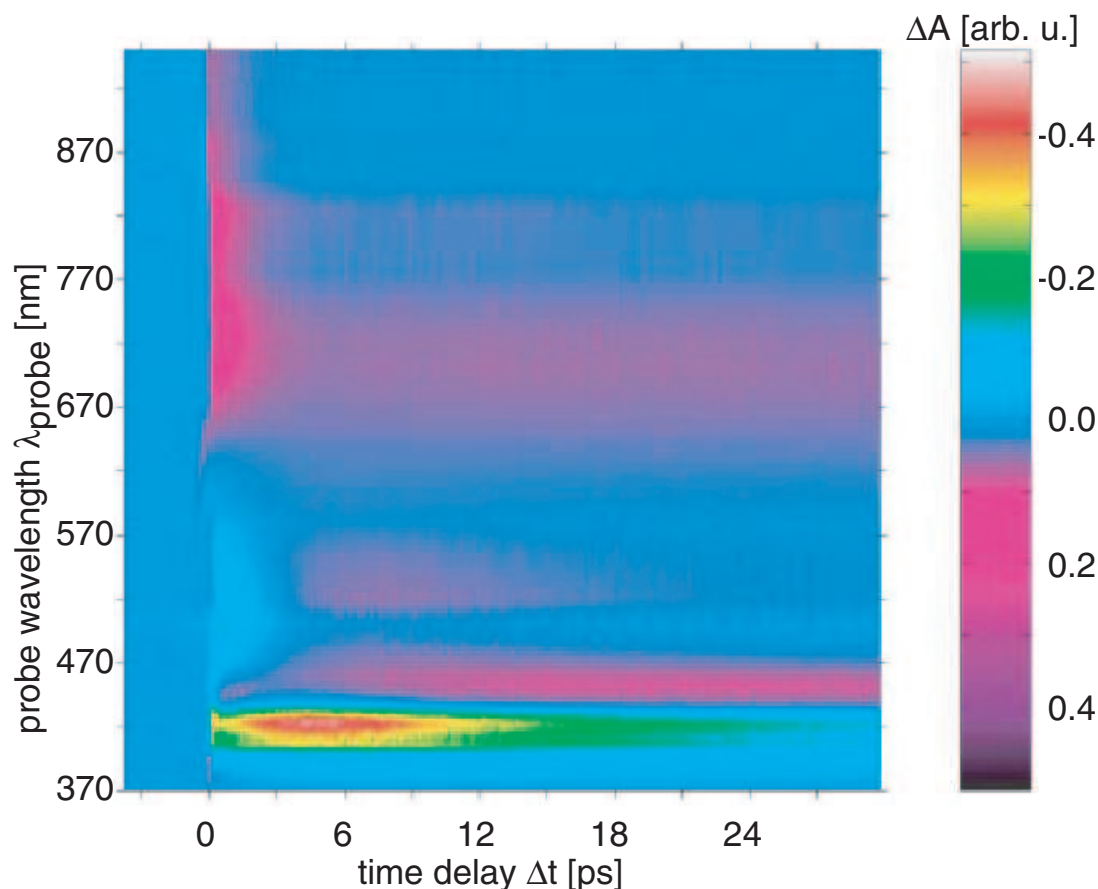


Figure 4.2: Spectrally resolved pump-probe transients. The z-axis ( $\Delta A$ ) of the contour plot describes the change in absorption of the probe-light. While red denotes a high transmission (decrease in absorption) through the sample, purple marks increased absorption of the probe-beam.

strongly intensity dependent and vanishes for excitation laser pulse energies smaller than  $0.25 \mu\text{J}$ . To clarify the origin of the offset additional experiments on potassium iodide (KI) in methanol have been carried out. In these experiments, only the solvent and the molecule are changed, whereas other laser parameters are kept constant. As can be seen in Figure 4.4, the transient obtained in pure methanol has only one contribution different from zero which is the coherent artifact at the origin of the time axis. In the case of KI dissolved in methanol there is an absorption signal in addition to the coherent artifact, but in contrast to NK88 there is no contribution that decays on a short time scale. Of course the coherent artifact also exists for NK88 dissolved in methanol, but it vanishes in the rising edge of the absorption.

At the red side (600 nm to 950 nm) of the wavelength region accessible with the probe pulses, an additional feature of negative absorption becomes visible (see the



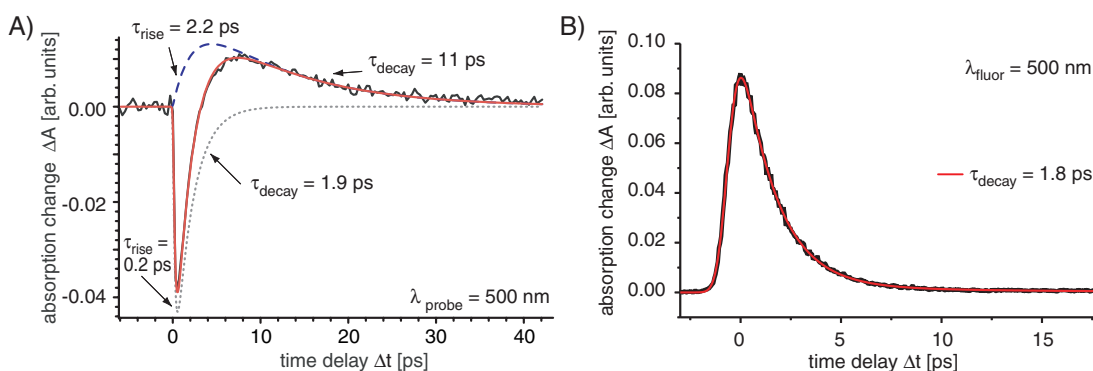


Figure 4.3: A) Transient at a probe wavelength of 500 nm. Black shows the experimental data points, while red marks the fitted curves. Dotted gray and dashed light blue show the contributions that superpose to the complete fit, namely stimulated emission and an absorptive signal, respectively. B) Fluorescence upconversion transient for a fluorescence wavelength of 500 nm. Black shows the experimental data points, while red marks the fitted curve.

transient at 900 nm in Figure 4.5D). This feature has rise and decay time constants of 3 ps and 8 ps, respectively. Careful analysis of the transient absorption at 750 nm (data not shown) shows that this emissive contribution is also present at this wavelength, but with a very small amplitude compared to the other features present at 750 nm. The transient at 900 nm also exhibits a fast absorption signal with a time constant of 1.4 ps, and a slight offset similar to the transient at 700 nm.

The most difficult feature to analyze is the absorption starting at the blue edge of the observation window below 360 nm and going up to 440 nm. At almost all wavelengths in this area at least one further process contributes to the total signal. In the region where the steady-state absorption spectrum (Figure 4.1) is different from zero, the effect of pump-depletion exists. If the probe pulse comes before the pump pulse, all molecules are still in the ground state. In the opposite situation, i.e. when the probe pulse comes after the pump pulse, the probe beam experiences less absorption, causing a band of pump-depletion (manifested as decreased absorption, the so-called ground-state bleach). Farther on the red side, the absorption bands of the product states and hot ground states as well as the stimulated emission arise. Therefore, the transient at 360 nm is appropriate in order to investigate the absorption band which starts in the near-ultraviolet and goes up to 440 nm. Only a small contribution of pump depletion (compare with Figure 4.1) can be found there. Nevertheless, especially from the logarithmic plot in Figure 4.5C it can be seen that the underlying dynamics are very complex at a probe wavelength of 360 nm.

At very early pump-probe delay times in the 360 nm transient shown in Figure 4.5A-C, a rapid decay is visible after which the decay becomes slower and then changes again to a slightly faster decay. This decay behavior can be explained by the superpo-

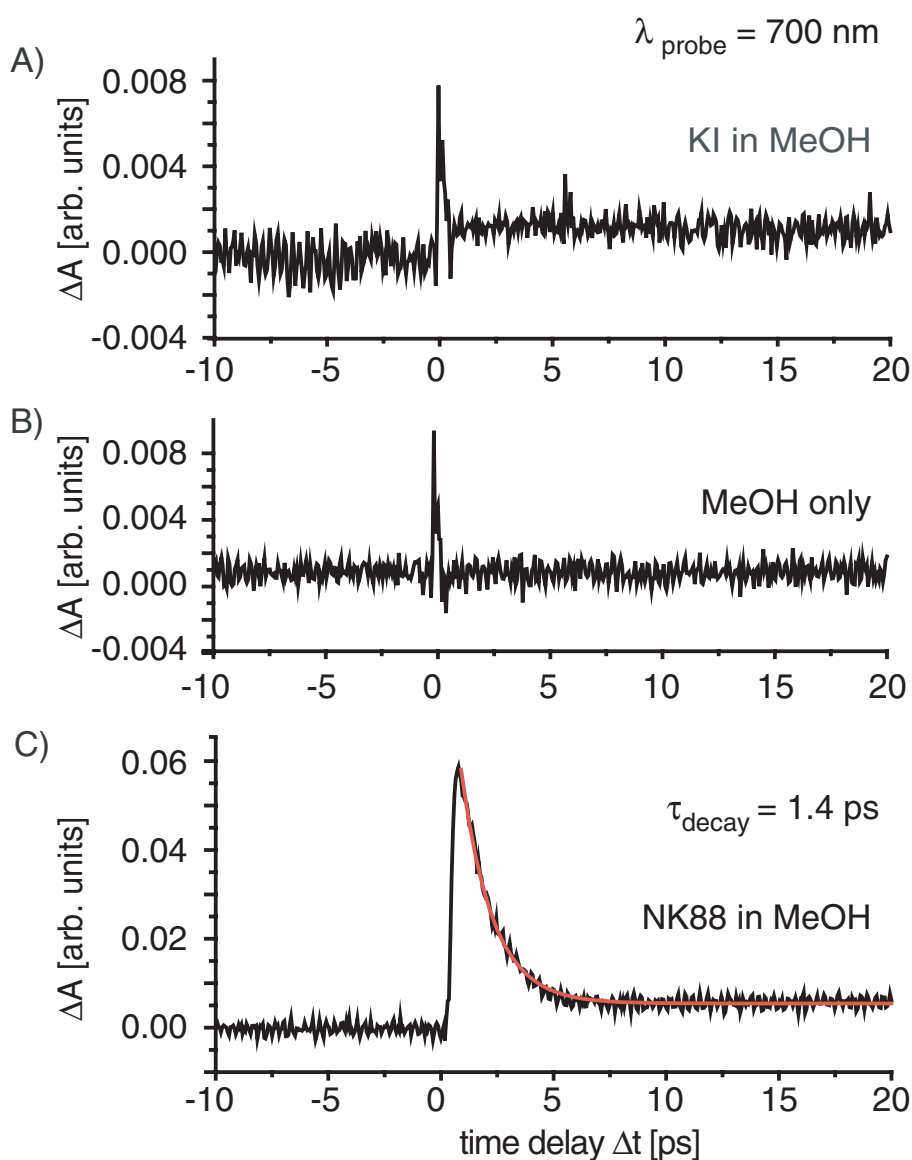


Figure 4.4: Transient at a probe wavelength of 700 nm for the cases A) KI in methanol, B) methanol only and C) NK88 in methanol for the first 20 ps. Black represents the experimental data points, while red marks the fitted curves.

sition of different contributing components. The fits in Figure 4.5A-C show these two contributions together with a small bleach component whose shape and time constants are derived from the transient at 400 nm (see Subsection 4.4). The initial absorption has a rise time that is below the time resolution and a decay time constant of 1.2 ps, while for the second absorption signal rise and decay time constants are 1.8 ps and 9 ps, respectively. These fast features (decaying with 1.2 ps and 9 ps, respectively) cannot be explained by the overlapping rest of the pump depletion (recovering with

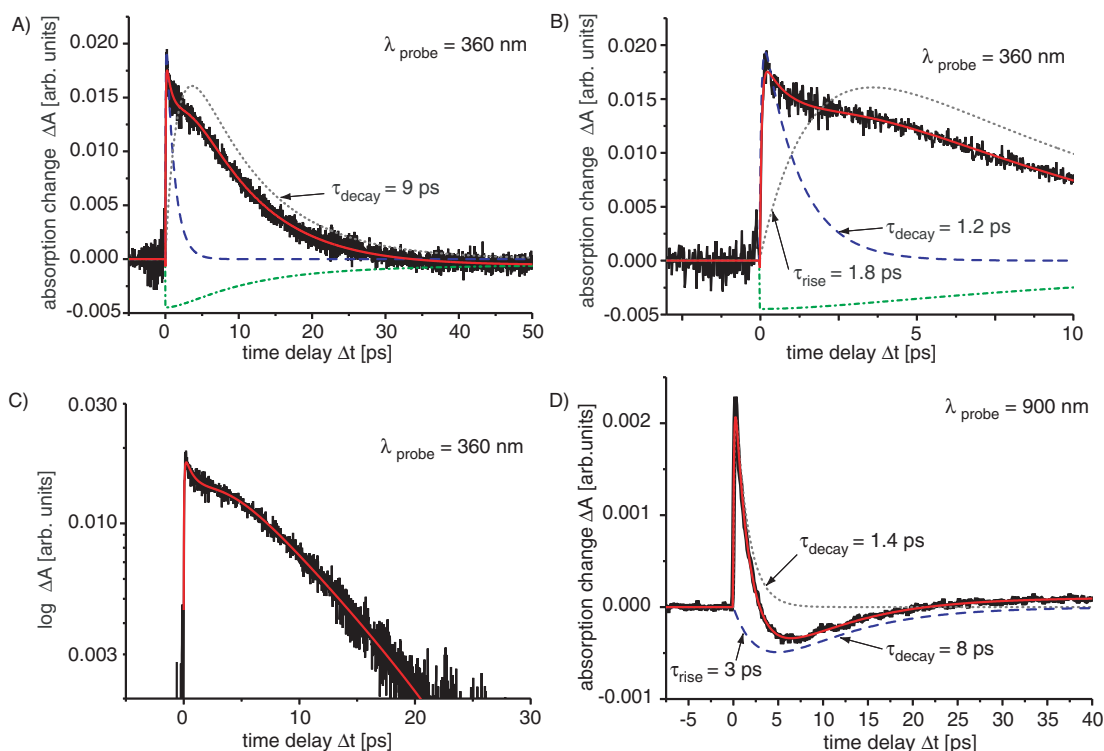


Figure 4.5: Transient at a probe wavelength of 360 nm on a long A) and on a short B) time scale, as well as in a logarithmic representation C). Black represents the experimental data points after subtraction of the coherent artifact, while red marks the fitted curves. The three contributions of ground state bleach (dot-dashed green), initial (dashed blue) and succeeding (dotted orange) excited state absorption are also shown. D) Transient at a probe wavelength of 900 nm. Black shows the experimental data points, while red marks the fitted curves. Gray (dotted) and blue (dashed) show the contributions that superpose to the complete fit, namely excited state absorption and stimulated emission, respectively.

10 ps, 45 ps and 600 ps see Subsection 4.4), since the time scales are different. Therefore, two superposing processes must give rise to this absorption signal. The reason for assuming these processes in the fit model becomes evident in the discussion.

For comparison and assignment of the absorptions at 360 nm and 500 nm, transients in the more viscous solvent ethylene glycol are presented in Figure 4.6. Similar to the case of NK88 dissolved in methanol, the transient at 360 nm is not purely monoexponential as can be seen in the inset. The reason for this is the superposition of two absorptive signals and a small contribution of pump depletion analogously to the case of methanol. The decay times of the two absorptive contributions are about 6 ps and 56 ps, respectively.

In contrast to methanol as the solvent, the 500 nm transient of NK88 in ethylene

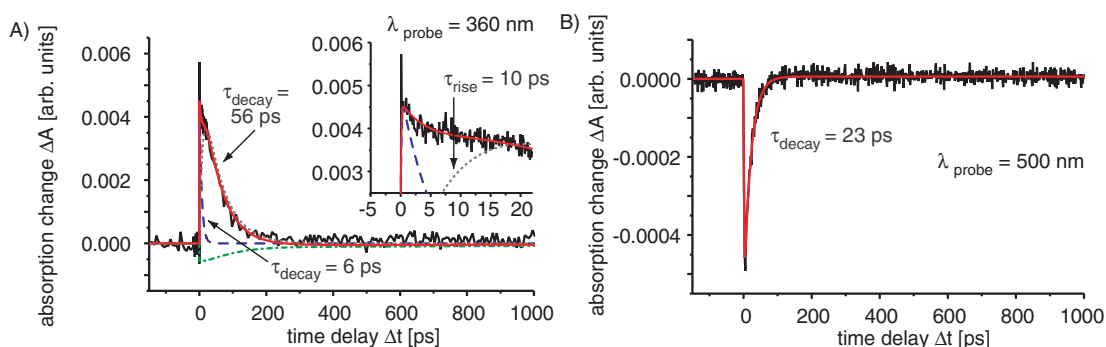


Figure 4.6: Transient at probe wavelengths of A) 360 nm and B) 500 nm for NK88 in ethylene glycol. Black represents the experimental data points, while red marks the fitted curves. The inset in A) shows the first 20 ps of the 360 nm transient. The three contributions to the 360 nm transient, namely ground state bleach (dot-dashed green), initial (dashed blue) and succeeding (dotted gray) excited state absorption, are also shown.

glycol has only a contribution of decreased absorption that decays with 23 ps, while there is basically no absorptive component (see also Section 4.4).

### 4.3.2 Results of the computations

Figure 3.4B shows the structure of the trans isomer (the Franck-Condon structure) of NK88 computed at PBE0/6-31G\* level of theory. Relevant atomic labels and dihedral angles are indicated. By using the same approach previously applied to the study of a simpler model of NK88 (where the Et- groups are substituted by H- groups) [26], here the minimum energy path from the Franck-Condon structure to the  $S_1$  absolute minimum is approximately described through a series of excited state optimizations at fixed values of the  $\varphi'$  ( $N'_3 - C'_2 - C_0 - C_2$ ) angle, performed by the CIS/6-31G\* method. The path, reported in Figure 4.7, starts with a conrotatory motion of  $\varphi$  and  $\varphi'$  that preserves the  $C_2$  symmetry up to a local minimum  $S_1 \text{Min}C_2$  at  $\varphi = \varphi' = 153^\circ$ . After that, crossing a very weak barrier (estimated to be  $\approx 0.015$  eV), the system breaks the symmetry by a disrotatory motion and reaches the global TICT  $C_1$  minimum (see Figure 3c in reference [26]). This behavior is qualitatively similar to that predicted for small cyanine models by accurate CASSCF calculations [29]. At  $C_1$  structures the  $S_0 \rightarrow S_1$  transition acquires a charge-transfer character. TD-DFT presents known deficiency in treating this kind of transitions [254] over-stabilizing the  $S_1$  energy, and in fact a TD-PBE0/def-SV computation of the  $C_1$  path, fails to reproduce its first  $C_2$ -like part.

Additionally the feasibility of a different path is investigated which preserves the  $C_2$  symmetry ( $\varphi = \varphi'$ ) up to pseudo-perpendicular arrangements. This alternative path might be relevant for the production of the  $C_2$  *d-cis* isomer, that is obtained from the *trans* structure rotating both the  $\varphi$  and  $\varphi'$  dihedrals. Figure 4.7 reports the  $C_2$  path

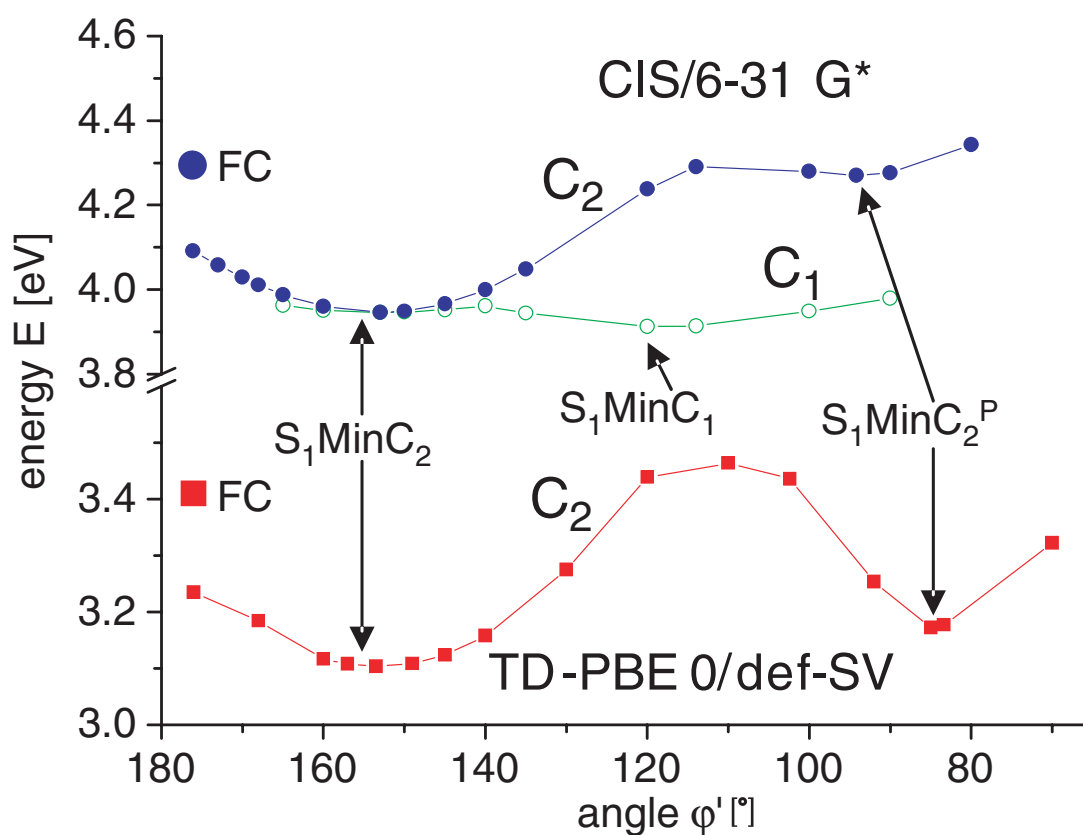


Figure 4.7: Symmetry-constrained ( $C_2$ ) and free ( $C_1$ ) paths on the  $S_1$  surface of NK88 computed at CIS/6-31G\* and TD-PBE0/def-SV level of theory. The energy of the Franck-Condon structure is indicated respectively as a dot or a square. The calculation are performed by F. Santoro and R. Improta

obtained in gas phase both at CIS/6-31G\* level and at TD-PBE0/def-SV level. CIS method, giving a more balanced description of the charge transfer excitations [255], is expected to be reliable when comparing the relative stability of the two  $C_1$  and  $C_2$  paths. On the other hand, when charge transfer is not present (as in the  $C_2$  path) the  $S_1$  TD-PBE0 energies are clearly more reliable than the CIS ones. On small model cyanine TD-PBE0 has indeed proven to give results in good agreement with accurate CASMP2 method (see [26]).

Figure 4.7 shows that the CIS  $C_1$  and  $C_2$  paths almost coincide up to about 140 degrees where the  $C_1$  path splits from the  $C_2$  one, becomes energetically favored and drives the system toward the  $C_1$  minimum  $S_1\text{Min}C_1$ . The energy along the  $C_2$  path instead increases up to a barrier at  $\varphi = \varphi' \approx 115^\circ$ . The barrier with respect to the local minimum  $S_1\text{Min}C_2$  is  $\approx 0.35$  eV and it lays to an energy about equal to the initial energy of the system, i.e. the energy at the Franck-Condon region (reported in the figure as a dot). Beyond the barrier, a new  $C_2$  minimum is computed at  $\varphi = \varphi' = 94^\circ$ . However, it must be kept on mind that, at pseudo-perpendicular molecular arrangements the

CIS (as the TD-DFT) results might be biased by the neglecting of double-excitations.

The CIS  $S_1$  energies are largely overestimated, as seen by the comparison of the computed Franck-Condon energy (4.29 eV) with the experimental absorption maximum (2.93 eV). The agreement is much better for TD-PBE0/dev-SV calculations (3.41 eV). Nevertheless the shape of the CIS and TD-PBE0  $C_2$  path is very similar with a barrier at about  $\varphi = \varphi' \approx 115^\circ$  and a pseudo-perpendicular  $C_2$  minimum ( $S_1\text{Min}C_2^P$ , a frequency analysis confirms that it is a true minimum). The barrier predicted by TD-PBE0 (0.36 eV) is very close to the CIS one even if in this case its energy is slightly higher than the Franck-Condon one (about 0.05 eV). In Section 4.4 it will be shown that the DFT isomerization barriers on  $S_0$  are lowered (by about 0.1 eV) by a proper consideration of dispersive non-bonding interactions, more important at the perpendicular arrangements of the transition states. Since these interactions are at work also in the excited state, it is reasonable to think that also the  $C_2$   $S_1$  barrier is overestimated by a similar amount. Furthermore, the inclusion of bulk solvent effect stabilizes twisted geometries by  $\approx 0.05$  eV over planar ones. On the balance, the computations thus provide an estimated value of the energy barrier of about 0.2 eV.

The  $S_0/S_1$  oscillator strength has a clearly different behavior along the two paths. Along the  $C_1$  path it drops steeply after the  $S_1\text{Min}C_2$  structure because of the charge-transfer character of the electronic transition, while it decreases much more smoothly along the  $C_2$  path. Both at the  $S_1\text{Min}C_2^P$  and  $S_1\text{Min}C_1$  minima the oscillator strength is small but not zero. As intuitive, the  $S_1 - S_0$  energy gap is lower at the  $C_2$  minimum (2.18 eV, CIS value) than at the  $C_1$  one (2.75 eV, CIS value). As already discussed, the CIS  $S_1$  energies are always clearly overestimated. Along the  $C_2$  path at  $\varphi' = 94^\circ$  (corresponding to the CIS minimum) the TD-PBE0  $S_1 - S_0$  gap is  $\approx 1.3$  eV.

### 4.3.3 Assessing the excited-state dynamics from the experimental data

From the data presented in Section 4.3.1, it will be derived in the following that the dynamics on the  $S_1$  excited-state energy surface is governed by two different time regimes. The faster one is governed by a decay with a time constant less than 2 ps, while the slower one is characterized by a time constant of about 9 ps. This behavior can be interpreted in the context of the theoretical results. In the following, the emission signals will be discussed (i), afterwards the absorption signals (ii).

#### i) Emission signals

Measuring the temporal behavior of the fluorescence is a direct way to gain insight into the excited-state dynamics. Information about the fluorescence behavior can be gathered either by fluorescence upconversion or by measuring the stimulated emission in a transient absorption experiment.

##### i.1) Stimulated emission measured at 500 nm

The stimulated emission can be seen very well in Figure 4.2 as a region of reduced

absorption during the very first picoseconds in the wavelength range between 420 nm and 600 nm. This is the same wavelength range where many of the following processes connected to the ground-state dynamics also have their absorption bands. To a certain extent these are the absorption bands of the product isomers, excited-state absorptions, the contributions of ground-state bleach, as well as possible hot ground-state absorptions. Careful analysis has shown that around 500 nm there is only one non-negligible absorption contribution, in addition to stimulated emission. This makes the fit in Figure 4.3A more reliable, because only two contributing signals must be considered. The fit results in a 1.9 ps decay time constant for the emission at 500 nm. Since the steady-state absorption spectrum has no contribution at this wavelength and the pure solvent also shows no signal, only the possibility of stimulated emission remains.

i.2) *Stimulated emission measured at 900 nm*

A contribution of decreased absorption is found with a decay time constant of about 8 ps in the transient absorption at 900 nm (see Figure 4.5D). Again, at 900 nm, neither the steady-state absorption spectrum nor the pure solvent show a signal. Thus, the signal of decreased absorption at 900 nm can be attributed to stimulated emission. As this wavelength corresponds to a small energy gap ( $\approx 1.38$  eV) the emission must occur where the two electronic surfaces are closer together.

i.3) *Fluorescence upconversion measured at 500 nm*

Since stimulated emission is often superimposed by absorption components, the upconversion measurement gives a more direct access to the information [61, 256]. The temporal behavior of the fluorescence measured by fluorescence upconversion of the dye NK88 is shown in Figure 4.3B. The fluorescence signal peaks after a few hundreds of femtoseconds and then decays with 1.8 ps.

The value of 1.8 ps from the fluorescence upconversion is in very good agreement with the indirect measurements by A.C. Craig and coworkers in the mid-seventies, who predicted a decay time of 1.7 ps by evaluating fluorescence spectra [220]. Also, the time constant of 1.8 ps matches very well the decay time constant of 1.9 ps found by the stimulated emission.

ii) *Absorption signals*

The fluorescence can, but does not necessarily need to be a good observable for understanding the excited-state dynamics completely, because it is known that many molecules have dark states which do not fluoresce [44, 238]. The problem is particularly serious in molecules undergoing chemical reactions which imply large amplitude motions, since it is likely that the system does not fluoresce all along the reaction pathway. Therefore, also other signals in addition to the fluorescence will be investigated in order to investigate the motion on  $S_1$  more adequately, e.g. excited-state absorption, because it can have another Frank-Condon window than fluorescence [61, 63, 256]. Dark states that do not fluoresce may thus be observed, because they do not emit but can absorb [44, 238]. Of course also the excited-state absorption does not necessarily probe all dynamics on the first excited surface, but it can furnish useful information in

addition to fluorescence measurements.

In the case of NK88 dissolved in methanol, there are two bands which are correlated with excited-state absorption. Several absorption contributions exist on the red side of the steady-state absorption window (600 nm to 950 nm). They have very different decay times, which allow an easy distinction between them.

ii.1) *Excited-state absorption measured at 700 nm*

A representative transient for the absorption between 600 nm and 950 nm is shown in Figure 4.4C for a probe wavelength of 700 nm. There are two decay times, 1.4 ps and a contribution with a very long decay time constant which could not be determined. Several explanations are possible for the contribution with the very long decay time constant at 700 nm:

First, the signal could originate from solvated electrons. To test this hypothesis, additional experiments with KI dissolved in methanol are performed (see Figure 4.4A and B). Dissolved KI exists as  $I^-$  and  $K^+$ . Irradiated by 400 nm light  $I^-$  can absorb two photons and produce a solvated electron which shows an absorption in the near-infrared [71, 257]. The iodine anion is a common species of both NK88 and KI. In solution, NK88 exists as cationic salt and  $I^-$ , so that a possible explanation for the observed offset for pump pulse energies higher than 250 nJ in the measurement of NK88 dissolved in methanol could be the production of solvated electrons from the  $I^-$  also present in the solution.

Second, the offset could also be due to a fragmentation process. The steady-state absorption spectrum of NK88 is measured immediately after extensive exposure to pump light, but no absorption around 700 nm or any other change compared with the fresh sample was observed. In case photodissociation occurs, the photofragments have to react back to the initial molecule in a few seconds.

Third, the absorption could be due to triplet states. When an effective intersystem crossing exists, the population transfer to triplet states can occur very fast, even on a sub-picosecond time scale as observed in metal ligands [19, 258–260]. However, it cannot be determined which of all the conceivable scenarios is the origin of the observed absorption.

The fast contribution (1.4 ps) observed in the 700 nm transient of NK88 in methanol is neither seen in the pure solvent transient nor in the KI transient, so it must originate from NK88. As the 1.4 ps time constant is close to the one measured by fluorescence upconversion (1.8 ps) and by stimulated emission (1.9 ps) it is reasonable to assign the signal with a decay time constant of 1.4 ps to excited-state absorption. The fact that it has a slightly shorter decay constant could be due to a situation in which the Frank-Condon overlaps for  $S_1 \rightarrow S_n$  and for  $S_1 \rightarrow S_0$  transitions behave differently.

ii.2) *Excited-state absorption measured at 360 nm*

In the work of P. Plaza and coworkers [75], it is concluded that the band of absorption, starting below 360 nm and going up to 440 nm, originates from excited-state



absorption. Figure 4.5A-C shows a transient at 360 nm that is mainly dominated by this absorption. In Figure 4.5C the same transient is plotted with a logarithmic ordinate. The data and the fit show that the signal is not purely monoexponential, i.e. there are possible contributions from other processes. Taking the steady-state absorption spectrum shown in Figure 4.1C into account, it is found that at 360 nm there is still a non-negligible amount of absorption by the *trans* form, resulting in a ground-state bleach contribution in the time-resolved measurements. The transient absorption measurement (Figure 4.5A-C) for the first 2 ps shows a rapid decay followed by a slower decrease of the signal. This time dependence cannot be explained by the superposition of a monoexponential absorption signal ( $\Delta A > 0$ ) and the bleach contribution ( $\Delta A < 0$ ) only. As can be seen from the analysis of the data (Figure 4.5A-C) the initial temporal behavior of the bleach contribution has a very different time scale, so that two absorption contributions with decay time constants of 1.2 ps and 9 ps, respectively, must be taken into account.

The origins of these two time constants (1.2 ps and 9 ps) can be interpreted as follows in the context of the previously discussed measurements. Since it is already known that the initial excited-state dynamics takes place on a 1.8 ps time scale or faster, it is a reasonable assumption that this behavior is also reflected in the excited-state absorption band which starts in the ultraviolet and goes up to 440 nm. From the calculations and measurements at 900 nm it is already known that there is another motion on  $S_1$  on a longer time scale (8 ps). It is likely that the dynamics observable at 900 nm can also be probed by the absorption signal at 360 nm, because it might be irrelevant which specific arrangement is adopted by the molecule due to the high density of excited states accessible with 360 nm. Summing up, two  $S_1$  dynamics (< 2 ps and  $\approx$  9 ps) can be inferred from the combined analysis of the measurements at 500 nm and 900 nm. These explain why two absorption components in addition to the ground-state bleach contribution are introduced in the fit for the 360 nm transient. The fit itself reproduces all features of the transient and the resulting time scales agree well with the assigned molecular states.

#### ii.3) Absorption measured at 500 nm

A third method in order to obtain information about the excited-state dynamics comprises the measurement of the appearance time of the ground-state species. Unfortunately, the early-time dynamics of the corresponding spectroscopic signals are hard to determine since, besides product ground-state absorption, also stimulated emission and excited-state absorptions obscure the transient signal in the respective spectral regions around 460 nm. This makes it very difficult to determine the rise time of one of these many contributions accurately. In contrast to these signals the absorption at 500 nm is only superimposed by stimulated emission (see Figure 4.3A).

As already pointed out before, the analysis of the transient at 500 nm gives only one absorption contribution. The time constant of 11 ps is similar to the slow component of 9 ps, found in the fit for the excited-state absorption around 360 nm. Concerning the rise time of the absorption contribution in the 500 nm transient, a fit which involves

two predecessor states for the absorption results in identical time scales of 2.2 ps for the dynamics of these two states, the same as when only one rise time is included in the model. A fit with a fixed rise time larger than 3 ps and a free decay time does not converge to the data points at all.

To prove the different nature of the absorption signals at 500 nm and 360 nm, additional experiments are performed with NK88 dissolved in ethylene glycol. As can be seen in Figure 4.6, while the stimulated emission at 500 nm is elongated from 1.9 ps to 23 ps, the absorption signal at 500 nm (as well as the emission at 900 nm, data not shown) is not present anymore. In contrast, the slower component of the excited-state absorption probed at 360 nm still exhibits a strong signal with a time constant of 56 ps. Due to the higher viscosity of the solvent the time scales are elongated in the case of ethylene glycol, but the time constants of the initial dynamics are elongated differently. A possible scenario for the absence of the absorption signal at 500 nm and the emission signal at 900 nm in the case of ethylene glycol is based on less molecular torsion due to the higher viscosity of the solvent, so that the  $S_1 - S_0$  transition occurs at configurations that are less twisted and therefore do not allow an observation of the signals [238]. However, in this scheme the formation of photoproducts should be intuitively suppressed in ethylene glycol as well, which is not the case according to the data, presented here. Further discussion of this topic is given at the end of the next subsection in the context of the theoretical results.

In summary, the experimental results indicate the existence of two time regimes in the dynamics on the excited state  $S_1$ . The faster one is seen in signals which show a rise time of few hundreds of femtoseconds (or too short to measure) and a decay time within 2 ps, namely the fluorescence upconversion at 500 nm (1.8 ps decay time), the stimulated emission at 500 nm (1.9 ps decay time), and the faster component of the excited-state absorption in the 700-900 nm region (1.4 ps decay time) and at 360 nm (1.2 ps decay time). The slower dynamics is detected by signals with a rise time of  $\approx 2-3$  ps and a decay time of  $\approx 9$  ps, namely the stimulated emission at 900 nm (rise time 3 ps, decay time 8 ps), the slower component of the excited-state absorption at 360 nm (rise time 1.8 ps, decay time 9 ps) and the very small component in the fluorescence upconversion (decay time 9 ps). The deviations among the time constants quoted for each of the two time regimes might originate from the fact that they were determined with different probe wavelengths (thus probing different regions on the  $S_1$ ) and different types of signal (excited-state absorptions, stimulated emission, and fluorescence upconversion), for whom the FC windows might behave differently. A further absorption signal at 500 nm shares approximately the same time scale of the slow  $S_1$  dynamics (rise time 2.2 ps and decay time 11 ps) but cannot be unambiguously assigned and will be discussed in detail below.

### 4.3.4 Interpreting the excited state dynamics

In this section, by performing a synoptical comparison of the available experimental and computational results, it is discussed what picture of the photoisomerization of NK88 can give better account of the observed excited-state two-time dynamics.

First, TD-PBE0 computations show that *the two-time dynamics originate entirely on the  $S_1$  surface*, ruling out a possible alternative explanation, i.e. that a second excited state is involved in the dynamics, as it has been suggested in other systems, for example in the retinal photoisomerization [69]. Indeed, in the FC region  $S_2$  is almost dark and is remarkably less stable than  $S_1$  (at least 0.75 eV), and it does not come closer to  $S_1$  along the possible photoisomerization pathways.

Once this point has been assessed, two different explanations are possible for the two different observed time-regimes :

(a) They are due to the existence of two different reactive pathways (namely the symmetric  $C_2$  and the asymmetric  $C_1$  one).

(b) They simply arise from different structures along the same pathway (the energetically favored  $C_1$  one).

In the *hypothesis (a)*, after the system has passed the  $S_1$ -Min $C_2$  structure, beyond following the  $C_1$  pathway it can also follow the  $C_2$  pathway and get to the local  $S_1$ -Min $C_2^P$  minimum after crossing the  $C_2$  barrier. Several experimental results find a consistent explanation within this description.

Right after the excitation, the system evolves along the minimum energy pathway toward  $S_1$ -Min $C_2$  (at this stage  $C_2$  and  $C_1$  pathways coincide). It is also possible that a part of it already starts to remove the  $C_2$  symmetry (see Reference [26]), but this pathway, though barrierless, should have a scarce driving force. The FC region and the fluorescent region of the  $S_1$ -Min $C_2$  structure are abandoned in about 1-2 ps, and this motion is recorded by the fast decaying signals. After this stage (it is assumed that the dephasing is complete and adopt a statistical perspective), a fraction of the molecules of the sample goes quickly to  $S_1$ -Min $C_1$  following the  $C_1$  pathway (the faster dynamics); then it reaches the  $S_1 - S_0$  CI and goes to  $S_0$  in about 2-3 ps. The remaining fraction of the molecules overcomes the  $C_2$  barrier and is trapped around the pseudo-perpendicular  $C_2$  local minimum  $S_1$ -Min $C_2^P$  from where it reaches  $S_0$  at longer times (on the time scale of 10 ps). The faster pathway to  $S_0$  is responsible for the 500 nm hot ground-state absorption which decays with 11 ps, because of the molecular cooling. It is also responsible for the fastest repopulation time of the *trans* isomer (see Subsection 4.4) which in fact exhibits a time constant of  $\approx 10$  ps. On the contrary, the fraction of the molecules of the sample traveling on the  $C_2$  pathway is responsible for the slowly decaying stimulated emission at 900 nm which rises with 3 ps (the time for reaching the  $S_1$ -Min $C_2^P$  minimum) and decays with 9 ps (the time for reaching the  $S_1 - S_0$  conical intersection). In fact, along the  $C_2$  pathway the  $S_1 \rightarrow S_0$  transition preserves a non-vanishing oscillator strength also close to the minimum  $C_2$ . For example at TD-

PBE0 level it is still 0.08 at  $\varphi'=100^\circ$  with a  $S_1 - S_0$  gap of about 1.6 eV, compatible with the 900 nm emission ( $\approx 1.4$  eV).

When the molecule is embedded in ethylene glycol, the energy dissipation is more effective, and this disfavors the more energetic  $C_2$  pathway which becomes not observable anymore. The system follows only the  $C_1$  pathway and as a consequence the 900 nm stimulated emission disappears. In this case it is plausible that also the 500 nm hot ground-state absorption disappears since in this case the system reaches the  $S_0$  surface only at strongly asymmetric structures close to the  $C_1$  CI (see Reference [26] for details). The solvent viscosity could hence prevent the molecule to recover a  $C_2$  arrangement (and hence a non-null  $S_0 - S_1$  oscillator strength) while it is still vibrationally hot (as required for an absorption at 500 nm). In fact to go back to a  $C_2$  arrangement the molecule needs to twist simultaneously both the side-rings and this can be difficult in a viscous solvent.

The two-pathways scenario also furnishes a possible explanation to the formation of the isomer *d-cis* discussed in Subsection 4.4. In fact, the fraction of the molecules oscillating around  $S_1$ -Min $C_2^P$ , could eventually decay on  $S_0$  at a  $C_2$  CI different from the minimum-energy  $C_1$  one computed in Reference [26], in a region from which the *d-cis* well is directly accessible since both  $\varphi$  and  $\varphi'$  are rotated to  $\approx 90^\circ$ . It is worthy to notice that such a pseudo-perpendicular  $C_2$  CI has been indeed documented by accurate CAS calculations in a small-model cyanine where it lies 22.3 kcal/mol below the FC energy [29].

Finally, please note that this is the only possible scenario if the 11 ps absorption at 500 nm is assigned as a hot ground-state absorption. Hot ground-state absorption is indeed often located in the same wavelength region as stimulated emission from the  $S_1$  surface [43, 261] and often also has major contributions at wavelengths where no steady-state absorption can be found [44]. This would imply that a fraction of the molecules of the sample is on  $S_0$  within 2-3 ps, and, since some signals from  $S_1$  survive for about 10 ps, consequently the existence of the two  $S_1$  competing pathways is accepted.

The critical feature for assessing the consistency between the above described scenario and the experimental results is the height of the energy barrier on the  $C_2$  pathway. If the value computed at TD-PBE0/6-31G(d) level in the gas phase ( $\approx 0.35$  eV) would be accurate, the  $C_2$  pathway would be clearly much slower than the  $C_1$  one. Therefore, the fraction of the molecules moving on it, if any exists, should be trapped around  $S_1$ -Min $C_2$  for a much longer time, hence resulting in a clear biexponential fluorescence at 500 nm (with the longtime decay much longer than 1.8 ps). This feature is not seen in experiments, apart from a negligible component. Nevertheless, as discussed in the result section the barrier is probably overestimated by the calculations, and the  $S_1$ -Min $C_2^P$  minimum is therefore more easily accessible. Moreover, the laser pump at 400 nm furnishes to the system about 0.15-0.2 eV above the energy of the FC structure (roughly identified with the absorption maximum at 423 nm), further facilitating the

access to the  $S_1$ -Min $C_2^P$  region.

An alternative scenario for the  $S_1$  dynamics follows instead the *hypothesis (b)*. The system follows only one pathway, preserving the  $C_2$  symmetry up to the small barrier after the  $S_1$ -Min $C_2$  structure and then turning to  $C_1$  structures. According to this picture, all the signals recorded are excited-state signals; the faster ones originate from structures at which the  $C_2$  and  $C_1$  pathways collapse onto each other, and the slower ones by structures lying on the  $C_1$  pathway when it has split from the  $C_2$  one (after passing through  $S_1$ -Min $C_2$ ). This picture well fits with the fact that the decay of the faster signals and the rise of the slower ones are roughly simultaneous, and naturally explain the mono-exponential decay of the fluorescence at 500 nm. In this scenario the 500 nm transient absorption arises from an  $S_1 \rightarrow S_n'$  excited-state absorption. This is in line with the fact that the determined time constant of 11 ps roughly matches with the 9 ps of the excited-state absorption at 360 nm. The results of a CAS surface hopping study on a small model cyanine [221] (where the  $\pi$ -delocalized rings are substituted by  $\text{CH}_2$ -methine groups and as a consequence the dynamics is much faster than for NK88) [26], seem to support this hypothesis, identifying the faster dynamics with the motion out of the FC region (along the reactive twisting) and the slower dynamics with the motion toward the conical intersection.

Three findings do not straightforwardly fit into this picture. First, it is not very likely that, when embedded in ethylene glycol, the reaction pathway is modified so to destroy the possibility of the  $S_1 \rightarrow S_n'$  500 nm absorption but not the  $S_1 \rightarrow S_n$  absorption at 360 nm. On the other hand, the disappearance of the 500 nm absorption can not be explained by a possible large solvent shift, which is very unlikely since the ground-state absorption spectra of NK88 in ethylene glycol and in methanol are very similar (shifted by only 3 nm, see Figure 4.1C), and in fact also the other signals (see for example the 360 nm one) do not show marks of such a shift.

Furthermore, this scenario predicts indeed that the passage on  $S_0$  takes place with the slower dynamics ( $\approx 10$  ps) but this is the same time scale of the fastest repopulation time of the ground-state *trans* isomer. This requires an almost instantaneous cooling on the  $S_0$  ground surface which, though it cannot be excluded, is not very likely. As an example the fast cooling of p-nitroaniline in water, due to effective H-bond solute-solvent interactions, takes place in about 1 ps, and this time increases up to 6 ps for dimethylamino-p-nitroaniline in acetonitrile where no H-bond plays a role. NK88 in methanol is expected to be not very different from the latter situation for the weakness of the possible H-bonds [26]. Finally in this picture the 900 nm emission should come from the  $C_1$  structures close the minimum  $S_1$ -Min $C_1$ . Apart from the fact that at this point the  $S_1 - S_0$  gap is estimated to be too large to be compatible with the experimental wavelength (around 2.0-2.2 eV, see [26]) it would remain to be explained why the emission is quenched in ethylene glycol. In fact, as discussed in the previous subsection, the possible explanation that the  $S_1$ -Min $C_1$  structure is not reached in the viscous solvent and that the  $S_1 \rightarrow S_0$  transition takes place at geometries closer to planarity, conflicts with the fact that this would imply a suppression of the product

isomers, which is not observed.

In conclusion, the photoisomerization of the short-chained cyanine dye 3,3'-diethyl-2,2'-thiacyanine dissolved in methanol and ethylene glycol has been investigated. Excited onto the  $S_1$  surface, this molecule passes a conical intersection and isomerizes either to the *cis* and *d-cis* photoisomers, or relaxes back to the *trans* form (see Section 4.4). To observe this complex excited state dynamics absorption spectroscopy has been used covering a spectral range from 360 nm up to 950 nm in two different solvents as well as fluorescence upconversion. The interpretation of the results has been supported by a theoretical investigation by F. Santoro and R. Improta on the possible excited state reaction paths, performed at CIS/6-31G\* and TD-PBE0/def-SV computational level.

The observation evidences a two-time dynamics on the  $S_1$  surface, while the computations suggest the existence of a main reaction path  $C_1$ , in which the symmetry of the molecule is broken quickly, already at moderately twisted geometries  $\phi' \approx 140^\circ$ , and a possibly competitive second path  $C_2$  in which on the contrary the symmetry is preserved up to pseudo-perpendicular configurations. The experimental results better fit with a scenario where both the paths are pursued: the  $C_1$  path leads to the faster decay to  $S_0$  ( $<2$  ps), while the  $C_2$  path, being less favored energetically, is responsible for the slower decay ( $\approx 9$  ps). It is also plausible that the two paths connect to the  $S_0$  via two different conical intersections [262] as it happens for a small model cyanine [29], which would give a natural explanation to the formation of the *d-cis* isomer predicted in the most likely model presented in the next section. The actual feasibility of the  $C_2$  path depends on the true height of the barrier, which can be hardly computed accurately for such a large molecule in solution.

Alternative explanations could give account of the observed excited state dynamics: (i) the path on the  $S_1$  surface is unique (the  $C_1$  one) and the signals decaying with different times come out from different structures along this single path (ii) part of the wave packet undergoes asymmetrization already in the Franck-Condon region and does not pass through  $S_1\text{Min}C_2$ , and this is the origin of the splitting of the reaction path. However, although the above pictures cannot be completely ruled out either experimentally or theoretically, as discussed in the above sections several findings make them less likely.

## 4.4 Ground state dynamics after photoexcitation

Several time-resolved studies investigating the ground state dynamics of cyanine dyes have been performed in the last decade [59–62, 64, 137, 144, 237, 263, 264]), indicating that certain structural features lead to distinct differences in the photoisomerization characteristics.

It has been shown that certain cyanines exist in more than two geometric conformers in the ground state [75, 207, 265]. Recent theoretical studies on thiacyanines [26]

suggest this possibility to be also true for the symmetric molecule NK88.

Under room temperature conditions, only the most stable isomer is present in solution. This can be confirmed by the absence of known product isomer ground state absorption in the steady state spectrum of NK88 in methanol [75]. X-ray analysis of the crystal structure of NK88 [266] and NMR experiments on similar thiacyanines [267, 268] as well as theoretical calculations have revealed that this is the *trans* conformer (see Section 4.4.2). Both experiment [266] and theory [26] have shown that the geometrical structure of the *trans* isomer is close to planarity.

The ground state dynamics of the molecule NK88 can be best investigated by the transient absorption spectroscopy data in the range from 350 nm to 630 nm. Together with theoretical simulations a conclusive picture of the overall kinetics of the molecule NK88 can be drawn.

#### 4.4.1 Results of the experiments

The overall dynamical behavior of the molecule for the first thirty picoseconds after 400 nm excitation is displayed in Figure 4.2. In the wavelengths region from 360 nm to 500 nm, one can easily determine two main regions, decreased absorption ranging approximately from 390 to 430 nm and increased absorption around 460 nm. Additionally, during the first few picoseconds, there is a spike of decreased absorption starting at about 420 nm going up to 600 nm as well as a contribution of increased absorption from 360 nm up to 440 nm, both having different time constants (since these features decay rapidly, they can be better identified in the associated transients). The latter has been assigned to excited state absorption by Plaza and coworkers [75]. The overall short time behavior reveals that the molecular dynamics during the first few picoseconds are manifold since a big variety of different molecular contributions superpose to the resulting signal (see Section 4.3).

As can be seen from Figure 4.2 as well as by the nature of the process itself, we there are two different time regions on which the reaction takes place: the initial twisting process during the very first few picoseconds on the one hand and the thermalization process on a time scale of several 100 ps on the other hand. This section focuses on the ground state dynamics following photoexcitation and passage through a conical intersection, the short time behavior on the  $S_1$  potential energy surface is discussed in the previous section. The long time behavior of the reaction is investigated by analyzing transients covering, in the case of methanol, a time delay of two times the longest time constant of the contributing processes. Therefore, transients spanning 1200 ps are presented in Figure 4.8A and C.

During the first few picoseconds of the transient at 460 nm excited state dynamics dominate, followed by a biexponential decay of the absorption with  $\tau_1 = 45$  ps and  $\tau_2 = 600$  ps. The individual contributions are shown as well in the same plot to visualize the amplitude of the different parts. The repopulation in the absorption of the 400 nm transient can be fitted satisfactorily by both a biexponential or a triexponential

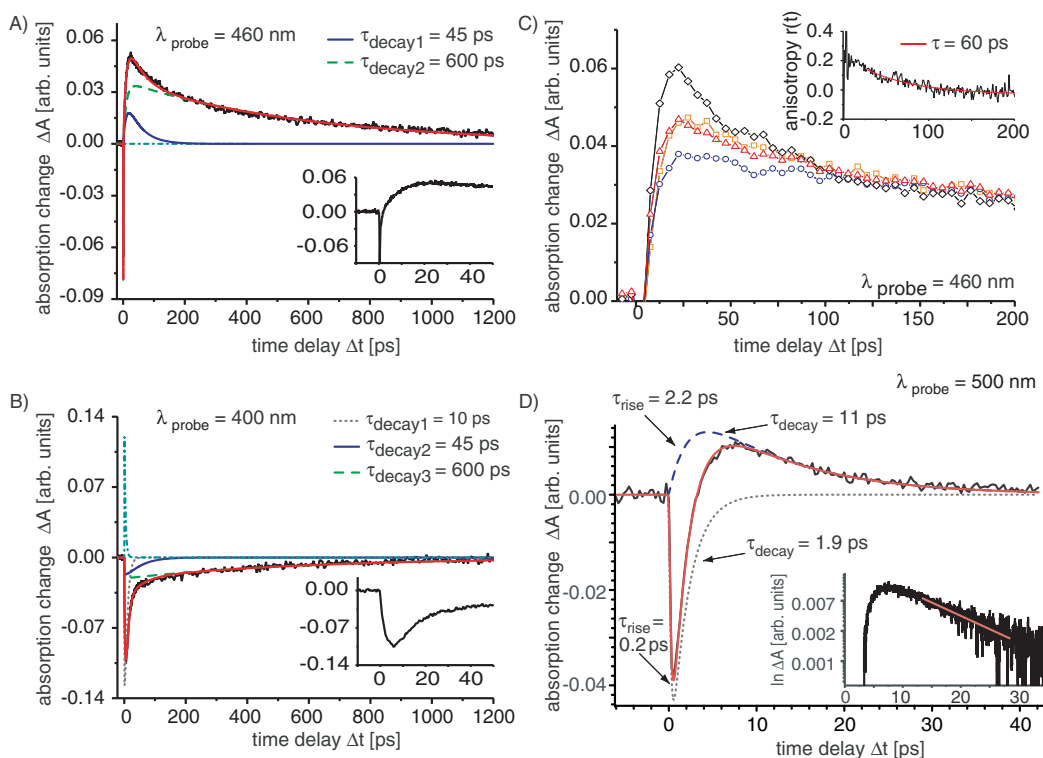


Figure 4.8: Transients at probe wavelengths of A) 460 nm and C) 400 nm. Black shows the experimental data points, while red (gray) marks the fitted curves. The individual contributions are also shown as well to visualize amplitudes of each contribution. The inset shows the behavior of the transients during the first 50 ps. B) Transients for the pump polarization and the probe polarization set to different angles at the probe wavelength of 460 nm. The black (diamond) line shows the experimental data for the pump polarization parallel to the probe polarization, the blue (circle) the data for the perpendicular case, orange (square) for the case of measured and red (triangle) for the case of calculated magic angle data. The inset shows the behavior of the 460 nm anisotropy  $r(t)$ . The red line represents a monoexponential fit for later delay times. D) Transient at a probe wavelength of 500 nm. Black shows the experimental data points, while red marks the fitted curves. The inset shows the data on a logarithmic scale for easier verification of a monoexponential long time decay.

curve. The triexponential fit yields time constants of 600 ps, 45 ps and 10 ps. The first time constant reappears in the transient at 460 nm. Again, the individual contributions are also displayed in the plot. Unfortunately, the signal-to-noise ratio is not sufficiently high to clearly favor either the biexponential or triexponential fit model. In the case of the biexponential fit, the longest time constant becomes shorter and the shortest slightly longer to compensate for the missing contribution. As will be seen in the discussion section, because the longer time constant drops to the value of 470 ps, this fit model is not so likely in relation to the time scales found for other processes.



Because the 45 ps contribution at a probe wavelength of 460 nm is a quite interesting feature, for additional information and to reconfirm the measurements, transients at this wavelength for the pump pulse polarization parallel and perpendicular to the probe pulse polarization are recorded. With this additional information, the anisotropy  $r(t)$  of the system can be calculated (see Equation 1.4) with the help of the signals  $I_{\parallel}(t)$  which is the intensity of the signal in which the pump pulse polarization is parallel to the probe pulse polarization and  $I_{\perp}(t)$  in which the two polarizations are perpendicular. The anisotropy  $r(t)$  reflects the change of the orientation of the transition moment, responsible for the respective transients, while the magic-angle transients records the change in the population.

The magic angle data itself can be reconstructed from the signals  $I_{\perp}(t)$  and  $I_{\parallel}(t)$  (see Equation 1.11). The different signals  $I_{\parallel}(t)$ ,  $I_{\perp}(t)$ , the calculated magic angle signal  $I_{MA}(t)$  and the directly measured  $I_{MA}(t)$  (with the magic angle between the polarization directions of the pump and the probe beam) are shown in Figure 4.8B. Clearly it can be seen that the calculated magic angle data agrees well with the directly measured transient. The transient in which the probe pulse and the pump pulse polarizations are parallel to each other can only be fitted by a clear biexponential decay, the same holds for the magic-angle data. However, the amplitude for the faster contributions in the latter case is smaller than for the parallel polarization measurement. Last, the transient for the case in which the pump-pulse polarization is perpendicular to the probe-pulse polarization is basically monoexponential. The anisotropy  $r(t)$  data for these measurements is displayed in the inset in Figure 4.8B. As explained in Section 1.4, the total anisotropy  $r(t)$  for many different contributions in a transient absorption experiment is the superposition of the anisotropy of each contribution weighted with the normalized intensity.

The fit of the total anisotropy  $r(t)$  at the probe wavelength of 460 nm for delay times after the first few picoseconds results in a monoexponential behavior with a decay time of 60 ps. Due to the magnitude of the decay time, the responsible process can most likely be attributed to the effect of rotational diffusion [20, 21]. Omitting the complicated short time behaviour, the anisotropy for later delay times is only affected by the two absorptive contributions as seen from the fits of the magic angle data. In principle they can have individual anisotropies, but for the case of rotational diffusion the anisotropy values are expected to be similar for the different contributions. This will then explain the monoexponential behavior of the fit to the anisotropy data.

The above mentioned decay time of roughly 10 ps in the transient at 400 nm also reappears in the spectrum observed at 500 nm (Figure 4.8D). The spike at the beginning which is due to stimulated emission from the  $S_1$  surface vanishes in less than 2 ps, while the final decay in the absorption also obeys an exponential decay of 11 ps and is basically monoexponential.

For ethylene glycol, the transients for the same wavelengths are presented in Figure 4.9. The 400 nm signal shows a fast contribution of 70 ps and a slower one of several ns which cannot be determined accurately by recording transients over 2 ns.

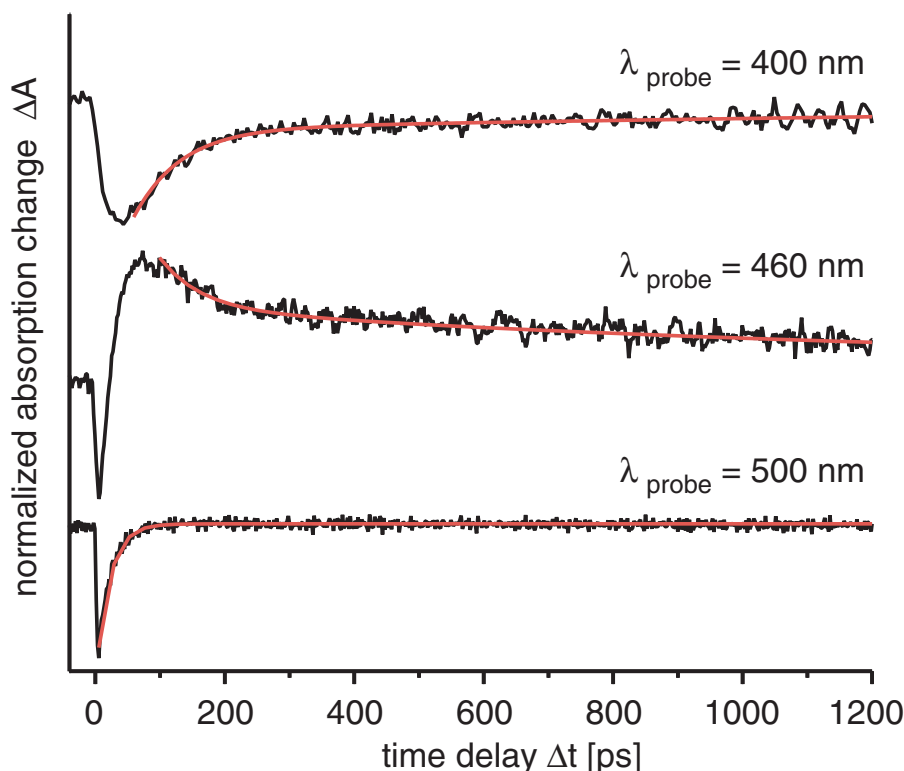


Figure 4.9: Normalized transients of NK88 dissolved in ethylene glycol. The probe wavelengths are at  $\lambda_{probe}=400$  nm, 460 nm, and 500 nm (from top to bottom). Black shows the experimental data points, while red marks the fitted curves.

In the case of 460 nm, the signal of reduced absorption is about 10 times longer than in methanol, before one can observe an increased absorption at longer delay times that decays biexponentially with  $\tau_1 = 60$  ps and a second decay time in the nanosecond regime. The transient recorded at a wavelength of 500 nm exhibits only a single feature, namely a peak of reduced absorption that decays with 23 ps.

#### 4.4.2 Results of the computations

The calculations in this section are carried out by F. Santoro and R. Improtà. PBE0/6-31G(d) optimizations, show that the NK88 cation can exist in three different isomeric forms on the ground  $S_0$  surface, depending on the arrangement at the  $N_3 - C_2 - C_0 - C'_2$  ( $\varphi$ ) and  $N'_3 - C'_2 - C_0 - C_2$  ( $\varphi'$ ) dihedral angles. The three structures are sketched in Figure 4.10. The structure named *trans* has actually a *trans* arrangement at both  $\varphi$  and  $\varphi'$  and shows a  $C_2$  symmetry, while in the  $C_1$  *cis*-isomer  $\varphi'$  is rotated so to assume a *cis* configuration. Finally, *d-cis* (*double-cis*) has a  $C_2$  symme-

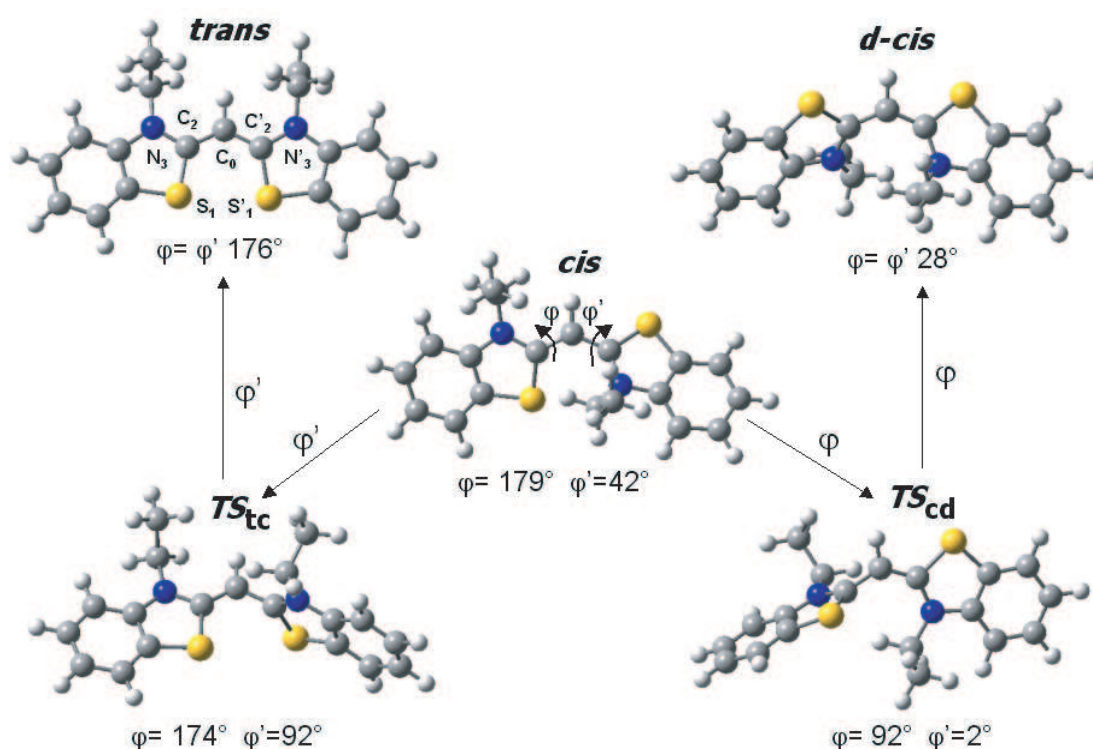


Figure 4.10: Structures of the three isomers (*trans*, *cis* and *d-cis*) and the two transition structures ( $TS_{tc}$  and  $TS_{cd}$ ) of NK88 computed at PBE0/6-31 G(d) level of theory. A frequency analysis confirms that the stable isomers have no imaginary frequency while the transition structures have one imaginary frequency. The relevant atomic labels are indicated on the *trans* structure, while the values of the  $\varphi$  and  $\varphi'$  angles, sketched on the *cis* structure, are reported for all structures. Calculations performed by F. Santoro and R. Improta.

try with a *cis* arrangement at both  $\varphi$  and  $\varphi'$  dihedral angles. Table 4.4.2 reports the energies in vacuum ( $E_{vac}$ ) of the different isomers computed at PBE0 and MP2 level. It also gives the thermal contribution (at room temperature) to the Gibbs free energy in vacuum, computed at PBE0/6-31G(d) level, and the electrostatic solvation free energy  $\Delta G_{sol}^{el}$ , computed by PCM [249, 250] at PBE0/6-31+G(d,p) level. According to both PBE0 and MP2, the *trans* species is the only one significantly populated at room temperature.

Table 4.4.2 includes also the data relative to the transition states (TS) for the *trans*  $\leftrightarrow$  *cis* and *cis*  $\leftrightarrow$  *d-cis* reactions,  $TS_{tc}$  and  $TS_{cd}$  respectively, whose structures are sketched in Figure 4.10. The energies of the transition states with respect to the stable species are generally lower at MP2 level than at PBE0 level. This is mainly due to the dispersive interactions important in the stabilization of the transition structures which are better described at MP2 level [245–248]. An analysis of the interatomic distances of the TS

| <i>trans</i>                         | $TS_{tc}$ | <i>cis</i> | $TS_{cd}$ | <i>d-cis</i> |
|--------------------------------------|-----------|------------|-----------|--------------|
| $E_{vac}$ (PBE0) <sup>(a)</sup>      |           |            |           |              |
| 0                                    | 12.39     | 7.37       | 17.78     | 10.18        |
| $E_{vac}$ (MP2) <sup>(b)</sup>       |           |            |           |              |
| 0                                    | 10.84     | 6.74       | 16.01     | 8.23         |
| $(G_{vac} - E_{vac})$ <sup>(c)</sup> |           |            |           |              |
| 0                                    | -0.73     | -0.90      | -0.67     | -0.16        |
| $\Delta G_{sol}^{el}$ <sup>(d)</sup> |           |            |           |              |
| 0                                    | -0.89     | -0.73      | -1.78     | -0.50        |

Table 4.1: Relative energies and free energies (in kcal/mol) for the *trans*, *cis* and *d-cis* isomers of NK88 and the  $TS_{tc}$  and  $TS_{cd}$  transition structures. Notes: (a) PBE0/6-31+G(d,p)//PBE0/6-31G(d) calculations. (b) MP2/6-311+G(2d,2p)//PBE0/6-31G(d) calculations. (c) thermal correction to Gibbs free energy, computed at T=298.15 K, in harmonic approximation by PBE0/6-31G(d) (it includes the effect of zero point energy). (d) electrostatic solvation free energy computed at PCM/PBE0/6-31+G(d,p) level. Calculated by F. Santoro and R. Improta.

structures suggest that the perpendicular arrangements of the two fused rings allow the formation of van der Waals interactions between the  $\pi$  systems and the sulphur atoms lone pairs (in  $TS_{tc}$ ) and the ethyl-substituent in ( $TS_{cd}$ ), respectively. Also the *d-cis* structure appears to be significantly stabilized by MP2, probably because of the interaction between the  $\pi$  system and the ethyl substituents, and this explains why the energy difference between  $TS_{cd}$  and *d-cis* varies little from PBE0 to MP2.

Table 4.4.2 reports the vertical excitation energy (VEE) in vacuum and in methanol computed at TD-PBE0/6-31+G(d,p) level for the three NK88 isomers. As already shown in Reference [26] the computed VEE for the *trans* and *cis* isomers are close to experimental absorption maxima (with a blue-shift of  $\approx 0.35$  eV) and the VEE difference between the two species matches almost perfectly the experimental result. Finally the VEE of *d-cis* is very close (0.07 eV lower) to the VEE of *cis*.

### 4.4.3 discussion

The transients and the fits presented above contain many prominent aspects of the isomerization dynamics of NK88. After the excitation the system evolves on the first excited surface and decays back to the ground state either by stimulated emission or through a conical intersection. At this conical intersection the hot molecule can either relax back to the original educt structure (*trans* form) or isomerize to two product isomer configurations, the *cis* and the *d-cis* isomer.

As it has been shown above, the calculations predict that the maxima of absorption

| gas phase                 | solution <sup>(a)</sup>   | exp <sup>(c)</sup> |
|---------------------------|---------------------------|--------------------|
| <i>trans</i>              |                           |                    |
| 3.37(1.01) <sup>(b)</sup> | 3.29(1.19) <sup>(b)</sup> | 2.93               |
| <i>cis</i>                |                           |                    |
| 3.18(0.81) <sup>(b)</sup> | 3.11(0.97) <sup>(b)</sup> | 2.73               |
| <i>d-cis</i>              |                           |                    |
| 3.11(0.81)                | 3.04(0.95)                |                    |

Table 4.2: Vertical excitation energy (in eV) for the *trans*, *cis* and *d-cis* isomers of NK88. TD-PBE0/6-31+G(d,p)//PBE0/6-31G(d) calculations. Oscillator strengths are given in parentheses. Notes: (a) PCM calculations. (b) from Reference [26]. (c) from Reference [75]. Calculated by F. Santoro and R. Improta.

of *cis* and *d-cis* ground state isomers are very close in energy, with the latter absorbing at slightly longer wavelengths ( $\approx 0.07$  eV), and have comparable oscillator strengths. As a consequence, since the experimental maximum of the absorption of the *cis* isomer is at  $\approx 454$  nm, the signal at 460 nm (0.03 eV red-shifted) would monitor the sum of the *cis* and *d-cis* populations, if both are accessible, without the possibility to discriminate among them.

The longest time constant in the measurements in methanol is 600 ps which arises at two prominent places. First in the decay of the absorption at 460 nm, and second in the rise at 400 nm. Due to the long duration, this feature has to be ascribed to a product state. The theoretical calculations, as carried out in more detail at the end of this chapter, suggest an assignment to the absorption of the produced *d-cis* isomer which undergoes thermal back relaxation via the *cis* to the *trans* configuration. Consequently, the same time constant reappears in the transient at 400 nm, which is mainly caused by pump-depletion and thus directly reflects the repopulation of the *trans* ground state. The interpretation supports the triexponential fit model for the 400 nm transient, presented in the result section.

The shorter time constant of roughly 45 ps in the triexponential fit of the 400 nm transient is also directly related to the signal observed at 460 nm of the same time constant. According to the calculations (vide infra), these components correspond to the thermal backreaction to the *trans* ground state by molecules that directly turned to the *cis* isomer after passing the conical intersection. As already experimentally seen by other groups who analyzed the similar molecule 1144C [137], the ground state dynamics cannot simply be understood in the standard one-dimensional picture of a double-well potential diagram, but it is necessary to include a more complex potential shape to take the complete isomerization process into account.

Nevertheless, because the rotational diffusion time constant is very similar, one could conjecture that the biexponential decay is caused by badly polarized beams or similar effects. Therefore, additional polarizers are used to care for possible polariza-

tion distortions and additionally calculated the magic angle signal from the individual measurements with the pump pulse polarization set parallel and perpendicular to the probe pulse polarization. As shown in the Section 4.4.1 the transients are also fitted for parallel and perpendicular polarization individually to ensure the correctness of the magic angle measurement and compared the calculated with the directly measured data.

Because the 400 nm transient can also be fitted satisfactorily by a biexponential model and it is not possible to distinguish between the two fit models only by the 400 nm data, it is interesting to additionally discuss its consequences, although it has already been shown that the triexponential model is more likely. In the case that no contribution of about 45 ps exists in the repopulation of the 400 nm signal, it would mean that there is no corresponding state decaying to the *trans* ground state with 45 ps. In this scenario, because such a decay time is visible in the 460 nm transient, the according process would have to first populate the state with the longer decay time of 600 ps, before a relaxation back the *trans* ground state occurs. Thus, the fast time constant of 45 ps would reappear in the temporal behavior of the 400 nm transient as a rise time for the absorption corresponding to the repopulation of the *trans* ground state.

The *trans* repopulation is not only dominated by the 600 ps and 45 ps time constant, but also by a shorter one of 10 ps, which can also be found within the transient at 500 nm in Figure 4.8D (see also Section 4.3). There, the absorption decays with 11 ps and can therefore be ascribed to absorption by a hot ground state temporarily populated by molecules which decay directly from the  $S_1$  potential energy surface to the ground state [43, 261]. A similar temporal behavior can be found in the case of *trans* stilbene, where the cooling process continues on a 10 ps time scale [43].

Hot ground state absorption is often located in the same wavelength region as stimulated emission from the  $S_1$  surface [261]. The stimulated emission can be seen as strong contribution of negative absorption during the first few picoseconds in Figure 4.8D (the fluorescence peaking around 500 nm decays in less than 2 ps, too [220]). As already pointed out in Section 4.3 and as can be seen in Figure 4.2 the 11 ps absorption component and the stimulated emission cover the same wavelength region, which is in agreement with the assumption that the observed absorption is indeed hot ground state absorption.

In order to further verify the assumption that the absorption at 500 nm originates from a hot ground state, additional experiments are performed in the more viscous solvent ethylene glycol. Figure 4.9 shows that the features corresponding to the photoisomerization process behave in a similar way, but on different time scales compared to the case of methanol. Focusing on the 500 nm transient, it can be seen that there is no contribution of absorption, only stimulated emission can be observed with a time constant that is elongated to 23 ps. Possible scenarios which explain this feature are discussed in Section 4.3.

One can now ask whether the assignment of the 45 ps absorption contribution, seen in the 460 nm transient, does not originate from the *cis* isomer. In this case, it would

have to be some hot ground state absorption from the *trans* form. Consequently, there should be no process repopulating the ground state within the observed 10 ps, because vibrational cooling would limit the process to time scales larger than 45 ps. In this scenario, the process visible at 500 nm could not cause the contribution to the *trans* ground state repopulation with 10 ps, because the probe energy corresponding to 460 nm is closer to the ground state minimum than the one corresponding to 500 nm. This would mean that the potential surface region probed at 500 nm would have to be some kind of hotter state than the one responsible for the 460 nm contribution and thus would only account for a 10 ps initial rise of the 460 nm absorption, while there should not be a time constant of 10 ps observed in the transient at 400 nm.

The most reasonable scenario illustrating the repopulation of the *trans* ground state includes vibrational cooling of that fraction of the molecules of the sample which after the  $S_1 \rightarrow S_0$  transition directly accesses the *trans* well of the  $S_0$  surface, while the longer time constants are related to thermal relaxation between the ground state isomers.

It is reasonable to assume that the cooling in the  $S_0$  potential wells of the other species (*cis* and *d-cis*), formed after the  $S_1 \rightarrow S_0$  transition, occurs on a similar time scale of  $\approx 10$  ps. Therefore, in the analysis of the long-time decay of the transients at 460 nm and at 400 nm (time constants  $\tau_1 \approx 45$  ps and  $\tau_2 \approx 600$  ps), any role of the excess vibrational energy due to the electronic transition can be safely neglected and adopt the simple rate equation theory 1.6 to investigate the thermal reactions among the ground state isomers. Figure 4.11 reports the relative Gibbs free energies (bold numbers) of the relevant NK88 species on the  $S_0$  ground state, computed from the values in Table 4.4.2, adding the more reliable the MP2/6-311+G(2d,2p) energy in vacuum with the thermal correction to free energy in vacuum ( $G_{vac} - E_{vac}$ ) and with the solvation free energy  $\Delta G_{sol}^{el}$  term. The activation free energies  $\Delta G^\ddagger$  at room temperature for the four processes *trans*  $\rightarrow$  *cis*, *trans*  $\leftarrow$  *cis*, *cis*  $\rightarrow$  *d-cis*, and *cis*  $\leftarrow$  *d-cis*, are reported as italic numbers. The direct *trans*  $\leftrightarrow$  *d-cis* reactions do not need to be considered as they are too slow, requiring the simultaneous breaking of both the  $C_0 - C_2$  and  $C_0 - C'_2$   $\pi$  bonds.

Figure 4.11 also reports the inverse values of the kinetic constants from the rate equation theory for the four processes ( $k = (k_b T/h) \exp(-\Delta G^\ddagger/k_b T)$ ,  $k_b$ =Boltzmann constant,  $h$ =Planck constant). The inspection of the numbers shows that  $k_{tc}$  and  $k_{cd}$ , the kinetic constants of the *trans*  $\rightarrow$  *cis* and *cis*  $\rightarrow$  *d-cis* processes are much slower than  $k_{ct}$  and  $k_{dc}$ , the constants relative to the *trans*  $\leftarrow$  *cis* and *cis*  $\leftarrow$  *d-cis* reversed processes, and can therefore be neglected. This allows us to adopt the following kinetic scheme:



which has a simple analytic solution. Naming  $N_t$ ,  $N_c$  and  $N_d$  the population of the three species *trans*, *cis* and *d-cis* respectively, and  $N_{0t}$ ,  $N_{0c}$  and  $N_{0d}$  their initial values with

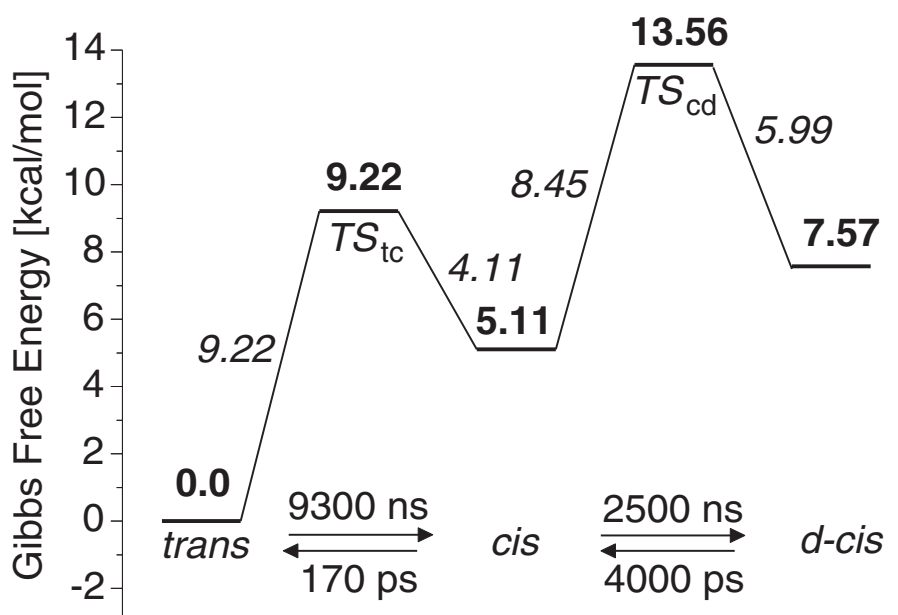


Figure 4.11:  $S_0$  isomers and transition states. Relative free energies (bold numbers) for the relevant species of the NK88  $S_0$  surface and isomerization activation free energies (italic numbers). The inverse of the isomerization kinetic constants, obtained by the Absolute Rate Theory are reported. Notice that  $d$ -cis and  $trans$  can convert to  $cis$  along two equivalent paths (rotating  $\phi$  or  $\phi'$ ); this fact is automatically considered in the  $\Delta G^\ddagger$  values through the symmetry numbers in the rotational partition function. Calculations performed by F. Santoro and R. Improta.

$N_{0c} + N_{0d} = 1$ , and  $N_{0t} = 0$ , one gets

$$N_c(t) = \frac{(N_{0c}k_{ct} - k_{dc})e^{-k_{ct}t} + N_{0d}k_{dc}e^{-k_{dc}t}}{k_{ct} - k_{dc}} \quad (4.2)$$

$$N_d(t) = N_{0d}e^{-k_{dc}t} \quad (4.3)$$

$$N_t(t) = 1 - N_c(t) - N_d(t) \quad (4.4)$$

$$= 1 - \frac{(N_{0c}k_{ct} - k_{dc})e^{-k_{ct}t} + N_{0d}k_{ct}e^{-k_{dc}t}}{k_{ct} - k_{dc}} \quad (4.5)$$

According to the previous equation, if  $N_{0c}$  and  $N_{0d}$  are both different from zero, i.e. if after the  $S_1 \rightarrow S_0$  transition both the  $cis$  and  $d$ -cis species are populated, the model predicts a biexponential decay of the  $N_c + N_d$  populations and a consequent increase of  $N_t$  (with the same time constants). This gives account for the experimental results concerning the signals at 400 nm (monitoring  $N_t$ ), and at 460 nm (monitoring  $N_c + N_d$ ).

The faster and the slower decay of the experimental signals may therefore be assigned to the  $cis \rightarrow trans$  and  $d$ -cis  $\rightarrow cis$  back-reactions, respectively. The calculations underestimate the experimental  $k_{ct}$  and  $k_{dc}$  by a factor  $\approx 3$  and  $\approx 6$ , respectively, which



is a satisfactory agreement. In fact, the kinetic constants are drastically dependent on the precise value of  $\Delta G^\ddagger$  which is the sum of many contributions, each subject to a computational error. Specifically, extracting the experimental  $\Delta G^\ddagger$  values from the 45 ps and 600 ps time constants in methanol one gets 3.5-3.6 kcal/mol and 4.9-5.0 kcal/mol, respectively. Therefore the error of the computed values reported in Figure 4.11 is  $\approx 1$  kcal/mol or less, which is the maximum degree of accuracy expectable at the state of the art for such a large system in condensed phase. Moreover, it must be observed that also dynamic effect of the solvent, not considered in the frame of the rate equation theory, can play a role in determining the rate of a reaction. An example is given by the difference of the results in methanol and in the viscous ethylene glycol.

In summary, the experimental and computational results indicate that both the *cis* and *d-cis* species are populated following the excitation to  $S_1$ , and that the most likely triexponential repopulation of the 400 nm signal and biexponential decay of the 460 nm signal are due to the thermally coupled back-reactions  $d\text{-cis} \rightarrow cis \rightarrow trans$  on the  $S_0$  surface.

Two hypothesis can be done on the formation of *d-cis*: (a) once prepared in the Franck-Condon region of  $S_1$ , all the molecules in the sample make a transition to  $S_0$  at the  $S_1/S_0$  conical intersection characterized in Reference [26], where only the  $\varphi'$  dihedral (see Figure 4.10) is rotated to  $\approx 90^\circ$ ; after that, on the  $S_0$  surface the system not only goes to *trans* and *cis*, rotating  $\varphi'$  respectively back to  $180^\circ$  or forward to  $40^\circ$ , but utilizes the excess vibrational energy to rotate also the  $\varphi$  dihedral and populate the *d-cis* well, too. (b) a fraction of the molecules of the sample rotate both  $\varphi$  and  $\varphi'$  on  $S_1$  to  $\approx 90^\circ$ , and reaches a different  $S_1/S_0$  conical intersection from where it can directly access the  $S_0$  *d-cis* well. The existence and the accessibility of such a conical intersection has been indeed documented for a small model cyanine [29].

A true dynamical study based on really accurate electronic calculations is necessary to discriminate between these two possibilities. TD-PBE0  $C_2$  constrained optimizations on the  $S_1$  surface, reported in the Section 4.3, show the existence of a  $C_2$  barrier separating the Franck-Condon region from a  $C_2$  minimum  $S_1\text{Min}C_2^P$  in which both  $\varphi$  and  $\varphi'$  are  $\approx 90^\circ$ . The barrier is estimated to be at an energy lower than the Franck-Condon energy and therefore it can be in principle crossed, but an accurate knowledge of its height would be necessary to really evaluate the feasibility of the hypothesis (b) and this is hardly obtainable for such a large molecule in a solvent. On the other side, after the  $S_1/S_0$  transition the system has a large excess vibrational energy and therefore the first hypothesis (a) is realistic. The experimental data on the short-time dynamics are better interpreted assuming that the  $S_1\text{Min}C_2^P$  is actually reached by the system.

In conclusion, the ground state dynamics after isomerization of the cyanine dye 3,3'-diethyl-2,2'-thiacyanine has been investigated. The experimental results are in agreement with the theoretical calculations presented here and in Reference [26]. In thermodynamical equilibrium nearly all molecules have *trans* geometry. By irradiation of light with the proper wavelength the molecule can be excited onto the first excited surface. After decaying through a conical intersection, in the most likely model the

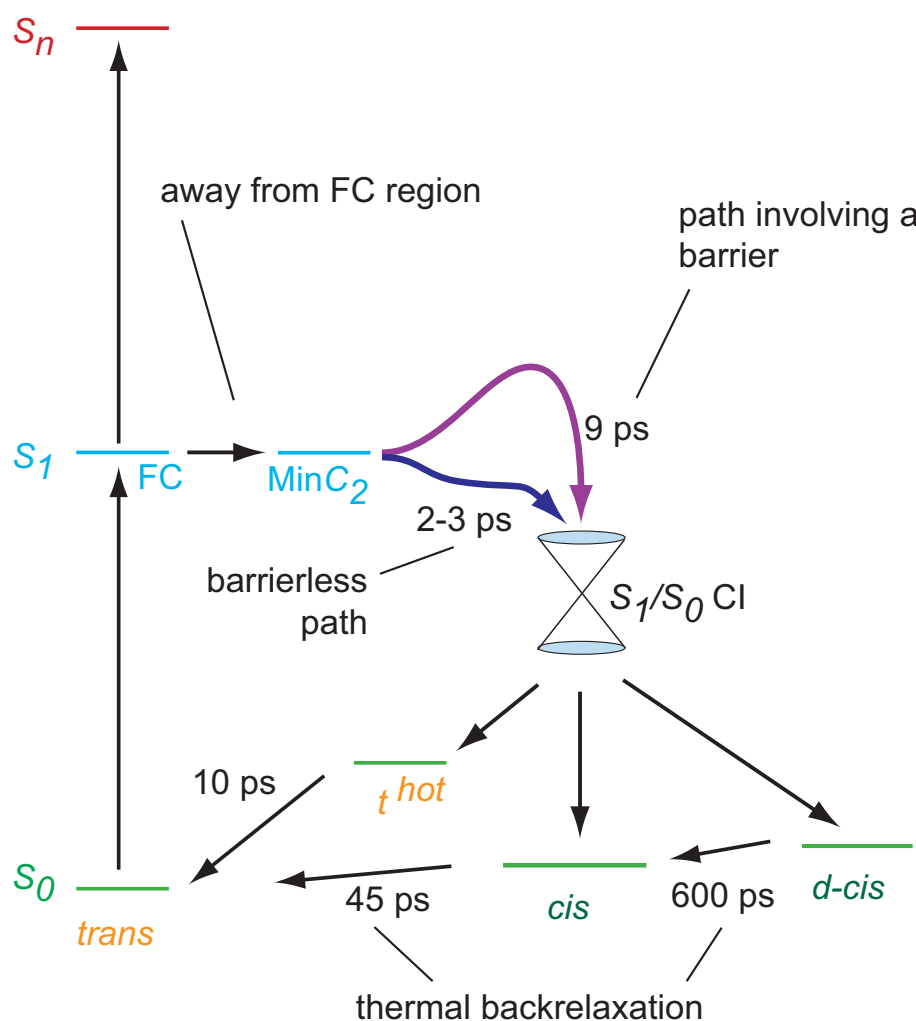


Figure 4.12: Term scheme of the molecule NK88 illustrating the molecular dynamics during isomerization. After excitation onto the first excited potential energy surface, the molecule moves out of the Franck-Condon (FC) region and reaches a conical intersection (CI) via two competitive pathways. From there, it isomerizes either to the *trans*, the *cis* or the *d-cis* form. Since both the *cis* and the *d-cis* have a higher ground state energy, the population relaxes back with 45 ps and 600 ps to the *trans* form. Note that the fast and slow paths from S<sub>1</sub>MinC<sub>2</sub> could drive to two different conical intersections, the first of C<sub>1</sub> symmetry leading to *trans* and *cis* on S<sub>0</sub>, and the second of C<sub>2</sub> symmetry leading to *d-cis*

molecule isomerizes either to the *trans*, the *cis* or the *d-cis* form. Since both the *cis* and *d-cis* have a higher ground state energy the population relaxes back with 45 ps and 600 ps to the *trans* isomer. With the experimental and theoretical results a conclusive scheme of the dynamics after the isomerization process is presented, which is summa-

rized in Figure 4.12.

The elementary steps taking part in the photoisomerization process feature diversity and complexity, highlighting that the rationalization of the large amount of valuable information provided by pump and probe experiments requires a very careful analysis at the molecular level. On this respect, the semiquantitative agreement between the experimental and computational picture is particularly encouraging, and it confirms that the combined use of time-resolved experiments and accurate computational results facilitates a detailed and reliable description of the overall kinetics of medium-size molecules in the condensed phase.

## 4.5 Optimal control of the photoisomerization efficiency

Over the last decade remarkable theoretical and experimental progress was achieved in the field of optimal control of chemical reactions [1, 2, 6, 7, 9]. The method is also applicable in the liquid phase, where interactions with the solvent molecules increase the complexity. None of the liquid-phase control experiments so far [6, 7, 9, 132] have yet tried to control the modification of the molecular structure. As shown in various chapters in this thesis, the *cis-trans* isomerization has attracted much attention because of its importance in chemistry and biology (see especially Sections 3.2, 3.3 and 3.4). Another example of rearrangement of the molecular structure is the conversion between enantiomers. The control of this stereochemical process with shaped laser fields has attracted great theoretical interest in recent years [269–272].

As seen in the previous sections the molecule NK88 is a good candidate for performing optimal control experiments on the issue of controlling the isomerization efficiency. Therefore, in the following different attempts for controlling the isomerization are presented. First simple single-parameter control schemes are tested. These include the variation of the excitation pulse energy and the second order spectral phase. Then the concept of multiparameter adaptive femtosecond pulse shaping is directly applied to the problem of changing the isomerization efficiency.

### 4.5.1 Experimental details

The phase-shaped 800 nm femtosecond laser pulse is frequency-doubled in a 400  $\mu\text{m}$  thick LBO crystal. The resulting laser pulse at 400 nm is therefore shaped in spectral phase and amplitude (see Section 2.5). The maximum pulse energy of the second harmonic at 400 nm is 1.5  $\mu\text{J}$  with a pulse duration of 100 fs for a bandwidth-limited 800 nm fundamental laser pulse. The shaped 400 nm pump pulse is then focused into a 200  $\mu\text{m}$  flow cell where the sample ( $OD = 0.3$ ), dissolved in methanol, is constantly exchanged. A white-light continuum centered around 400 nm is used as probe

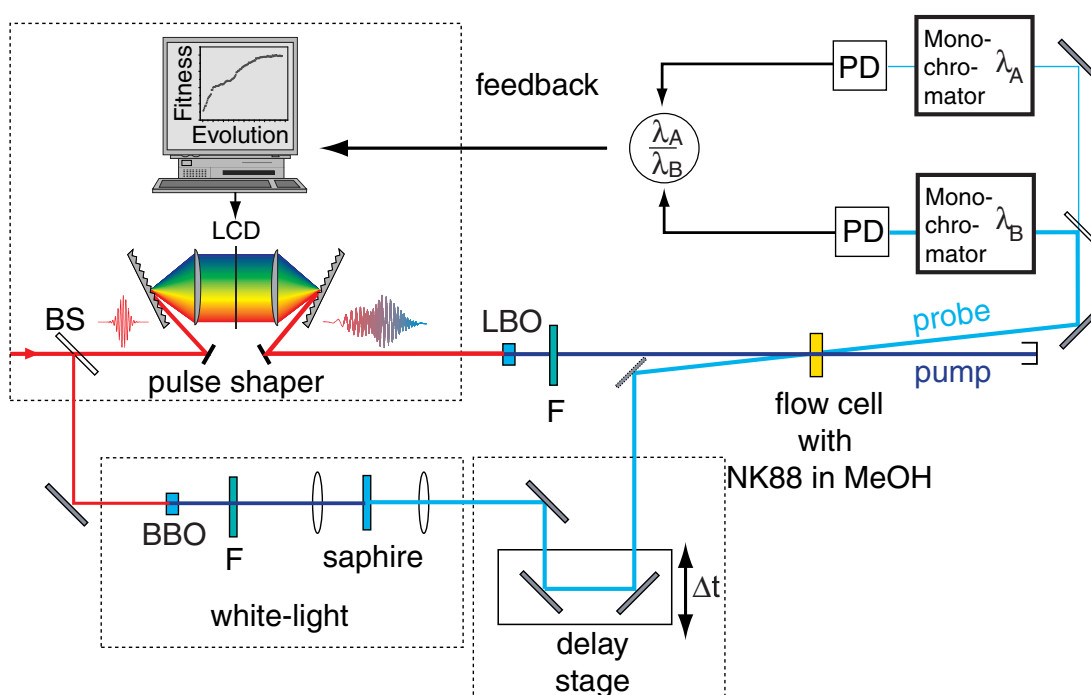


Figure 4.13: Sketch of the setup for controlling the isomerization efficiency. The 800 nm pump-pulse is phase-shaped and then frequency-doubled in a LBO crystal. This results in amplitude- and phase-shaped laser pulses at a central wavelength of 400 nm. As probe pulse a white-light continuum centered around 400 nm is produced by focusing a 400 nm pulse into a sapphire plate. Pump and probe pulses are spatially overlapped in the sample. The probe beam is split into two fractions after the passage through the sample. This allows the simultaneous acquisition of transient absorption signals at two distinct wavelengths. These signals can then be used in an adaptive femtosecond quantum control experiment as feedback-signals.

pulse (for more details see Section 4.1). The white-light laser pulse is delayed via a computer-controlled delay stage and focused into the sample under an angle of about  $10^\circ$  with respect to the pump laser beam. The white-light probe laser beam is split into two light beams after passing through the flow cell and sent to separate monochromators. This allows the simultaneous acquisition of transient absorption signals at two distinct wavelengths. The complete setup is presented as a sketch in Figure 4.13.

#### 4.5.2 Feedback signal and single-parameter control schemes

As seen in Section 4.4, the pump-probe transients recorded at probe wavelengths of 400 nm and 460 nm for large delay are times mainly affected by one of the two isomers, respectively. The pump-probe signal at 400 nm for larger delay times is proportional to the amount of *trans*-molecules that were initially excited, while the curve at 460 nm

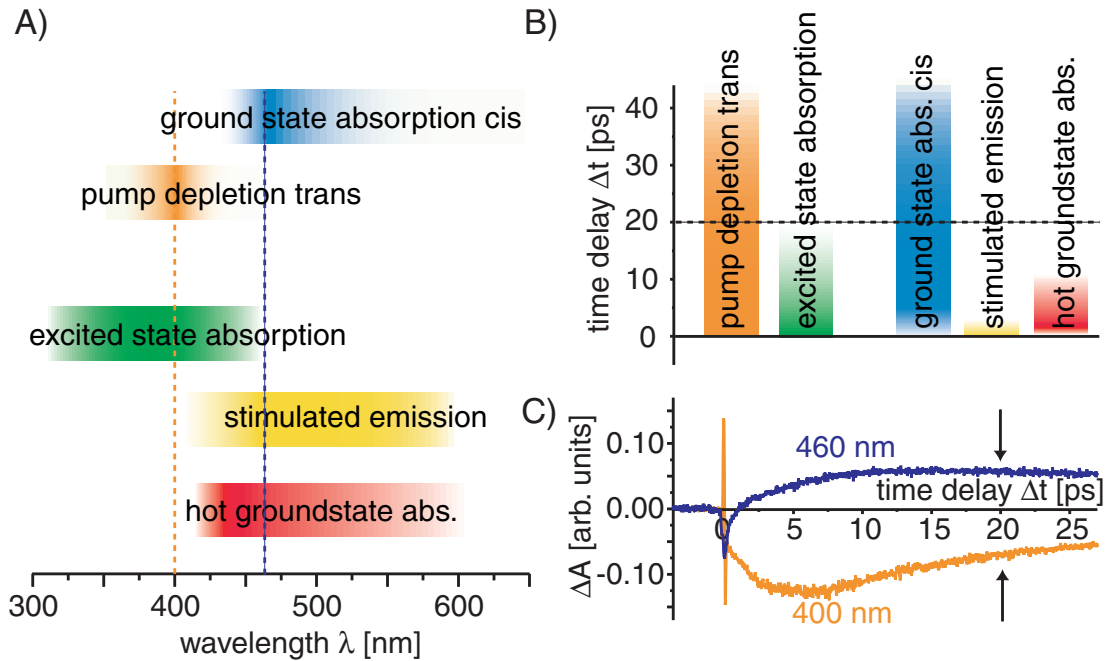


Figure 4.14: These plots summarize the results of the investigations on the dynamics of the molecule NK88. Figure A) shows the spectral regions, in which different states can be detected by various effects, recordable by transient absorption spectroscopy. In B) the temporal behaviour is sketched. Plot C) shows the two transients, whose signal at 20 ps is used as a feedback signal for controlling the isomerization efficiency. The feedback signal is as well marked in A) and B) by the dashed lines.

measures the fraction of molecules that actually undergo *trans-cis* isomerization. The ratio of the probe signals  $\Delta A(460\text{nm})/\Delta A(400\text{nm})$  at a delay time of 20 ps therefore reflects the isomerization efficiency (i.e., quantum yield) directly. Additionally, an appreciable influence of stimulated emission and absorption to higher lying states as well as hot ground state absorption is limited to very early pump-probe delay times and therefore is negligible at a pump-probe delay time of 20 ps. This situation is summarized in Figure 4.14.

In the beginning single-parameter control schemes are tested on the problem. First, the influence of varying the pulse energy of the pump pulse is investigated. It is found that the ratio between the generated ground state *cis*-isomers and the excited *trans*-isomers does not change significantly for pump pulse energy variations of a factor of five (from 200 nJ to 1125 nJ).

Another single-parameter variable frequently used in coherent control schemes is chirp. Under the given experimental conditions, the ratio between the generated ground state *cis*-isomers and the excited *trans*-isomers changes only by about 15% when for varying the second order spectral phase from  $-7500 \text{ fs}^2$  to  $+7500 \text{ fs}^2$ . To further investigate this observation, Figure 4.15A shows a cutout of the chirpscan from  $-2500 \text{ fs}^2$

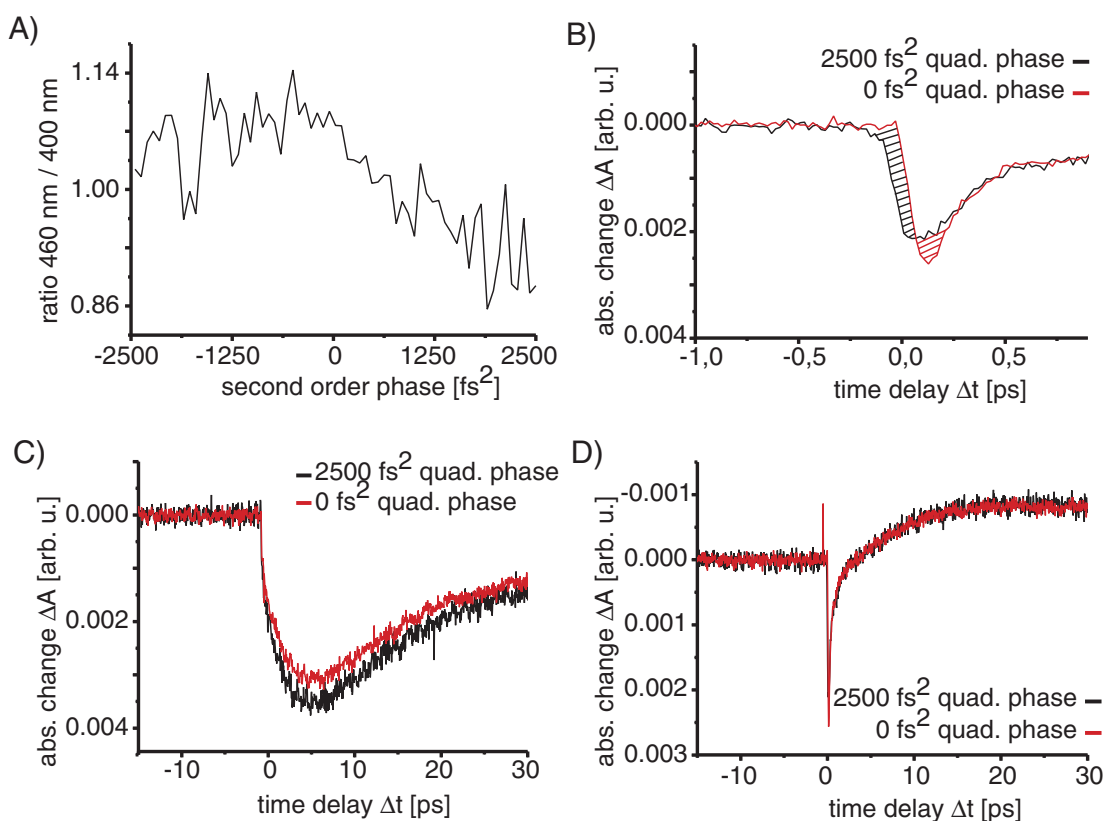


Figure 4.15: Plot A) shows the ratio of the probe-signals at 460 nm and 400 nm at a time delay of 20 ps for a scan of the second order spectral phase from  $-2500 \text{ fs}^2$  to  $2500 \text{ fs}^2$  imposed on the pump-pulse. As can be seen, a small change of the ratio can be observed, comparing very positive and very negative values. C) Transients for pump pulses with  $0 \text{ fs}^2$  (red line) and  $2500 \text{ fs}^2$  (black line) second order spectral chirp for a probe wavelength of 400 nm. The pulse energies of the chirped and unchirped pump pulses are attenuated to be equal. D) The same situation, but for a probe wavelength of 460 nm. To verify the influence of the chirp on the stimulated emission the first few picoseconds of the transient in C) are measured with high resolution. The transients in B) to D) reflect the behavior of the chirpscan in A). For the interpretation see the text.

to  $2500 \text{ fs}^2$  imposed on the pump pulse. The y-axis describes the ratio of the probe signals at 460 nm and 400 nm for a pump-probe delay time of 20 ps. As one can see, there is a small variation of the ratio with the value of the second order spectral phase. To verify this observation, transients are recorded for the values of  $0 \text{ fs}^2$  and  $2500 \text{ fs}^2$  second order phase (see Figure 4.15C and D). The pulse energy has been attenuated to be the same for both cases. Because the chirped pulse alters the excitation efficiency slightly, one of the transients at 460 nm is scaled to be equal to the other for long delay times to allow better comparison of the data. The respective 400 nm transients are then rescaled with the same factor. Clearly the two plots C and D show, that the isomeriza-

tion ratio is slightly different for the two cases of using a pump pulse with no chirp and one with a chirp of  $2500 \text{ fs}^2$ . In the latter case, the isomerization ratio is lower than in the case of an unshaped pulse as can be seen from the signals at 20 ps delay time by comparing the transients for 400 nm and 460 nm.

A very interesting question is how the stimulated emission behaves under these two excitation conditions. The stimulated emission is recordable by the small negative spike at the beginning of the 460 nm signal. This signal should behave similar to the pump depletion at 20 ps, since both reflect the amount of excited molecules. This means, for pulses that suppress the isomerization, there have to be more excited molecules to achieve the same amount of produced isomers. Therefore the stimulated emission and the pump depletion have to be considerably larger for the chirped pulse than in the case of the unchirped pulse, while the absorption of the produced isomers remains the same.

Because the isomerization takes place very efficiently, the stimulated emission decays very rapidly (see Section 4.3). Therefore the signal will be strongly effected by a shaped pump-pulse and the height of the emission spike can not be compared directly. To get an impression of the behaviour of the signal, the first few picoseconds are recorded with a high resolution (see Figure 4.15B). In this plot the area of the signal from -500 fs to +500 fs is compared for the two pump pulses. At 460 nm in this regime mainly stimulated emission takes place. The difference of the two signals is hatched to guide the eye. The exact calculation of the area yields a 10% higher value in the case of the chirped pump pulse. This comparison is widely correct since due to the simple pulse shape of a chirp, this pulse is not shifted in time with respect to with the unshaped pulse. Additionally, the coherent artifact should not influence this signal significantly, because it will occur in both cases, the chirped and the unchirped excitation. Furthermore, in the given case it is relatively small compared to the molecular signal. Moreover, the integral of the main part which is the electronic contribution, is equal to zero (see Section A.1 and Reference [76]). The behaviour of the stimulated emission is just as expected from the comparison of the signals at different wavelengths and a delay time of 20 ps. The stimulated emission is larger while the amount of produced isomers stays the same. That means that the isomerization efficiency is slightly smaller for the chirped pulse compared to the unchirped pulse.

This result is especially interesting, because it is achieved by applying different chirps. Due to the symmetric nature of this spectral phase, geometric shifts of the beam due to bad alignment are not expected. Furthermore also a change in the excitation frequency is not the case for these pulse shapes. In principle, a shift in the excitation wavelength can have an influence on the isomerization efficiency [60]. Normally, this shift has to be several tens of nanometers, but in the present case only a small shift of maybe two nanometer can be achieved within the parameters given by the system used here. A change of the isomerization efficiency due to a modulation of the pulse spectrum is not very likely to happen in the present case. Additionally the measurement of all information within a single transient provides very reliable information, since most unwanted effect such as offsets can be easily excluded.

### 4.5.3 Multiparameter control

As seen in the single parameter control schemes, it is only possible to vary the isomerization efficiency to a small amount, and only suppression is possible. Nevertheless, these experiments already show, that the variation of the spectral phase has an influence on the isomerization reaction. The goal is now to demonstrate that adaptive femtosecond quantum control is able to effectively control the *cis-trans* isomerization of a complex molecule in the liquid phase. As already discussed above, the pump pulse is sent through a femtosecond pulse shaper capable of producing complex laser pulse shapes by spectral phase modulation. An automated “learning loop” is then employed, where an experimental feedback signal from the physical control object itself guides the evolutionary algorithm to find laser fields optimized for the control task.

In the present case, as feedback signal the ratio of *cis*-isomers in the ground state after the photoisomerization process to the amount of initially excited *trans*-isomers (i.e., the relative reaction yield) has been chosen. To determine these quantities, the transient absorption signal at the two wavelengths of 400 nm and 460 nm at a given specific pump-probe delay time has been recorded. The pump-probe delay time during the optimization experiment was set to 20 ps, because both transients show only small changes at this large delay time. The ratio between the two signals can be changed only negligibly by the time-shift of the tailored pump pulse. Additionally, an appreciable influence of stimulated emission or absorption to higher lying states is limited to very early pump-probe delay times and therefore is negligible at a pump-probe delay time of 20 ps (see Section 4.5.2).

By employing the automated learning loop, laser pulse shapes are determined which enhance or reduce the isomerization reaction. The evolution of the *cis/trans* ratio as a function of generation number is shown in Figure 4.16 for the two cases of enhancement and reduction of isomerization. Each data point is the average of the ten best laser pulse shapes of the generation. In order to monitor the stability of the experimental conditions an unshaped laser pulse is applied after each generation of the evolutionary algorithm. The statistics of this reference measurement are ten times smaller than in the case of the shaped laser pulses.

In the case of maximization of the *cis/trans* ratio, i.e. the enhancement of the isomerization, the evolution of the optimization is shown in Figure 4.16A. The *cis/trans* ratio for unshaped laser pulses is essentially constant over the time of the optimization (open circles). In contrast, the *cis/trans* ratio measured with modulated and optimized laser pulses clearly rises above that level as a function of generation number and converges finally to an optimum (solid circles). This shows the ability to increase the ratio between the amount of *cis*- to *trans*-molecules using adaptively shaped femtosecond laser pulses. On the other hand, the algorithm is able to minimize that ratio (Figure 4.16B) as well. In this case a laser pulse shape is found that reduces the isomerization efficiency.

The optimized laser fields were characterized by the XFROG technique. This pulse



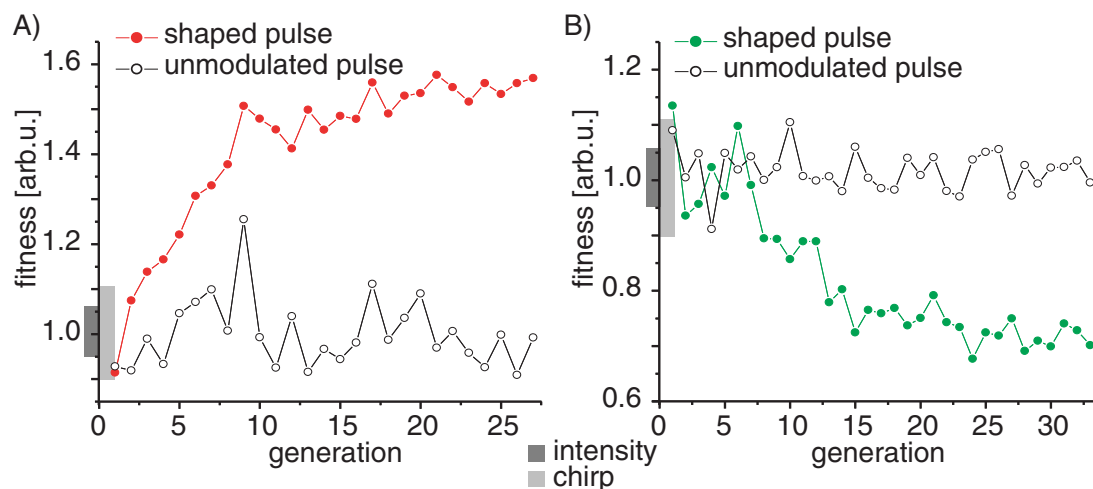


Figure 4.16: A) Maximization and B) Minimization of the *cis/trans* ratio as a function of iterations using an evolutionary algorithm. The filled dots represent results obtained with shaped laser pulses (average of the ten best individuals). The open dots show the reference signal obtained with an unshaped laser pulse that is sent after each generation. On the y-axis of both graphs the achievable ratio changes for the single parameter control schemes of pulse energy (dark grey,  $2\sigma$  width) and quadratic spectral phase (light grey) variation are also shown. The pulse energy was varied from 200 nJ to 1125 nJ and the chirp from  $-7500 \text{ fs}^2$  to  $7500 \text{ fs}^2$ .

characterization scheme is based on spectrally resolved crosscorrelation of the modulated 400 nm pulse and an unmodulated 800 nm reference pulse (see Reference [190] and Section 2.6.2). The XFROG-traces of the optimized pulse shapes are shown in Figure 4.17A for the maximization and in Figure 4.17C for the minimization, respectively.

One possibility for control might be the creation of different coherent vibrational wave packets on the  $S_1$  surface by the differently shaped laser pulses. Subsequently, the nature of the wave packet controls the passage through the conical intersection [273] and thereby the isomerization efficiency. However, the measurements presented in Section 4.3 indicate that higher-lying electronic states are involved. One can see from Figure 4.17A that in the case of maximization, an only slightly modified laser pulse compared to the unshaped one is needed to increase this efficiency even more. The almost unshaped laser pulse for the maximization means that a strong laser pulse is necessary for nonlinear transitions. It may well be the case that upper potential energy surfaces  $S_n$  are reached in a nonlinear multi-photon excitation which allows a direct motion through the conical intersection to reach the *cis* electronic ground state without any vibrational wave packet dynamics. In contrast to maximizing photoisomerization the suppression of this process obviously needs a train of laser pulses with reduced intensity for each of them. One possible interpretation is that here vibrational wave packet dynamics in upper ( $S_n$ ) potential energy surfaces are necessary to open an exit

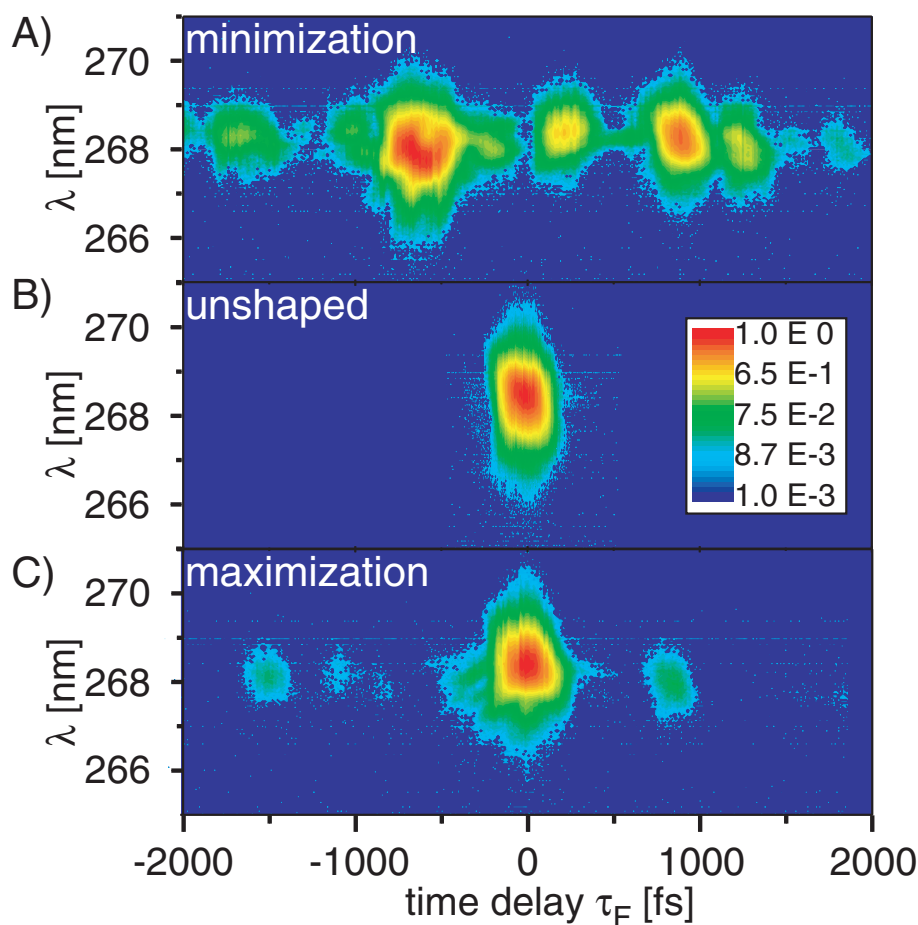


Figure 4.17: XFROG traces of the optimal pulse shapes for A) maximizing and C) minimizing the ratio between the *cis*- and *trans*-isomer. For comparison the XFROG trace of the unmodulated pulse is shown in B).

to the *trans* ground state via the conical intersection. The laser pulse train probably induces electronic transitions between these different excited potential energy surfaces. Each of the (differently) shaped individual laser pulses which are still coherent to each other, changes the vibrational wave packet dynamics accordingly.

In summary, without the result of theoretical work including the influence of higher lying states, it seems impossible to accurately assign the involved dynamics on the upper potential energy surfaces. However, the optimal laser pulses still give an indication what sort of dynamics is required for maximizing and for minimizing photoisomerization.

The results of the single-parameter variations are shown as bars in Figure 4.16A and B. The bars in both cases show the  $2\sigma$  width of the standard deviation of the two measurements, i.e. 95 % of all data points lie within this range. Furthermore, in or-

der to avoid very small *trans* excitation signal with low signal-to-noise ratio to enter into the fitness function and thereby to cause physically meaningless high values of the *cis/trans* ratio a suitable discriminator is used as a lower threshold [274]. This discriminator is given by the lowest measurable denominator for the signal-to-noise ratio. Hence the experimental results clearly demonstrate that optimally shaped femtosecond laser pulses open up a new level of quantum control in complex molecular systems.

In summary, these experiments demonstrate, that adaptive femtosecond pulse shaping is able to control isomerization reactions of a complex molecule in the liquid phase. By optimizing the ratios of the *trans*- and *cis*-isomers in a multi-parameter optimal-control experiment, it is demonstrated that isomerization efficiencies can either be enhanced or reduced. This can be regarded as a first step towards controlled stereoselectivity in photochemistry.

## 4.6 Effects of the fluorescence efficiency on the isomerization

It has been shown in the previous section, that it is possible to control the isomerization efficiency. As feedback, signals that are proportional to the amount of excited molecules and to the amount of produced isomers are used. A remaining question is the influence of the fluorescence as possible decay channel on the amount of produced isomers.

C. V. Shank and coworkers have shown in 1996 for one-photon transitions in a high intensity regime that the amount of excited molecules depends on the pulse shape [275]. For the investigated system, there are pulse shapes which causes significantly more or less excited molecules, although they have identical pulse energies. For a simple system, the amount of excited molecules will influence the total fluorescence yield. Therefore the quotient of the fluorescence yield to the pulse energy shows the efficiency of a pulse shape to produce fluorescence and is called fluorescence efficiency.

The theoretical calculations suggest, that there are different ways on the first excited surface, connecting the Franck-Condon region with the conical intersection. These ways are thought to have different oscillator strengths in respect to the ground state surface. Therefore the fluorescence should mainly arise from one of the two possible paths. Because of this it is thinkable, that by influencing the initial wave packet in a way to enhance the fluorescence can also have an impact on the isomerization process. If the path that exhibits more fluorescence is favoured, this could result in a lower amount of produced isomers. In this case, there is a big possibility, that the wave packet takes the fluorescence decay channel before reaching the conical intersection. The decay by emitting a photon will result in a population of the *trans* ground state.

Furthermore there is the possibility, that the different paths are connected with different individual isomerization efficiencies that result in an average molecular isomer-

ization efficiency. This assumption is not unlikely, because the conical intersection is reached from different directions. If one of the two paths have a higher possibility to fluoresce, the enhancement of the fluorescent channel could result in a preferred population of the corresponding path. If the paths are now connected with different individual isomerization efficiencies, this could vary the averaged molecular isomerization efficiency.

To address this issue, an optimal control experiment is performed, in which the enhancement of fluorescence is the control objective. The optimal pulse from this experiment is then tested by transient absorption spectroscopy regarding its influence on the isomerization efficiency.

### 4.6.1 Experimental details

Most of the setup for this experiment is identical to the one used in the previous section. In addition, a certain fraction of the shaped pump pulse is focused by a microscope objective with a focal length of 10 mm into a second cell containing the molecule NK88 dissolved in methanol. A second identical microscope objective collects the fluorescence produced by the excited molecules. To avoid any stray-light from the pump-pulse, the fluorescence is collected under an angle of  $30^\circ$  with respect to the direction of the pump pulse. For the same reason a 500 nm bandpass filter with a FWHM of 40 nm is used in front of the photodiode which collects the fluorescence.

A second fraction of the pump beam is monitored by another photodiode, whose signal is therefore proportional to the pulse energy. These two signals, the pulse energy and the fluorescence can be used in an femtosecond adaptive quantum control experiment as feedback signals. Similar to the setup in the previous section, the effect of the shaped pulses on the isomerization can be tested by transient absorption. Two different probe wavelengths can be independently monitored and used for further investigation of the control mechanism (for details see Section 4.5.1). This setup is sketched in Figure 4.18.

### 4.6.2 Results and Discussion

Several experiments on the optimization of the fluorescence have already been performed previously [6–8]. These experiments have shown, that it is possible to find pulse shapes which enhance or suppress the fluorescence of a molecular system. The experiments of the group of K. Wilson have shown that the control mechanism in their case essentially bases on a higher or a lower excitation efficiency, respectively, due to an intrapulse pump-dump mechanism [6].

Own experiments using the concepts of adaptive femtosecond quantum control have proven that it is well possible to enhance the fluorescence yield of the molecule NK88 dissolved in methanol by nearly a factor of two in comparison with the unshaped pulse. The evolution of the ratio of fluorescence to pulse energy for this optimization is shown

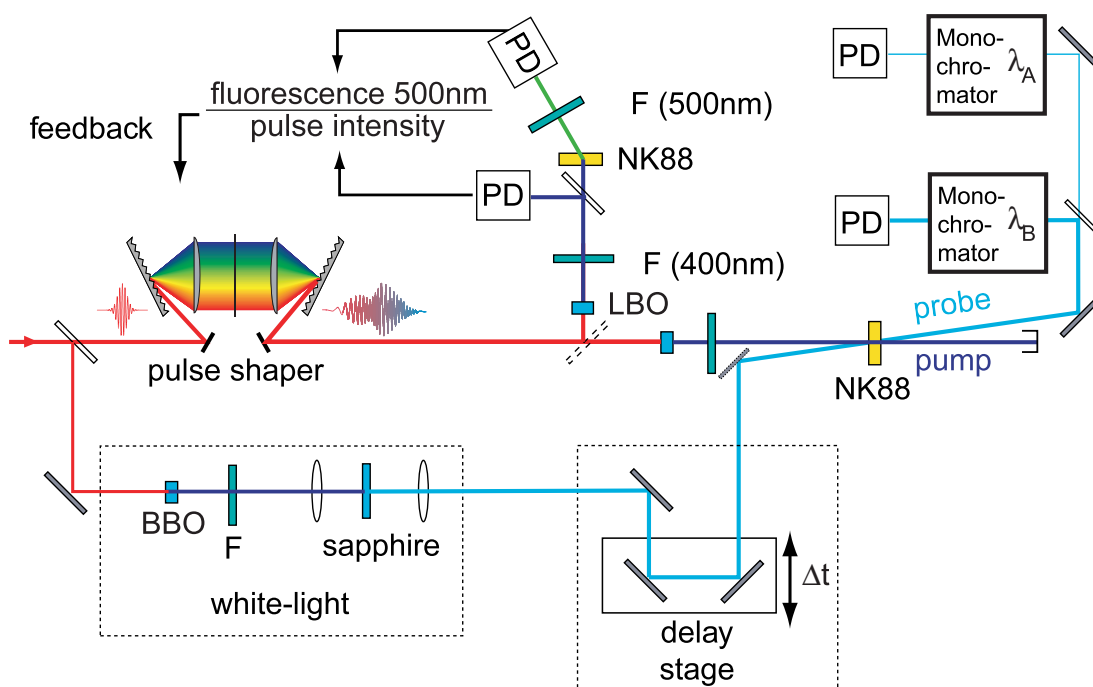


Figure 4.18: Sketch of the setup for performing experiments concerning the influence of the fluorescence on the isomerization reaction. A certain fraction of the phase-shaped and frequency-doubled pump pulse is guided into a flow cell, containing the molecule NK88 dissolved in methanol. The fluorescence is recorded by a photodiode. A second photodiode records the pulse energy. These two signals can be used as feedback in an adaptive femtosecond quantum control experiment. The effect of the shaped pulse on the dynamics can be additionally measured in a pump-probe experiment. For probing, a white-light continuum is generated by focusing a 400 nm pulse into a sapphire plate. Pump and probe pulses are spatially overlapped in a second flow cell containing the molecule dissolved in methanol. The probe pulse is split into two fractions after passing the sample. This allows to monitor two different wavelengths simultaneously.

as inset in Figure 4.19B. Each point is the average of the signal of all individuals of a generation. After each generation the ratio for an unshaped reference pulse is recorded and used for normalization of the optimization curve. In the following the success of this optimization will be shown with two additional measurements. Therefore the outcome of this femtosecond adaptive femtosecond quantum control experiments is confirmed by three methods. Because this optimization has been very successful, the optimized pulse is used for further investigations.

After the successful adaptive femtosecond quantum control experiment, the effect of the optimized pulse shape on the isomerization reaction is tested by transient absorption spectroscopy. Several interesting features can be seen by comparing the two transients at 400 nm and 460 nm for both cases of excitation with the optimized and an

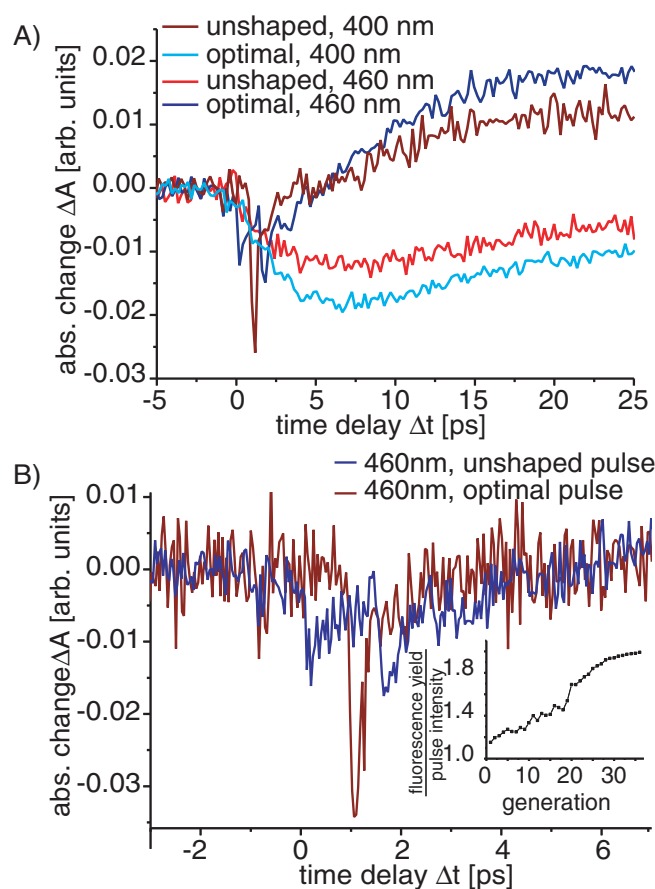


Figure 4.19: Plots A) and B) show the influence of an optimized pulse shape for enhancement of the fluorescence on the transient signals at 400 nm and 460 nm. As inset of Plot B) the evolution curve of the ratio of the fluorescence to the pulse energy is shown. Each point is the average of the signal of all individuals of a generation. After each generation the ratio for an unshaped reference pulse is recorded and used for normalization of the optimization curve. An enhancement by a factor of two can be achieved. The optimal pulse shape is used as pump pulse in the transient absorption experiments. The transient signal at 400 nm (bright colors) and 460 nm (dark colors) are shown up to 25 ps for the two cases of optimized (blue) and unshaped (red) pulses in plot A). Clearly an enhancement of the absolute signal of the shaped to the unshaped case can be seen comparing the same wavelength. In contrast, the ratio of the two signals at 400 nm and 460 nm at a delay time of 20 ps remains the same when using optimized and unshaped pulses for excitation. Plot B) shows the first few picoseconds of the transient at 460 nm for optimized (dark blue) and unshaped (dark red) pump-pulses. The negative signal is caused by fluorescence and, in the case of excitation with the optimized pulse, it is strongly effected by the pulse shape.

unshaped pulse.

At early delay times, the transient at 460 nm is mainly influenced by stimulated emission. Since the enhancement of the fluorescence was the optimization objective, the stimulated emission should be enhanced as well. Therefore Figure 4.19B shows a cutout of the first few picoseconds of the signal at 460 nm. This figure shows the two transients for the case of an unshaped (red) and an optimized (blue) excitation pulse. Both pulses have been attenuated to have the same pulse energy. As one can see from this plot, the stimulated emission in the case of the optimized pulse has a more complicated structure than in the case, in which the unshaped pulse is used for excitation. This results directly from the fact that the optimized pulse has a quite complicated structure which exhibits in the given case a double pulse like structure. To investigate the influence of the optimization, the area that is covered by the negative signal (stimulated emission) is integrated. It turns out that the area in the case of excitation with the optimized pulse is 1.6 times bigger than for the case of the excitation with the unshaped pulse. Because this analysis is very difficult, the result is only used to be compared with the direct measurement of the fluorescence as provided by the photodiodes. Nevertheless, these two different measurements show the same tendency. This supports the analysis of the stimulated emission on the one hand and the success of the optimization on the other.

The transients at 400 nm and 460 nm for a delay time of up to 25 ps and for the different cases of optimized and unshaped excitation pulses are shown in Figure 4.19A. The transient at 400 nm mainly reflects the amount of excited molecules and the one at 460 nm for late delay times the amount of produced isomers (compare Section 4.5.2). To investigate the effect of the fluorescence optimization on the isomerization the values at a delay time of 20 ps are compared. It turns out, that the ratio in the case for the optimized pulse is 0.62 and in the case of the unshaped pulse is 0.60. Within the given signal-to-noise ratio of the measurement, this variation of less than 4% cannot be accounted for a change in the isomerization efficiency.

Additionally it is very interesting to analyze the ratio of the amount of produced *trans*-isomers to the pulse energy which is as well measured for the experiments. As already visible from Figure 4.19A, the amount of produced isomers is higher in the case of using the optimized pulse for excitation compared to the case of using the unshaped pulse. From the exact evaluation it turns out that the ratio is enhanced by a factor of about 2.1. Because the isomerization efficiency is nearly unchanged, this value is carried forward to the amount of initially excited molecules. This can also easily be seen in the plot for the case of the 400 nm transient. The evaluation agrees very well with the fluorescence optimization result which also yields a factor of 2 for the enhancement of the fluorescence.

The measurements have shown by three different methods that the fluorescence yield has been successfully enhanced. The transient absorption experiments have proved that the amount of produced isomers and the amount of excited molecules is enhanced by the same factor. This allows the conclusion that the isomerization efficiency

is not altered for the case of enhancing the radiative decay channel.

## 4.7 Conclusion

The presented experiments have shown the versatility of the molecule NK88. The dynamics of this molecule dissolved in different solvents have been investigated by transient absorption spectroscopy in a wavelength region from 360 nm to 950 nm. The excited state dynamics were additionally observed by fluorescence upconversion spectroscopy. Moreover, the influence of the concentration on the steady state spectrum was investigated. In cooperation with F. Santoro and R. Improta a conclusive description of the molecular dynamics could be obtained. The theoretical calculations and the experimental results show dynamics on two time scales on the first excited potential energy surface after excitation. These two time scales are attributed to two different reaction paths. On one, the symmetry is broken earlier, on the other later. After decaying through the conical intersection the molecule can either decay back to the thermodynamically most stable *trans* ground state or to the product isomers. In the most likely model two product isomers are assumed, the *cis* and the *d-cis* form. Since both lie energetically higher, the population finally relaxes back to the *trans* ground state. From a general point of view the work on the dynamics shows that a critical and joined use of different experimental and theoretical approaches is necessary to get a realistic picture of very complex phenomena, such as the photoisomerization of a large molecule in the condensed phase. Furthermore, though many features can be assessed only by true dynamical theoretical computations, the recent advances in time-resolved spectroscopic techniques and in quantum mechanical computational methods make the understanding and the fine tuning of excited state processes a realistic goal.

Based on this information about the molecular dynamics, the adaptive femtosecond quantum control experiments with the objective of altering the isomerization efficiency were performed. Both enhancement and suppression of the isomerization yield have proven to be possible. In an additional experiment the fluorescence efficiency was increased by adaptive femtosecond quantum control. These measurements have shown that the optimal pulse shape for enhancing the fluorescence does not influence the isomerization process significantly. The obtained optimization results show that adaptive femtosecond pulse shaping can be applied to many challenges in physical, chemical, and biological research where isomerization reactions are of vital importance.



## Chapter 5

# Bacteriorhodopsin - an important isomerization in nature

The importance of isomerization to many processes in physics, chemistry and biology has already been stressed in the previous chapters. This chapter mainly deals with the spectroscopy and control of the isomerization process in the very complex biological system bacteriorhodopsin. The fundamental information for this system is already introduced in Section 3.3.2.

The photoisomerization of retinal in bacteriorhodopsin as initial step for proton-pumping has been subject to many publications as soon as time resolution became short enough to resolve the dynamics (see [31,276] and references therein). The retinal molecule is able to form several isomers such as *9-cis*, *11-cis*, *13-cis* or *all-trans*. The thermodynamically stable ground state as well as the efficiency of the isomerization to each of the possible isomers is strongly dependent on the surrounding environment. Both the selectivity as well as the efficiency is poor in solvents such as methanol. Starting from the *all-trans* form, it isomerizes with 6 % to the *11-cis* and also with 6 % to the *13-cis* form [69,277]. In contrast, embedded in the protein environment of bacteriorhodopsin the isomerization efficiency from the thermodynamically stable *all-trans* form to the *13-cis* form is 65 %, while 35 % relax back to the *all-trans* ground state. The situation for retinal embedded in rhodopsin, the system responsible for the visualization process in the human eye, is similar. In this case, the educt isomer is the *11-cis* form which isomerizes with a quantum yield of 67 % to the *all-trans* geometry [34,278]. This shows that the protein environment makes the photoisomerization both highly selective and efficient.

Optimal control has shown, both experimentally and theoretically, to be able to change the quantum yield of many different processes [2–9, 98, 101, 109–112, 221, 228–233]. These include investigations in the gas phase as well as in the liquid phase. Most of the investigated systems have been of small or medium size. Recently, the

group of M. Motzkus published a work on a highly complex system of biological importance [9]. In this experiment, it has been shown that the energy flow in the light-harvesting antenna complex LH2 from *Rhodospseudomonas acidophila* can be controlled. It turned out that the energy transfer could be reduced by optimal shaped laser pulses in a coherent manner. An increase of the energy transfer could not be observed.

As seen in Chapter 4, it is possible to enhance or reduce the isomerization efficiency of a medium-complex molecular system dissolved in methanol [112]. In this case, the molecule is not embedded in an environment already optimized by nature for a certain problem, as in the case of LH2. Therefore, it is very interesting to investigate the combination of both aspects, the control of the isomerization efficiency and a complex system relevant for nature.

First steps towards this goal have been performed by different pump-dump-probe schemes [95, 279, 280]. The corresponding experiments have shown that it is possible to reduce the isomerization efficiency [279, 280].

In this work the traditional pump-dump-probe method is improved to a pump-shaped-dump-probe scheme to control and investigate molecular dynamics. In a different context, shaped Stokes pulses were used to achieving selective ground-state population within coherent anti-Stokes Raman spectroscopy [281, 282]. In the pump-shaped-dump-probe scheme, the dump-pulse frequency is chosen to lie in the near infrared to have the chance to influence the isomerization process at a point where the ground state surface and the first excited state surface are close to each other. This is the case near conical intersections which are thought to play an essential role in the isomerization process of retinal in bacteriorhodopsin. Therefore, with this scheme, the influence of a tailored laser field on the isomerization dynamics close to the conical intersection can be investigated. This method tries to reproduce active control schemes which are often employed in theoretical studies (see Chapter 3.4). In these cases, the laser field guides the wave packet all the way to the desired product channel. With these concepts it has been possible to successfully influence the isomerization efficiency in computational model systems of bacteriorhodopsin [228].

An illustrative example for this improved pump-shaped-dump-probe scheme is shown in Figure 5.1. There, the molecule is excited by a pump pulse resulting in a wave packet in the Franck-Condon region of the first excited-state ( $S_1$ ) potential energy surface. This wave packet evolves under the influence of the excited-state Hamiltonian. At the conical intersection the wave packet can propagate back to the ground state ( $S_0$ ). The probability for populating different product configurations on the ground-state potential energy surface is directly related to the dynamics at the conical intersection. In the displayed example, the decay occurs with a certain probability either to the right or to the left well of the ground-state potential energy surface, such as *cis* or *trans* structures in the case of an isomerization reaction. The shape and the velocity of the wave packet close to the conical intersection depend on the nature of the  $S_1$  potential energy

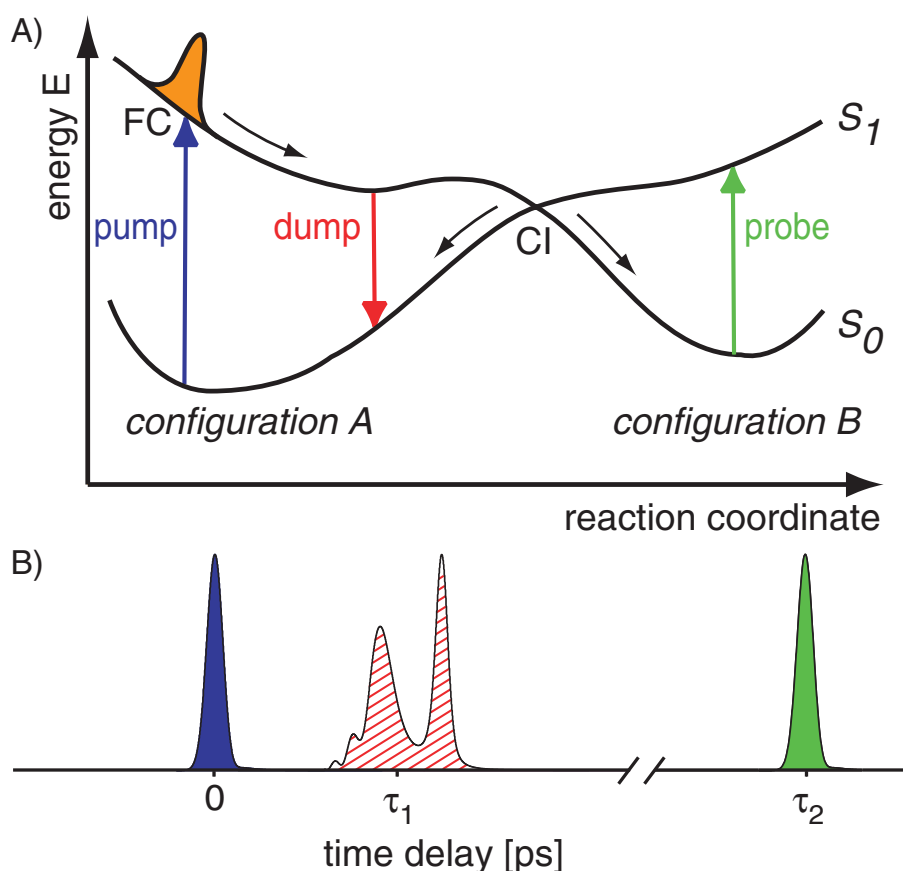


Figure 5.1: A) Potential energy surface scheme for a typical molecule. After  $S_0 \rightarrow S_1$  excitation by a pump pulse, the induced wave packet moves from the Franck–Condon region (FC) to the conical intersection (CI), where it can decay back to the  $S_0$  potential energy surface. With a certain probability, either molecular configuration A or B is populated. B) Pump–shaped–dump–probe sequence. In this example, the shaped dump pulse (red/hatched) is delayed by  $\tau_1$  with respect to the pump pulse (blue/dark gray). The impact of the dump pulse, i.e. the final population in configuration B, is monitored by the probe pulse (green/light gray), which arrives at a time delay  $\tau_2 \gg \tau_1$  after the pump pulse.

surface.

In order to study and control the excited-state evolution, quantum control with a shaped dump pulse is implemented. This has the potential of influencing the dynamics in the vicinity of a conical intersection, which is of essential importance to the final reaction outcome. The end result is measured by an additional time-delayed probe pulse. With adaptive quantum control the optimal shape for the dump pulse can be obtained, and together with systematic variations of parameterized dump pulse shapes, information on the potential energy surfaces close to the conical intersection can be deduced.

Hence, the pump–shaped-dump–probe scheme allows both improved optimal control experiments and provides a better understanding of the excited-state time evolution of the system under study.

The first part of this chapter will introduce different models that can be found in the literature which try to explain the early time dynamics. In addition, the spectroscopic signals, as relevant for the experiments, are presented. The second part will show the results of the improved pump–shaped-dump–probe scheme, as introduced above. Two aspects are illuminated: the potential of shaped dump pulses to extract information about the molecular dynamics on the one hand and the capability to efficiently control reactions on the other hand. Finally, the third part demonstrates first attempts to control the isomerization efficiency by shaping the excitation pulse. The excitation will take place into a higher-lying excited state. The higher density of states in this regime is connected with an increased number of conical intersections. This opens alternative reaction pathways that can be accessed by optimally designed excitation pulses.

## 5.1 Dynamics and spectroscopic signals

The very first step of the isomerization of retinal determines the dynamics for the rest of the photocycle of bacteriorhodopsin. Because of this importance, the first steps of the photocycle have been subject to many publications. Since the first experiments on the ultrafast dynamics of bacteriorhodopsin, four different groups of models have been developed, trying to explain the big variety of different experimental observations (see Figure 5.2). Model 5.2A and B are the oldest and most commonly used models to explain different experimental results. They principally differ in the fact where the vibrational equilibration takes place after the molecule has been excited by a photon of the proper wavelength. In model A the equilibration happens already on the first excited surface while in B the equilibration mainly takes place in the ground state.

In these both models, the excited state surface is “reactive” along the isomerization (torsional) coordinate and drives the photoexcited *all-trans* isomer towards the *13-cis* product isomer along a barrierless path. The stimulated emission decays on multiple time scales, with decay times of about 200 fs and 1 ps [227]. The temporal behavior of the stimulated emission additionally changes with the wavelength region in which the signal is monitored. A similar behavior can be seen in the excited state absorption. In addition, the earliest absorption bands in the vicinity of the photoproduct absorption at 625 nm also appear with a multiexponential rise function that has a significant contribution corresponding to a decay time of about 500 fs or less [69, 283]. This led to the conclusion that the isomerization essentially takes place within the first 500 fs. The 200 fs time scale was accounted for a damped torsional movement out of the Franck-Condon region. The succeeding state is named  $J_{625}$ -species and is populated within 500 fs. This one finally decays to the  $K_{590}$ -state with about 3.5 ps. The  $K_{590}$ -state can be identified as the ground state of the *13-cis* photoisomer.

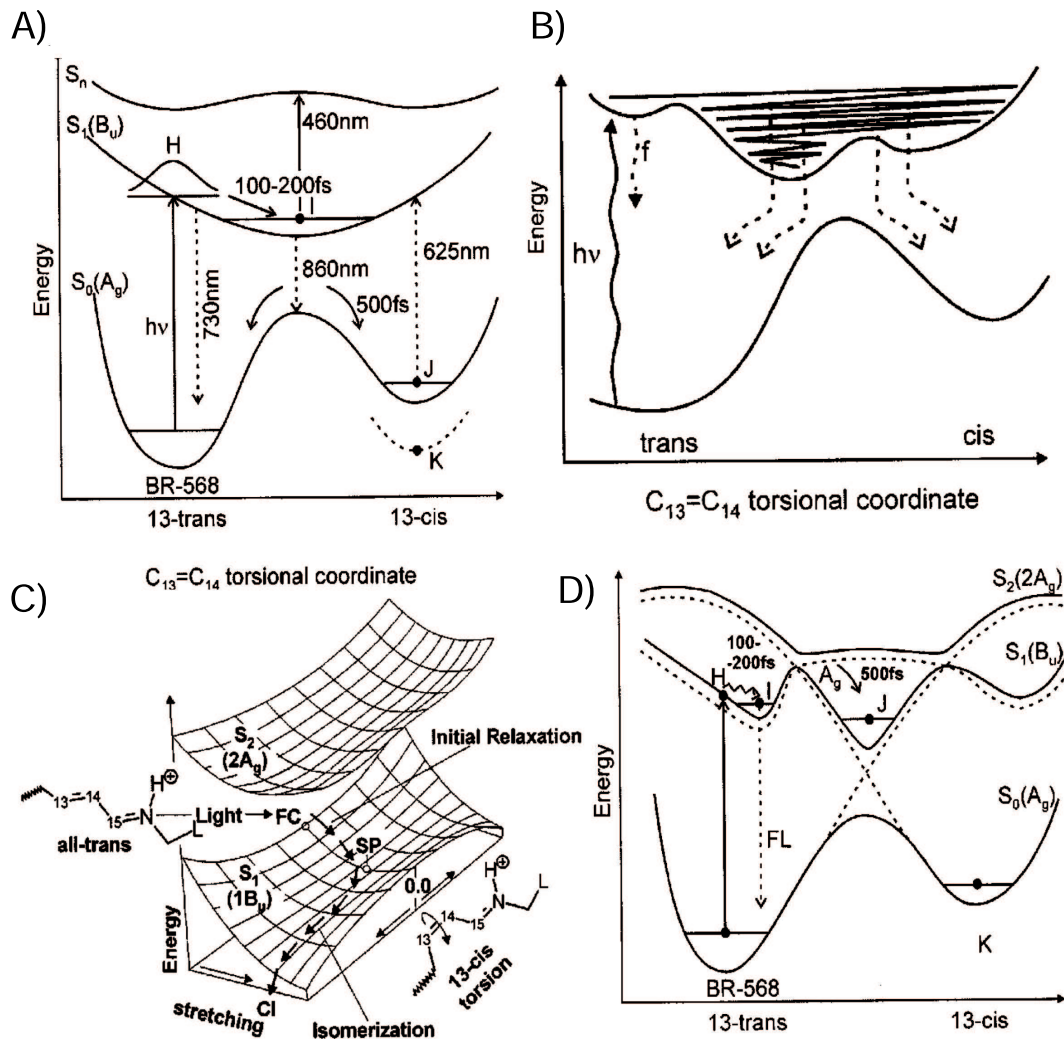


Figure 5.2: Different models that have been used in the literature to explain the molecular dynamics of bacteriorhodopsin. A) In this most often used two-state overdamped model, the isomerization is essentially finished after 500 fs in which the intermediate state  $J_{625}$  is populated. The  $J_{625}$ -state decays with 3.5 ps to the  $K_{590}$ -state. Model B) differs from A) in the fact that the vibrational equilibration is assumed to take place already on the first excited surface. Also the relaxation pathway is mostly determined on the excited surface. In C) recent theoretical results lead to a two-state two-mode model (a stretching and a torsional mode). conical intersection denotes the conical intersection, SP a stationary point and FC the Franck-Condon region. Model D) incorporates experimental findings that indicate the existence of a small barrier. This is explained as a result of nonadiabatic coupling between the first two excited states. (taken from [227]).

The exponential behavior can in principle be explained by different curvatures of the excited surface within the Models A and B. Further experiments with different excitation wavelengths [283], and older experiments at different temperatures (see [69] for a review) indicate that a small barrier could exist on the first excited surface. These experimental results led to the model 5.2D.

This model tries to explain the existence of a small barrier with the help of strong nonadiabatic coupling between the first two excited states. In this case, the  $J_{625}$ -state is thought to be on the first excited surface, close to a point where the ground state surface and the first excited state surface come very close to each other and thus facilitate an efficient decay to the ground state [227].

Nevertheless, more recent studies on the temperature dependence of bacteriorhodopsin's excited state lifetime again support a barrierless nature of the retinal excited state at physiological temperatures in contradiction to the earlier results [284]. These earlier results were based on steady-state spectroscopy and time-resolved spectroscopy with a time-resolution of 30 ps and could be explained within the new experiments. Two time scales appear at very low temperatures, a fast dominant one, remaining basically unchanged as a function of temperature, and a slower one. The latter could be responsible for the older observations.

Theoretical calculations including a further coordinate to the already employed torsional coordinate, namely the high frequency stretching, lead to a new model, called two-state two-mode model (Figure 5.2C). The studies indicate that no avoided crossing is likely to occur [285]. Nevertheless, these calculations show that there is at least a plateau or even a small barrier on the first excited surface.

None of these models succeeded in explaining all experimental findings [227]. Especially, differences in the stimulated emission spectrum and the fluorescence upconversion spectrum can not be explained. This shows that the initial molecular dynamics is far from being simple and can not be explained in strongly reduced schemes. Many different modes and electronic states have to be accounted in order to describe the early time kinetics properly [227]. A model explaining the discrepancy between the stimulated emission and the fluorescence upconversion spectrum implies a  $CH_3$  rock mode, a hydrogen out of plane (HOOP) vibration and a torsional mode. Within this model the different absorption bands are situated in such a way that the stimulated emission is partly canceled by the HOOP absorption. This model is shown in Figure 5.3 as a sketch.

Commonly, light at 568 nm is used for the excitation of bacteriorhodopsin, because this wavelength corresponds to the *all-trans*  $S_1$  absorption maximum. Irradiation with 400 nm light results in excitation to the third excited surface  $S_3$  [283]. Most of the dynamics is comparable to the case of excitation at 570 nm, with the exception of a slight shift of the rise times of the  $J_{625}$ -state to a clear double exponential behavior with 150-200 fs and 1600-2500 fs, respectively. In addition, a new absorption feature peaking at 740 nm arises. On the one hand, this can be attributed to vibrational hot molecules on the first excited surface after the nonradiative decay from the  $S_3$  to the

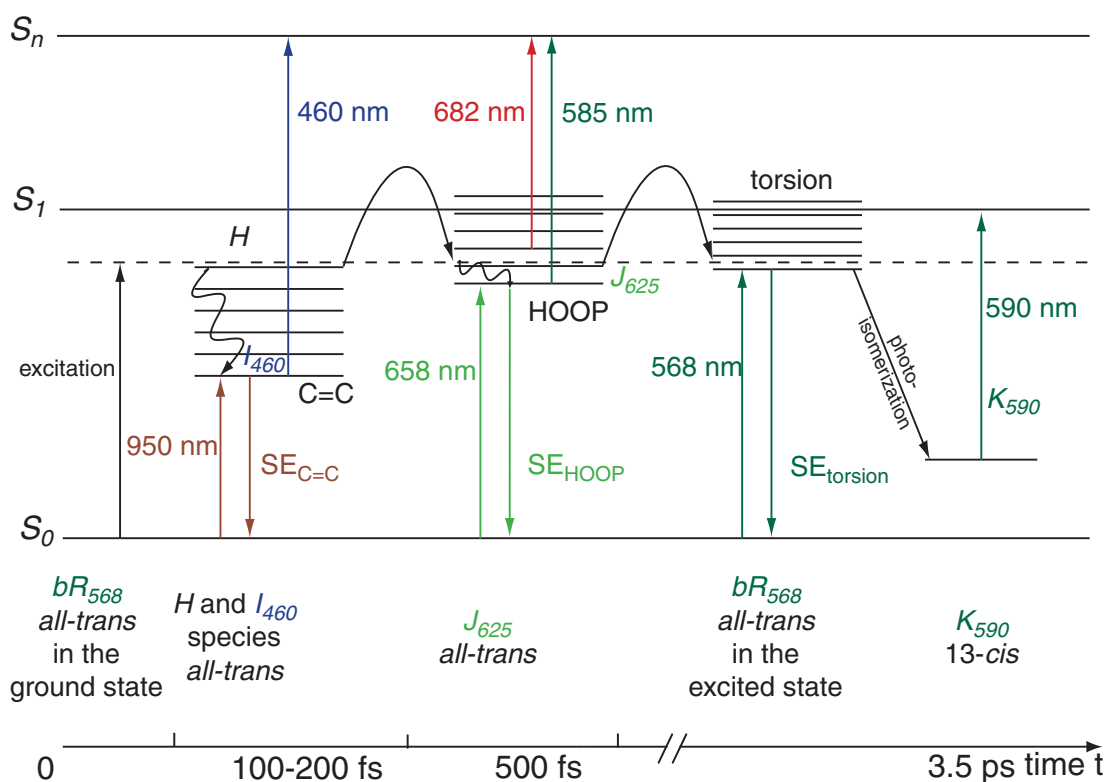


Figure 5.3: Sketch of the two-state many modes model adapted from reference [227]. This model is capable to explain the discrepancy between the stimulated emission and the fluorescence upconversion spectrum. The used modes are the  $CH_3$  rock, the hydrogen out of plane (HOOP) vibrations and the torsional mode. SE stands for stimulated emission. In this model, the molecule gets excited to the Franck-Condon region and from there the wave packet moves to the  $H$ -state. Then, either the  $I_{460}$ -state or the  $J_{625}$ -state is populated. From the first one radiative decay to the *all-trans* ground state is possible. From the second one radiative decay to the *all-trans* ground state is possible as well, but also the population of the  $K_{590}$ -ground state. During this step the torsional modes become important and therefore the  $K_{590}$ -state has already *13-cis* geometry.

$S_1$  surface which takes place in less than 50 fs. On the other hand, the shape of the emission spectrum is also likely to be changed, so that the negative contribution to the complete absorption signal at the questionable wavelength of 740 nm is reduced and an overall absorption emerges [283].

Three-pulse experiments have shown that the  $S_1$  state relaxes even faster when populated nonradiatively from the  $S_n$  rather than directly by  $S_0 \rightarrow S_1$  excitation [95]. The same experiments lead to the conclusion that the relaxation from a higher  $S_n$  state is likely to end up in a different state  $S'_1$  which is close to the state on the  $S_1$  surface reached by direct  $S_0 \rightarrow S_1$  excitation, but not identical to it. Although there are certain

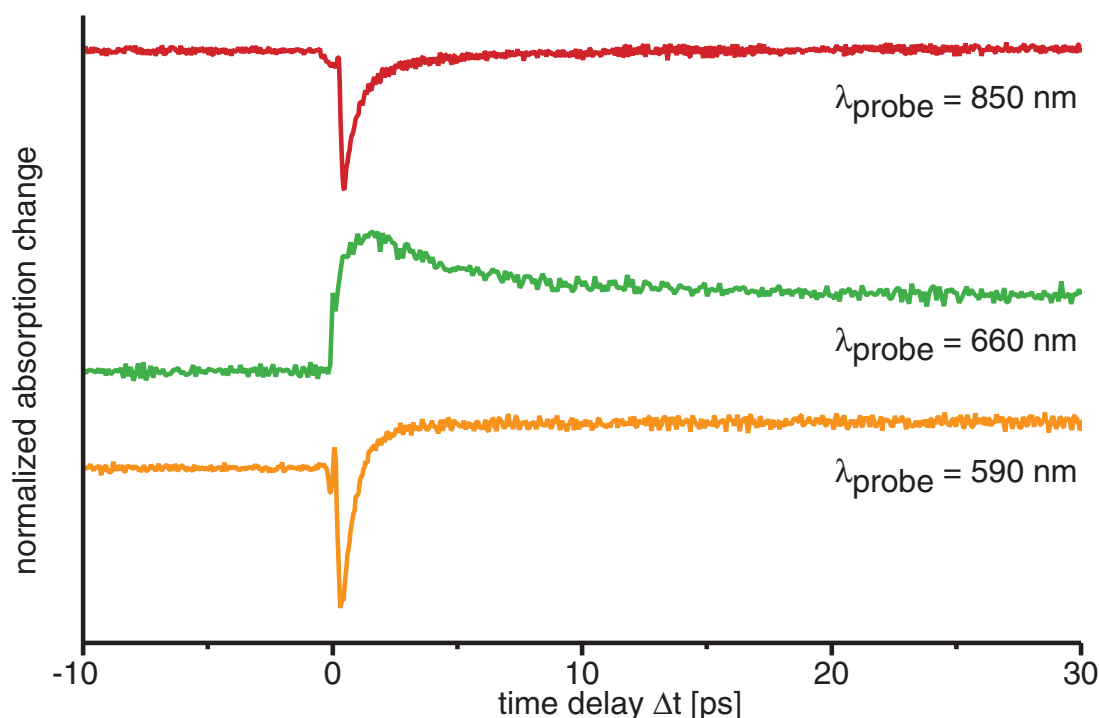


Figure 5.4: Transient absorption signals of bacteriorhodopsin excited at 400 nm. At the probe-wavelength of 660 nm the signal is dominated by the J- and the K-state absorption. At 590 nm in addition to these contributions, there is a signal with an opposite sign which can be assigned to pump-depletion. The excited-state population can be monitored with the help of the stimulated emission at 850 nm or above.

differences in the dynamics concerning the cases of excitation at 400 nm and 568 nm, the quantum yield of the reaction does not change significantly [283].

In the experiments concerning bacteriorhodopsin in this work, excitation is also carried out at 400 nm. One reason is that this wavelength is easily obtainable by the laser system used for the experiments in this thesis. Another reason will be given in Section 5.3. The experimental transients for the transient absorption signals at probe-wavelengths of 590 nm, 660 nm and 850 nm are shown in Figure 5.4. These transients are capable to give the necessary information for the desired experiments.

As seen above, all models agree that the population of the *13-cis* ground state ( $K_{590}$ -state) takes place with about 3.5 ps. The absorption signal of this state can still be monitored at 660 nm although the maximum of the absorption is at 590 nm. At the same wavelength of 660 nm also the  $J_{625}$ -state contributes to the complete molecular absorption, although having its maximum at 625 nm. But since this state decays with 3.5 ps, this signal has only a non-negligible contribution at the first few ten picoseconds. Therefore the transient signal at 660 nm at late delay times is proportional to the amount of produced *13-cis* isomers.



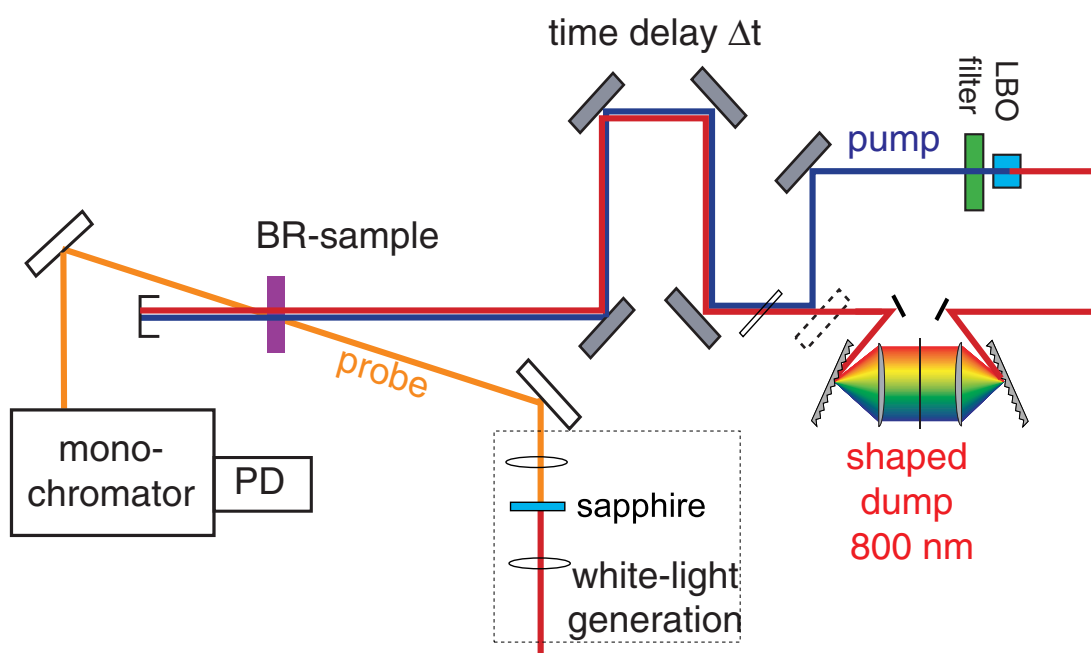


Figure 5.5: Sketch of the setup for the pump–shaped-dump–probe experiment. The 800 nm dump pulse can be phase-modulated with the help of a phase-only pulse shaper. The pump pulse is frequency-doubled in a nonlinear crystal and collinearly recombined with the shaped dump-pulse. By focusing a small fraction of the 800 nm beam into a sapphire plate a sufficiently broad white-light continuum is generated that can be used as probe pulse. The probe pulse on the one hand and the pump and shaped dump-pulses on the other hand are spatially overlapped in the sample. Different probe wavelengths can be selected by a monochromator after passing the sample.

The decay time of the  $K_{590}$ -state itself is known to be in the microsecond regime and thus for time delays accessible in the presented experiment, no significant decay due to the  $K_{590}$ -state depopulation is observable.

The transient at 590 nm has two overlapping contributions of different sign: the  $J_{625}$ - and the  $K_{590}$ -state absorption, but also the bleach signal from the *all-trans* ground state which dominates at early delay times.

Finally, the excited state population can for example be monitored at wavelengths equal to 850 nm or higher by stimulated emission.

## 5.2 Reducing the isomerization yield by active control schemes

### 5.2.1 Experimental details

To realize a pump–shaped–dump–probe control scheme, the 800 nm pulse is split up into three fractions. The first one is used for generating a white light continuum by being focused into a sapphire disc. This white light continuum covers all desired probe wavelengths necessary for the experiment. The second fraction is frequency-doubled in a 300  $\mu\text{m}$  LBO crystal to generate pulses centered at 400 nm. The pulse energy was attenuated to at most 500 nJ. These pulses were used to excite the molecules. The third fraction is shaped by a liquid crystal display spatial light modulator within a zero-dispersion compressor and is then recombined collinearly with the 400 nm pump pulse. This 800 nm pulse acts as a shaped dump pulse. If no phase modulation is applied to the pulse shaper, the 400 nm pump pulse and the 800 nm dump pulse overlap not only in space but also in time. Both the pump and the shaped dump pulses are focused by a 200 mm lens into the sample. The probe pulse is spatially overlapped with the pump and the shaped dump pulses after passing a 150 mm lens. The probe pulse has an angle of  $10^\circ$  with respect to the pump and the shaped dump pulses.

After passing the sample different wavelengths can be selected out of the white light continuum of the probe pulse by a monochromator. The delay between the probe pulse on the one hand and the pump and shaped dump pulses on the other hand can be modified by a computer-controlled delay stage. This setup is shown as a sketch in Figure 5.5.

Light-adapted bacteriorhodopsin is used as a thin film (see e.g. [286]). The sample has been purchased from Munich Innovative Biomaterials (Martinsried, Germany) containing the wild type of bacteriorhodopsin in a film of less than 100  $\mu\text{m}$  thickness with approximate optical densities of 1 at 570 nm and 0.25 at 400 nm, respectively. This sample is both perpetually rotated and translated in a specially designed sample holder to probe different portions with each laser shot and to avoid thermal heating of one spot in the sample (see Appendix A.4).

### 5.2.2 Reverse control by pump–shaped–dump–probe scheme

The pump–shaped–dump–probe scheme can be used to efficiently control reactions and to extract information about molecular dynamics. In this subsection these two aspects will be demonstrated for the molecular system retinal in bacteriorhodopsin.

Since the characteristics of excited-state potential energy surfaces determine both photophysical and photochemical processes, it would be desirable to use the power of pulse-shaping technology for specifically studying excited-state dynamics. In order to

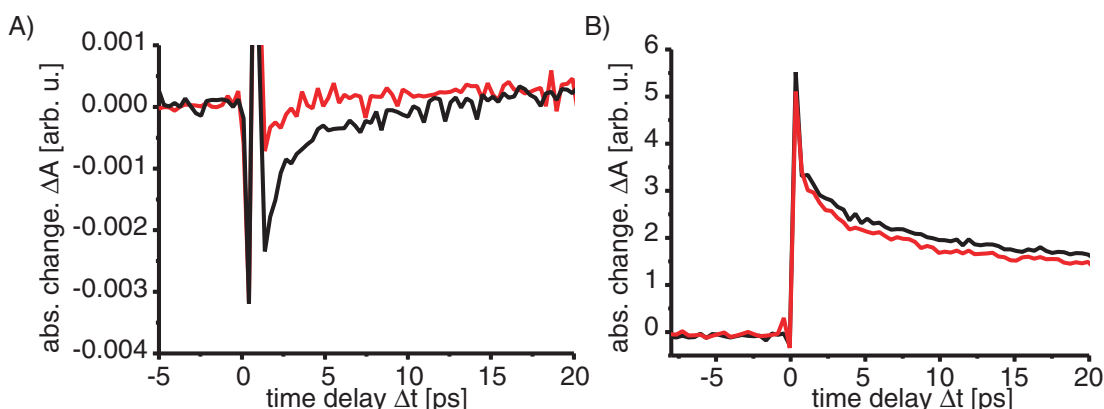


Figure 5.6: A) Stimulated emission at 900 nm and B) *13-cis* product isomer yield at 660 nm without a dump pulse (black) and with a bandwidth-limited dump pulse (red) set to a delay time of 200 fs.

facilitate such analysis, the usual quantum-control procedure is reversed: instead of looking for optimal excitation starting from the ground state, optimal *de-excitation* is sought starting from the excited state. Hence the properties of the excited system can be studied more directly, retaining the capabilities of shaped-pulse analysis. The idea is that the optimally shaped de-excitation pulse (dump pulse) contains information on the propagating excited-state wave packet and thus on the shape of the excited-state potential energy surface.

Here, the molecule is excited at 400 nm which causes an initial transition to the  $S_3$  potential energy surface [283]. As shown by the group of R. Hochstrasser, non-radiative decay to the  $S_1$  potential energy surface takes place in less than 50 fs [283]. From there, after propagation on  $S_1$ , the wave packet returns to the ground-state potential energy surface via a non-radiative transition. For bandwidth-limited excitation pulses, the *all-trans* isomer is repopulated with a quantum efficiency of  $\approx 35\%$ , while the *13-cis* isomer is produced with  $\approx 65\%$  [34].

The amount of *13-cis* isomers could in principle be monitored by the absorption of the  $K_{590}$ -state at 590 nm. As already stated in the previous subsection, in order to avoid ground-state bleach contributions from the *trans* species, which are present at 590 nm, the probe wavelength is set to 660 nm instead. There, the *13-cis*  $K_{590}$ -state still absorbs, but no *trans* ground-state bleach occurs. In the same wavelength region, a precursor of the  $K_{590}$ -state, labeled  $J_{625}$ -state, absorbs as well. However, this intermediate state has a lifetime of about 3 ps and therefore a non-negligible contribution is only visible at early delay times. Thus the probe delay is set to 150 ps for which the signal is directly proportional to the amount of produced *13-cis* molecules [227, 283, 287].

Employing a bandwidth-limited dump pulse at the correct time delay can efficiently dump a certain part of the excited state population. Naturally, this influences the time-dependent signal of the stimulated emission, since it is proportional to the excited state

population. The stimulated emission probed at 900 nm is shown in Figure 5.6A for the cases with (red) and without (black) dump pulse. The time delay for the dump pulse with respect to the pump pulse was set to 200 fs by applying a corresponding linear spectral phase onto the dump pulse. This results in a shift to later delay times. From Figure 5.6A it can be seen very well that a certain part of the excited state population is transferred by the dump pulse into other states that do not fluoresce at 900 nm. The transient signal drops significantly after the dumping act.

If a dump pulse at 800 nm is employed, both excited-state absorption ( $S_1 \rightarrow S_n$ ) and, to a larger extent, stimulated emission ( $S_1 \rightarrow S_0$ ) can occur. Therefore, a certain fraction of the population is transferred from the  $S_1$  state to the *all-trans* ground state. As a consequence, the initially excited molecules which have been dumped to the *all-trans* ground state cannot reach the  $K_{590}$ -state anymore, so that the dump pulse significantly influences the photoisomer yield, as illustrated in detail by the groups of P. A. Anfinrud [280] and S. Ruhman [279]. This can be visualized, if the transient absorption signal at a wavelength of 660 nm is monitored, where the  $K_{590}$ -state absorption is dominant [287]. This signal shows that the population of the  $K_{590}$ -state is also affected by the dumping process (see Figure 5.6B). Thus, employing a dump pulse alters the isomerization efficiency.

In the experiments, presented here, shaped dump pulses are used to manipulate molecular dynamics. In a first step, the mean temporal position of the wave packet in the dumping region is determined by scanning the first-order spectral phase of the dump pulse, shifting it in time (Fig. 5.7A). At time zero, the pump and the dump pulses have full temporal overlap in the sample. For negative (positive) linear spectral phases the dump pulse comes before (after) the pump pulse. Depending on this parameterization, the amount of produced *13-cis* isomers (probe signal at 660 nm) is measured. As can be seen from Fig. 5.7A, most effective dumping (i.e. smallest product absorption) in the case of bandwidth-limited pulses occurs at a delay time of about 200 fs with respect to the pump event.

In the second step, the amount of produced *13-cis* isomers is measured in dependence on second-order spectral phase of the dump pulse, with a fixed additional setting of 200 fs for the previously optimized first-order phase (Fig. 5.7B). The sign convention is such that negative values of second-order spectral phase correspond to negative temporal chirp, i.e. higher frequencies preceding lower ones. The dumping yield is highest for unchirped pulses, but furthermore an asymmetry with respect to the sign of second-order phase is visible, indicating the shape of the potential energy surface difference between  $S_0$  and  $S_1$ . The dumping yield for negative chirps is higher, i.e., the *13-cis* product absorption is lower, than for corresponding positive chirps. This reflects the energetic separation between the  $S_1$  and  $S_0$  potential energy surfaces in the transition region accessible with dump pulses at 800 nm and the given spectral bandwidth. While the wave packet evolves on  $S_1$ , the gap to  $S_0$  is getting smaller, so that negative chirps can dump more efficiently. This interpretation is in analogy to chirped laser pulse excitation, but instead of intrapulse dumping [97, 275] with separate pump

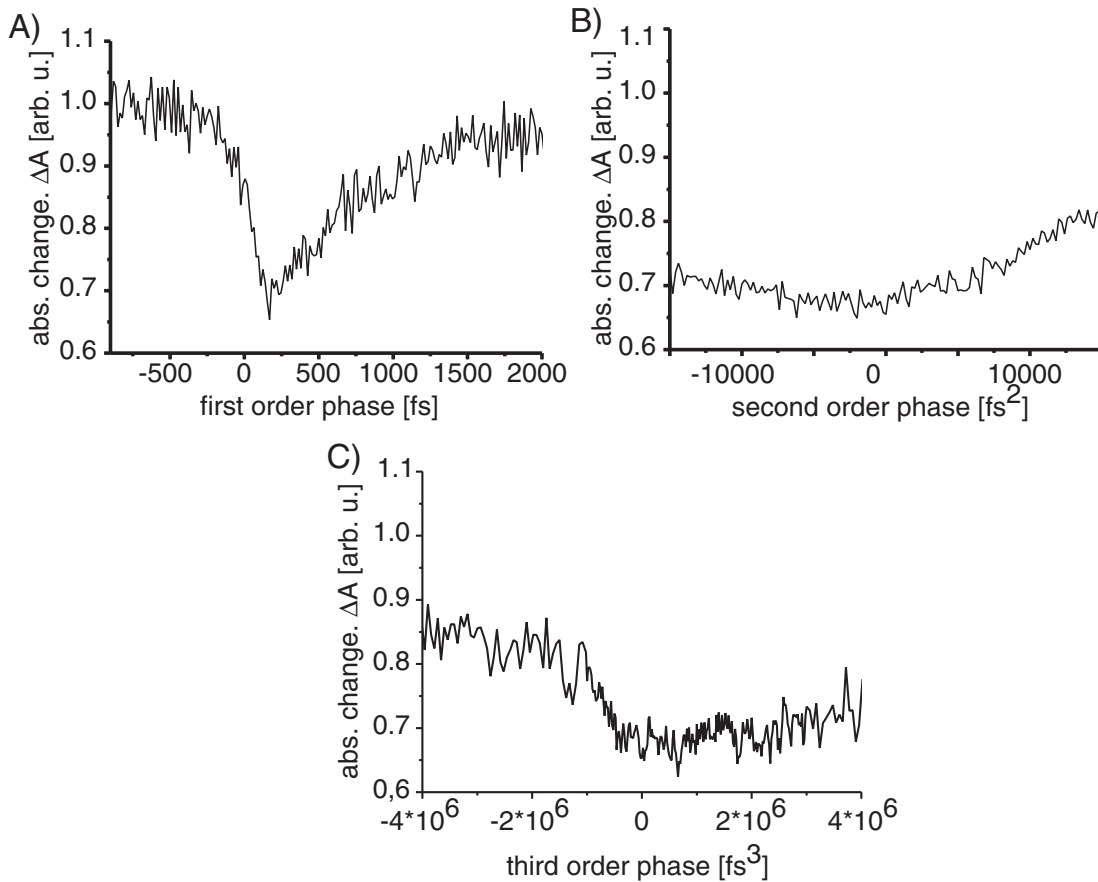


Figure 5.7: Transient absorption signal (400 nm pump, 800 nm dump, 660 nm probe, 150 ps pump–probe delay) which is proportional to the amount of produced *13-cis* isomers. A) Absorption difference in dependence on the first-order spectral phase of the dump pulse. B) The same signal as a function of the second-order spectral phase (i.e., linear chirp), with an additional linear phase offset of 200 fs. Figure C) shows the same signal again, but for the third order spectral phase with an additional linear phase offset of 200 fs. The curves are normalized to the signal level in the absence of a dump pulse. D) Sketch of laser pulse with a third order spectral phase of  $10^6$  fs<sup>3</sup>.

and chirped dump pulses. Due to the second-order spectral phase, the dump pulse is also stretched in time, so that the shaped dump pulse starts to overlap with the pump pulse, and parts of the dump pulse might arrive too early to dump the wave packet (thus reducing the dumping yield). However, this effect should be identical for positive and negative chirps for the given laser bandwidth and thus does not explain the observed asymmetry. Therefore, the potential energy surface difference close to the conical intersection can be inferred from the spectral phase variation data in Fig. 5.7. Calculations are currently performed in order to obtain a more quantitative analysis.

Similarly to the variation of the second-order spectral phase the third-order spectral

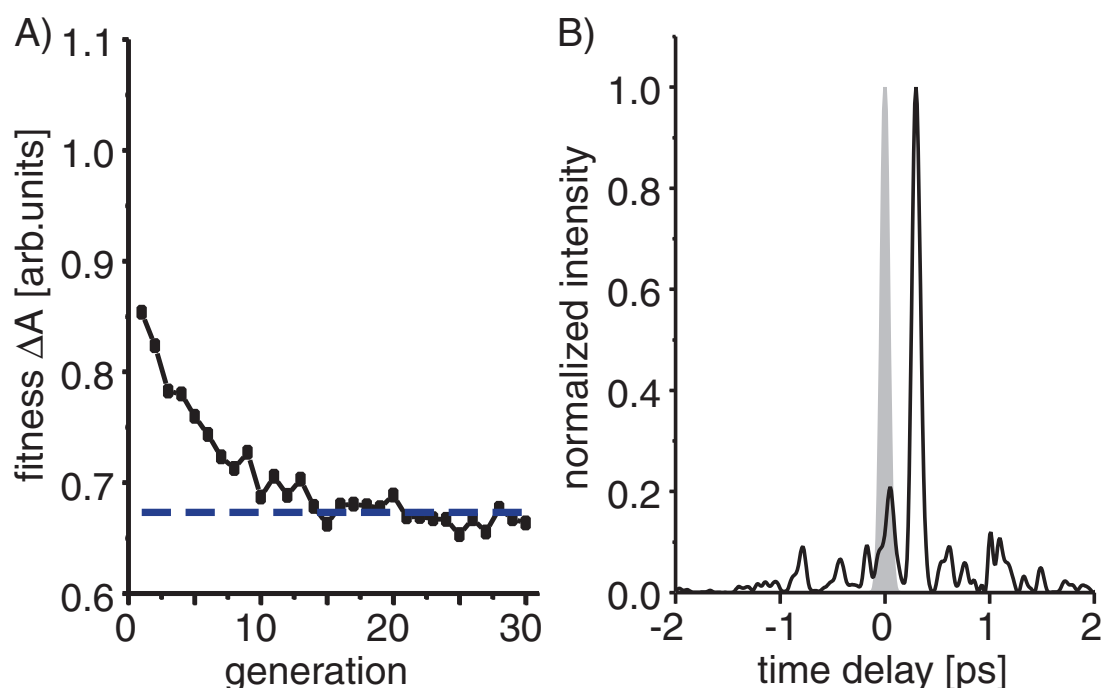


Figure 5.8: A) Evolution curve for optimizing the dumping effect. Each data point represents the average of the transient absorption signal (400 nm pump, 800 nm dump, 660 nm probe, 150 ps pump–probe delay) of the ten fittest individuals of one generation. The dashed line indicates the signal level of a bandwidth-limited pulse with a linear spectral phase of 200 fs. B) The resulting temporal intensity profile of the optimal pulse as calculated from the phase mask pattern, because self-referencing pulse characterization methods like FROG, SPIDER or MIIPS give no information about linear spectral phase, which is important in the experiment discussed here. The position of the pump pulse is indicated in gray.

phase is varied in addition to a linear phase offset of 200 fs. As can be seen from Figure 5.7C, the dumping yield is higher (and therewith the product absorption lower) for positive values than negative values of the third order spectral phase.

In the case of the third order phase, for negative values a part of the shaped-dump-pulse intensity is temporally shifted to times before the excitation by the pump pulse occurs. Therefore, it can not contribute to the dumping process. For positive values the temporal broadening results in a less effective dumping. Although third order phase leads to postpulses that arrive at times where dumping is still possible (see example in Figure 5.7D), the total effect of such pulses is still smaller than for an unmodulated pulse of same energy at 200 fs. However, these postpulses can contribute to the dumping process in contrast to prepulses that are more than 200 fs before the main pulse. This explains the asymmetry in the third-order spectral phase scan.

Now the effect of different dump pulse shapes with higher generality and flexibility

by using adaptive control is discussed. This concept is employed with the objective of minimizing the *13-cis* isomer yield as the fitness function in an evolutionary algorithm. All 128 pulse-shaper pixels are varied independently starting from a random distribution, and hence the algorithm is unbiased with respect to any expected wave-packet evolution. The fitness in dependence on generation number (Fig. 5.8A) shows that the evolutionary algorithm successfully finds pulse shapes that are better adapted to the control objective than the random pulse shapes of the first generation. The dashed horizontal line represents the level of the signal for a bandwidth-limited pulse with a linear spectral phase of 200 fs as inferred from Figure 5.7A.

The temporal intensity profile of the optimal pulse shape (Fig. 5.8B) is an almost transform-limited pulse whose maximum is shifted in time. The optimal delay for most efficient dumping is consistent with the linear spectral phase scan (Figure. 5.7A). One can conclude that best dumping results can be achieved by a short near-bandwidth-limited dump pulse at a delay time of about 200 fs after the excitation.

The experiment is repeated in a second base for the spectral phase, in which coefficients of a Taylor expansion of the spectral phase up to the order of four are used as individuals. Again a nearly bandwidth-limited pulse shifted by 200 fs was found to dump most efficiently.

The results from the optimal control experiment indicate that even for a complex molecular system like bacteriorhodopsin, the wave-packet dynamics can be fairly simple. The initial temporal width of the created excited-state wave packet is determined by the width of the pump pulse. During propagation on the  $S_1$  potential energy surface, the wave packet might get dispersed or even subdivided or further elongated if a barrier were present. The unmodulated dump pulse exhibits the same temporal width as the pump pulse. Thus, an appreciable change of the wave packet during the time between the pump and the dump pulse should affect the pulse shape found in an optimal control experiment. The corresponding dump pulse shape is rather simple and in comparison to Figure 5.7A, the dumping yield does not significantly exceed the values of the linear phase scan. It can be concluded that the wave packet remains basically unchanged until it reaches the Franck-Condon region where most effective dumping is possible with the 800 nm pulses. Using pulses in other wavelength regions and of shorter duration promises to gain additional insight into the molecular dynamics.

In summary, a quantum control pump–dump–probe scheme was demonstrated in which the dump pulse is additionally phase-shaped. In contrast to other approaches in which the initial excitation field is modulated, the concept presented here enables one to manipulate the dynamics at a later time when the decisive step for the reaction under study actually occurs, for example near conical intersections. This opens the possibility to control photochemical reactions more efficiently.

Specifically, the *trans-cis* isomerization reaction of retinal in bacteriorhodopsin was controlled with this pump–shaped-dump approach. The resulting optimal dump pulse

structure for this complex system is surprisingly simple and leads to the qualitative conclusion that the excited-state wave packet is still quite compact in the dumping region. In general, the technique demonstrated here provides a handle on the control of complex systems with a broad spectral distribution of transitions, but it also allows retrieving information on the shape and evolution of excited-state wave packets and underlying potential energy surfaces.

### 5.2.3 The pump–dump–repump–probe scheme

In different theoretical publications on the control of the isomerization efficiency, pump-dump-repump-probe schemes were proposed to have the capability to even increase the isomerization yield [98, 228]. The principle has been already been sketched in Subsection 3.4 and has been theoretically demonstrated for exactly the system, which is of interest here [228]. Briefly, the pump pulse creates a wave packet on the first excited potential energy surface. This wave packet is then dumped to the ground state with a energy close to the top of the potential barrier that separates the two isomers. Therefore, to a certain time a non-negligible part of the wave packet can be in the product isomer region. There, it can be transferred to the target state by a rapid repump-dump process, which can in principle be realized with a single pulse of sufficient broad spectrum by intrapulse dumping. In the following this pump-dump-repump sequence is tested systematically by employing colored-double pulses after the excitation step.

Colored double pulses can be produced by applying a linear phase to a certain part of the spectrum according to (see also Section 1.9):

$$\phi(\omega) = \text{UnitStep}(\pm(\omega - (\omega_0 - \delta\omega))) \cdot \Delta S \cdot (\omega - (\omega_0 - \delta\omega)) \quad (5.1)$$

In this equation  $\Delta S$  is the spectral phase slope. In contrast to the expression for the double-pulse generation in Section 1.9, this time the spectral phase slope is the pulse separation and not only half the value. To differentiate between these two cases the letter  $S$  chosen.  $\omega_0 - \delta\omega$  is the breakpoint frequency, at which the transition from the unshifted to the shifted part of the spectrum occurs.  $\text{UnitStep}(x)$  is the step function with 0 for  $x < 0$  and 1 for  $x \geq 0$ . The positive argument within the  $\text{UnitStep}$ -function results in the shift of the blue part of the spectrum, while a negative argument shifts the red part. The other part's spectral phase is set to a constant value of  $0^\circ$ . Therefore this part remains unshifted. Measuring the system's response for such double pulse shapes, whose relative amplitude and pulse separation is systematically varied, results in a fitness landscape. This fitness landscape can provide information about the molecular reaction dynamics and in the present case information about the sensitivity of the isomerization reaction of retinal in bacteriorhodopsin to pump–dump–repump control mechanisms.



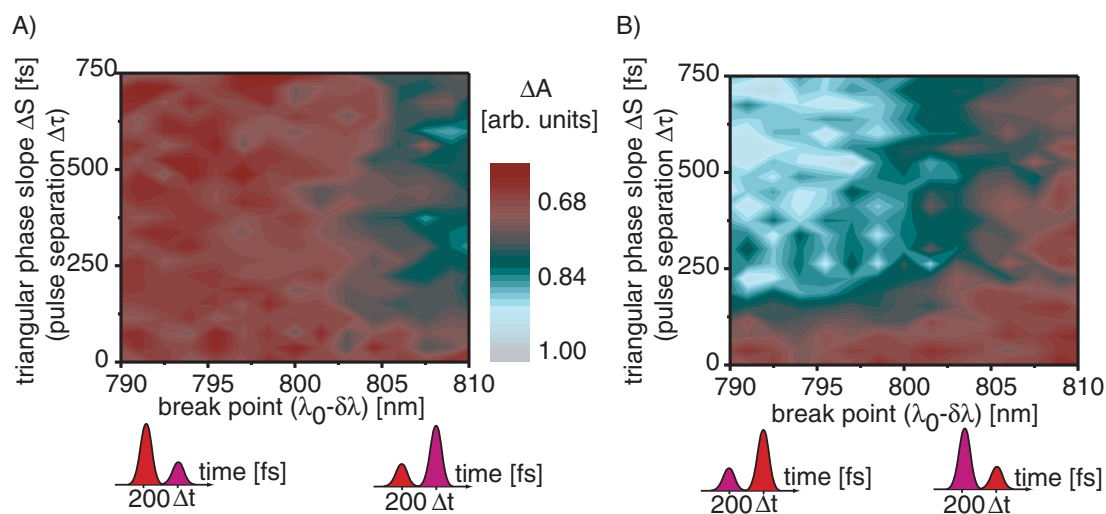


Figure 5.9: A) and B) show the change of the product isomer yield as transient signal at 660 nm at a delay time 150 ps for different colored double pulses. The breakpoint wavelength controls the spectral width of the individual pulses and the phase slope the temporal distance. In A), the red part of the spectrum is fixed at 200 fs after the pump pulse and the blue part is further delayed while the situation in B) is vice versa, as indicated in the sketches underneath the data plots.

Figure 5.9 shows the outcome for these two cases in dependence on different breakpoint wavelengths and phase slopes. Additionally, again a linear spectral phase offset of 200 fs is applied. Also measurements without additional linear offset imposed onto the spectral phase have been performed. However, in both cases an increase of the isomerization yield compared to the case of no dump pulse could not be achieved.

As can be seen in Figure 5.9, most effective dumping can be achieved in the case that both pulses are centered at 200 fs after the pump-act. For breakpoint in a region, where the spectrum of the laser pulse has only a small amplitude, there will basically be only one very intense pulse. If the breakpoint moves to the central wavelength of the initial unshaped pulse, two pulses of the same height will be the result. In Figure 5.9A the red individual subpulse is fixed at 200 fs after the pump-pulse and the blue one is delayed. Most efficient dumping is achieved for breakpoints at about 790 nm which means that the unshifted pulse contains most of the available amplitude. For a breakpoint at 810 nm, only if both pulses overlap, efficient dumping occurs. Otherwise if the second more intensive pulse is delayed, the dumping yield rapidly drops. This situation is identical with the first order spectral phase scan in Figure 5.7A. In general from Figure 5.9 it can be seen, that a lower dumping yield is received when the breakpoint wavelength is chosen in such a way that the fixed pulse at 200 fs has only a small amplitude.

In contrast to the theoretical predictions, the product yield never rises over the value for the case of no shaped-dump pulse. Therefore it is tried to increase the product

yield by adaptively shaping the dump pulse with the control objective of maximal *13-cis* isomer yield. If more complicated pulse shapes such as a chirped repump pulse or triple pulses of different central wavelength are able to increase the product isomer yield, such a solution should be discovered by using adaptive femtosecond quantum control. However, the learning algorithm failed to find a pulse shape, that can enhance the product isomer yield and therewith the isomerization efficiency.

The results of the adaptive femtosecond quantum control experiments and the systematic scans using colored-double-pulse control-landscapes can be due to different reasons: It could be possible, that the spectrum of the shaped pulse pulse is not sufficient broad to fully realize the proposed pump-dump-repump for the system retinal in bacteriorhodopsin as discussed in the beginning of this Subsection. Another explanation can be given in agreement with the observations of an optimal control experiments, performed by the group of M. Motzkus for another biological system. There the maximization of the energy transfer in the light harvesting antenna complex LH2 failed as well. This can indicate that further improvement by shaped laser pulses of a reaction that has already been optimized by nature is not possible. [9].

### 5.3 Reducing the isomerization yield by shaping the excitation pulse

In the previous section, a novel scheme has been presented, in which the excited state wave packet is influenced close to the conical intersection. This can be understood as the experimental approach for actively controlling the evolution of the wave packet on the first excited surface (see Section 3.4). A different attempt is presented in this section, which is traditionally applied in most experimental optimal control experiments [6–8, 109, 2–5, 9]. This time, a wave packet shall be prepared in the Franck-Condon region by specifically designed pump laser pulses. In the given case, the excitation will occur to the third excited potential energy surface by irradiation with 400 nm light. The wave packet then evolves under the influence of the potential energy surfaces. As experimentally shown and already discussed previously, the non-radiative decay from the  $S_3$  to the  $S_1$  potential energy surface takes place in about 50 fs [283]. Therefore, the initial shape of the wave packet is crucial for the following processes. Since the bandwidth of the 400 nm shaped laser pulse is about 4 nm, an influence on the first excited surface by a dumping process, as demonstrated in the previous section, is not very likely to occur. However, excitation to higher-lying states is still possible.

The initial excitation to higher-lying states by the pump pulse can open up new possibilities for control mechanisms. Higher-lying states generally become more dense and thus the number of conical intersections increase. Excitation into this regime and shaping the wave packet can take advantage of this issue, since many different reaction pathways may now be available.

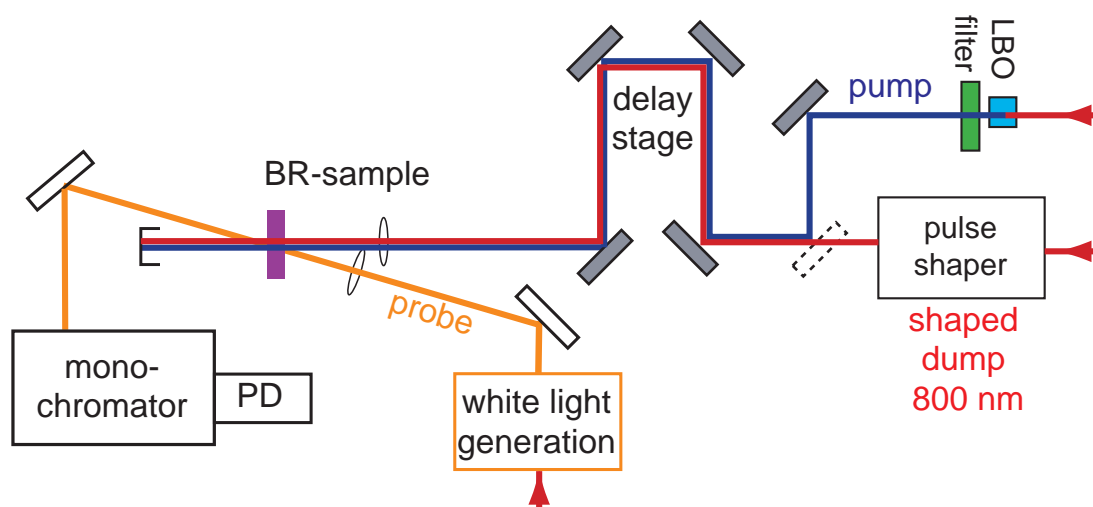


Figure 5.10: Sketch of the setup for controlling the isomerization dynamics in the case of the molecule bacteriorhodopsin by shaping the excitation pulse. The shaped 800 nm pump pulse is frequency doubled in a nonlinear crystal. By focusing a second 800 nm pulse into a sapphire plate, a white-light continuum is created which can be used for monitoring the dynamics. Pump and probe pulses are spatially overlapped in the bacteriorhodopsin sample. The probe pulse can be monitored at two different wavelengths simultaneously. With photodiode PD1 the pump energy of the pump beam before and with photodiode PD2 after passing the sample can be monitored.

## 5.4 Experimental details

The laser pulse from the femtosecond laser system is split into two fractions, one for the pump pulse and another one for the probe pulse. The pump pulse is phase-shaped and then frequency-doubled in a 400  $\mu\text{m}$  thin LBO crystal. Therefore the resulting pulses are shaped in both phase and amplitude (see Section 2.5). These pulses are focused by a 200 mm lens into the sample. The maximum energy of the shaped pump pulses is limited by a neutral density wheel to 500 nJ at the sample. In order to measure the absorption of the pump pulse by the sample, a small fraction of the pulse energy is directed before and after the sample into two identical photodiodes (PD). The output of the photodiodes is integrated by two BOXCAR integrators and recorded with an Analog to Digital Converter-card (ADC-card). The two signals are adjusted to have the same amplitude without sample. Before the experiment, the linearity of the photodiode-signal as a function of the pulse intensity over the used range was carefully checked.

The probe pulse is focused into a sapphire plate to generate a white-light continuum centered around 800 nm. The spectrally broadened pulse is focused by a 150 mm lens into the sample, where it spatially overlaps with the pump pulse. After passing the sample, different wavelengths can be selected out of the white-light continuum by two

monochromators. For this experiment, one monochromator is set to 660 nm, while the other monitors the signal at 850 nm. The delay between the two pulses can be modified by a computer-controlled delay stage. This setup is shown as a sketch in Figure 5.10.

## 5.5 Results and Discussion

The investigation of the possible change of the isomerization efficiency is the main interest of this section. Therefore it is necessary to monitor the educt and product channels. Since it is desired to investigate the isomerization yield, the product channel is the produced *13-cis* isomer. In principle there are two candidates for probing the amount of produced isomers, either by the amplitude of the absorption of the  $J_{625}$ -state or of the  $K_{590}$ -state (see Sections 3.3.2 and 5.1). Using the population of the  $J_{625}$ -state as a feedback-signal has two disadvantages compared to the population of the  $K_{590}$ -state: First, it is still under discussion whether the  $J_{625}$ -state is already the direct precursor of the photoproduct-isomer, in a sense that no backrelaxation on a fast time scale to the *all-trans* ground state can occur. And second, since the  $J_{625}$ -state decays in a few picoseconds, from the experimental side it is very difficult to use the signal as feedback.

The  $K_{590}$ -state which has been shown in various experiments to have a *13-cis* geometry, has a decay time of 2  $\mu$ s. Therefore the amount of produced *13-cis* -isomers can be easily monitored with the help of the  $K_{590}$ -state absorption after several tens of picoseconds. In contrast to the  $K_{590}$ -state absorption, most other signals decay on a time scale of a few picoseconds or less, except the bleach signal. The bleach signal itself arises from the missing ground state absorption due to the excited molecules that have not yet relaxed back. Therefore this component must have a contribution with a similar temporal behavior as the produced *13-cis* isomer.

At wavelengths larger than 660 nm a contribution of pump depletion to the resulting signal can be neglected, because nearly no ground state absorption arises at these wavelengths. In contrast, the absorption of the  $K_{590}$ -state is still very prominent at a wavelength of 660 nm [287]. Therefore, in order to monitor the amount of produced *13-cis* isomer, the transient absorption signal is recorded at a delay time of 30 ps and at a wavelength of 660 nm, where basically all other signals have a negligible contribution.

As a second signal it is necessary to either monitor the amount of initially excited *all-trans* molecules or the amount of molecules which directly relax back into the *all-trans* ground state. The last one turns out to be difficult to measure in the given case. In principle the pump depletion has at least two decay components. A fast one, originating from the molecules that directly repopulate the *all-trans* ground state and a slow one from those that first convert to the *13-cis* isomer. Unfortunately, the fast pump-depletion component which could serve as a good feedback signal, is always overlapped by other components within the wavelength range accessible by the used

setup. Therefore, it can not serve as a suitable feedback signal.

Another spectroscopic signal that yields the amount of excited molecules can be obtained by either monitoring the excited state absorption or the stimulated emission. The  $S_1$  excited state dynamics can in principle be monitored by a probe pulse around 460 nm [287]. Unfortunately because the white-light is generated with a 800 nm seed beam in a sapphire disc, transients can only be measured down to 480 nm at least. Therefore, the signal at a wavelength of 460 nm is not measurable by the used setup simultaneously with 660 nm signal.

The absorption of the hot molecules that have decayed to the  $S_1$  and can be monitored around 740 nm is still overlapped by other contributions such as the  $K_{590}$ -state absorption. Therefore it is difficult to interpret this signal, because both contributions are influenced by the modulated pulse in a contradictory manner.

The other possibility, the stimulated emission, is visible at wavelengths larger than 850 nm [283], with only a very small contribution of an additional absorption. This can in principle serve as a signal for the amount of initially excited molecules.

In this context, in the case that complex shaped pulses are used for excitation, one has to hold in mind that some of those previously mentioned spectroscopic signals do not necessarily monitor the amount of excited *all-trans* molecules. It is well thinkable that for example the excited state population is transferred by a specially shaped pump laser pulse via a non-fluorescent channel to the product state. In this case the stimulated emission would have a low value, although there could even be more molecules excited, compared to the case of unshaped pump pulses. A second problem arises in the case of complex shaped laser pulses. Since the stimulated emission is a rather short signal with a decay time of 700 fs to 800 fs [283] one has to carefully take into account the effect of the pulse shape onto the transient. This makes it difficult to use the signal as feedback in a closed loop experiment. Still it is very interesting to monitor the stimulated emission and compare it with the optimization result.

The amount of initially excited molecules is proportional to the absorption that the pump beam experiences by passing through the sample. Therefore, the pump energy can be monitored before and after passing the bacteriorhodopsin film. The difference of these two signals is the amount of absorbed pump light, and thus proportional to the amount of initially excited *all-trans* molecules and can very well serve as feedback signal.

Due to the modulation of the pump pulses in phase and amplitude, the difference of the pump pulse energy before and after the sample must be normalized to the pump pulse energy. The optimization goal is thus the ratio of the normalized amount of produced *13-cis* molecules to the normalized amount of initially excited *all-trans* molecules for the maximization and vice versa for the minimization. In this quotient the normalization is canceled, because both the numerator and the denominator is normalized by the same value.

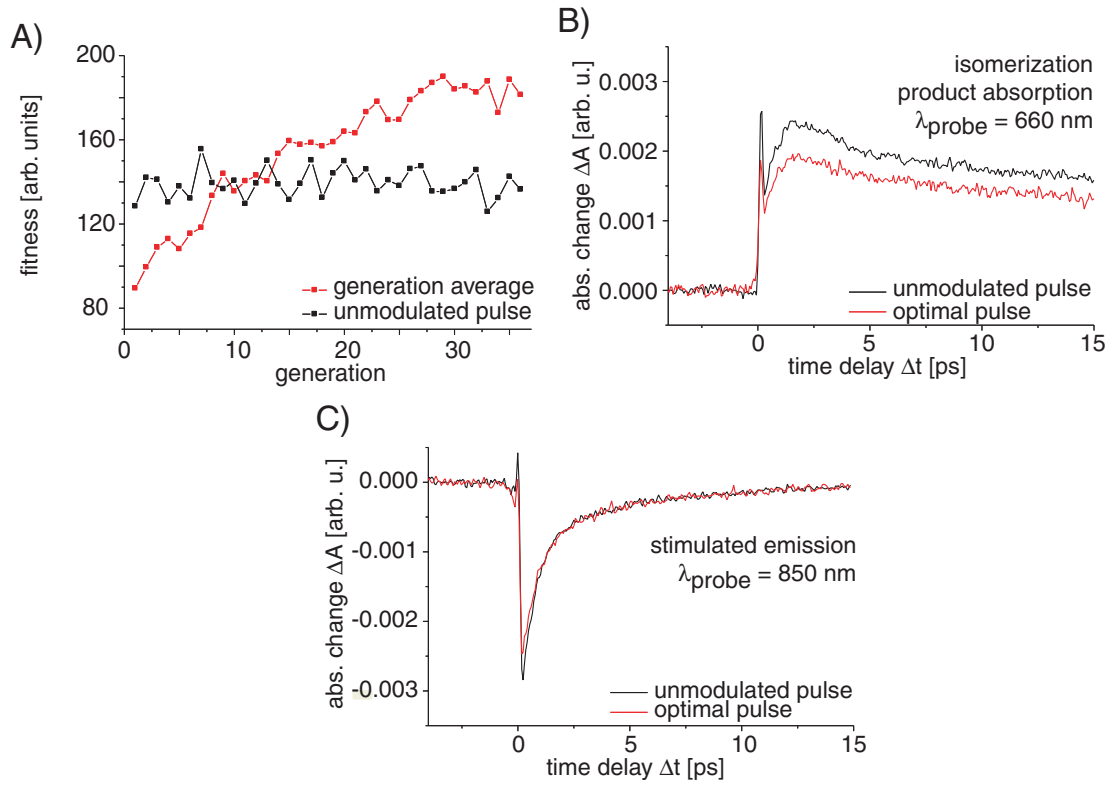


Figure 5.11: A) Optimization of the fitness as a function of the generation. Black denotes the unshaped reference pulse which is sent after each generation to monitor the laser stability. Red stands for the evolution of the optimally shaped pulses. Each point is the average of the signal of all individuals of a generation. Plot B) shows the transients at 660 nm and plot C) at 850 nm for the two cases of the optimal pulse shape (red) and an unshaped pulse (black) of the same pulse energy. As can be seen, the stimulated emission shown in C) is fairly identical in both cases, while the signal of the produced isomers at 660 nm is different in the case of the optimized pulse compared to the unmodulated pulse. The decay time for the stimulated emission is reported to be about 700 fs to 800 fs for unmodulated pulses [283].

$$\begin{aligned}
 \text{Fitness} &= \frac{\frac{\text{produced 13-cis isomers}}{\text{pulse energy}}}{\frac{\text{initially excited molecules}}{\text{pulse energy}}} \\
 &= \frac{\text{produced 13-cis isomers}}{\text{initially excited molecules}} \quad (5.2)
 \end{aligned}$$

The optimization curve is shown in Figure 5.11 as red line. Each point is the average of the signal of all individuals of a generation. The black line shows the signal for

an unmodulated pulse that is applied after each generation to monitor the stability of the system. As one can see, this reference signal does not vary significantly during the optimization. While a reduction of the isomerization efficiency could be achieved, no pulse shape could be found that enhances the isomerization efficiency. The explanation for this can again be that reaction, which are already optimized by nature, can not be further optimized with the help of shaped laser pulses.

Figure 5.11B and C show the transients at 660 nm and at 850 nm recorded for the case of the optimal pulse shape and an unshaped pulse of the same pulse energy. Although not intended, the optimized pulse additionally alters the excitation efficiency slightly. Thus, for better comparison both transients for the case of excitation with the optimized pulse are rescaled with the same parameter. This parameter is chosen in a way that the two transients at 850 nm for the case of unshaped and optimized pulse have nearly the same amplitude. As can be seen in Figure 5.11B the optimal pulse produces less *13-cis* isomers compared to the unshaped case. The absorption in the sample is the same for both excitation pulses. As discussed above, the transient at 850 nm shows a strong feature of stimulated emission. In contrast to the transient at 660 nm, the transients at 850 nm are very similar for both cases of optimized and unshaped pulses. The transient for the optimal pulse shows a slight change in its shape at the very beginning which is a consequence of the modulated pulse shape. Within the above mentioned limitations, the stimulated emission can be used to measure the amount of initially excited molecules. Although the unchanged amount of stimulated emission does not necessarily prove that the amount of excited molecules stays constant, this behavior is consistent with the result of the other presented method of measuring the amount of pump-absorption.

In general the measurements for a successful optimization took at least 12 hours and the XFROG setup for the pulse characterization did not remain aligned over this period of time. This prevented the measurement of reliable pulse shapes directly after the experiment, yet. Therefore a complete and final explanation for the mechanism that is responsible for the control of the isomerization reaction of the retinal molecule within the very complex biological system bacteriorhodopsin observed in the presented experiment cannot be given at the moment. The increased density of the higher-lying states to which the excitation takes place leads to a higher number of conical intersections and therefore to an increased number of possible reaction pathways. One of these pathways could have been selected with the optimal pulse in comparison to the pathway which is chosen, if the molecule gets excited by an unshaped laser pulse.

## 5.6 Conclusion

In the first part of this chapter an improved pump–dump–probe scheme in which the dump pulse is additionally phase-shaped, is presented. Several theoretical publications concerning the control of isomerization indicate that similar control schemes can have an influence on the isomerization efficiency, if time delays and frequencies are chosen

properly.

This scheme is employed to the very well investigated system of light-adapted bacteriorhodopsin which undergoes isomerization from the *all-trans* form to the *13-cis* form. The wavelength of the dump pulse was chosen to be centered at about 800 nm which bridges a gap where the first excited potential energy surface lies close to the ground state surface. The amount of produced *13-cis* isomers observable by absorption at a wavelength of 660 nm and a delay time of 150 ps was used as probe signal.

The influence on the product-isomer yield of different phase-functions applied to the dump pulse is systematically investigated including first, second and third order spectral phase. Second and third order spectral phase were imposed onto an additional linear phase offset to investigate the influence at the point of most effective dumping.

Because different theoretical publications predict an important role of a pump-dump-repump sequence on the isomerization process, the here presented scheme was further expanded to a pump-dump-repump-probe scheme [98, 228]. This pump-dump-repump-probe scheme is then applied to the molecule bacteriorhodopsin. Finally adaptive femtosecond quantum control was used to investigate the cases that are not covered in the previous schemes.

The experiments show that at an excitation wavelength of 400 nm and a dump wavelength of 800 nm, most effective dumping occurs with bandwidth-limited pulses at a delay time of 200 fs. The overall results could be interpreted in the two-states many-modes model given in [227]. The pump-shaped-dump-probe scheme allows control of molecular systems away from the initial Franck-Condon window in those regions of the potential-energy landscape where the decisive reaction step occurs, and it additionally provides information on wave-packet evolution.

In the second part, the control of isomerization efficiency of bacteriorhodopsin was investigated by directly shaping the excitation pulse. It has been shown that it is possible to reduce the isomerization efficiency, while it was not possible to find a pulse shape that can enhance it. Of course, this is not necessarily a proof that it cannot be achieved by optimal control. A similar situation has turned out in the case of LH2, where it was also only possible to reduce the energy transfer by optimal shaped laser pulses [9]. This could indicate, that these two systems, being relevant in nature, are already optimized to the best and no further enhancement can be achieved by shaping the exciting electric field.

The experiments that are presented in this chapter demonstrate that optimal control by adaptive femtosecond quantum control is also applicable in cases of complex molecular rearrangement reactions in the case of large biological molecules.



## Chapter 6

# Analysis of femtosecond quantum control mechanisms with double pulses

In many cases it is quite difficult to extract the control mechanism of a pulse shape obtained in an optimal control experiment. Approaches, such as for example using different basis sets for closed loop optimizations, need a high number of successful optimizations [139–141]. When measuring the dynamics of complex systems a signal with a good signal-to-noise ratio is often very difficult to obtain. Therefore a sufficient high number of different optimizations to carefully investigate the control mechanism is often not possible.

As already introduced in Section 1.9, investigating the systems's response on parameterized pulse shapes can provide an alternative solution to this problem and produce very informative fitness landscapes. As shown in many experiments and by several theoretical calculations pump-dump or pump-repump schemes can often influence the dynamics significantly (see Section 5.2). To be sensitive to the molecular dynamics for a given case, different parameters concerning the pump and the dump pulses have to be optimized. These are for example the time delay between the pulses, the central wavelengths, the amplitudes and the difference of the absolute phase of the individual pulses [87, 95, 110, 117, 279, 280].

The theory for generating double pulses has been developed in Section 1.9. The double pulses can be controlled by three parameters: the phase slope  $\frac{\Delta\tau}{2}$  controls the pulse separation which has the value  $\Delta\tau$ . With the parameter spectral breakpoint  $\lambda_0 - \delta\lambda$ , the amplitude ratio of the two individual pulses can be varied. Finally, the height of a phase step  $A$  influences the absolute phase difference between the individual pulses of the double pulse.

In this chapter the presented scheme is experimentally characterized and then tested in a second-harmonic experiment. These frequency-doubled pulse shapes are especially interesting, because with pulses in this wavelength region photochemically interesting and relevant reactions can be addressed. Therefore in the second part, effects of such frequency-doubled double-pulses in a chemically relevant system are investi-

gated experimentally and compared with theoretical simulations.

In the next part of this chapter, the capability of the presented parameter-scan scheme to investigate control mechanisms is demonstrated in a prototype experiment. There, the third harmonic yield from a setup that forces double pulses to be the optimal solution is adaptively optimized. This experiment has the advantage, that effect of the different pulse shapes can be intuitively understood and mathematically calculated. The comparison of the adaptively determined pulse shape with the information from the double-pulse fitness-landscape helps to understand the control mechanism.

In the last part of this chapter the dependence of the excitation efficiency (i.e. the dependence of the amount of excited molecules on different pulse shapes in relation to their pulse energy) of the solvated dye molecule IR140 on selected pulse shapes in two parameterizations is investigated by using transient absorption spectroscopy. The results show that very different pulse profiles can be equivalently adequate to maximize a control objective. Only to mention at this point, another very interesting application can be found in Section 5.2 of the previous chapter. There, the method of double-pulse generation has been used to investigate complex pump-dump-*repump*-probe schemes.

## 6.1 Characterization of the double-pulse generation method

The generation of double pulses has been introduced in detail in Section 1.9. Different calculated examples are presented in that section as well as in Appendix A.5. Because of the experimental importance, double pulses are often desired at wavelengths in the UV regime. Pulses with a central wavelength around 400 nm can be easily obtained by frequency-doubling of the 800 nm pulses, which are provided by Ti:sapphire laser systems. Frequency doubling of 800 nm double pulses will generally produce double pulses centered at 400 nm. As discussed in Section 1.9 and Appendix A.5, the frequency doubling process will effect the spectrum of the pulse shapes whose shape can differ significantly from the shape of the 800 nm spectrum.

The double pulses can be verified by using the pulse characterization method XFROG which is introduced in Section 2.6.2. Two representative examples are shown in Figure 6.1 for a pulse separation of 1000 fs, a breakpoint  $\lambda_0 - \delta\lambda$  that coincides with the central wavelength of the unshaped pulse and a phase step  $A = 0$ . The difference in the two figures A and B lies in the sign of the phase slope  $|\frac{\Delta\tau}{2}|$ . Clearly the two individual pulses can be seen in both figures. Also very well visible is the fact, that the individual pulses have different central wavelengths. By comparing the two figures, the effect of the different signs of the triangular phase slope is observable. In the case for  $\frac{\Delta\tau}{2} = 500$  fs, the pulse which has a more red-shifted central wavelength comes earlier in time and the blue-shifted one arrives later. In the case for  $\frac{\Delta\tau}{2} = -500$  fs the situation is the opposite. Because of the curvature of the potential energy surfaces, this can be of crucial importance for influencing molecular dynamics with such double pulses as

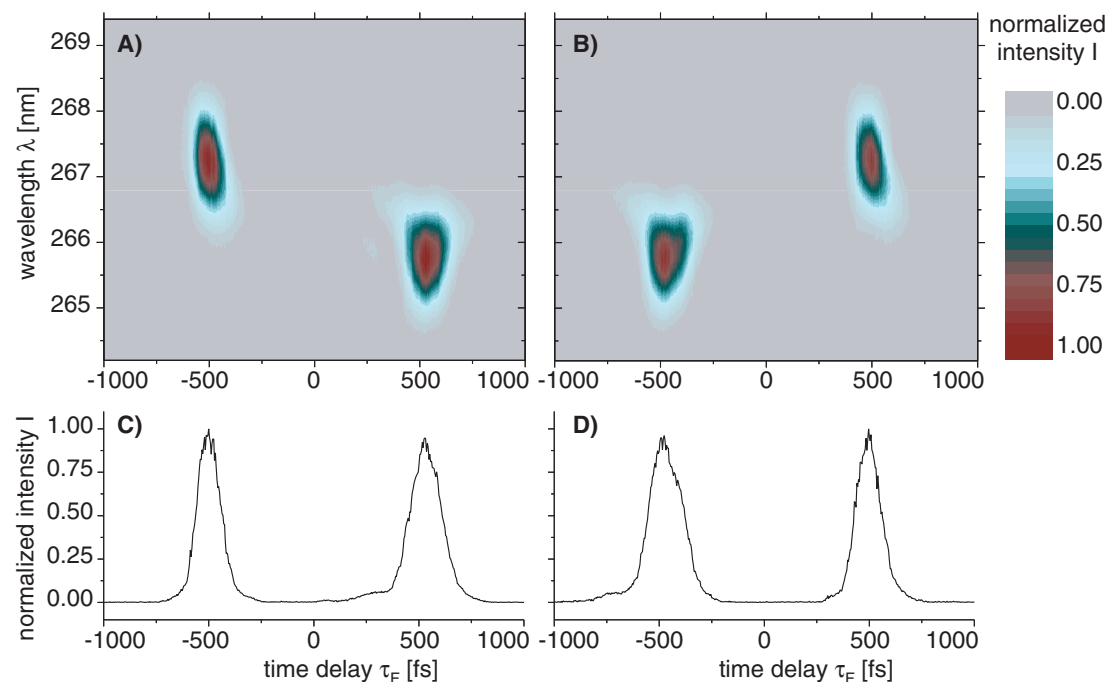


Figure 6.1: XFROG traces for two different sets of double-pulse parameters. The central wavelength is 800 nm of the unshaped pulse and coincides with the spectral breakpoint  $\lambda_0 - \delta\lambda$ . The phase step  $A$  is equal zero. The difference between the plot A) and B) is the value of the triangular phase slope  $\frac{\Delta\tau}{2}$  which is in the first case 500 fs and in the second case -500 fs. These plots show very nicely that, in the case for  $\frac{\Delta\tau}{2} = 500$  fs, the pulse that has a more red-shifted central wavelength comes earlier in time and the blue-shifted arrives pulse later. In the case for  $\frac{\Delta\tau}{2} = -500$  fs the situation is the opposite. Plots C) and D) shows the cross-correlation of the two pulses used shown in plots A) and B) respectively. In these cross-correlation plots, it can be clearly seen that the spectral information is lost in comparison to the XFROG-traces.

shown by C. V. Shank and Coworkers [275] and as can be seen in the experiments later on.

Figures 6.1C and D show the cross-correlation of the pulses, visualized in the XFROG-traces in A and B. The spectral information can not be gained from these cross-correlation traces. One can only determine that a double pulse has been created, because only the temporal behaviour of the pulse can be measured by a cross-correlation. Therefore for a complete characterization, methods like XFROG are required.

Second harmonic generation is very well understood and can be theoretically simulated. Therefore the intensity after frequency-doubling in a suitable crystal is a very good candidate for the demonstration and characterization of a double-pulse parameter scan.

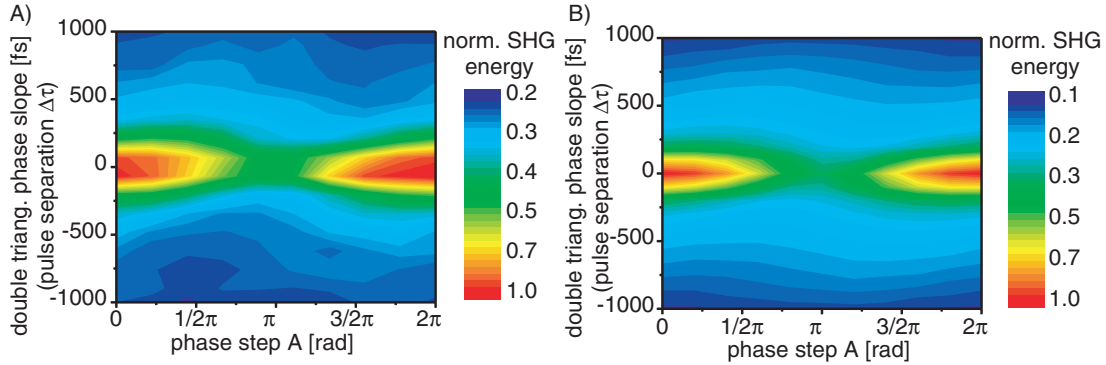


Figure 6.2: This contour plot shows the signal of the second harmonic of the shaped pulse after frequency-doubling in a  $400 \mu\text{m}$  thin nonlinear crystal. The signal is normalized to its maximum value. The spectral phase step  $A$  is scanned from  $0$  to  $2\pi$  and the double triangular phase step  $\frac{\Delta\tau}{2}$  from  $-1000$  fs to  $1000$  fs which results in pulse separation of up to  $1000$  fs. For positive values of  $\frac{\Delta\tau}{2}$ , the spectrally red-shifted pulse precedes the blue-shifted pulse in time and for negative values vice versa. The break-point  $\lambda_0 - \delta\lambda$  is fixed at the central wavelength of the unshaped pulse ( $800$  nm). Plot A) shows the experimental measurement and plot B) the result of a simulation.

The setup for this experiment is quite simple. The  $800$  nm pulse from the laser system is spectrally shaped and then frequency-doubled in  $400 \mu\text{m}$  thin LBO crystal. The  $800$  nm light is blocked by a filter that is transparent at  $400$  nm. The pulse energy of the  $400$  nm beam is then recorded by a photodiode.

Figure 6.2A shows the pulse energy of the second harmonic in dependence of the phase step  $A$  and the triangular phase slope  $\frac{\Delta\tau}{2}$ , for a fixed breakpoint at the central frequency. The phase step  $A$  is varied from  $0$  to  $2\pi$  and the double triangular phase slope from  $-1000$  fs to  $1000$  fs. For pulses with a relatively large temporal separation, the variation of the parameter  $A$  should not affect the temporal pulse profile. In contrast, as shown in Section 1.9, if the triangular phase slope  $\frac{\Delta\tau}{2}$  is equal to zero but the phase step  $A$  has a value between  $0$  and  $2\pi$ , the temporal pulse profile exhibits a certain modulation (see Section 1.9). For example in the case that  $A$  has the value  $\pi$ , this results in a double pulse structure, too.

These two extreme cases can be easily understood. The pulse shape in between these two extremes can be thought as mixtures of the extreme cases. To visualize the effect of the pulse shapes in between the two extreme cases, for comparison in Figure 6.2B the simulated double-pulse trace is shown, using the theory described in Section 1.9. These plots demonstrate that the experiments agree very well with the theory.

As shown in Section 1.9, the amplitude ratio of the individual pulses can be varied by the parameter  $\lambda_0 - \delta\lambda$ . Because the second harmonic yield is quadratic with the pulse amplitude, double pulses of equal height have the lowest second harmonic yield. This behaviour can be very well seen from Figure 6.3A (experiment) and B (theory).

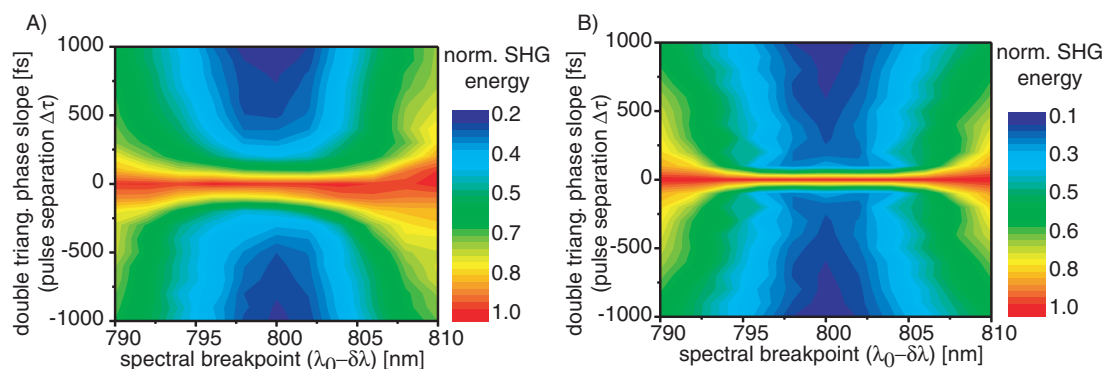


Figure 6.3: This contour plot shows the signal of the second harmonic of the shaped pulse by frequency-doubling in a  $400 \mu\text{m}$  thin nonlinear crystal. The signal is normalized to its maximum value. The breakpoint  $\lambda_0 - \delta\lambda$  is scanned from 790 nm to 810 nm and the double triangular phase step  $\frac{\Delta\tau}{2}$  from -1000 fs to 1000 fs which results in pulse separation of up to 1000 fs. For positive values of  $\frac{\Delta\tau}{2}$ , the spectrally red-shifted pulse precedes the blue-shifted one in time and for negative values vice versa. The spectral phase step  $A$  is fixed to zero. Plot A) shows the experimental measurement and plot B) the result of a simulation.

In these plots the spectral breakpoint  $\lambda_0 - \delta\lambda$  is varied from 790 nm to 810 nm, while the central wavelength is 800 nm. Again the double triangular phase slope starts at -1000 fs and ends at 1000 fs. Both the experimental trace and the theoretical trace coincide well with each other.

These different examples show that in the presented regime, the desired double pulses can be efficiently generated. Especially for higher values of the triangular phase slope, what results in a bigger pulse separation, the number of unwanted artifacts due to the pulse shaper setup increases. Therefore, this regime is not suitable for double pulse generation when using a 128 pixel spatial light modulator (for example double pulses with a pulse separation of  $\Delta\tau > 2 \text{ ps}$  cause very substantial pulse copies).

## 6.2 The effect of spectral modulation on the fluorescence efficiency of NK88

A very frequently investigated problem is the optimization of the fluorescence yield which is often a consequence of an optimized excitation efficiency [6, 143, 144]. Using for example different shaped laser pulses, the amount of excited molecules can be varied. This can then influence other signals, such as for example the fluorescence yield. Here, the fluorescence yield of the molecule NK88 will be investigated using a systematic double-pulse scan and comparing the result with a simulation. For excitation light at a central wavelength of 400 nm is used for excitation.

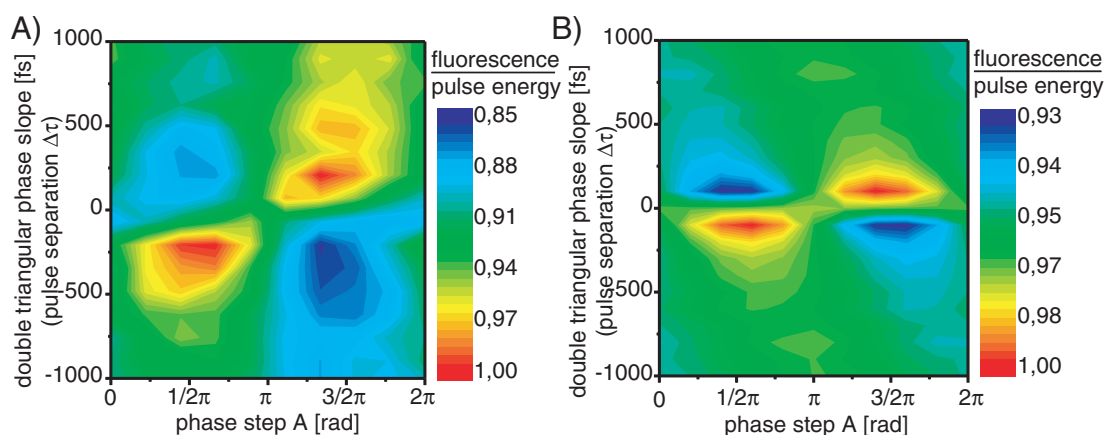


Figure 6.4: Contour plot of fluorescence yield of NK88 dissolved in methanol in relation to the pulse energy for different double-pulse parameters. The signal is normalized to its maximum value. The phase step  $A$  is varied from  $0$  to  $2\pi$  and the double triangular phase slope  $\frac{\Delta\tau}{2}$  is scanned from  $-1000$  fs to  $1000$  fs. For positive values of  $\frac{\Delta\tau}{2}$ , the spectrally red-shifted pulse come in time before the blue-shifted and for negative values vice versa. The spectral breakpoint  $\lambda_0 - \delta\lambda$  is identical to the central wavelength of the unshaped laser pulse. Plot A shows the experimental result and plot B the simulation including the influence of the modulated spectrum with respect to the molecular absorption spectrum.

The complex isomerization behaviour of the molecule NK88 dissolved in methanol has been discussed in Chapters 3 and 4. This section will deal with the optimization of the fluorescence yield of this molecule. While the pure fluorescence signal can be measured sensitively with respect to the wavelength, no temporal information can be gained from such an experiment. However, of course the excitation step with shaped femtosecond laser pulses still is sensitive to the short time dynamics.

The fluorescence optimizations in Section 4.6 have already shown that optimized pulse shapes can be found by adaptive femtosecond quantum control which enhance the fluorescence yield in relation to the pulse energy by a factor of two. Therefore, it is interesting to investigate this problem by using a double-pulse parameter scan.

The setup for this experiment is similar to the one used for the optimization in Section 4.6. Briefly, the spectrally shaped  $800$  nm pulse is frequency-doubled in a  $400 \mu\text{m}$  thin LBO crystal and then focused into a flow cell containing the molecule NK88 dissolved in methanol. The fluorescence is collected under an angle of about  $30^\circ$  with respect to the pump pulse and recorded by a photodiode. Pump stray light is suppressed by using a  $500(\pm 20)$  nm bandpass filter. The pulse energy is measured by using a second photodiode that registers a small fraction of the frequency-doubled pump pulse that is split off before the pump pulse is focused into the flow cell. Because the shaped and frequency-doubled pulses have different intensities, this will naturally directly result in different fluorescence yields. To account for this trivial effect, in the

following, the ratio of the fluorescence yield and the pulse energy is used to explain the experiments [8].

The ratio of the fluorescence yield and the pulse energy for a double-pulse parameter scan is shown in Figure 6.4A. There the triangular phase slope  $\frac{\Delta\tau}{2}$  and the phase step  $A$  is varied. The spectral breakpoint  $\lambda_0 - \delta\lambda$  is identical to the central wavelength of the unshaped fundamental pulse. The double triangular phase slope is varied from -1000 fs to 1000 fs, resulting in double pulses with a spacing of up to 1000 fs. The phase step  $A$  is varied from 0 to  $2\pi$ .

In dependence on these parameters, the ratio of the fluorescence to the pulse energy varies about 15% and shows a characteristic chessboard-like pattern. The ratio is much lower than the one obtained in the optimal control optimizations, in which all pixels of the liquid-crystal display are independently optimized. Obviously, the double-pulse parameterization can influence the fluorescence efficiency, but does not seem to provide a main mechanism for producing an optimal fluorescence signal. Nevertheless, it is interesting to understand how the observed change of the fluorescence is connected with the different double-pulse parameters.

To answer this question, additional simulations are performed. The influence of the modulated spectrum of the generated pulses with respect to the absorption spectrum of the molecule is investigated in this simulation. As demonstrated in Section 1.9, the spectrum of the frequency-doubled double pulses has not the same shape as the spectrum of the fundamental pulse. To understand the molecular answer visible in Figure 6.4A, several representative pulse shapes have been calculated and presented in Appendix A.5. As can be seen for the case of negative values for triangular phase slope and for a phase step of  $A = \frac{\pi}{2}$ , most of the intensity is shifted to the red side of the spectrum. For positive values of the triangular phase slope, the behaviour is the opposite.

The absorption spectrum of the molecule NK88 dissolved in methanol is shown in Figure 4.1. As can be seen, in the area which is covered by the laser spectrum, the absorption spectrum increases from blue wavelengths to red wavelengths. Therefore pulses, whose spectrum is red-shifted will result in a higher excitation yield compared to blue-shifted pulses. Carried forward to the given problems, double pulses with a negative value of the triangular phase slope at a phase step of  $A = \frac{\pi}{2}$  can be expected to excite more molecules than for the case of a positive value for the triangular phase slope. This will also directly effect the yield of the fluorescence which can be expected to be higher for the case of negative triangular phase slopes and a phase step of  $A = \frac{\pi}{2}$  and vice versa for pulses of positive triangular phase slopes at the same phase step value.

This behavior is also qualitatively expressed in the simulation shown in Figure 6.4B. This simulation can reproduce the chessboard-like structure of the experimental trace shown in Figure 6.4A. Features that differ significantly from the simulated trace would be caused by effects that do not result from changing the excitation efficiency by shifting the spectrum. This example shows that the control effect of a complicated pulse structure can be caused by rather simple effects. Because the optimal pulse shape from

the adaptive fluorescence optimization is much more effective, other mechanisms than those discussed here are more likely to play a major role.

## 6.3 Adequacy of fitness landscapes for interpretation of control mechanisms

In this section, the capability of colored double pulse fitness landscapes to illuminate adaptively determined optimal pulse shapes shall be demonstrated. For this, an experiment is built in which on the one hand a double pulse best fulfills the control objective and where on the other hand the effect of different pulse shapes can be intuitively understood and mathematically calculated. The yield of third harmonic generation (THG) from a specially designed setup is chosen as control objective.

### 6.3.1 Details of the experimental setup

The standard method to produce the third harmonic (267 nm) of the fundamental (800 nm) laser pulse is given by first frequency-doubling the 800 nm pulse (second harmonic generation, SHG) in a SHG crystal (BBO: beta barium borate, thickness: 100  $\mu\text{m}$ ,  $\phi=29.2^\circ$ ) and consecutive sum-frequency mixing (SFM) of the second harmonic (400 nm) with the fundamental 800 nm pulse again (see Fig. 6.5A) in a THG crystal (BBO, 300  $\mu\text{m}$ ,  $\phi=44.3^\circ$ ). Such a setup is generally called “tripler”. In order to obtain a high conversion efficiency, a good temporal overlap has to be ensured. If the temporal overlap and/or all crystal angles are not perfectly set, a bandwidth-limited pulse will not produce the highest yield. In contrast, for a temporal delay between 800 nm and 400 nm beams, double pulses will be the best solution (see Fig. 6.5B). If the optical path of the 800 nm beam is made slightly shorter than necessary, so that the 800 nm pulse arrives 450 fs earlier at the THG crystal than the 400 nm pulse, nearly no 267 nm yield can be measured for unshaped pulses. An evolutionary algorithm controlling the pulse shaper and using the THG signal as a feedback should find optimal pulses which show a clear double-pulse structure.

### 6.3.2 Results and Discussion

First, the optimal pulse for producing the highest third harmonic yield is determined for a tripler setup in which the temporal overlap in the THG crystal is slightly detuned (see Fig. 6.5). Fig. 6.6A shows the evolution curve for the optimization. Clearly, the algorithm finds a laser pulse shape that is much better adapted to the given problem than the randomly shaped laser pulses from the first generation of the evolution. Unshaped laser pulses do produce nearly no third harmonic in comparison to the optimally



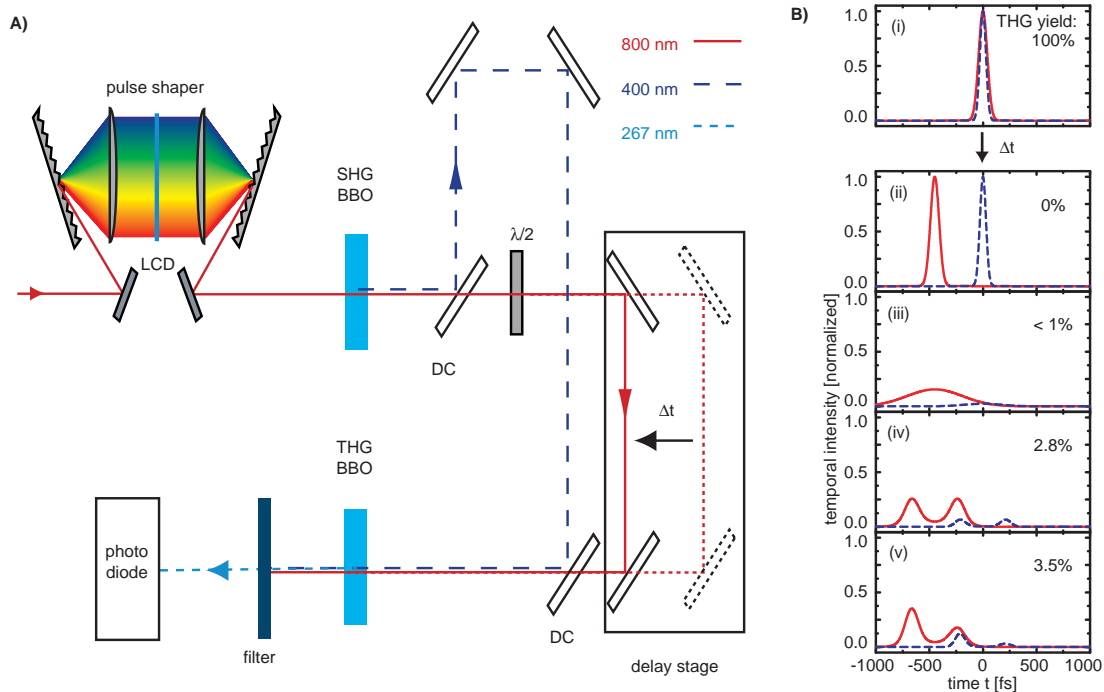


Figure 6.5: A) Setup for an experiment in which a double pulse results in the highest third harmonic yield. It is based on a standard design for THG (generally called “tripler”). The 800 nm laser beam coming from the pulse shaper is frequency-doubled in a SHG crystal. Second harmonic (400 nm) and fundamental (800 nm) are separated by a dichroitic mirror (DC). The 800 nm pulse passes over a delay stage (dotted red line) and is temporally and spatially overlapped with the 400 nm pulse in a THG crystal. The  $\lambda/2$  waveplate ensures the correct polarization of the beam. When a temporal delay is introduced (indicated by the delay stage moved to the left, so that the unshaped 800 nm pulse is  $\Delta t$  ahead of the 400 nm pulse at the THG crystal), there will be less temporal overlap in the THG crystal, and thus, less third harmonic (267 nm) radiation. However, with the pulse shaper it is possible to generate laser pulses whose shapes are adapted to the additional temporal delay, so that 267 nm production is increased. B) Sketch of the temporal intensity profiles revealing the influence of the pulse shape on the THG. In the case of temporal overlap ( $\Delta t = 0$  fs), the THG yield is maximal. When a temporal delay  $\Delta t$  (here: 450 fs) between the 800 nm (red) and the 400 nm (blue) beam is introduced, unshaped laser pulses will not create any 267 nm light (ii). Chirping the initial 800 nm pulse, and thus elongating it, improves the overlap between the 800 nm and 400 nm pulses in the THG crystal, but only little 267 nm light is produced (iii). A double pulse with a pulse separation of 450 fs where the energy is spread equally over the two subpulses yields more 267 nm light (iv). A double pulse where the first subpulse has twice the peak intensity of the second subpulse leads to even more 267 nm light. The asymmetry accounts for the nonlinear SHG process (v).

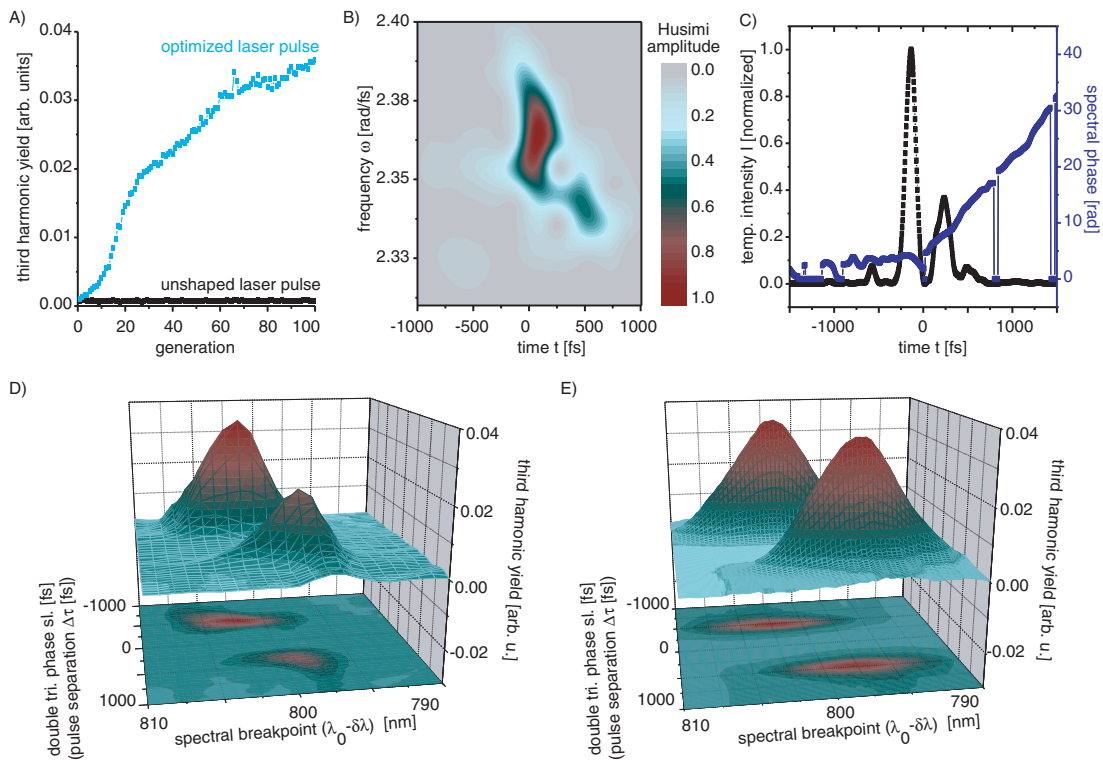


Figure 6.6: A) Evolution curve for optimizing the THG yield of a detuned tripler with a time delay of 450 fs between 800 nm and 400 nm pulses. Blue (grey) line: Each data point is the average of the ten best individuals of one generation. Black line: reference signal of an unshaped laser pulse. Clearly the learning algorithm successfully finds a pulse shape that can produce a higher third harmonic yield than the initial randomly shaped laser pulses or unshaped laser pulses. B) Husimi representation of the optimal pulse shape for the third harmonic optimization calculated from the phase pattern of the LCD and the measured pulse spectrum. The first individual pulse has significantly more amplitude than the second one and is blue-shifted. C) Temporal intensity and phase as derived from an SHG-FROG measurement. As expected due to the sketch in Fig. 6.5B, a double-pulse-like feature is visible. D) 3D representation of the measured colored double pulse fitness landscape of third harmonic generation by the modified tripler design. E) Calculated third harmonic yield. The differences in the calculated and measured fitness landscapes are due to experimental imperfections (especially slight misalignments of the phase-matching angles of the used crystals).

shaped laser pulses (see Fig. 6.6A).

In Figure 6.6B, the optimal pulse shape is shown as Husimi representation calculated from the phase pattern of the liquid crystal display and the measured pulse spectrum. The parameters of the smoothing Gaussian are chosen to be symmetric in both axes and fulfill the uncertainty principle. Figure 6.6C visualizes the temporal intensity

and phase measured by SHG-FROG (frequency resolved optical gating) [176]. In both figures, additional features such as slight pre- and post-pulses are visible as well.

To explain these observations, a colored double-pulse fitness landscape of the third harmonic yield for this particular control objective is measured. This fitness landscape is shown in Figure 6.6D, where two regions for a high third harmonic yield can be identified. One local maximum for a double triangular phase slope of +450 fs (double pulse with 450 fs pulse separation and the red shifted pulse comes first) and a spectral breakpoint of  $\approx 799$  nm (the red pulse has a higher intensity than the blue one). The second and larger maximum in the fitness landscape of Figure 6.6D is at a double triangular phase slope of -450 fs (double pulses with 450 fs pulse separation and the blue-shifted laser pulse precedes the red-shifted one) and a spectral breakpoint of  $\approx 802$  nm (thus, the blue-shifted laser pulse has a higher intensity than the red-shifted one). The pulse shape responsible for the global maximum as well as the corresponding value of the 267 nm yield are very similar to the pulse shape and the 267 nm yield found by adaptive femtosecond quantum control. However, it is possible that the algorithm would have found an even higher fitness value at a later generation than tested.

Figure 6.6E shows the calculated fitness landscape for an ideal case, where no misalignments are present, such as deviation of the phase matching angles of the nonlinear crystals from the ideal value. The effects of the pixellation of the liquid crystal display are included in the simulations. The simulated fitness landscape is very similar to the measured landscape except that the two maxima are of equal height and slightly different shape. This suggests that it is necessary to have a double pulse, with the first pulse having a higher amplitude than the second.

This calculated and measured results are intuitively understandable. The SHG is a second order process, while the subsequent SFM is only linear in the 800 nm pulse. Therefore, it is advantageous to invest a lot of intensity in the initial second order step of SHG (i.e. to produce a 400 nm double pulse with an intense first subpulse), and then to mix this intense first 400 nm subpulse with the second 800 nm subpulse at the optimal temporal delay (see Figure 6.5B). The reason for the experimental measurement having two maxima of different height can be explained by phase-matching imperfections. Therefore certain central frequencies for the individual pulses are better adapted to the given configuration.

On the basis of this knowledge, one can easily understand the optimal pulse shape derived from the adaptive femtosecond quantum control experiment. The determined pulse separation in Figure 6.6C matches the pulse separation giving the highest yield in the parameter scan of Figure 6.6D. Just like there, the maximum is achieved with a double pulse whose first subpulse has a higher peak intensity compared to the second one. Also, the first subpulse consists of higher frequencies than the second one, in accordance with the parameter scan. Additional small peaks can be explained as slight adaptations to the given experimental situation or as features not yet smoothed by the

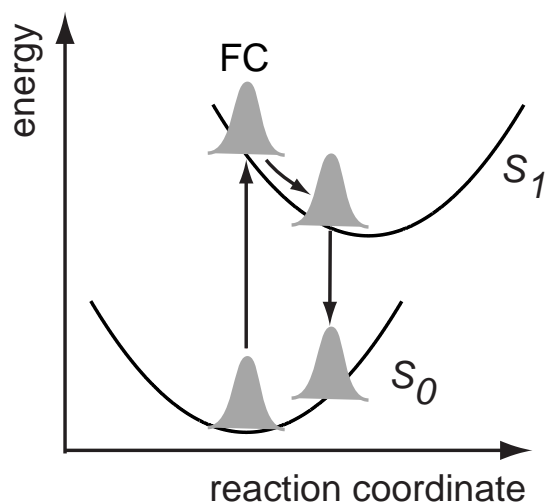


Figure 6.7: Scheme of the potential energy surfaces illustrating the intrapulse dumping and pump-dump mechanisms (adapted from [275]). FC stands for the Franck-Condon region on the  $S_1$  potential energy surface, where the excited wave packet is initially generated.

learning algorithm, either because they will not contribute substantially to the fitness or because the algorithm would have to run for a longer time.

## 6.4 Analysis of the intrapulse dumping mechanism

Many investigations in time-resolved femtosecond molecular spectroscopy have revealed that certain control objectives can be realized by pump-dump processes. This is for example the case for intrapulse dumping [275, 288], where two electronic transitions occur with an adequately linearly chirped laser pulse. Other possibilities are two-pulse pump-dump scenarios [280, 279], where two laser pulses of different colors and at a certain temporal delay interact with the system under study. In both cases, the effect originates from wave-packet dynamics on the first excited-state ( $S_1$ ) potential energy surface. Between the first and second interaction with the electric field, the wave packet propagates on  $S_1$  away from the Franck-Condon region (see Figure 6.7). During this motion, the energy gap between the ground-state ( $S_0$ ) and  $S_1$  potential energy surfaces is in general continually shrinking, so that for the second interaction, a photon of lower frequency in comparison to the first interaction is required.

C. V. Shank and coworkers have shown in 1996 that in the case of one photon excitation, the amount of excited molecules significantly depends on the chirp imposed on the exciting laser pulse [275]. A downchirped pulse, where high frequencies precede low ones, excites significantly less molecules than an upchirped pulse of the same

pulse energy. In the case of upchirped pulses, dumping is minimized, so that one can excite more efficiently [275].

It is now interesting to investigate whether it is equivalent to guide the wave packet along the shrinking energy gap, i.e. by a linearly chirped pulse, so that both interactions occur within the same elongated laser pulse, or to split the laser pulse energy into two subpulses, one for each of the two interactions. Therefore two time-domain parameterizations will be used, linearly chirped pulses (where the momentary frequency of the laser pulse changes linearly with time) and colored double pulses. Employing the stimulated emission of the dye molecule IR140 under strong-field illumination, the influence of the different pulse shapes on a molecular system can be studied directly.

The setup for this experiment is similar to the one described in Section 5.3. Transient absorption spectroscopy is used to determine the amount of excited IR140 (5,5'-dichloro-11-diphenylamino-3,3'-diethyl-10,12-ethylene thiatricarbocyanine perchlorate) molecules by measuring their stimulated emission. The initial 800 nm laser beam is split into two parts in front of the pulse shaper. One part is sent through the pulse shaper and is used as modulated pump, while the other part is used for the probe beam. The shaped 800 nm pump pulse is focused by a lens (focal length: 200 mm) into a flow-cell containing the sample IR140 dissolved in methanol. To measure the stimulated emission at 870 nm, the second part of the initial beam is focused into a sapphire plate to generate a white-light continuum centered around 800 nm. Using a lens of 150 mm focal length, the white-light probe laser pulse is spatially overlapped with the shaped 800 nm pump pulse in the sample. Probe and pump laser pulses can be delayed with respect to each other employing a computer-controlled delay stage.

This effect of chirped pulses is demonstrated on the excitation efficiency for the dye-molecule IR140 dissolved in methanol and excited at a wavelength of 800 nm. The excited state lifetime of this molecule dissolved in ethanol is reported to be 500 ps [75]. This is for example observable in the stimulated emission decay, which can be probed at a wavelength of 870 nm. Therefore the transient absorption signal at a fixed probe delay time of 150 ps and at a probe wavelength of 870 nm is proportional to the amount of excited molecules. Figure 6.8B) shows the corresponding amount of stimulated emission in dependence on different chirp values (blue triangles). From this figure, it is clearly visible that downchirped pulses excite significantly less molecules than upchirped pulses, which is in agreement with the observations made for other molecular systems [6, 143, 275, 288].

The temporal envelope of chirped pulses still has a Gaussian shape, if the unshaped pulse can be assumed to be Gaussian as well. Now it will be investigated, whether this intrapulse dumping effect can also be realized and confirmed by colored double pulses although the temporal pulse profiles are extremely different (see Figure 6.8A). Therefore a double-pulse fitness landscape is measured for this problem, shown in Figure 6.8C. This figure clearly shows that the amount of stimulated emission and therewith the amount of excited molecules clearly varies for different pulse parameters. The highest yield can be achieved for double pulses with a spectral breakpoint of

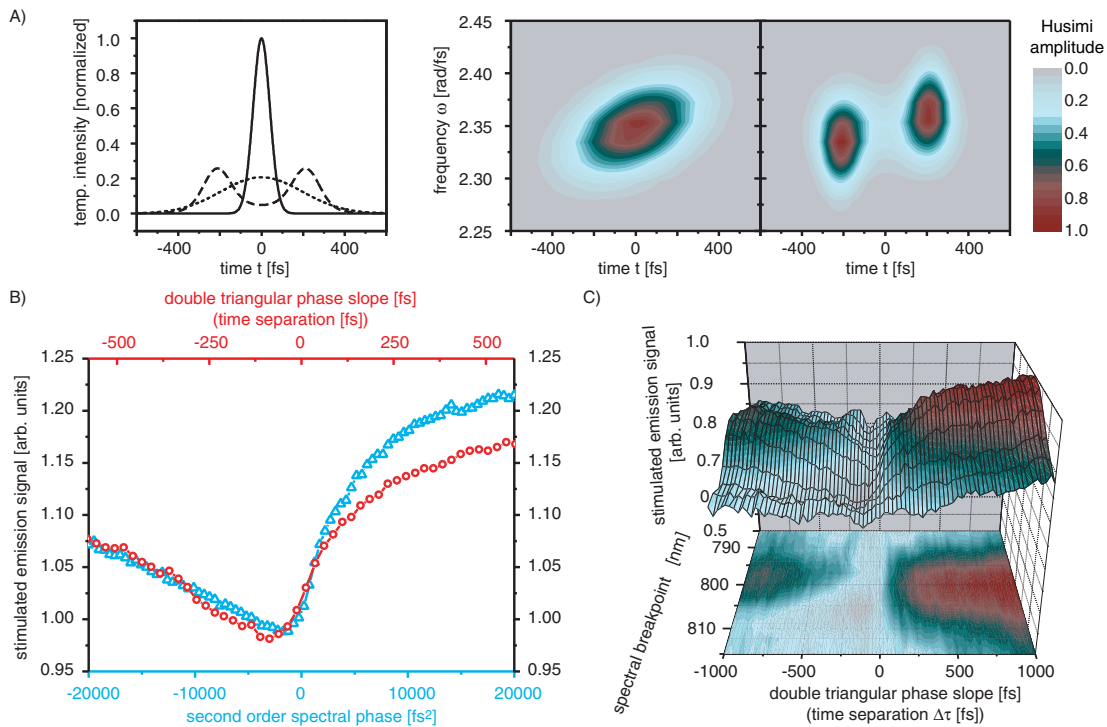


Figure 6.8: A) Simulation of the temporal intensity of a colored double pulse with  $\Delta\tau = 450$  fs (dashed), and a chirped pulse with second order spectral phase coefficient  $b_2 = 15400$  fs<sup>2</sup> (dotted). On the right, the two corresponding normalized Husimi representations can be seen. The solid line shows the temporal intensity of a bandwidth-limited pulse for comparison; B) Stimulated emission of IR 140 pumped with shaped 800 nm laser pulses and probed at 870 nm at a delay time of 150 ps. The graph shows two parameter scans. In the one corresponding to the lower abscissa (blue triangles), the second order spectral phase (i.e. the linear chirp) is varied from  $-20000$  fs<sup>2</sup> to  $20000$  fs<sup>2</sup>. In the other one corresponding to the upper abscissa (red circles), double pulses (breakpoint at  $\omega_0$ ) are generated with the time separation varied from  $-577$  fs to  $577$  fs. The interrelation between the two abscissae is calculated, so that the central frequencies of the double pulses correspond to the momentary frequencies in the chirped pulse at the respective time. C) 3D representation of the stimulated emission in dependence on a double pulse separation from  $-1000$  fs to  $+1000$  fs and a spectral breakpoint variation from  $785$  nm to  $815$  nm.

800 nm and for positive double triangular phase slopes.

To understand this effect a cut of this fitness landscape for a fixed breakpoint value of 800 nm is discussed. This cut is shown together with the chirp-scan in Figure 6.8B (red circles). Positive values of the double triangular phase means that the first individual pulse is red-shifted and the second one is blue-shifted, while the situation is vice versa for negative double triangular phase slopes. As can be seen from Figure 6.8B, double pulses with positive double triangular phase slope excite the system much more

efficiently than those with a negative double triangular phase slope. This effect can be similarly explained as the intrapulse-dumping mechanism of chirped pulses and thereby confirms this particular effect. If the first individual pulse that initially induces the wave packet on the upper surface has a higher frequency than the second one, then the second one can again dump a part of the population. The efficiency of the dumping process depends both on the amplitude and the pulse separation as can be seen in the fitness landscape (Figure 6.8C). Thus, simple colored double pulses are equivalently adequate to induce intrapulse dumping, as can be seen through the good agreement of the two curves (corresponding to downchirp and negative triangular phase slopes, respectively) in Figure 6.8B.

These experiments demonstrate that two parameterizations leading to clearly different pulse shapes can fulfill a control objective similarly. The data indicate that the effect of intrapulse dumping observable with chirped pulse excitation can be mimicked by colored double pulses. The Husimi plots of the pulses in Figure 6.8A show that matching the momentary frequency to the  $S_0$ - $S_1$  energy gap at two points in time results in a similar outcome as when the momentary frequency is continuously adapted by a linear chirp.

## 6.5 Conclusion

The presented experiments using colored double-pulse fitness-landscapes show the capability of this method to investigate molecular dynamics and to analyze control mechanisms. In this chapter, this method is first carefully characterized and then tested in simple second harmonic experiments. The results match qualitatively with the theoretical simulations.

In a second example, the effects of molecular excitation with frequency doubled shaped pulses is tested on a dye molecule in solution. By frequency doubling, a wavelength regime can be accessed that is very relevant for photochemical reactions. Because of the second harmonic generation, the spectrum of the shaped pulses is amplitude modulated as well which must be considered by additional simulations. This is demonstrated for the example of investigating the fluorescence efficiency of the molecule NK88.

In a further exemplary experiment, the yield of the third harmonic in a setup where certain double pulses represent the best solution was studied. This experiment had the advantage that the optimal pulse shape, determined in a separate adaptive femtosecond quantum control experiment, can be intuitively understood and compared to mathematical calculations. The colored double pulse basis has thus proven to be a valuable tool among systematic parameterizations used to investigate control mechanisms, also with regard to more complex problems.

Often very different control pulse shapes can fulfill a control objective similarly. Such pulse shapes correspond to different extrema in the space of all possible solutions and can lead to difficulties in finding the global optimum and in the interpretation

of adaptively found optimal pulses. In a last experiment, the stimulated emission of the dye IR140 dissolved in methanol under strong-field laser illumination was investigated. It was shown that two clearly different parameterizations can have a similar effect. The experiments showed that well-known effects like intrapulse dumping usually observed under chirped-pulse excitation can be induced in a virtual equivalent way by colored double pulses. This scenario demonstrated that parameter scans and fitness landscapes can give an indication how a molecular system can be controlled, but in a closed-loop optimization, the algorithm may take advantage of several mechanisms to optimize the control goal, which are again hard to distinguish.



# Summary and outlook

The formation of different isomers by rearrangement of the molecular structure plays a substantial role in many areas in physics, chemistry and biology. The process of vision in the human eye for instance starts with an ultrafast isomerization reaction. The control of such reactions is therefore a very appealing task. Directly connected to the control is the observation and characterization of the dynamics. As such reactions often take place on an ultrashort time scale, sophisticated methods are required to investigate the molecular kinetics.

Within the last years, adaptive femtosecond quantum control has proven to be a very powerful tool to control chemical reactions. Although the natural environment for most chemical reactions is the liquid phase, adaptive femtosecond quantum control experiments have been mostly performed in the gas phase. Nevertheless some prototype experiments based on simple reactions already have shown that the concept of femtosecond quantum control is also applicable for molecules in a condensed environment.

This thesis deals with the observation and control of such isomerization reactions in chemically and biologically relevant systems. Therefore the reaction dynamics of a medium size prototype molecule of the family of the cyanine dyes in solution were investigated. To monitor the rich kinetics, it was necessary to employ a transient absorption spectroscopy setup capable to measure transients in a broad wavelength region from 360 nm to 950 nm. To gather additional information about the excited state dynamics, a second setup for fluorescence upconversion has been built. The transient absorption experiments were carried out in different solvents, included measurements of the anisotropy and considered the effect of different concentrations on the steady state spectrum.

In cooperation with F. Santoro and R. Improta a detailed and reliable description of the overall kinetics was achieved. In agreement with their quantum mechanical simulations, the experimental observations evidences a two-timescale dynamics on the first excited potential energy surface after excitation. The shorter timescale is less than 2 ps and the longer one is about 9 ps. These two time regimes are attributed to two competing reaction pathways differing in the molecular twisting on the excited surface after photoexcitation. After decaying through a conical intersection, the molecule isomerizes either to the thermodynamically most stable *trans* isomer or to the less stable product isomers. The most likely model for the explanation of the experimental data

and the computational results assumes two product isomers, the *cis* and the *d-cis* form. Since both the *cis* and *d-cis* isomer have a higher ground state energy the population finally relaxes back to the *trans* ground state.

Adaptive femtosecond quantum control experiments were performed on this system with the objective to control the isomerization process. Both enhancement as well as reduction of the isomerization efficiency, i.e. the relative yield of the educt to the product isomers, were achieved. Single parameter control mechanisms such as applying different chirps or varying the excitation laser pulse energy failed to change the ratio of the photoproducts. As a second objective, the fluorescence efficiency after excitation of the molecule from its ground state to the first excited state was enhanced successfully by applying the concepts of adaptive femtosecond quantum control. This enhancement of the radiative decay was shown to have no effect on the isomerization process.

These control studies on the isomerization process of a medium size molecule in the condensed phase motivated experiments on the very complex biological system of retinal embedded in bacteriorhodopsin. The molecule retinal is also the chromophore responsible for the first step in vision. In first adaptive femtosecond quantum control studies the excitation pulse was shaped. These experiments indicate that a reduction of the isomerization efficiency of this molecule, optimized by nature, is possible while the reverse, an enhancement could not be achieved.

In a next step, the traditional pump–dump–probe method was extended to a new pump–shaped–dump–probe scheme to control molecular systems in those regions of the potential-energy landscape where the decisive reaction step occurs. By this, the wave packet can be guided all the way to the desired product state. Different theoretical simulations on the enhancement of the isomerization yield predict that pump–dump–repump–probe mechanisms can control the reaction dynamics. Using the novel scheme, such a four-pulse technique with a double-pulse-like shaped dump pulse can be realized and its impact on the reaction process can be systematically investigated. With further parameterized scans of specialized phase functions, such as different orders of chirp, the dynamics of the dumping process has been illuminated. Finally by adaptively shaping the dump pulse the information from the systematic scan has been refined and completed. These experiments show that optimal dumping occurs with nearly bandwidth-limited laser pulses delayed by 200 fs with respect to the pump pulse. The resulting optimal dump pulse structure for this complex system is surprisingly simple and leads to the qualitative conclusion that the excited-state wave packet is still quite compact in the dumping region. In general, the technique demonstrated here provides a handle on the control of complex systems with a broad spectral distribution of transitions. Additionally, it allows retrieving information on the shape and evolution of excited-state wave packets and underlying potential energy surfaces.

Very often, adaptively obtained optimal laser pulse shapes are very complicated and can contain structures, that contribute to a certain control mechanism to different degrees. Consequently, it can be difficult to identify the control mechanism of such

---

optimal pulses. Especially pump-dump scenarios often play an important role in the acquired optimal solution and therefore deserve to be investigated separately. For this, colored double pulses are employed and both the pulse separation and the relative amplitude or phase difference of the two subpulses are systematically scanned.

This further developed method was first characterized by simple experiments. Then, a setup forcing double-pulses to obtain the highest third harmonic yield was designed. The control objective of maximizing the third harmonic yield has the advantage that the optimal pulse shape can be calculated and intuitively understood. Adaptive femtosecond quantum control experiments were performed with this control objective. With additional measurements of colored double-pulse control landscapes the control mechanism of the adaptively obtained optimal pulse shape can be extracted and confirmed.

In a further experiment, the dependence of the excitation efficiency of a complex dye molecule dissolved in methanol on selected pulse shapes probed by transient absorption spectroscopy was studied. The results show that very different pulse shapes are equally adequate to fulfill the control objective. This can cause a learning algorithm, which is used in adaptive femtosecond control experiments, to be trapped in local minima and prevent finding the optimal solution. Colored double pulse scans thus can give an insight into the control mechanism of adaptively obtained pulse shapes and provide information about reaction dynamics.

Investigations on various processes of different molecular classes using the methods developed and applied here are a promising and realistic goal for the near future. The presented experiments demonstrate a successful manipulation of geometrical rearrangement reactions in chemically and biologically relevant systems by adaptive femtosecond quantum control. These studies on the control of isomerization reactions in condensed environments can be regarded as a first step towards stereoselectivity in photochemistry.



# Zusammenfassung und Ausblick

Die Bildung verschiedener Isomere durch Änderung der molekularen Struktur spielt eine wichtige Rolle in vielen Gebieten der Physik, Chemie und Biologie. So basieren zum Beispiel die ersten Vorgänge des Sehprozesses im menschlichen Auge auf einer ultraschnellen Reaktion, bei der sich die Anordnung der Atome ändert. Die Kontrolle dieser Reaktionen ist daher eine sehr interessante Herausforderung und von großer Bedeutung für viele verschiedene Bereiche. Direkt damit verbunden ist die Beobachtung und Charakterisierung der ablaufenden Prozesse. Da diese auf einer Femtosekunden-Zeitskala stattfinden, sind entsprechende Methoden notwendig, um die molekulare Dynamik untersuchen zu können.

Die Entwicklung der letzten Jahre hat gezeigt, dass adaptive Femtosekunden Quantenkontrolle eine ausgesprochen geeignete Methode ist, um chemische Reaktionen zu kontrollieren. Obwohl die gängigste Umgebung chemischer Reaktionen die kondensierte Phase ist, wurden die meisten adaptiven Quantenkontrollexperimente an Systemen in der Gasphase durchgeführt. Allerdings zeigen schon einige Modellexperimente, basierend auf einfachen Reaktionen, die Anwendbarkeit des Konzeptes für Systeme in der flüssigen Phase.

Die vorliegende Arbeit behandelt die Beobachtung und Kontrolle von solchen Isomerisierungsreaktionen in biologisch und chemisch relevanten Systemen. Dazu wurde die Reaktionsdynamik eines in Methanol gelösten Modellmoleküls mittlerer Größe untersucht, das zu der Familie der Cyanine gehört. Um dessen komplexe Dynamik studieren zu können, wurde ein Aufbau zur transienten Spektroskopie in einem Wellenlängenbereich von 360 nm bis 950 nm konstruiert. Da zusätzliche Informationen über den Ablauf der Reaktion auf der ersten angeregten Potentialfläche gewonnen werden sollten, war die Entwicklung und Errichtung eines Aufbaus zur zeitaufgelösten Messung der Fluoreszenz nötig. Die Experimente zur transienten Spektroskopie wurden in verschiedenen Lösungsmitteln durchgeführt. Desweiteren wurden Messungen des Anisotropieverhaltens berücksichtigt, ebenso wie der Einfluss verschiedener Konzentrationen auf das Grundzustands-Absorptionsspektrum.

In Kooperation mit F. Santoro und R. Improta konnte eine detaillierte Beschreibung der ablaufenden Prozesse gefunden werden. In Übereinstimmung mit den von ihnen durchgeführten quantenmechanischen Simulationen hat sich herausgestellt, dass sich die Dynamik auf der ersten angeregten Potentialfläche nach der Anregung auf zwei

Zeitskalen abspielt. Die kürzere Zeitskala beträgt 2 ps und die längere 9 ps. Beide Zeitbereiche wurden konkurrierenden Reaktionswegen zugesprochen, die sich durch den genauen Ablauf der atomaren Umstrukturierung während der Isomerisierung unterscheiden. Nach dem Passieren einer konische Durchschneidung isomerisiert das Molekül entweder zum thermodynamisch stabileren *trans* Isomer oder zu den instabileren Produktisomeren. Im wahrscheinlichsten Modell zur Erklärung der experimentellen und theoretisch simulierten Daten werden zwei Produktisomere angenommen, die *cis* und die *d-cis* Form. Da sowohl das *cis* als auch das *d-cis* Isomer eine höhere Grundzustandsenergie haben, relaxiert die Population aus den zugehörigen Bereichen zurück zum *trans* Grundzustand.

An diesem System wurden nun adaptive Femtosekunden Quantenkontrollexperimente durchgeführt, mit dem Ziel den Isomerisierungsprozess zu beeinflussen. Es konnte erfolgreich gezeigt werden, dass die Isomerisierungseffizienz (die relative Menge von Edukt- zu Produktisomeren) sowohl erhöht als auch verringert werden kann. Einzel-Parameter Kontrollmechanismen wie zum Beispiel das Verwenden verschieden gechirpter Anregeimpulse oder unterschiedlicher Anregeimpulsenergien ergaben einen nur geringen Einfluss auf die Isomerisierungseffizienz. Als zweites Ziel wurde durch Anwenden des Konzeptes der adaptiven Femtosekunden Quantenkontrolle die Fluoreszenz-Ausbeute erfolgreich gesteigert. Dabei hat sich herausgestellt, dass der optimierte Strahlungszerfall keinen Effekt auf die Isomerisierungseffizienz hat.

Diese Kontrollstudien über den Isomerisierungsprozess eines mittelgroßen Moleküls in der kondensierten Phase haben weiterführende Experimente an dem sehr komplexen biologischen System Retinal innerhalb des Proteins Bakteriorhodopsin motiviert. Bei dem Molekül Retinal handelt es sich um dasselbe Chromophor, das auch für die ersten Schritte im Sehprozess verantwortlich ist. Adaptive Femtosekunden Quantenkontrollstudien, bei denen der Anregeimpuls geformt wurde, zeigen, dass eine Verringerung der Isomerisierungseffizienz dieses durch die Natur optimierten Systems möglich ist. Das Gegenteil, eine Erhöhung der Isomerisierungseffizienz, konnte hingegen nicht erreicht werden.

Im nächsten Schritt wurde die traditionelle Anrege–Abrege–Abfrage Technik zu einem neuen Anrege–geformten–Abrege–Abfrage Konzept erweitert. Dadurch können molekulare Systeme in den Regionen der Potentialenergie-Landschaft kontrolliert werden, in denen der entscheidende Reaktionsschritt stattfindet. Das Konzept ermöglicht, das Wellenpaket den ganzen Weg zum gewünschten Produktzustand zu führen. Verschiedene theoretische Berechnungen zum Problem der Erhöhung der Isomerisierungseffizienz stellen in Aussicht, dass Anrege–Abrege–Wiederanrege–Abfrage Mechanismen eine Möglichkeit der effektiven Beeinflussung der Reaktionsdynamik eröffnen. Mit der weiterentwickelten Methode können solche Vier-Puls-Techniken durch Verwendung von Abregungsimpulsen, die als Doppelimpuls geformt sind, realisiert und ihr Einfluss auf den Reaktionsprozess systematisch untersucht werden. Zusätzlich wurde mittels Variation von parametrisierten spektralen Phasenfunk-

tionen, wie verschiedene Ordnungen Chirp, die Dynamik des Abregungsprozesses beleuchtet. Durch Formen des Abregungsimpulses mittels adaptiver Femtosekunden Quantenkontrolle wurden die Informationen aus den systematische Untersuchung vervollständigt. Diese verschiedenen Experimente zeigen, dass die effektivste Abregung für einen nahezu bandbreitebegrenzten Abregungsimpuls mit einer Verzögerung von 200 fs relativ zum Anregeimpuls auftritt. Die resultierende Struktur des optimalen Impulses für den Abregungsprozess ist überraschend einfach und veranlasst die Schlussfolgerung, dass das Wellenpaket auf der angeregten Potentialfläche in der Abregungsregion verhältnismäßig kompakt ist. Im Allgemeinen erlaubt die hier vorgestellte Technik eine gezielte Kontrolle komplexer Systeme. Zusätzlich ermöglicht sie, Informationen über die Form und Entwicklung von Wellenpaketen in angeregten Zuständen und über die Potentialflächen zu erhalten.

Häufig sind die aus einem adaptiven Femtosekunden Quantenkontrollexperiment erhaltenen optimalen Laserimpulsformen sehr kompliziert und enthalten zudem Strukturen, die zu einem unterschiedlichem Grad zum Kontrollmechanismus beitragen können. Folglich kann sich die Identifikation des Kontrollmechanismus solcher optimaler Impulse schwierig gestalten. Besonders Anrege–Abrege Szenarien spielen oft eine wichtige Rolle in den ermittelten optimalen Lösungen und sollten daher gesondert untersucht werden. Dazu können verschiedenfarbige Doppelimpulse verwendet werden, bei denen man sowohl den Pulsabstand als auch die relative Amplitude oder die Phasendifferenz der beiden Einzelpulse systematisch ändert.

Diese weiterentwickelte Methode wurde mittels einfacher Experimente charakterisiert. In einem weiteren Schritt wurde ein Aufbau entworfen, der Doppelimpulse erfordert, um ein maximale Ausbeute von Licht bei einer Wellenlänge von 266 nm zu erhalten. Dieses Kontrollproblem hat den Vorteil, simulierbar und intuitiv verständlich zu sein. Mit dem Kontrollziel der maximalen dritten Harmonischen Ausbeute wurden adaptive Femtosekunden Quantenkontrollexperimente durchgeführt. Durch zusätzliche Messungen von verschiedenfarbigen Doppelimpuls-Kontrolllandschaften konnte die optimale Pulsform ermittelt und bestätigt werden.

In einem abschließenden Experiment wurde die Abhängigkeit der Anregeeffizienz eines komplexen, in Methanol gelösten Farbstoffmoleküls auf verschiedene Impulsformen untersucht. Aus den Ergebnissen wird ersichtlich, dass sehr unterschiedliche Impulsformen ein Kontrollziel ähnlich gut erfüllen können. Dadurch kann der bei der adaptiven Kontrolle benötigte Lernalgorithmus in einem lokalem Minimum gefangen werden und das Auffinden der optimalen Impulsform dadurch verhindern werden. Verschiedenfarbige Doppelimpuls-Kontrolllandschaften können einen Einblick in Kontrollmechanismen von adaptiv gefundenen Impulsformen ermöglichen und Informationen über die Reaktionsdynamik liefern.

Mittels der angewandten und weiterentwickelten Methoden mehr über verschiedene Prozesse unterschiedlicher Molekülklassen zu lernen ist ein viel versprechendes und realistisches Ziel für die Zukunft. Die präsentierten Experimente zeigen, dass es möglich ist, geometrische Änderungsreaktionen in chemisch und biologisch relevan-

ten Systemen durch adaptive Femtosekunden Quantenkontrolle zu steuern. Die erfolgreiche Manipulation von Isomerisierungsreaktionen von Molekülen in der flüssigen Phase kann als erster Schritt zur Kontrolle von chiralen Molekülen angesehen werden.



# **Appendix**



# Appendix A

## A.1 The coherent artifact

The ‘‘coherent artifact’’ or ‘‘coherent spike’’, as it is often called, generally appears in every liquid phase pump-probe experiment. This coherent artifact is very well understood, both theoretically and experimentally [76] and is composed of different contributions. In the non-resonant case, where no molecular absorption takes place, three different parts are important, the instantaneous electronic response with the amplitude  $\sigma_e$ , high- ( $\omega_n \gg \frac{1}{\tau}$ , with  $\tau$  being the pulse duration) and low- ( $\omega_n \leq \frac{1}{\tau}$ ) frequency nuclear vibrations with a vibrational dephasing rate constant  $\gamma_n$  in the ground state. The high-frequency modes contribute only at fixed probe frequencies  $\omega_2 = \omega_{01} \pm \omega_n$  with  $\omega_{01}$  being the pump carrier frequency. In contrast the low-frequency vibrational and the coherent electronic part give a transient signal at all probe wavelengths. The electronic part of the transient signal is usually 5-6 times higher in magnitude than the signal from the low-frequency vibrations. The differential optical signal of this most important contribution can be described by [76]

$$\Delta A_e(\omega_2, t_d) \propto e^{-\frac{[t_d + t_0(\omega_2)]^2}{\tau_1^2}} \sin \left[ \frac{1}{2\beta\tau_1^2} - \frac{[t_d + t_0(\omega)]^2}{\beta\tau^4} - \frac{t_0(\omega_2)[t_d + t_0(\omega_2)]}{\beta\tau_2^2\tau_1^2} \right] \quad (\text{A.1})$$

with  $\omega_2$  being the instantaneous frequency of the probe pulse and  $t_d$  the time delay between the pump and the probe pulse and  $\tau_1$  the pulse duration of the pump and  $\tau_2$  the pulse duration of the probe pulse.

The probe continuum, as used in the experiments in this thesis, is generated by white-light generation in a sapphire plate. This causes the probe pulse to be chirped (see Section 2.3). For simplicity the probe pulse is written as:

$$E_2(t) = e^{-\frac{t^2}{2\tau_2^2}} e^{i(\omega_{02}t + \beta t^2)} \quad (\text{A.2})$$

$\omega_{02}$  is the central frequency and  $\beta = \frac{1}{2} \left[ \frac{d\phi}{dt^2} \right]_{t=0}$  the chirp rate. Thus the instantaneous frequency (see Equation 1.30) is  $\omega_{02}(t) = \frac{d\phi}{dt} = \omega_{02} + 2\beta t$ . Since different spectral

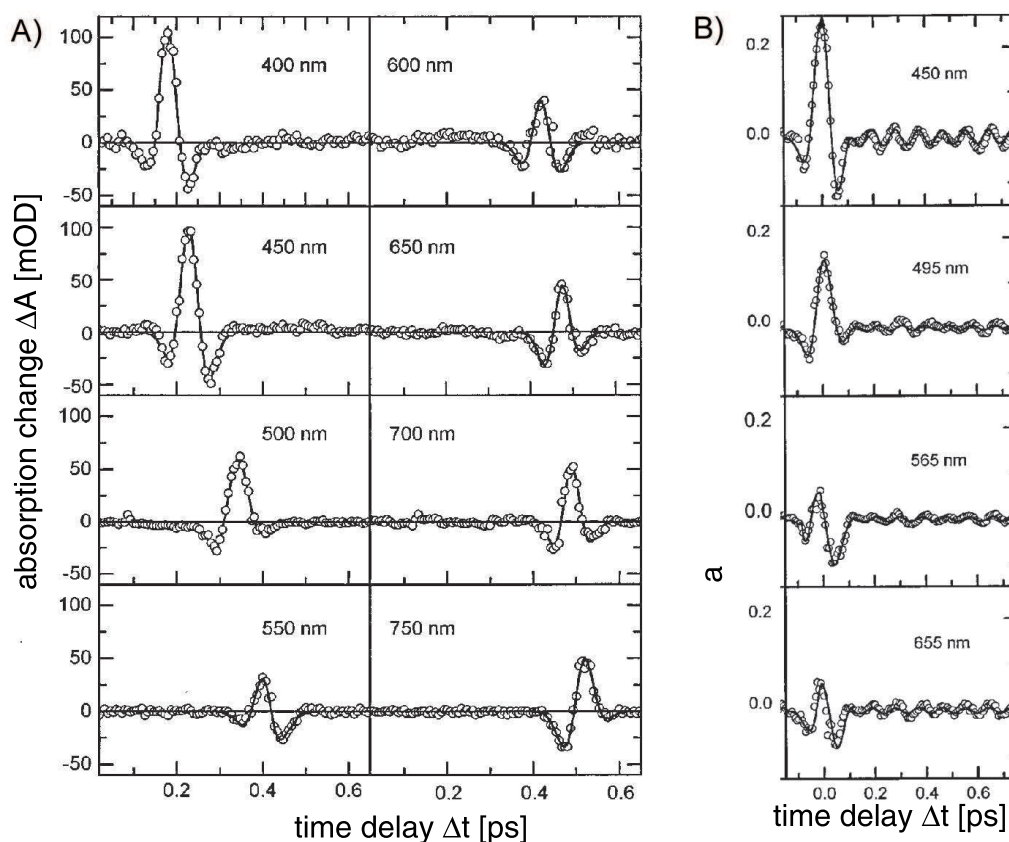


Figure A.1: A) Experimental signal  $\Delta A(\omega_2, t_d)$  obtained from fused silica windows (thickness: 0.16 mm, pump pulse energy: 1.6  $\mu\text{J}$  at a central pump wavelength of 476 nm). The solid lines are the best fit according to Equation A.1 B) Same signal for a medium (chloroform), showing strong impulsive stimulated Raman scattering (ISRS). The black lines show the best fits according to both the electronic contribution and the ISRS (taken from [76]).

components of the supercontinuum interact with the pump pulse at different delay times, the time zero of the pump-probe interaction can be best described by [76]:

$$t_0(\omega_2) \approx \frac{(\omega_2 - \omega_{02})}{2\beta} \quad (\text{A.3})$$

The main behaviour of the coherent artifact can be very well seen from Equation A.1 and Figure A.1A. In this figure the transient electronic signal is shown for different probe wavelengths calculated with the Equation A.1. The parameters for the specific calculation are given in the figure caption. The characteristic positive spike and the negative wings before and after the time zero can be easily realized from the fact that this electronic behaviour can be described by a Gaussian function multiplied with a sine function.

The “impulsive-stimulated Raman-scattering” (ISRS) arises from low-frequency vi-

brations excited by an ultrashort pump pulse. This contribution is mainly proportional to the product of an exponential decay and a sine function [76]:

$$\Delta A_{ISRS}(\omega_2, t_d) \sim e^{-\gamma_n[t_d+t_0(\omega_2)]} \sin[\omega_n(t_d + t_0(\omega_2))] \quad (\text{A.4})$$

The molecular signal will correspond to a vibration whose amplitude decays exponentially as can be seen in Figure A.1B.

The last contribution that can occur is the Raman contribution. It can be described by [76]:

$$\Delta A_R(\omega_2, t_d) \propto e^{-\frac{[t_d+t_0(\omega_2)]^2}{\tau_1^2}} \times \left[ \frac{\gamma_R}{\gamma_R^2 + (\omega_2 - \omega_{01} - s\omega_R)^2} - \frac{\gamma_R}{\gamma_R^2 + (\omega_2 - \omega_{01} + \omega_R)^2} \right] \quad (\text{A.5})$$

with  $\gamma_R$  being the decay rate constant for vibrational coherence. There is an emission (negative signal) at the Stokes frequency  $\omega_2 = \omega_{01} - \omega_R$  and an absorption (positive signal) at the anti-Stokes side  $\omega_2 = \omega_{01} + \omega_R$ . In general, the Raman signal can be much stronger than the electronic contribution and thus lead to an enhanced spike around the time zero.

From these explanations it is clear that the signal around the time-zero must be handled with special care. It can be either treated theoretically as shown here, or must be measured in an additional experiment. In such an experiment, the contributions due to the interaction of the pump and probe pulses with the solvent and the cell have to be measured separately from the measurements to the molecule under investigation dissolved in the solvent. Thus the additional signals which are not related with the molecule can be subtracted from the overall signal. This procedure has been performed with the data when the effects close to the time-zero have been of special interest.

## A.2 Short-time anisotropy measurements on NK88

To investigate the effect of rotational diffusion in the case of NK88 dissolved in methanol, long-time anisotropy measurements have already been discussed in Section 4.4. For completeness the short-time anisotropy behavior is presented in this section. The measurements of the anisotropy in the case of excitation at 400 nm and probe wavelengths 360 nm, 460 nm and 500 nm are shown in Figure A.2. The transients for the pump pulse polarization being parallel (red line) and perpendicular (black line) to the probe pulse are displayed in the left column. The anisotropy calculated with Equation 1.4 is shown in the right column. Because of the additivity law of anisotropies (see Equation 1.12), in most cases the anisotropy for the short time regime is very complex. This is especially the case if there are both positive and negative contributions to the transient signal, as it is the case in the 460 nm and 500 nm transients (see Chapter 4).

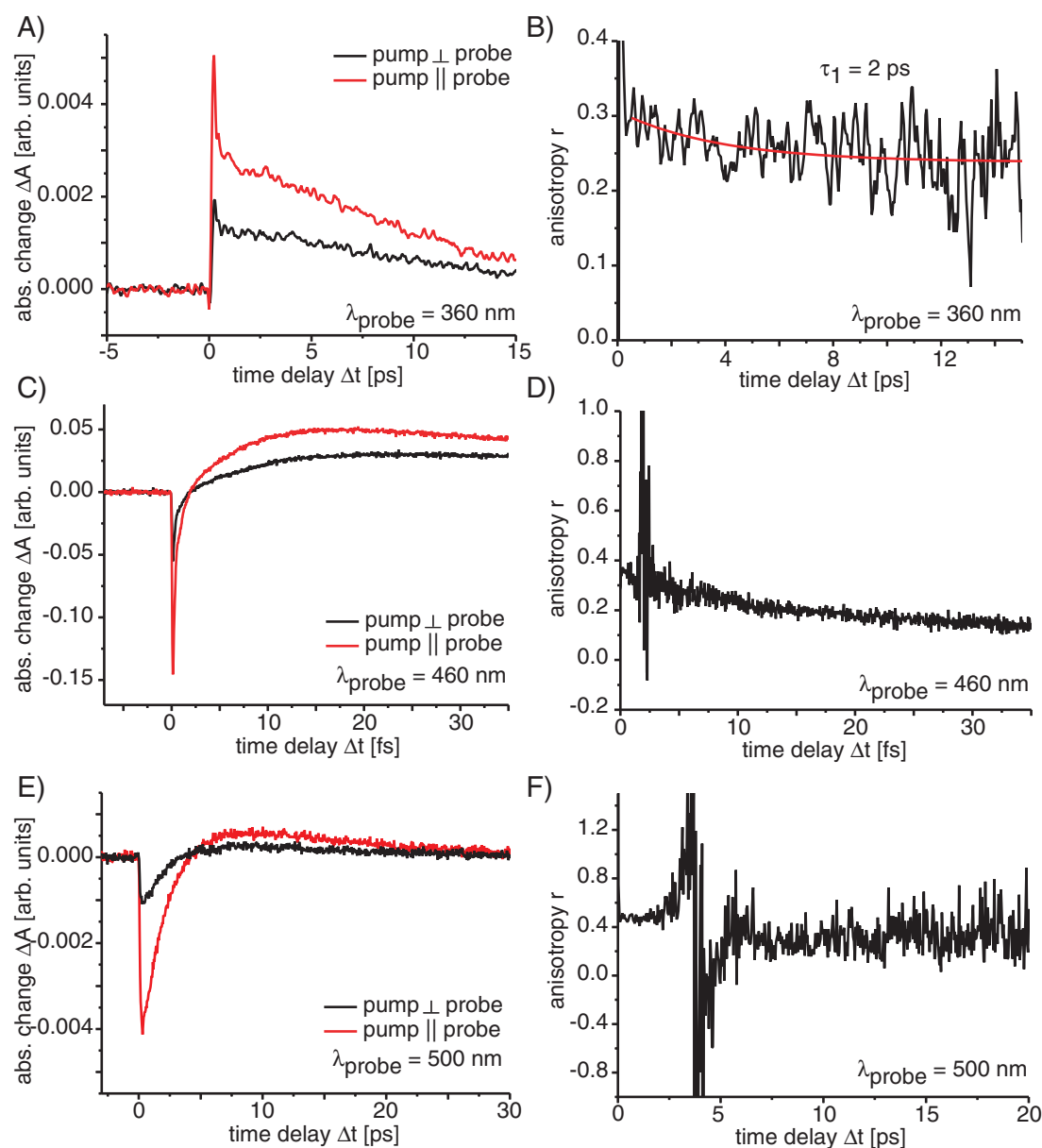


Figure A.2: Short time anisotropy behaviour of NK88 dissolved in methanol, when excited with 400 nm pump light. The left column show the transients for the pump pulse polarization being parallel (red line) and perpendicular (black line) to the probe pulse for A) 360 nm C) 460 nm and E) 500 nm. The right column shows the anisotropy calculated with Equation 1.4 for the wavelengths B) 360 nm D) 460 nm and F) 500 nm.

There, stimulated emission (negative absorption signal), hot ground state absorption (positive absorption signal), *cis* and *d-cis* ground state absorption (positive absorption signal) have non-negligible contributions. This causes singularities in the anisotropy  $r(t)$  (see Figure A.2D and F). The individual components are very difficult to isolate

in such cases.

The transient at the wavelength of 360 nm has only two positive contributions (see Chapter 4). A biexponential fit to the anisotropy yields a short time constant of about 2 ps and a very long time constant that can not be accurately determined and which is expected to be due to rotational diffusion (see Figure A.2B). The short time reflects the change of the orientation of the transition dipole moment due to the molecular dynamics.

### A.3 Wave packet dynamics of $I_3^-$ and photodissociation

The dynamics of a wave packet can be very well visualized in the case of the molecule  $I_3^-$  dissolved in ethanol. If the molecule gets excited by a sufficiently short laser pulse of the proper wavelength, coherence will not only be generated in the excited state but also amongst the ground state vibronic levels [289, 290]. This process is known as “resonant impulsive stimulated Raman scattering” (RISRS). Before the excitation, the system has an equilibrium vibrational population in the electric ground state. With the first interaction with the pump field, a part of the amplitude is transferred to the first excited state. The system wave function now has contributions on both the excited and the ground state. The excited state wave function propagates under the influence of the excited state Hamiltonian. A second interaction with the pump field transfers a certain amount of amplitude back to the electronic ground state. Thus the ground state population is in a nonequilibrium state and evolves under the ground state Hamiltonian. The dynamics of the ground state population can now easily be measured by monitoring the time-dependent bleach signal.

In the case of  $I_3^-$  dissolved in ethanol, the absorption maximum peaks at 375 nm and the absorption band spans up to 450 nm (see [291]). The first excited surface has a dissociative character and leads to the photoproducts  $I_2^-$  and  $I$  [292, 293]. The potential schemes are shown in Figure A.3A and B. Excitation with a sufficiently short laser pulse of 400 nm induces a ground state wave packet. The ground state wave function immediately after the pulse ( $t = t_f$ ) can be approximated by [289, 294, 295]:

$$\psi(\vec{r}, t_f) = e^{i\frac{E_g t_f}{\hbar}} e^{-\frac{i\Delta(\vec{r})t_f}{\hbar}} [\cos(\Omega \cdot t_f) + i \cos \theta \sin(\Omega \cdot t_f)] \psi_g(\vec{r}, 0) \quad (\text{A.6})$$

with

$$\Delta(\vec{r}) = \frac{1}{2} (V_e(\vec{r}) - V_g(\vec{r})), \quad (\text{A.7})$$

$$\Omega(\vec{r}) = \frac{1}{\hbar} (\varepsilon(t) \vec{\mu}(\vec{r})^2 + \Delta(\vec{r})^2)^{\frac{1}{2}} \quad (\text{A.8})$$

and

$$\cos \theta = \frac{|\Delta(\vec{r})|}{(\varepsilon(t) \vec{\mu}(\vec{r})^2 + \Delta(\vec{r})^2)^{\frac{1}{2}}}. \quad (\text{A.9})$$

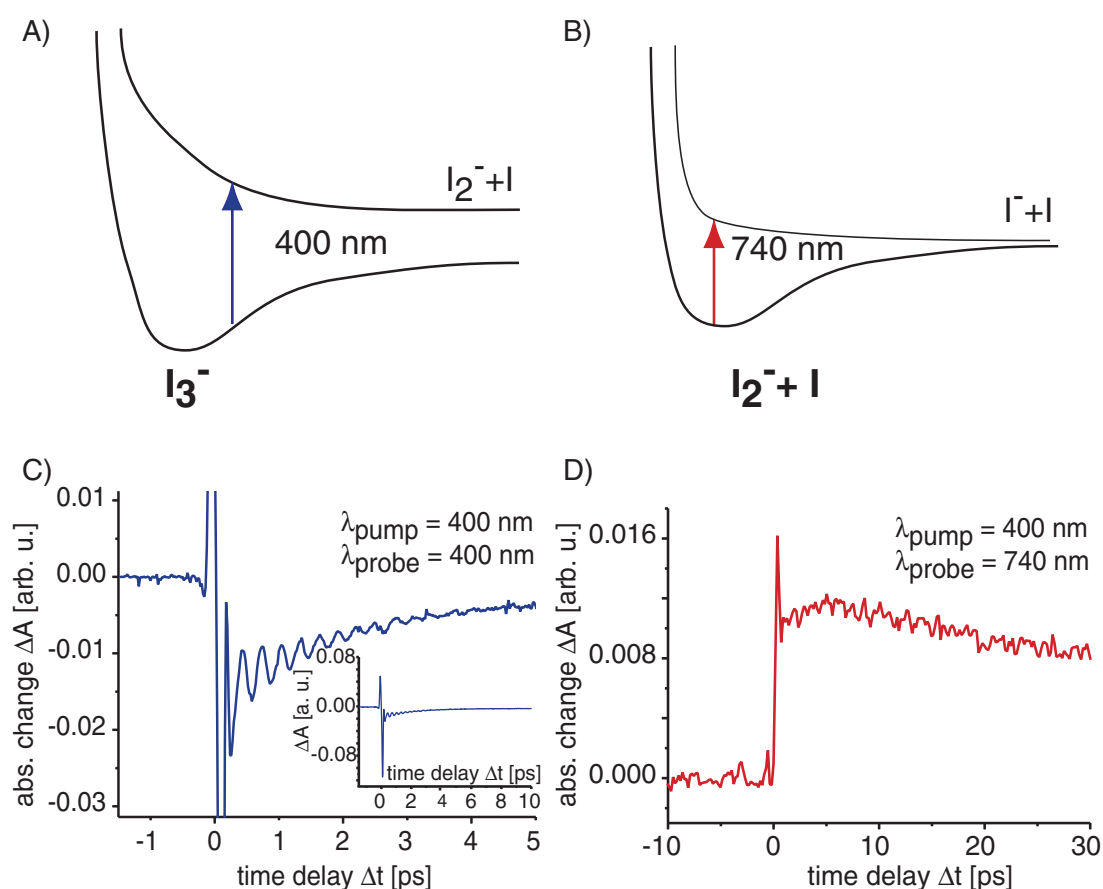


Figure A.3: Scheme A) shows the potential surfaces of the molecule  $I_3^-$  dissolved in ethanol. The molecule can be excited at an excitation wavelength of 400 nm. The first excited surface has a dissociative character and leads to  $I_2^-$  and  $I$ . The potential scheme of  $I_2^-$  itself is shown in B). Excitation by a 740 nm photon can lead to the formation of  $I^-$  and  $I$ . The transient signals of  $I_3^-$  at a pump wavelength of 400 nm and a probe wavelength of 400 nm is shown in C). There, the ground state dynamics which are caused by resonant impulsive stimulated Raman scattering (RISRS) can be very well seen from the sinusoidal modulation of the probe pulse intensity. The transient in D) shows the formation of  $I_2^-$ , which is probed at a 740 nm.

$\varepsilon(t)$  is the slowly varying field envelope for a field that can be written as  $E(t) = \varepsilon(t) e^{-i\omega_0 t}$ , with  $\omega_0$  being the carrier frequency.  $E_g$  is the energy eigenvalue of the ground state and  $\vec{\mu}$  the dipole operator. This equation is only valid for a pulse duration that is shorter than any induced nuclear motion.

Since the initial wave function at  $t = 0$  reappears on the right hand side of Equation A.6, the ground state wave function after the excitation act looks similar to the interaction before, but with an additional hole. The excitation pulse hollows out a piece of the original ground surface wave function which is eliminated via the excited surface. Therefore, the ground state dynamics can be very well described by the evo-



lution of the hole, which is governed by the ground state Hamiltonian. This evolution modulates the probe pulse absorption as a function of time and wavelength.

In the given case a good wavelength to monitor the ground state dynamics is at 400 nm. Figure A.3C shows the measured transient absorption signal of the probe beam for the first five picoseconds. The ground state dynamics can be seen very clearly as a sinusoidal modulation of the signal. The frequency of the sinusoidal modulation is 300 fs. This is still significantly longer than the pulse duration, but for a quantitative comparison of the theory with the experiment, a complete numerical evaluation of the Schrodinger equation would be necessary. However, the qualitative statements from above remain unchanged. As seen in Equation A.6, the laser pulse parameters have an important influence on the initial conditions of the wave packet and thus on the molecular dynamics.

Triiodide can dissociate into  $I_2^-$  and  $I$ . The absorption maximum of  $I_2^-$  in ethanol is at 750 nm. Therefore the dissociation process can be well monitored at a probe wavelength of 740 nm. By absorption of a photon of this wavelength the molecule  $I_2^-$  can dissociate into  $I$  and  $I^-$ . The transient signal at 740 nm is shown in Figure A.3D.

In the case that the molecule  $I_3^-$  is excited with 266 nm pump light instead of using 400 nm, in addition to the two-body dissociation that can be monitored at probe wavelengths around 750 nm, three-body dissociation happens as well. When excited at 400 nm, the transient for a probe wavelength of 400 nm basically shows no offset after a few picoseconds (see Figure A.3). Since a certain fraction of the molecules is expected to dissociate into  $I$  and  $I_2^-$  (this is evident from the transient at 740 nm in Figure A.3D), a pump-depletion signal with at least the time constant of the decay of the 740 nm signal is expected. The reason, why this can not be seen lies in the appearance of an isobestic point at a wavelength of 400 nm [292]. The absorption of the produced  $I_2^-$  (positive signal) directly cancels out the pump-depletion (negative signal). In the case of an additional product channel the amount of produced  $I_2^-$  molecules decreases and thus the  $I_2^-$ -absorption as well. Because the amplitude of the bleach signal stays unaffected, in such a case the superposed signal would be in general different from zero. The only chance to get again an isobestic point at 400 nm would be given, if the second product also absorbs at this wavelength.

This situation exists for the case of excitation with light at a frequency of 266 nm. Due to the different pump wavelength, the initial dynamics changes (see Figure A.4A). For later delay times the transient probed at 400 nm has a clear offset (see Figure A.4B, blue line). For better comparison the probe signal for a blocked pump pulse is shown to mark the baseline (see Figure A.4B, orange line). The offset of the molecular signal at late delay times is proportional to the amount of molecules that have been excited through a decay channel different from the  $I_2^-$  production. This additional decay channel was identified as three-body dissociation of  $I_3^-$  into  $I^-$  and two  $I$  atoms [292].

Therefore the molecular system of  $I_3^-$  dissolved in ethanol is very suitable and highly interesting for adaptive femtosecond quantum control experiments concerning the control of dissociation into different products. This topic has been intensively in-

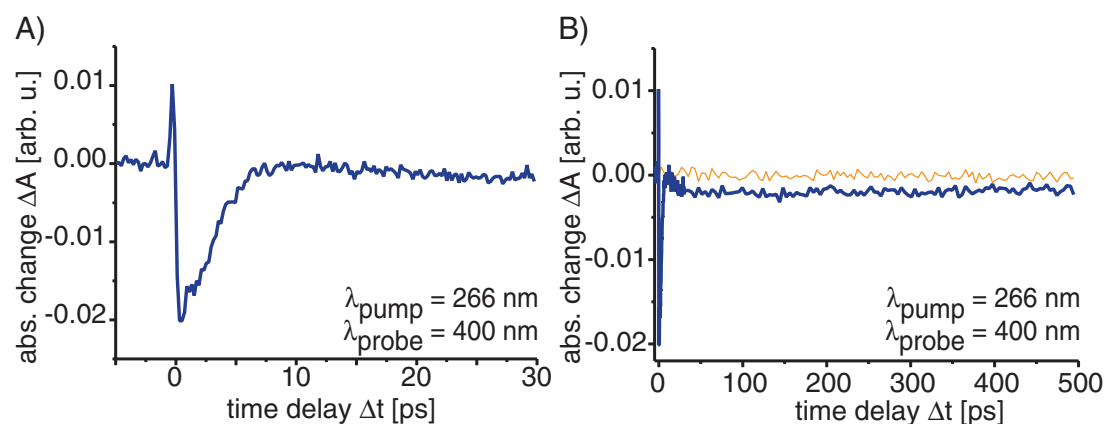


Figure A.4: A) The first thirty picoseconds of the transient absorption signal of  $I_3^-$  dissolved in ethanol, when excited at a wavelength of 266 nm and probed at 400 nm. The signal up to 500 ps is shown in plot B) as blue line. To mark the baseline, the transient signal for the case of a blocked pump pulse is shown as orange line. The offset at late delay times is caused by three-body dissociation.

investigated in the gas phase, where dissociation into many fragments can be more or less easily detected for example by means of mass spectroscopy. In contrast, in the liquid phase only a few publications can be found on the topic of dissociation into more than one product. Effective methods for the detection of photofragments like mass spectroscopy are not feasible in the condensed phase. Transient absorption spectroscopy that is commonly used in liquid phase experiments has the disadvantage to provide signals that are often difficult to interpret. But more important, a substantial amount of photoproducts is necessary to produce a detectable signal. Additionally the pulse energy can not be increased to such high values as they are sometimes used in gas phase experiments to allow efficient multiphoton transitions. Beside heating and other unwanted effects, at a certain point white-light generation (see Section 2.3) will occur in the sample medium. The stray light of this signal will make it nearly impossible to record transients of a sufficient quality.

For the case of the system  $I_3^-$  dissolved in ethanol these problems could be successfully circumvented as shown in this section. Excited by a 266 nm photon, the molecule can either perform a two-body or a three-body dissociation. The first event can be monitored in the near-infrared region and the second event at a wavelength of 400 nm. Therefore for an adaptive femtosecond quantum control experiment a shaped pump pulse centered around 266 nm and two probe pulses at 400 nm and 800 nm are required. A recently developed method for shaping pulses in the UV region based on frequency-doubling and sum-frequency mixing could provide the modulated excitation pulses at 266 nm [296]. The two probe wavelengths at 400 nm and 800 nm can be very easily obtained by frequency doubling of the 800 nm beam from the laser system. Only a certain fraction will be converted to 400 nm. Since the feedback signals are best obtained at late delay times the time difference between the two dif-

ferent probe-wavelength because of the creation process and the dispersion does not negatively influence the feedback signal. In an adaptive femtosecond quantum control experiment, the change of the ratio of these two signals would be directly connected with the change of the dissociation products. For a second test of the obtained results, in principle all information can be gained from the transient at 400 nm [292]. The ratio amplitude of the spike at early delay times can be used to estimate the number of initially excited molecules. With the help of this information, the quantum yield for the three-body dissociation can be gained by the comparison with the signal at later delay times.

This molecule makes the investigation of a possible control of the different dissociation channels very interesting, because the undergoing dynamics in this model system can be more easily theoretically described than for complicated molecules. From the pronounced coherent wave packet dynamics as visible in Figure A.3C one can expect that coherent control effects can play a major role in the control mechanism.

## A.4 Rotation–translation device for spectroscopy with small sample volumes

Many investigations carried out with optical spectroscopy focus on various properties of solvated molecules. In most methods, the liquid is cycled by a pump through a flow-cell [37] or a liquid jet [52, 297]. This procedure necessitates a certain sample volume to fill the flow tubes and a reservoir to ensure a gas-bubble-free flow cycle. Often, the amount of the molecular sample is too limited to use a flow-cell and to allow a high enough optical density of the solvated substance at the same time.

Instead of a flow-through geometry, a thin film of dissolved molecules can be used, sealed between two glass plates. Such films can be easily fabricated in most cases and necessitate only a small fraction of the sample volume in comparison to a flow-through setup. In addition to this, certain biological molecules are not stable in solvents with a very low viscosity used in a flow-cell or a liquid jet. This is for example the case for the system retinal in bacteriorhodopsin if solvated in certain organic solvents, where it may rapidly degrade [298]. In contrast, bacteriorhodopsin immobilized in a film [286] proves to be a more suitable environment which makes it possible to study the same sample over a long time.

Generally, in many time-resolved spectroscopic methods on thin films, such as transient absorption spectroscopy or fluorescence upconversion, the laser beam will only interact with a small fraction of the whole film (depending on its size). This interaction can cause the sample to locally degrade or to accumulate photoproducts. In femtosecond transient absorption spectroscopy, the used laser systems often work with a 1 kHz repetition rate. Certain photoproducts have lifetimes that exceed the period between two measurements (e.g. the *13-cis* isomer of retinal in bacteriorhodopsin has a lifetime of 8 ms [227]). Therefore repeated interaction with the same sample volume will

result in an undesired signal from the photoproduct generated with the preceding laser shot. Beside this, the continuous interaction with the laser beams will heat the sample and can cause signal artifacts or even lead to irreversible destruction of the molecular system.

To reduce these unwanted effects, it is desirable to exchange the region where the interaction with the laser beams takes place [299]. Scanning of the excitation and/or detection laser beams over the sample is usually difficult to accomplish. Therefore, it is advantageous to move the sample film. To ensure a new sample volume for each measurement, this movement has to occur fast enough. Assuming a diameter of the interaction region of 100  $\mu\text{m}$  means that the movement has to occur with a velocity of more than 0.1 m/s.

The desired movement can in principle be accomplished by two linear actuators [300]. Although this works well in certain situations where no degradation or photoproduct formation occurs, such linear actuators however cannot provide the necessary velocity to ensure a new sample volume in the case of femtosecond transient absorption spectroscopy with a 1 kHz repetition rate. To fulfill this requirement, the sample is often rotated [9, 59, 301, 302]. Although in such a setup the probed volume is exchanged from shot to shot, one does not make use of the whole sample area, but only a small ring of the sample area is probed. An additional translation of the sample film can result in much better coverage of the overall sample and therefore allow longer measurement periods with the same film.

Here a setup is demonstrated and characterized that is capable of rotating and translating the sample with a speed high enough to provide a new sample volume for each laser shot in a 1 kHz femtosecond transient absorption measurement. The setup is designed to cause as few vibrations as possible to ensure a good signal-to-noise ratio. The necessity of the proper adjustment of the sample film with respect to the laser beams is demonstrated in a study investigating different tilts of the molecular film. For a proper setup geometry, the signal-to-noise ratio is compared to that obtained with a standard flow-cell setup.

Additionally, the capability of the setup to reduce the effect of photoproduct accumulation is investigated. In the case of non-immobilized films such as liquid films produced by solvation of a substance in a certain solvent the influence of diffusion on the molecular signal must be considered. This effect is also investigated for the rotation–translation device.

#### **A.4.1 Design of the sample holder and experimental setup**

The rotational motion is realized in a very simple and stable way that consumes only little space by mounting the sample film in a tube which is held by two single-row radial deep-groove ball bearings. This ensures vibration-free movement without any tilting or slipping.

The translation can for example be realized by an eccentric tappet or by an ellip-

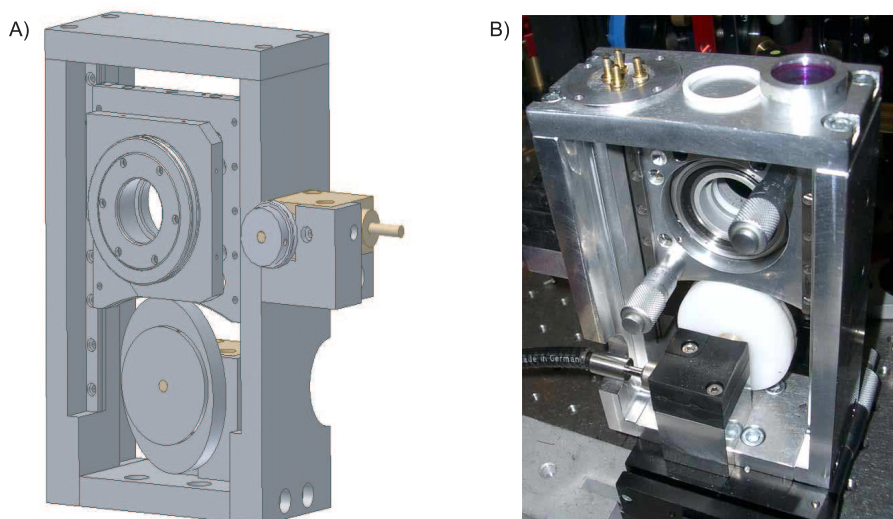


Figure A.5: Rotation–translation device. A) The three-dimensional CAD (computer-aided design) drawing and B) a photo of the sample holder constructed for the spectroscopy of thin films are shown. Linear and rotational motion of the sample film results in a rosette-like scanning motion of the laser beams over the film. The film can be tilted about two axes to adjust the film normal to be perpendicular to the linear motion and to allow optimal alignment. Flexible shafts for transferring mechanical motion make the design very compact and allow storing the DC motors at a certain distance from the experiment. On top of the sample holder, a bacteriorhodopsin film sample (right) from Munich Innovative Biomaterials (Martinsried, Germany) can be seen, which will be screwed into the holder with a teflon spacer (middle) and a fixing disk (left).

tically shaped actuator. This has the advantage to convert rotational motion, easily provided by a DC motor, into a periodic translation. In the present realization, the latter possibility of an ellipse to produce the necessary linear motion is implemented. The different lengths of the major and the minor axis are used to transfer the rotation into a translation by pushing a slide up and down (Figure A.5). Therefore, different amplitudes can be easily achieved by using different ellipses.

The desired movement of the sample is realized with two simple DC motors (from MFA/Comodrills, UK). By applying different voltages, the speeds of the linear and rotational motions can be easily adjusted. The rotational energy is transported with two flexible shafts from the motors to the sample device and therefore the DC motors can be positioned far away from the experiment. This makes the sample holder very compact and helps reducing vibrations, since the DC motors do not need to be attached onto the optical table. Furthermore, a greater distance to the experiments reduces the

influence of electromagnetic stray fields produced by the DC motors on sensitive electronic elements.

The translation direction of the linear motion has to be perpendicular to the sample film normal. Otherwise, the spatial overlap as determined by the pump and probe laser focal regions would move out of the sample volume as a consequence of the combined linear and rotational motion. To ensure probe overlap at all times, the bearing is embedded in a construction following the design of a mirror mount. This allows adjusting the tilt of the sample film with respect to the laser beams. Thus, using the two degrees of freedom of the mount, optimal alignment of the sample normal with the direction of the incoming pump light is achieved.

A further translation stage on the bottom of the sample holder helps for fine-tuning in the alignment procedure and to bring the laser focus into the center plane of the sample volume. Any film sealed between two windows with a diameter of 25.2 mm and thickness up to 15 mm, made of a glass type that does not influence the polarization of the laser beams, can be used in this setup.

This device is especially interesting and suitable for biomolecular samples, which are often only available in small quantities. Nevertheless, in order to characterize the setup, a film of the dye molecule IR125 (Indocyanine-green, 3,3,3',3'-tetramethyl-1,1'-di(4-sulfobutyl)-4,5;4',5'-dibenzo-indotricarbocyanine-iodide monosodium salt) dissolved in ethylene glycol is prepared. The dye was purchased from Lambda Physics and used as-is. The sample thickness was set to 0.2 mm by using two 0.1 mm thin ring-shaped spacers between the two glass plates. The optical density of the sample was measured by a Hitachi U-2000 spectrophotometer to be 0.21 OD at 800 nm for the photodegeneration experiment and 0.15 OD in the case of the signal-to-noise measurements (see below).

Furthermore, a flow-cell setup (Starna GmbH, Type 48I) was used to allow direct comparison between a conventional measurement and the rotation-translation device. The flow-cell sample path length was 0.2 mm (specified by the vendor). The sample has the same concentration as in the previous case and the optical density has been measured to be 0.18 OD at 800 nm for the photodegeneration experiments and 0.13 in the case of the signal-to-noise measurements. The difference in the optical densities is due to slight differences in the film or cell thickness, respectively.

The experimental characterization of the two spectroscopic setups was carried out by measuring the ultrafast dynamics induced by an 800 nm pump pulse in a femtosecond transient absorption experiment. The laser system used for these experiments consists of a Ti:Sapphire oscillator and a regenerative amplifier and provides 800 nm, 80 fs, 1 mJ laser pulses at a repetition rate of 1 kHz. To characterize the different samples, a pump-probe setup is employed. The initial laser beam is split into two fractions, one for the pump and the other for the probe beam. The pump beam is attenuated and focused by a 200 mm lens into the sample. For the experiments a pump pulse energy of 600 nJ is employed.

For the probe beam, a white-light continuum is created by focusing the 800 nm laser beam into a sapphire plate. This supercontinuum is focused by a 150 nm lens into the sample and is spatially overlapped with the pump laser pulse within the sample volume. Pump and probe beams have an angle of approximately  $10^\circ$  to each other. With the help of a monochromator, light of a wavelength of 830 nm is selected from the probe laser pulse and recorded by a photodiode. The pump laser pulses can be delayed with respect to the probe laser pulses using a computer-controlled delay stage.

To monitor the stability of the laser system, the 800 nm laser energy was also recorded during the different experiments.

### A.4.2 Experimental characterization

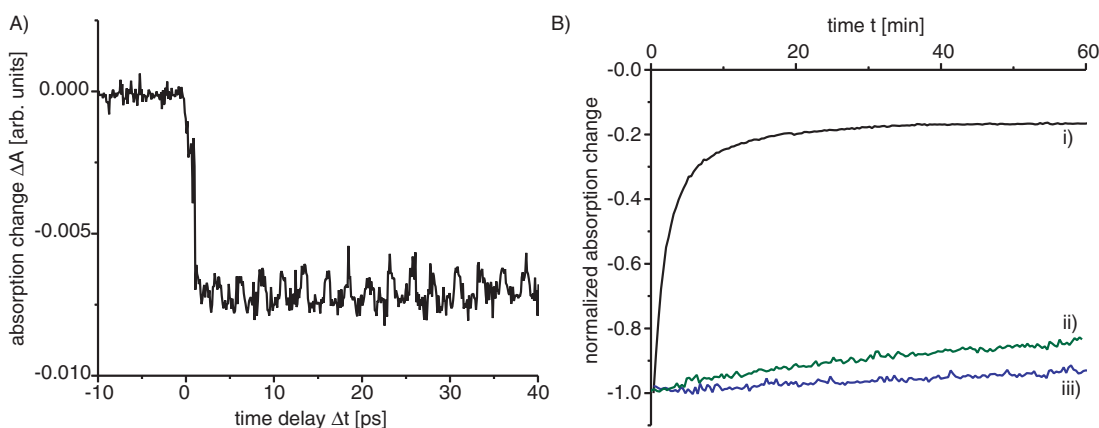


Figure A.6: A) IR125 transient absorption with deliberate misalignment of the rotation–translation device (pump wavelength at 800 nm, probe wavelength at 830 nm). For the demonstration of the effects of misalignment, the rotation has been interrupted and the speed of the linear motion reduced to a minimum. The vertical tilt of the sample film normal with respect to the laser beams was misaligned to be approximately  $10^\circ$ . This causes a slipping of the point of best spatial overlap between pump and probe and thereby an additional sinusoidal modulation of the measured signal, which significantly lowers the signal-to-noise ratio. B) IR125 absorption signal with an 800 nm pump and an 830 nm probe at a fixed pump–probe delay time of 60 ps. This graph demonstrates the effects of photodegradation and diffusion. i) Probing a certain spot on the sample film without any rotational or linear motion; ii) only rotational motion; iii) both linear and rotational motion.

The experimental characterization of the different setups was carried out with the laser dye IR125 dissolved in ethylene glycol. Employing ultrafast spectroscopic methods, this molecule has been used to investigate vibrational and vibronic dynamics of large molecules in solution [264, 288], excited-state life time [75], photoisomerization [75], and optimal control of excitation efficiency [6]. In ethylene glycol the ab-

sorption maximum of IR125 lies at 791 nm. Therefore, using pump laser pulses centered at 800 nm excite the sample close to its absorption maximum. Probing at 830 nm mainly records two effects: pump depletion and stimulated emission. Because the pump laser pulse excites a certain fraction of the molecules in the sample, this fraction does not contribute to the ground-state absorption anymore. Therefore, the probe beam experiences less absorption in the region of the steady-state absorption spectrum. This effect is labeled “pump depletion” and the amplitude has the same sign as an emission signal.

Using a probe wavelength that is shifted by 39 nm to the red side with respect to the absorption maximum, it can be expected that also stimulated emission can be monitored at the probe wavelength. For IR125 dissolved in ethanol or in dimethylsulfoxide the excited-state lifetime was reported to be several hundreds of picoseconds [75].

In addition to stimulated emission and pump depletion, the molecule has the capability to form several photoproducts. Like all the other members of the cyanine dye group, if not sterically hindered, IR125 has the potential to isomerize to different molecular geometries [75, 303]. Furthermore, intense laser fields can cause degradation of the sample by dissociation into smaller fragments [304] and under certain conditions, the photo-excited molecules form radicals and react with intrinsically present solvent ions and radicals [305]. Irrespective of the exact origin of the photodegradation, it will be shown in the following that it is possible to accumulate certain photoproducts under continuous excitation by a laser field. These photoproducts do not absorb at 800 nm anymore, which can be seen by recording the steady-state absorption spectra prior to and after intense laser radiation. Therefore, the stimulated emission and the pump depletion are reduced. As a consequence, the amount of stimulated emission and pump depletion, recordable at 830 nm, is a direct measure of the amount of IR125 molecules in their original configuration. This situation will be used in the experiments concerning photostability and diffusion.

To ensure a good signal-to-noise ratio, the rotation-translation device has to be aligned properly in the experimental setup. For demonstration of this fact, the sample surface with respect to the linear motion of the device is deliberately misaligned, and the speed of the linear motion of the film is reduced to a minimum for the measurement of femtosecond pump-probe transients. As can be seen from Figure A.6A), a sinusoidal modulation is present on top of the transient which is not due to molecular wavepacket dynamics but rather an artifact caused by the misalignment. This is a consequence of the fact that the position of optimal spatial overlap of the pump and probe beams moves from the film into the glass plate and back into the film. At a very low speed of the linear motion, as used here for demonstration purposes, this results in a sinusoidal modulation of the signal. At higher speed, this slipping would not be directly visible on the signal but the noise on top of the transient would be significantly increased with respect to the optimal case. With the help of experiments such as the one shown in Figure A.6A) and using the fine adjustment screws visible in Figure A.5, the alignment can be optimized, which has been done for all subsequent measurements.



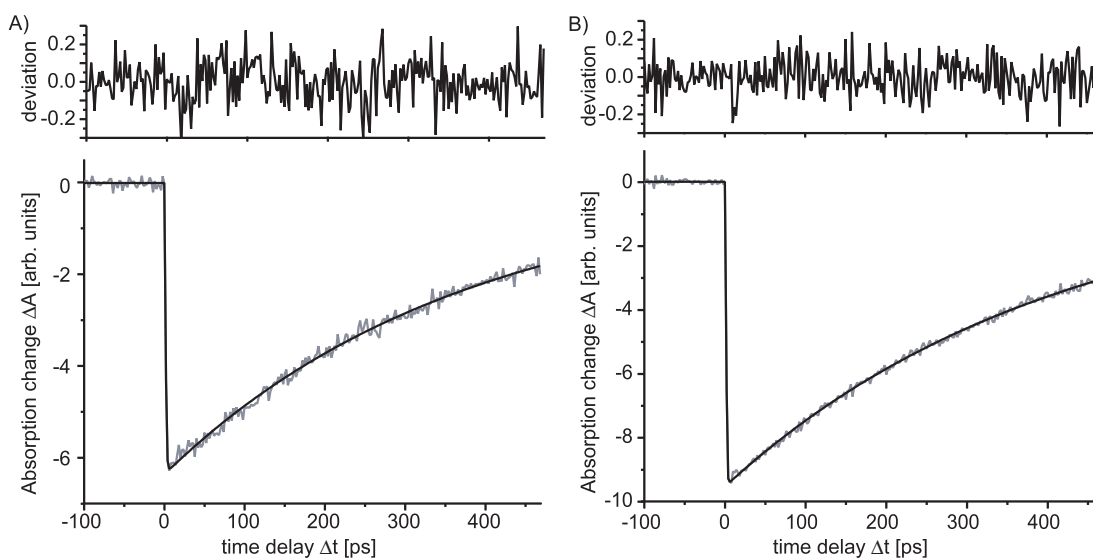


Figure A.7: Comparison of the signal-to-noise ratio for different types of experimental setups using transient absorption measurements of IR125 dissolved in ethylene glycol pumped at 800 nm and probed at 830 nm. To determine the signal-to-noise ratio, the transients are fitted by a sum of two exponentials. On top of each transient, the residuals are shown. A) Rotation–translation device. B) Flow-cell.

In order to characterize the signal-to-noise ratio for the flow-through setup and the rotation–translation device, pump-probe transients under identical conditions are recorded, i.e. in particular same signal averaging times, same number of data points and identical temporal delay positions. As mentioned in the previous section, the samples have the same concentrations but slightly different optical densities due to different sample thicknesses. The transients are recorded directly one after each other, using a geometry that allows changing between the two sample types (flow-cell/film) within less than five minutes. The different signal heights are caused by small misalignments in the z-position of the sample film.

Figure A.7 shows the results for the two measurements, carried out on the film with the rotation–translation device (Figure A.7A) and the flow cell (Figure A.7B). For both sample types, the respective transients are virtually identical and the noise does not differ significantly. These transients are fitted by a sum of two exponentials, to determine the residuals and to estimate the signal-to-noise ratio. The individual residuals are shown on top of each transient in Figure A.7. The standard deviation of the noise visible in the residuals results in a slightly better signal-to-noise ratio for the flow-cell geometry. From several measurements, it can be deduced that the differences in the signal-to-noise ratio are below 20%. The reason for those differences can be small misalignments, transfer of vibrations onto the optical table by the various moving parts of the film sample holder and small air-bubbles or other impurities in the film. Especially air bubbles, which are generally prevented in a flow-cell setup if

a reservoir is used, can lower the signal-to-noise ratio significantly. Nevertheless, the slightly lower signal-to-noise ratio will still be acceptable for most experiments and can perhaps even be avoided by a better film preparation.

A second possible disadvantage of using films instead of flow-through setups lies in the accumulation of photoproducts. If a flow-through setup is employed, this disadvantage can be circumvented with the help of a sufficiently big reservoir. When films are used and the photoproducts have a longer lifetime than the period after which the same sample volume is probed a second time, accumulation of the photoproducts will seriously affect the measured transients. In the case that the probed molecules are not immobilized in the film, the additional effect of diffusion has also to be taken into account. This is for example the case for the given molecular sample of the dye molecule IR125 dissolved in ethylene glycol as can be seen in the following.

To demonstrate the effect of photoproduct accumulation, a certain spot on the sample film is probed without any rotational or linear motion for one hour. As can be seen from Figure A.6B i), the probe signal decreases strongly with time. The reasons for the signal behavior are on the one hand the photodegradation of the molecules in the probed volume, and on the other hand the exchange with fresh molecules by diffusion.

In the case of a rotating sample, the integrated probed volume is much bigger and thus, the effect of photoproduct accumulation is accordingly reduced (see Fig. A.6B ii). The speed for the rotation has been set to 3 revolutions per second to ensure a new volume for each shot for a 100  $\mu\text{m}$  probe region. The probed area is furthermore drastically increased when an additional linear motion is applied. In the corresponding case illustrated in Fig. A.6B iii), the rotational speed was limited to 2 revolutions per second and the motion of the elliptical actuator to 0.5 revolutions per second (i.e. the linear motion was set to 1 Hz, since the elliptical actuator causes two up-and-down motions in one turn). Clearly, the signal level over one hour hardly changes in comparison to only rotational or no motion at all, thus demonstrating the suitability of the rotation–translation device for time-resolved optical spectroscopic experiments.

A different aspect arises for molecules which do not degrade, but where photoproducts are generated which relax back with a time constant longer than the time between two consecutive laser shots. Such a situation is existent, for instance, for the system retinal in bacteriorhodopsin. While consecutive laser shots hit different sample volumes, the time after which the same spot is probed a second time is significantly longer than the life time of the photoproducts. Therefore, accumulation of photoproducts will not occur. However, due to thermal heating, which cannot be completely circumvented even when using both the rotational and linear motion to scan most of the available sample film, degradation of the system will nevertheless occur. The additional linear motion in our the setup presented here further reduces the effect of heating on the overall signal. The studies on the particular biomolecular system bacteriorhodopsin, presented in Chapter 5, have proven that the setup is well suited

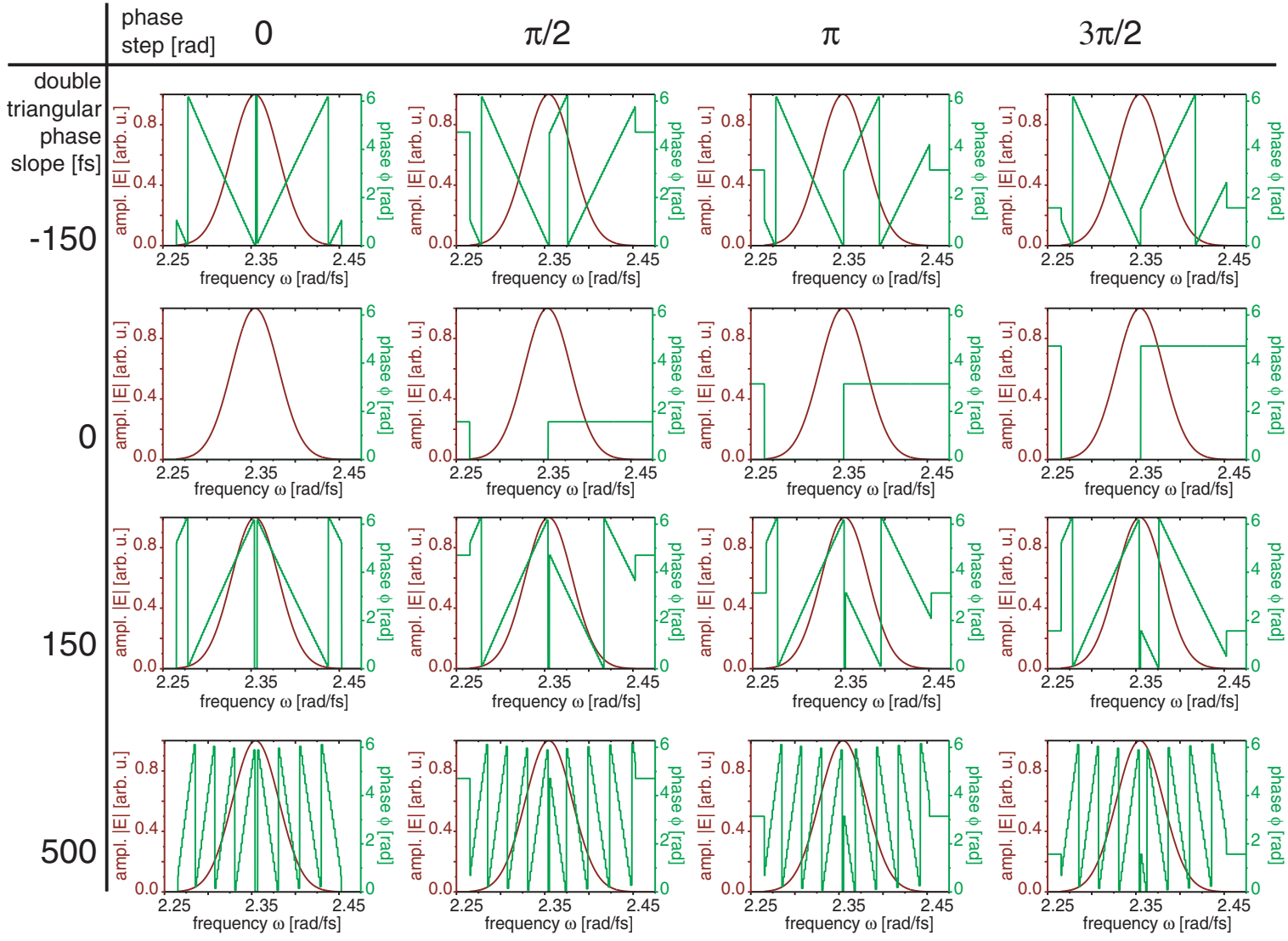
to work with the same sample for many hours. Thus, the setup presented here can be employed for spectroscopic studies of biomolecules prepared in thin films.

## A.5 Calculated double-pulse pulse shapes

To interpret the multi-parameter traces (see Section 1.9) it is very helpful to know the form of the pulse shapes for a certain set of parameters. This is especially true for the nontrivial case of scanning the triangular spectral phase slope  $\Delta\tau$  and the phase step  $A$ .

In the following figures (A.8-A.11), a set of representative electric fields is given for both the temporal and the spectral regime, for the fundamental frequency as well as for the frequency-doubled case. For all pulse shapes a carrier frequency of  $\omega_0 = 2.34 \text{ PHz}$ , an initial spectral phase equal to zero and a pulse duration of 80 fs are assumed. These graphs show the variation of a triangular phase with a slope  $\Delta\tau$  and a phase step  $A$  for multiple exemplary parameters. The rows represent different slope values  $\Delta\tau$  for the same phase step value  $A$  and the columns vice versa. The numerical calculations include the experimental artifacts that will result due to the pulse shaper and the crystal. The second harmonic generation takes place in a BBO with a thickness of  $100 \mu\text{m}$  is assumed to take place in a non-depleted regime. For the calculations, parts of the numerical package LAB II have been integrated in the computer code [147].

Figure A.8: Spectral pulse shapes and spectral phases used in the calculation. For details see the text before.



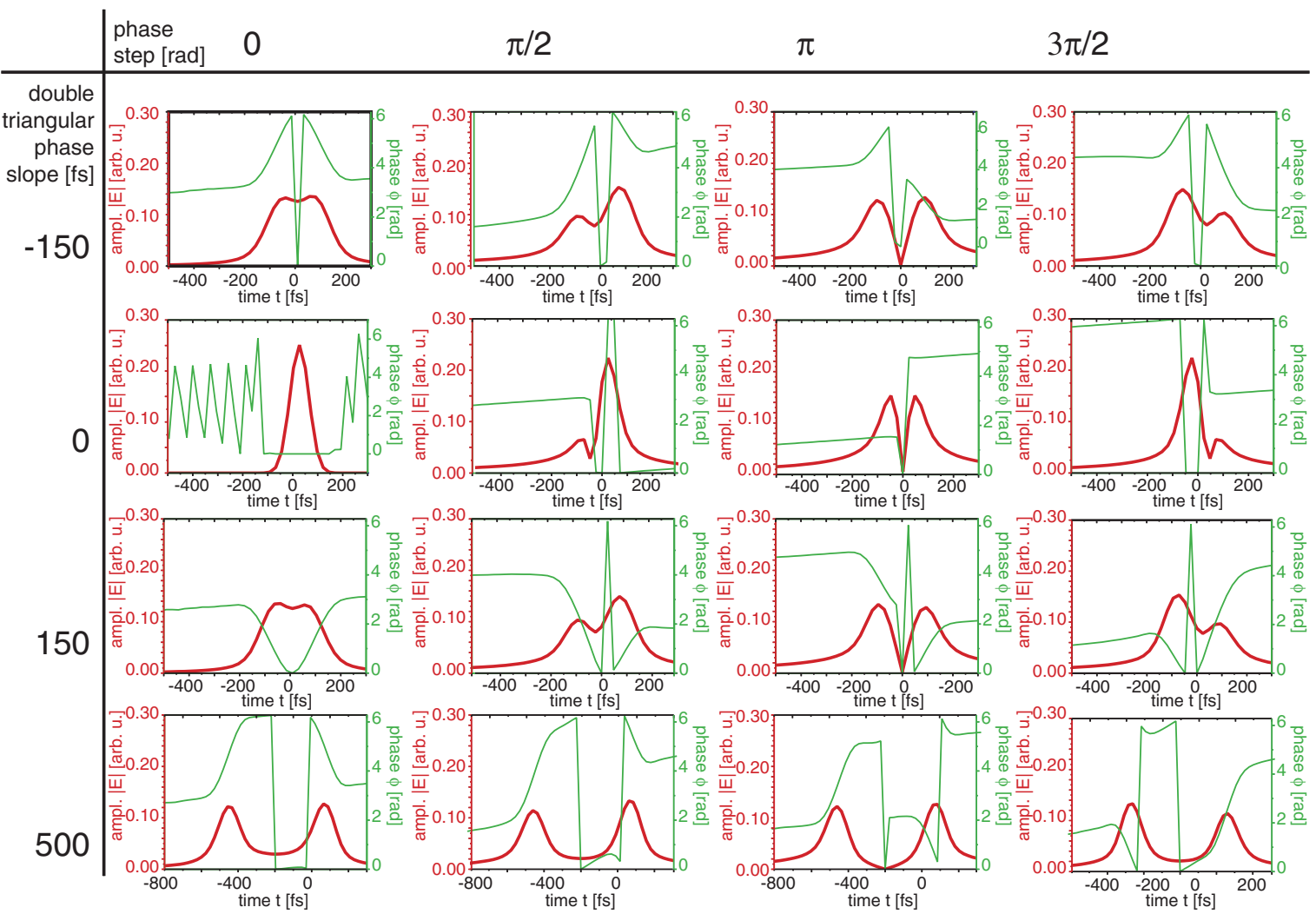


Figure A.9: Temporal pulse amplitude profiles and phases, calculated for the different spectral phases and amplitude profiles given in Figure A.8. For details see the text.

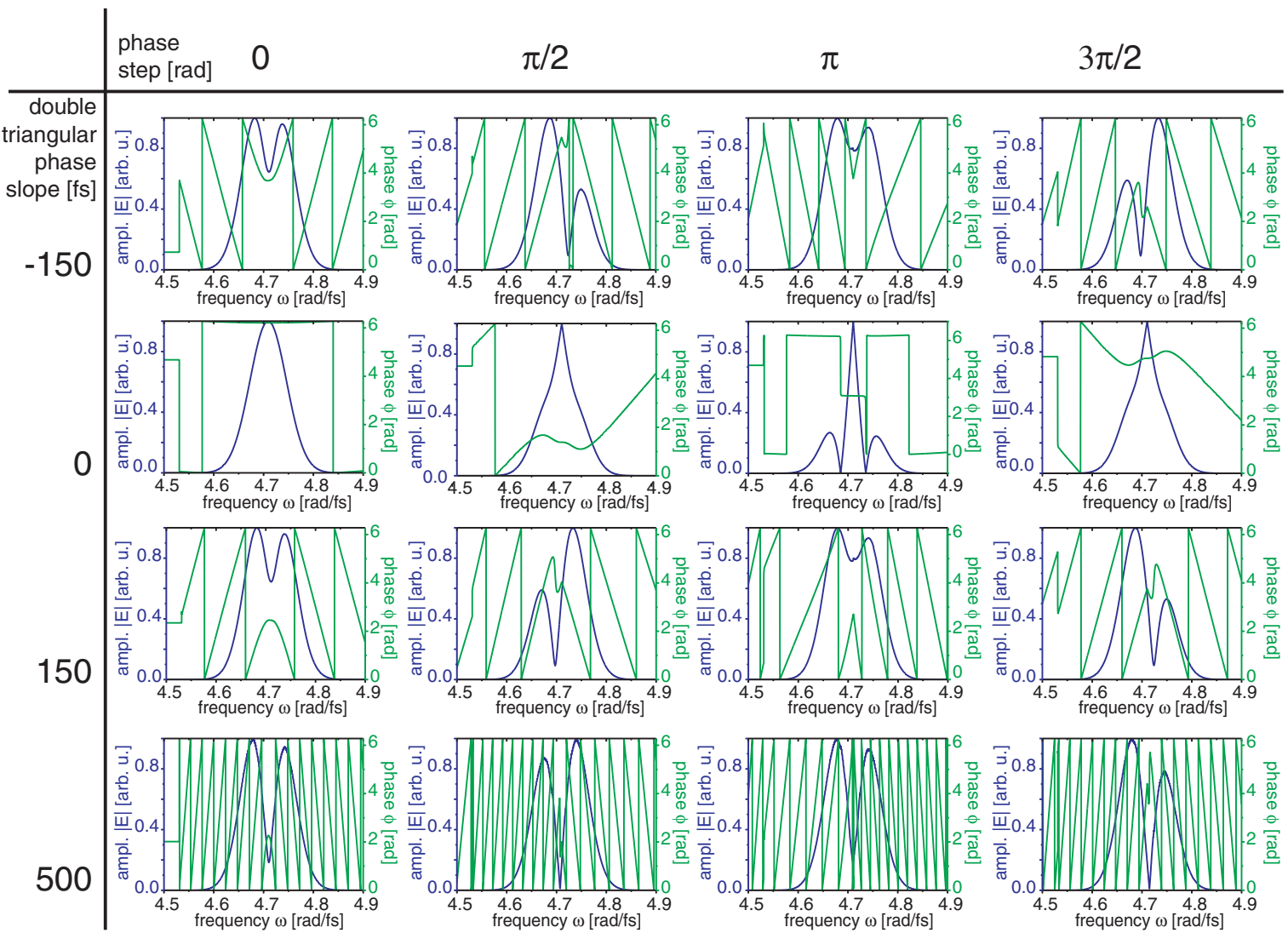


Figure A.10: Spectral pulse amplitude profiles and phases of the second harmonic for different spectral phases and amplitude profiles of the fundamental beam given in Figure A.8. For details see the text.

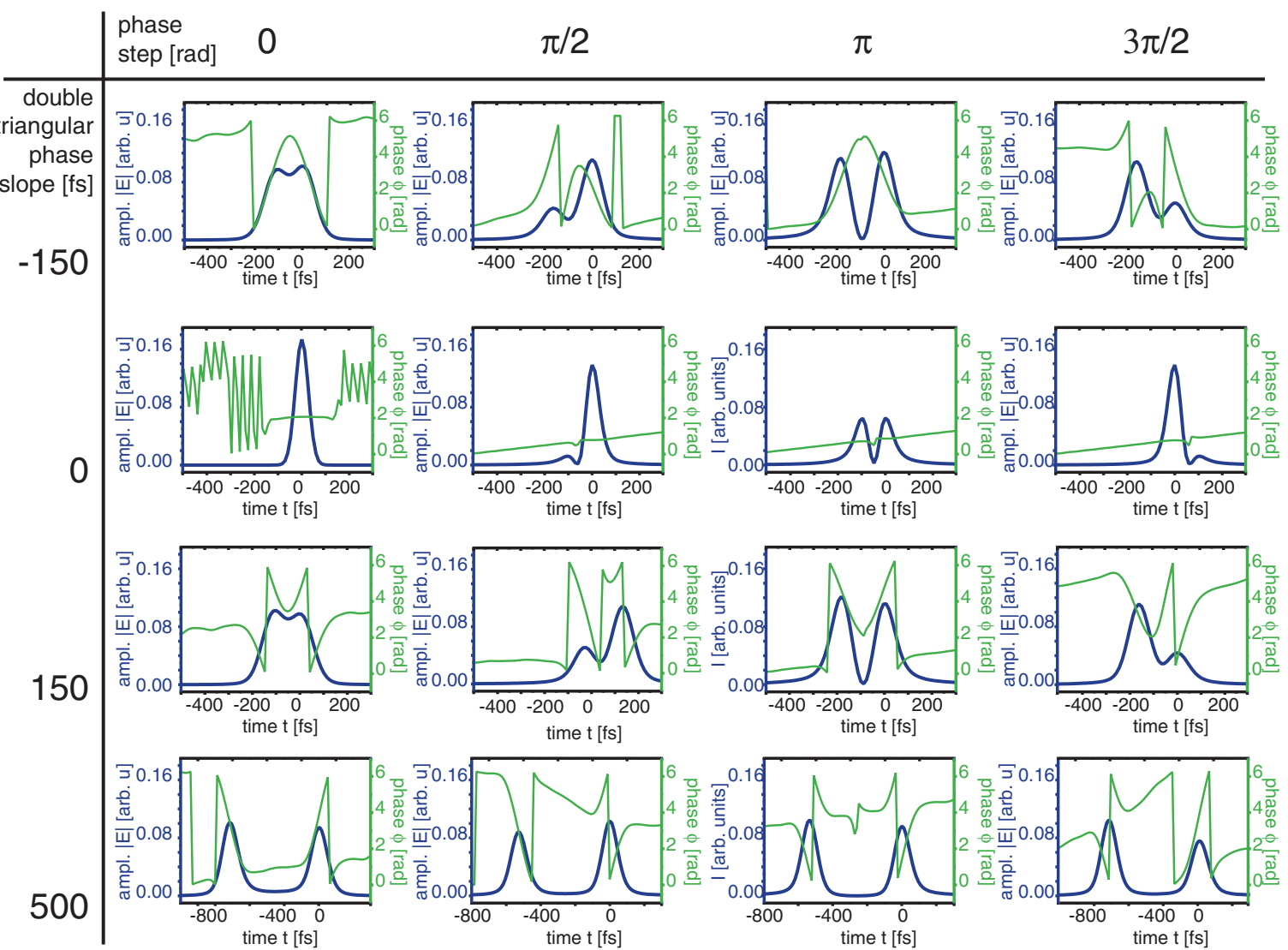


Figure A.11: Temporal pulse amplitude profiles and phases of the second harmonic for different spectral phases and amplitude profiles of the fundamental beam given in Figure A.8. For details see the text.





# Bibliography

- [1] R. S. JUDSON und H. RABITZ  
*Teaching lasers to control molecules*  
PRL **68** (10), 1500–1503 (1992)
- [2] A. ASSION, T. BAUMERT, M. BERGT, T. BRIXNER, B. KIEFER, V. SEYFRIED,  
M. STREHLE und G. GERBER  
*Control of chemical reactions by feedback-optimized phase-shaped femtosecond laser pulses*  
Science **282** (5390), 919–922 (1998)
- [3] M. BERGT, T. BRIXNER, B. KIEFER, M. STREHLE und G. GERBER  
*Controlling the femtochemistry of Fe(CO)<sub>5</sub>*  
J. Phys. Chem. A **103** (49), 10381–10387 (1999)
- [4] N. H. DAMRAUER, C. DIETL, G. KRAMPERT, S. H. LEE, K. H. JUNG und  
G. GERBER  
*Control of bond-selective photochemistry in CH<sub>2</sub>BrCl using adaptive femtosecond pulse shaping*  
Europ. Phys. J. D **103** (1), 71–76 (2002)
- [5] R. J. LEVIS, G. M. MENKIR und H. RABITZ  
*Selective bond dissociation and rearrangement with optimally tailored, strong-field laser pulses*  
Science **292** (5517), 709–713 (2001)
- [6] C. J. BARDEEN, V. V. YAKOVLEV, K. R. WILSON, S. D. CARPENTER, P. M.  
WEBER und W. S. WARREN  
*Feedback quantum control of molecular electronic population transfer*  
Chem. Phys. Lett. **280**, 151–158 (1997)
- [7] T. BRIXNER, N. H. DAMRAUER, P. NIKLAUS und G. GERBER  
*Photosensitive adaptive femtosecond quantum control in the liquid phase*  
Nature **414** (6859), 57–60 (2001)
- [8] T. BRIXNER, N. H. DAMRAUER, B. KIEFER und G. GERBER  
*Liquid-phase adaptive femtosecond quantum control: Removing intrinsic intensity dependences*  
J. Chem. Phys. **118** (8), 3692–3701 (2003)

- [9] J. L. HEREK, W. WOHLLEBEN, R. J. COGDELL, D. ZEIDLER und M. MOTZKUS  
*Quantum control of energy flow in light harvesting*  
Nature **417**, 533–535 (2002)
- [10] M. HESSE, H. MEIER und B. ZEEH  
*Spectroscopic methods in organic chemistry*  
Georg Thieme Verlag, Stuttgart (1997)
- [11] W. DEMTRÖDER  
*Laser spectroscopy. Basic concepts and instrumentation.*  
Springer, Berlin (2000)
- [12] R. SCHANZ, S. A. KOVALENKO, V. KHARLANOV und N. P. ERNSTING  
*Broad-band fluorescence upconversion for femtosecond spectroscopy*  
Appl. Phys. Lett. **79** (5), 566 (2001)
- [13] S. TAKEUCHI und T. TAHARA  
*Ultrafast fluorescence study on excited singlet-state dynamics of all-trans-retinal*  
J. Phys. Chem. A **101**, 3052 (1997)
- [14] W. DOMCKE, D. R. YARKONY und H. KÖPPEL  
*Conical Intersections - Electronic structure, dynamics & spectroscopy*  
World Scientific (2004)
- [15] A. T. YEH, C. V. SHANK und J. K. MCCUSKER  
*Ultrafast electron localization dynamics following photo-induced charge transfer*  
Science **289**, 935–938 (2000)
- [16] B. VALEUR  
*Molecular Fluorescence - Principles and application*  
Wiley-VCH (2002)
- [17] J. MICHL und E. THULSTRUP  
*Spectroscopy with polarized light*  
VCH (1995)
- [18] S. WALLIN, J. DAVIDSSON, J. MODIN und L. HAMMARSTRÖM  
*Femtosecond transient absorption anisotropy study on  $[Ru(bpy)_3]^{2+}$  and  $[Ru(bpy)(py)_4]^{2+}$ . Ultrafast interligand randomization of the MLCT State*  
J. Phys. Chem. A **109**, 4697–4704 (2005)
- [19] G. B. SHAW, C. L. BROWN und J. M. PAPANIKOLAS  
*Investigation of interligand electron transfer in polypyridyl complexes of OS(II) using femtosecond polarization anisotropy methods: examination of  $Os(bpy)_3^{2+}$  and  $Os(bpy)_2(mab)^{2+}$*   
J. Phys. Chem. A **106**, 1483–1495 (2002)
- [20] P. TOELE, H. ZHANG und M. GLASBEEK  
*Femtosecond fluorescence anisotropy studies of excited-state intramolecular double-proton transfer in [2,2'-bipyridyl]-3,3'-diol in solution*  
J. Phys. Chem. A **106**, 3651–3658 (2002)

- [21] K. WYNNE, G. D. REID und R. M. HOCHSTRASSER  
*Vibrational coherence in electron transfer: The tetracyanoethylene-pyrene complex*  
J. Chem. Phys. **105** (6), 2287–2297 (1996)
- [22] D. M. JONAS, M. J. LANG, Y. NAGASAWA, T. JOO und G. R. FLEMING  
*Pump-probe polarization anisotropy study of femtosecond energy transfer within the photosynthetic reaction center of rhodospirillum rubrum*  
J. Phys. Chem. **100**, 12660–12673 (1996)
- [23] D. ANESTOPOULOS, M. FAKIS, I. POLYZOS, G. TSIGARIDAS, P. PERSEPHONIS und V. GIANNETAS  
*Study of the isotropic and anisotropic fluorescence of two oligothiophenes by femtosecond time-resolved spectroscopy*  
J. Phys. Chem. B **109**, 9476–9481 (2005)
- [24] I. H. M. VAN STOKKUM, D. S. LARSEN und R. VAN GRONDELLE  
*Global and target analysis of time-resolved spectra*  
Biochimica et Biophysica Acta **1657**, 82–104 (2004)
- [25] K. WYNNE und R. M. HOCHSTRASSER  
*Coherent effects in the anisotropy of optical experiments*  
Chem. Phys. **171**, 179–188 (1993)
- [26] R. IMPROTA und F. SANTORO  
*A theoretical study on the factors influencing cyanine photoisomerization: the case of thiocyanine in gas phase and in methanol*  
J. Chem. Theo. Comp. **1**, 215–219 (2005)
- [27] S. HAHN und G. STOCK  
*Quantum-mechanical modelling of the femtosecond isomerization in rhodopsin*  
J. Phys. Chem. B **104**, 1146–1149 (2000)
- [28] S. HAHN und G. STOCK  
*Ultrafast cis-trans photoswitching: A model study*  
J. Chem. Phys. **116** (3), 1085–1091 (2001)
- [29] A. SANCHES-GALVEZ, P. HUNT, M. A. ROBB, M. OLIVUCCI, T. VREVEN und H. B. SCHLEGEL  
*Ultrafast Radiationless Deactivation of Organic Dyes: Evidence for a Two-State Two-Mode Pathway in Polymethine Cyanines*  
J. Am. Chem. Soc. **122** (12), 2911–2924 (2000)
- [30] A. J. WURZER, W. T. J. PIEL und E. RIEDLE  
*Comprehensive measurement of the  $S_1$  azulene relaxation dynamics and observation of vibrational wavepacket motion*  
Chem. Phys. Lett. **299**, 296–302 (1999)

- [31] S. L. DEXHEIMER, Q. WANG, L. A. PETEANU, W. T. POLLARD, R. A. MATHIES und C. V. SHANK  
*Femtosecond impulsive excitation of nonstationary vibrational states in bacteriorhodopsin*  
Chem. Phys. Lett. **188**, 61–66 (1992)
- [32] C. J. BARDEEN, Q. WANG und C. V. SHANK  
*Femtosecond chirped pulse excitation of vibrational wave packets in LD690 and Bacteriorhodopsin*  
J. Phys. Chem. A **102**, 2759–2766 (1998)
- [33] H. L. FRAGNITO, J. Y. BIGOT, P. C. BECKER und C. V. SHANK  
*Evolution of the vibronic absorption spectrum in a molecule following impulsive excitation with a 6 fs optical pulse*  
Chem. Phys. Lett. **160** (2), 101–104 (1989)
- [34] M. H. VOS und J.-L. MARTIN  
*Femtosecond processes in proteins*  
Biochimica et Biophysica Acta **1411**, 1–20 (1999)
- [35] N. P. ERNSTING, S. A. KOVALENKO, T. SENYUSHKINA, J. SAAM und V. FARZTDINOV  
*Wave-packet-assisted decomposition of femtosecond transient ultraviolet-visible absorption spectra: Application to excited-state intramolecular proton transfer in solution*  
J. Phys. Chem. A **105**, 3443–3453 (2001)
- [36] A. Z. SZARKA, N. PUGLIANO, D. K. PALIT und R. M. HOCHSTRASSER  
*Vibrational coherence in solution phase photoisomerization reaction of cis-stilbene*  
Chem. Phys. Lett. **240**, 25–30 (1995)
- [37] V. D. WAELE, M. BEUTTER, U. SCHMIDHAMMER, E. RIEDLE und J. DAUB  
*Switching dynamics of the photochromic 1,1-dicyano-2-(4-cyanophenyl)-1,8a-dihydroazulene probed by sub-30 fs spectroscopy*  
Chem. Phys. Lett. **390**, 328–334 (2004)
- [38] R. J. SENSION, S. T. REPINEC, A. Z. SZARKA und R. M. HOCHSTRASSER  
*Femtosecond laser studies of cis-stilbene photoisomerization reactions*  
J. Chem. Phys. **98** (8), 6291–6314 (1993)
- [39] M. BISCHOFF, G. HERMANN, S. RENTSCH und D. STREHLOW  
*Ultrashort processes of native phytochrome: Femtosecond kinetics of the far-red-absorbing form Pfr*  
J. Phys. Chem. A **102**, 4399–4404 (1998)

- [40] M. VENGRIS, I. H. M. VAN STOKKUM, X. HE, A. F. BELL, P. J. TONGE, R. VAN GRONDELLE und D. S. LARSEN  
*Ultrafast excited and ground-state dynamics of green fluorescent protein chromophore in solution*  
J. Phys. Chem. A **108**, 4587–4598 (2004)
- [41] D. K. PALIT, A. K. SINGH, A. C. BHASIKUTTAN und J. P. MITTAL  
*Relaxation dynamics in the excited states of LDS-821 in solution*  
J. Phys. Chem. A **105**, 6294–6304 (2001)
- [42] P. VÖHRINGER, R. A. WESTERVELT, T. S. YANG, D. C. ARNETT, M. J. FELDSTEIN und N. F. SCHERER  
*Solvent and frequency dependence of vibrational dephasing on femtosecond time-scales*  
J. Raman Spec. **26**, 535–551 (1995)
- [43] S. A. KOVALENKO, R. SCHANZ, V. M. FARZTDINOV, H. HENNIG und N. P. ERNSTING  
*Femtosecond relaxation of photoexcited para-nitroaniline: solvation, charge transfer, internal conversion and cooling*  
Chem. Phys. Lett. **323**, 312–322 (2000)
- [44] S. A. KOVALENKO, R. SCHANZ, , H. HENNIG und N. P. ERNSTING  
*Cooling dynamics of an optically excited molecular probe in solution from femtosecond broad transient absorption spectroscopy*  
J. Chem. Phys. **115** (7), 3256–3273 (2001)
- [45] G. STOCK  
*Classical description of nonadiabatic photoisomerization processes and their real-time detection via femtosecond spectroscopy*  
J. Chem. Phys. **103** (23), 10015–10029 (1995)
- [46] H. MIN, Y. N. KANG und J. PARK  
*Photoisomerization of symmetric carbocyanines*  
Bull. Korean Chem. Soc. **19** (7), 747–753 (1998)
- [47] M. R. V. SAHYUN und J. T. BLAIR  
*Photophysics of a simple “cyanine” dye*  
J. Photochem. Photobiol. A: Chem. **104**, 179–187 (1997)
- [48] J. C. OWRUTSKY und A. P. BARONAVSKI  
*Ultrafast infrared study of the ultraviolet photodissociation of  $Mn_2(CO)_{10}$*   
J. Chem. Phys. **105** (22), 9864–9871 (1996)
- [49] D. A. STEINHURST, A. P. BARONAVSKI und J. C. OWRUTSKY  
*Transient infrared spectroscopy of  $Mn_2(CO)_{10}$  with 400nm excitation*  
Chem. Phys. Lett. **361**, 513–519 (2002)

- [50] P. T. SNEE, H. YANG, K. T. KOTZ, C. K. PAYNE und C. B. HARRIS  
*Ultrafast infrared studies of the reaction mechanism of silicon-hydrogen bond activation by  $\eta^5$ -CpV(CO)<sub>4</sub>*  
J. Chem. Phys. **103** (49), 10426–10432 (1999)
- [51] P. T. SNEE, C. K. PAYNE, S. D. MEBANE, K. T. KOTZ und C. B. HARRIS  
*Dynamics of photosubstitution reactions of Fe(CO)<sub>5</sub>: An ultrafast infrared study of high spin reactivity*  
J. Am. Chem. Soc. **123**, 6909–6915 (2001)
- [52] N. PUGLIANO, S. GNANAKARAN und R. M. HOCHSTRASSER  
*The dynamics of photodissociation reactions in solution*  
J. Photochem. Photobiol A **102**, 21–28 (1996)
- [53] D. RAFTERY, E. GOODING, A. ROMANOVSKY und R. M. HOCHSTRASSER  
*Vibrational product state dynamics in solution phase bimolecular reactions: Transient infrared study of CN radical reactions*  
J. Chem. Phys. **101** (10), 8572–8579 (1994)
- [54] H. MIYASAKA, S. ARAKI, A. TABATA, T. NOBUTO, N. MATAGA und M. IRIE  
*Picosecond laser photolysis studies on photochromic reactions of 1,2-bis(2,4,5-trimethyl-3-thienyl)maleic anhydride in solutions*  
Chem. Phys. Lett. **230**, 249–254 (1994)
- [55] T. SAIKA, M. IRIE und T. SHIMIDZU  
*Thiophene Oligomers with a Photoswitch*  
J. Chem. Soc., Chem. Commun. S. 2123–2124 (1994)
- [56] N. TAMAI, T. SAIKA, T. SHIMIDZU und M. IRIE  
*Femtosecond dynamics of a thiophene oligomer with a photoswitch by transient absorption spectroscopy*  
J. Chem. Phys. **100** (12), 4689–4092 (1994)
- [57] A. H. ZEWAIL  
*Femtochemistry: Recent progress in studies of dynamics and control of reactions and their transient states*  
J. Phys. Chem. **100**, 1271–12724 (1996)
- [58] N. TAMAI und H. MIYASAKA  
*Ultrafast Dynamics of photochromic systems*  
Chem. Rev. **100**, 1875–1890 (2000)
- [59] U. ÅBERG, E. ÅKESSON, J. L. ALVAREZ, I. FEDCHENIA und V. SUNDSTRÖM  
*Femtosecond spectral evolution monitoring the bond-twisting event in barrierless isomerisation in solution*  
Chem. Phys. **183**, 269–288 (1994)
- [60] E. ÅKESSON, H. BERGSTRÖM, V. SUNDSTRÖM und T. GILLBRO  
*photochemical isomerization in the absence of a potential barrier*  
Chem. Phys. Lett. **126** (5), 385–393 (1986)

- [61] A. YARTSEV, J. L. ALVARES, U. ÅBERG und V. SUNDSTRÖM  
*Overdamped wavepacket motion along a barrierless potential energy surface in excited state isomerisation*  
Chem. Phys. Lett. **243**, 281–289 (1995)
- [62] U. ÅBERG, E. ÅKESSON und V. SUNDSTRÖM  
*Excited state dynamics of barrierless isomerization in solution*  
Chem. Phys. Lett. **215** (4), 388–394 (1993)
- [63] B. BAGCHI, U. ÅBERG und V. SUNDSTRÖM  
*Analysis of differing experimental results in barrierless reactions in solution*  
Chem. Phys. Lett. **162** (3), 227–232 (1989)
- [64] U. ÅBERG und V. SUNDSTRÖM  
*Photochemical isomerization in the absence of a potential barrier: origin of wavelength-dependent ground-state recovery kinetics*  
Chem. Phys. Lett. **185** (5,6), 461–467 (1991)
- [65] J.-L. ALVAREZ, A. YARTSEV, U. ÅBERG, E. ÅKESSON und V. SUNDSTRÖM  
*Resolving the turnover temperature dependence of the reaction rate in barrierless isomerization*  
J. Phys. Chem. B. **102**, 7651–7658 (1998)
- [66] R. W. SCHOENLEIN, L. A. PETEANU, R. A. MATHIES und C. V. SHANK  
*The first step in vision: Femtosecond isomerization of rhodopsin*  
Science **254**, 412–415 (1991)
- [67] D. OESTERHELT und W. STOECKENIUS  
*Rhodopsin-like protein from the purple membrane of halobacterium halobium*  
Nature New Biol. **233**, 149–155 (1971)
- [68] U. HAUPTS, J. TITTOR und D. OESTERHELT  
*Closing in on bacteriorhodopsin: Progress in understanding the molecule*  
Annu. Rev. Biomol. Struct. **28**, 367–399 (1999)
- [69] F. GAI, K. C. HASSON, J. C. MCDONALD und P. A. ANFINRUD  
*Chemical dynamics in proteins: The photoisomerization of retinal in bacteriorhodopsin*  
Science **279**, 1886–1891 (1998)
- [70] J. C. ALFANO, P. K. WALHOUT, Y. KIMURA und P. F. BARBARA  
*Ultrafast transient-absorption spectroscopy of the aqueous solvated electron*  
J. Chem. Phys. **98**, 5996–5998 (1993)
- [71] J. A. KLOEPFER, V. H. VILCHIZ, V. A. LENCHENKOV und S. E. BRADFORTH  
*Femtosecond dynamics of photoattachment of the iodide anion in solution: resonant excitation into the charge-transfer-to-solvent state*  
Chem. Phys. Lett. **298**, 120–128 (1998)

- [72] R. A. CROWELL und D. M. BARTELS  
*Multiphoton ionization of liquid water with 3.0-5.0 eV Photons*  
J. Phys. Chem. **100**, 17940–17949 (1996)
- [73] T. SCHEIDT und R. LAENEN  
*ionization of methanol: monitoring the trapping of electrons on the fs time scale*  
Chem. Phys. Lett. **371**, 445–450 (2003)
- [74] G. C. WALKER, E. AAKESSON, A. E. JOHNSON, N. E. LEVINGER und P. F. BARBARA  
*Interplay of solvent motion and vibrational excitation in electron-transfer kinetics: Experiment and theory*  
Chem. Phys. Lett. **96**, 3728–3736 (1992)
- [75] Y. H. MEYER, M. PITTMAN und P. PLAZA  
*Transient absorption of symmetrical carbocyanines*  
J. Photochem. Photobio. A **114**, 1–21 (1998)
- [76] S. A. KOVALENKO, A. L. DOBRYAKOV, J. RUTHMANN und N. P. ERNSTING  
*Femtosecond spectroscopy of condensed phases with chirped supercontinuum probing*  
Phys. Rev. A **59** (3), 2369–2384 (1999)
- [77] J. DIELS und W. RUDOLPH  
*Ultrashort laser pulse phenomena: fundamentals, techniques, and applications on a femtosecond time scale*  
Academic Press (1995)
- [78] H. ZEWEIL  
*Laser selective chemistry - is it possible?*  
Phys. Today **33**, 27–33 (1980)
- [79] H. ZEWEIL  
*Energy redistribution in isolated molecules and the question of mode-selective laser chemistry revisited*  
J. Phys. Chem **88** (23), 5459–5465 (1984)
- [80] Y. OHTSUKI, K. NAKAGAMI, Y. FUJIMURA, W. ZHU und H. RABITZ  
*Quantum optimal control of multiple targets: Development of a monotonically convergent algorithm and application to intramolecular vibration energy redistribution control*  
J. Chem. Phys. **114** (20), 8867–8876 (2001)
- [81] A. ASSION, T. BAUMERT, U. WEICHMANN und G. GERBER  
*Photofragmentation of  $\text{Na}_2^+$  in intense femtosecond laser fields: From photodissociation on light-induced potentials to field ionization*  
Phys. Rev. Lett. **86** (25), 5695 (2001)
- [82] T. FROHNMEYER, M. HOFMANN, M. STREHLE und T. BAUMERT  
*Mapping molecular dynamics ( $\text{Na}_2$ ) in intense laser fields: another dimension to femtochemistry*  
Chem. Phys. Lett. **312**, 447–454 (1999)



- [83] H. NIKURA, D. M. VILLENEUVE und P. B. CORKUM  
*Stopping a vibrational wave packet with laser-induced dipole forces*  
Phys. Rev. Lett. **92** (13), 133002 (2004)
- [84] M. WOLLENHAUPT, A. PRÄKELT, C. SARPE-TUDORAN, D. LIESE und  
T. BAUMERT  
*Strong field quantum control by selective population of dressed states*  
J. Opt. B. **7**, 270–276 (2005)
- [85] D. J. TANNOR, R. KOSLOFF und S. A. RICE  
*Coherent pulse sequence induced control of selectivity of reactions: Exact quantum  
mechanical calculations*  
J. Chem. Phys. **85**, 5805–5820 (1986)
- [86] D. J. TANNOR und S. A. RICE  
*Control of selectivity of chemical reaction via control of wavepacket evolution*  
J. Chem. Phys. **83**, 5013–5018 (1985)
- [87] T. BAUMERT, M. GROSSER, R. THALWEISER und G. GERBER  
*Femtosecond time-resolved molecular multiphoton ionization: The Na<sub>2</sub> system*  
Phys. Rev. Lett. **67** (27), 3753–3756 (1991)
- [88] R. J. GORDON und S. A. RICE  
*Active control of the dynamics of atoms and molecules*  
Annu. Rev. Phys. Chem. **48**, 601–641 (1997)
- [89] P. BRUMER und M. SHAPIRO  
*Control of unimolecular reactions using coherent light*  
Chem. Phys. Lett. **126**, 541–564 (1986)
- [90] S. M. PARK, S. P. LU und R. J. GORDON  
*Coherent laser control of the resonance-enhanced multiphoton ionization of HCl*  
J. Chem. Phys. **94**, 8622–8624 (1991)
- [91] C. CHEN, Y.-Y. YIN und D. S. ELLIOTT  
*Interference between optical transitions*  
Phys. Rev. Letters **64** (5), 507–510 (1989)
- [92] G. XING, X. WANG, X. HUANG, R. BERSOHN und B. KATZ  
*Modulation of resonant multiphoton ionization of CH<sub>3</sub>I by laser phase variation*  
J. Chem. Phys. **104** (3), 826–831 (1995)
- [93] S.-P. LU, S. M. PARK, Y. XIE und R. J. GORDON  
*Coherent laser control of bound-to-bound transitions of HCl and CO*  
J. Chem. Phys. **96** (9), 6613–6620 (1992)
- [94] M. SHAPIRO, J. W. HEPBURN und P. BRUMER  
*Simplified laser control of unimolecular reactions: Simultaneous ( $\omega_1, \omega_3$  excitation*  
Chem. Phys. Lett. **149** (5,6), 451–454 (1988)

- [95] S. L. LOGUNOV, V. V. VOLKOV, M. BRAUN und M. A. EL-SAYED  
*The relaxation dynamics of the excited electronic states of retinal in bacteriorhodopsin by two-pump-probe femtosecond studies*  
Proc. Nat. Ac. Scien. **98** (15), 8475–8479 (2001)
- [96] C. J. BARDEEN, J. CHE, K. R. WILSON, V. V. YAKOVLEV, C. C. M. V. A. APKARIAN, R. ZADOYAN, B. KOHLER und M. MESSINA  
*Quantum control of  $I_2$  in the gas phase and in condensed phase solid Kr matrix*  
J. Chem. Phys. **106** (20), 8486–8503 (1997)
- [97] B. KOHLER, V. V. YAKOVLEV, J. CHE, J. L. KRAUSE, M. MESSINA, K. R. WILSON, N. SCHWENTNER, R. M. WITNELL und Y. J. YAN  
*Quantum control of wave packet evolution with tailored femtosecond pulses*  
Phys. Rev. Letters **74** (17), 3360–3363 (1995)
- [98] M. ABE, Y. OHTSUKI, Y. FUJIMURA und W. DOMCKE  
*Optimal control of ultrafast cis-transphotoisomerization of retinal in rhodopsin via a conical intersection*  
J. Chem. Phys. **123**, 144508 (2005)
- [99] D. MESHULACH und H. SILBERBERG  
*Coherent quantum control of two-photon transitions by a femtosecond laser pulse*  
Nature **396**, 239–242 (1998)
- [100] D. MESHULACH und H. SILBERBERG  
*Coherent quantum control of multiphoton transitions by shaped ultrashort optical pulses*  
Phys. Rev. A **60** (2), 1287–1292 (1998)
- [101] S. P. SHAH und S. A. RICE  
*A test of the dependence of an optimal control field on the number of molecular degrees of freedom: HCN isomerization*  
J. Chem. Phys. **113** (16), 6536–6541 (2000)
- [102] H. RABITZ, R. DE VIVIE-RIEDLE, M. MOTZKUS und K. KOMPA  
*Wither the future of controlling quantum phenomena?*  
Science **288**, 824–828 (2000)
- [103] A. M. WEINER, D. E. LEAIRD, J. S. PATEL und J. R. WULLERT  
*Programmable femtosecond pulse shaping by use of a multielement liquid-crystal phase modulator*  
Opt. Lett. **15**, 326 (1990)
- [104] A. M. WEINER, D. E. LEAIRD, J. S. PATEL und I. J. R. WULLERT  
*Programmable shaping of femtosecond optical pulses by use of 128-element liquid crystal phase modulator*  
IEEE J. Quantum Electron. **28** (4), 908 (1992)
- [105] T. BRIXNER und G. GERBER  
*Femtosecond polarization pulse shaping*  
Opt. Lett. **26** (8), 557–559 (2001)

- [106] V. SEYFRIED  
*Beobachtung und Kontrolle molekularer Dynamik durch Femtosekundenlaserpulse*  
Dissertation, Universität Würzburg, Physikalisches Institut (1998)
- [107] T. BAUMERT, T. BRIXNER, V. SEYFRIED, M. STREHLE und G. GERBER  
*Femtosecond pulse shaping by an evolutionary algorithm with feedback*  
Appl. Phys B **65**, 779–782 (1997)
- [108] T. BRIXNER  
*Adaptive femtosecond quantum control*  
Dissertation, Universität Würzburg, Physikalisches Institut (2001)
- [109] V. I. PROKHORENKO, A. M. NAGY und R. J. D. MILLER  
*Coherent control of the population transfer in complex solvated molecules at weak excitation. An experimental study*  
J. Chem. Phys. **122**, 184502 (2005)
- [110] T. HORNING, R. MEIER und M. MOTZKUS  
*Optimal control of molecular states in a learning loop with a parameterization in frequency and time domain*  
Chem. Phys. Lett. **326**, 445–453 (2000)
- [111] T. C. WEINACHT, J. L. WHITE und P. H. BUCKSBAUM  
*Toward strong field mode-selective chemistry*  
J. Phys. Chem. **103** (49), 10166–10168 (1999)
- [112] G. VOGT, G. KRAMPERT, P. NIKLAUS, P. NUERNBERGER und G. GERBER  
*Optimal Control of Photoisomerization*  
Phys. Rev. Lett. **94**, 068305 (2005)
- [113] E. PAPASTATHOPOULOS, M. STREHLE und G. GERBER  
*Optimal control of femtosecond multiphoton double ionization of atomic calcium*  
Chem. Phys. Lett. **408** (1-3), 65–70 (2005)
- [114] C. DANIEL, J. FULL, L. GONZÁLEZ, C. LUPULESCU, J. MANZ, A. MERLI, Š. VAJDA und L. WÖSTE  
*Deciphering the reaction dynamics underlying optimal control laser fields*  
Science **299**, 536–539 (2003)
- [115] A. LINDINGER, C. LUPULESCU, M. PLEWICKI, F. VETTER, A. MERLI, S. M. WEBER und L. WÖSTE  
*Isotope selective ionization by optimal control using shaped femtosecond laser pulses*  
Phys. Rev. Lett. **93** (3), 033001 (2004)
- [116] Š. VAJDA, A. BARTELT, E.-C. KAPOSTA, T. LEISNER, C. LUPULESCU, S. MINEMOTO, P. ROSENDO-FRANCISCO und L. WÖSTE  
*Feedback optimization of shaped femtosecond laser pulses for controlling the wavepacket dynamics and reactivity of mixed alkaline clusters*  
Chem. Phys. **267**, 231–239 (2001)

- [117] T. HORNING, R. MEIER, R. DE VIVIE-RIEDLE und M. MOTZKUS  
*Coherent control of the molecular four-wave-mixing response by phase and amplitude shaped pulses*  
Chem. Phys. **267**, 261–276 (2001)
- [118] B. GANEM  
*Detection of noncovalent receptor-ligand complexes by mass spectrometry*  
J. Am. Chem. Soc. **113**, 6294–6296 (1991)
- [119] E. MAROTTA, A. LAPOLLA, D. FEDELE, A. SENESI, R. REITANO, R. SERAGLIA und P. TRALDI  
*Accurate mass measurements by Fourier transform mass spectrometry in the study of advanced glycation end products / peptides*  
J. Mass Spectrom. **38**, 196–205 (2003)
- [120] X. SHI, Y. NISHIMURA, S. AKASHI, A. TAKAMIZAWA und K. HIRAOKA  
*Evaluation of Binding Affinity of protein-mutant DNA complexes in solution by laser spray mass spectrometry*  
J. Am. Soc. Mass Spectrom. **17**, 611–620 (2006)
- [121] A. M. WEINER, D. E. LEAIRD, G. P. WIEDERRECHT und K. A. NELSON  
*Femtosecond pulse sequences used for optical manipulation of molecular-motion*  
Science **247**, 1317 (1990)
- [122] T. CHEN, A. VIERHEILIG, P. WALTER, M. HEID, W. KIEFER und A. MATERNY  
*Femtosecond laser-controlled selective excitation of vibrational modes on a multidimensional ground state potential energy surface*  
Chem. Phys. Lett. **326**, 375 (2000)
- [123] T. HELLERER, A. M. K. ENEJDER und A. ZUMBUSCH  
*Spectral focusing: High spectral resolution spectroscopy with broad-bandwidth laser pulses*  
Appl. Phys. Lett. **85**, 25 (2004)
- [124] K. P. KNUTSEN, J. C. JOHNSON, A. E. MILLER, P. B. PETERSEN und R. J. SAYKALLY  
*High spectral resolution multiplex CARS spectroscopy using chirped pulses*  
Chem. Phys. Lett. **387**, 436 (2004)
- [125] J. KONRADI, A. K. SINGH und A. MATERNY  
*Mode-focusing in molecules by feedback-controlled shaping of femtosecond laser pulses*  
Phys. Chem. Chem. Phys. **7**, 3574 (2005)
- [126] D. ORON, N. DUDOVICH, D. YELIN und Y. SILBERBERG  
*Quantum control of coherent anti-Stokes Raman processes*  
Phys. Rev. A **65**, 043408 (2002)
- [127] D. ORON, N. DUDOVICH, D. YELIN und Y. SILBERBERG  
*Narrow-band coherent anti-stokes Raman signals from broad-band pulses*  
Phys. Rev. Lett. **88**, 063004 (2002)

- [128] D. ORON, N. DUDOVICH und Y. SILBERBERG  
*Femtosecond phase-and-polarization control for background-free coherent anti-Stokes Raman spectroscopy*  
Phys. Rev. Lett. **90**, 213902 (2003)
- [129] T. POLACK, D. ORON und Y. SILBERBERG  
*Control and measurement of a non-resonant Raman wavepacket using a single ultrashort pulse*  
Chem. Phys. **318**, 163 (2005)
- [130] A. M. WEINER, D. E. LEAIRD, G. P. WIEDERRECHT und K. A. NELSON  
*Femtosecond multiple-pulse impulsive stimulated Raman-scattering spectroscopy*  
J. Opt. Soc. Am. B **8**, 1264 (1991)
- [131] B. J. PEARSON, J. L. WHITE, T. C. WEINACHT und P. H. BUCKSBAUM  
*Coherent control using adaptive learning algorithms*  
Phys. Rev. A **63**, 063412 (2001)
- [132] N. DUDOVICH, D. ORON und Y. SILBERBERG  
*Single-pulse coherently controlled nonlinear Raman spectroscopy and microscopy*  
Nature **418**, 512–514 (2002)
- [133] N. DUDOVICH, D. ORON und Y. SILBERBERG  
*Single-pulse coherent anti-Stokes Raman spectroscopy in the fingerprint spectral region*  
J. Chem. Phys. **118**, 9208 (2003)
- [134] B. VON VACANO, W. WOHLLEBEN und M. MOTZKUS  
*Actively shaped supercontinuum from a photonic crystal fiber for nonlinear coherent microspectroscopy*  
Opt. Lett. **31**, 413 (2006)
- [135] B. VON VACANO, W. WOHLLEBEN und M. MOTZKUS  
*Single-beam CARS spectroscopy applied to low-wavenumber vibrational modes*  
J. Raman Spectrosc. **37**, 404 (2006)
- [136] M. MOTZKUS, S. PETERSEN und A. H. ZEWAIL  
*Femtosecond real-time probing of reactions: 19. Nonlinear (DFWM) techniques for probing transition states of uni- and bimolecular reactions*  
J. Phys. Chem. **100**, 5620–5633 (1996)
- [137] Q. H. XU und G. R. FLEMING  
*Isomerization dynamics of 1,1'-diethyl-4,4'-cyanine (1144C) studied by different third-order nonlinear spectroscopic measurements*  
J. Phys. Chem. A **105**, 10187–10195 (2001)
- [138] H. GÜNZLER und H. M. HEISE  
*IR-Spektroskopie*  
VCH (1996)

- [139] D. CARDOZA, F. LANGHOJER, C. TRALLERO-HERRERO, O. L. A. MONTI und T. WEINACHT  
*Changing pulse-shape bases for molecular learning control*  
Phys. Rev. A **70**, 053406 (2004)
- [140] F. LANGHOJER, D. CARDOZA, M. BAERTSCHY und T. WEINACHT  
*Gaining mechanistic insight from closed loop learning control: The importance of basis in searching the phase space*  
J. Chem. Phys. **122**, 014102 (2004)
- [141] D. CARDOZA, C. TRALLERO-HERRERO, F. L. H. RABITZ und T. WEINACHT  
*Transformations to diagonal bases in closed-loop quantum learning control experiments*  
J. Chem. Phys. **122**, 124306 (2005)
- [142] J. L. WHITE, B. J. PEARSON und P. H. BUCKSBAUM  
*Extracting quantum dynamics from genetic learning algorithms through principal control analysis*  
J. Phys. B. **37**, L399–L405 (2004)
- [143] C. J. BARDEEN, V. V. YAKOVLEV, J. A. SQUIER und K. R. WILSON  
*Quantum control of population transfer in green fluorescent protein by using chirped femtosecond pulses*  
J. Am. Chem. Soc. **120**, 13023–13027 (1998)
- [144] K. MISAWA und T. KOBAYASHI  
*Wave-packet dynamics in a cyanine dye molecule excited with femtosecond chirped pulses*  
J. Chem. Phys. **113** (17), 7449–7553 (2000)
- [145] J. CAO, C. J. BARDEEN und K. R. WILSON  
*Molecular  $\pi$  pulses: Population inversion with positively chirped short pulses*  
J. Chem. Phys. **113** (5), 1898–1908 (2000)
- [146] M. RENARD, R. CHAUX, B. LAVOREL und O. FAUCHER  
*Pulse trains produced by phase-modulation of ultrashort optical pulses: tailoring and characterization*  
Optics Express **12** (3), 473–482 (2004)
- [147] B. SCHMIDT, M. HACKER, G. STOBRAWA und T. FEURER  
*LAB2-A virtual femtosecond laser lab*  
<http://www.lab2.de> (2005)
- [148] COHERENT  
*Operator's manual, Verdi V-5*  
Coherent, Inc (2002)
- [149] D. E. SPENCE, P. N. KEAN und W. SIBBETT  
*60-fsec pulse generation from a self-mode-locked Ti:sapphire laser*  
Opt. Lett. **16** (1), 42–44 (Januar 1991)

- [150] M. PESSOT, J. SQUIER und G. MOUROU  
*Chirped-pulse amplification of 100-fsec pulses*  
Opt. Lett. **14** (15), 797–799 (1989)
- [151] COHERENT  
*Evolution-15, User manual*  
Coherent, Inc (2005)
- [152] M. BASS, P. A. FRANKEN, J. F. WARD und G. WEINREICH  
*Optical rectification*  
Phys. Rev. Lett. **9**, 446–448 (1962)
- [153] Y. R. SHEN  
*The principles of nonlinear optics*  
John Wiley & Sons Inc. (1994)
- [154] L. BERGMANN und SCHAEFER  
*Optik*  
Walter de Gruyter (1993)
- [155] D. C. P. N. BUTCHER  
*The elements of nonlinear optics*  
Cambridge University Press (1990)
- [156] T. WILHELM, J. PIEL und E. RIEDLE  
*Sub-20-fs pulses tunable across the visible from a blue pumped single pass noncollinear parametric converter*  
Opt. Lett. **22** (5), 1494–1496 (1997)
- [157] A. BALTUŠKA, T. FUJI und T. KOBAYASHI  
*Visible pulse compression to 4 fs by optical parametric amplification and programmable dispersion control*  
Opt. Lett. **27** (5), 306–308 (2002)
- [158] T. KOBAYASHI und A. SHIRAKAWA  
*Sub-10-fs tunable pulses in visible and NIR and visible sub-5-fs pulses generated by noncollinear OPA*  
J. Luminescence **87-89**, 119–120 (2000)
- [159] T. KOBAYASHI und A. SHIRAKAWA  
*Tunable visible and near-infrared pulse generator in a 5 fs regime*  
Appl. Phys. B **70 Suppl.**, 239–246 (2000)
- [160] A. ASSION  
*Femtosekunden-zeitaufgelöste Untersuchungen molekularer Dynamik in schwachen und starken Laserfeldern*  
Dissertation, Universität Würzburg, Physikalisches Institut (1998)
- [161] L. C. LTD.  
*TOPAS - Travelling-wave Optical Parametric Amplifier of Superfluorescence - users's manual*  
Manual, Excel/Quantronix, Roentgenstr. 84, D-64291 Darmstadt (1999)

- [162] W. H. KNOX, R. L. FORK, M. C. DOWNER, R. H. STOLEN und C. V. SHANK  
*Optical pulse compression to 8 fs at 5 kHz repetition rate*  
Appl. Phys. Lett. **46**, 1120–1121 (1985)
- [163] J. E. ROTHENBERG und D. GRISCHKOWSKY  
*Observation of the formation of an optical intensity shock and wave breaking in the nonlinear propagation of pulses in optical fibers*  
Phys. Rev. Lett. **62**, 531–533 (1989)
- [164] J. E. ROTHENBERG  
*Pulse splitting during self-focusing in normal dispersive media*  
Opt. Lett. **17**, 583–586 (1992)
- [165] C. NAGURA, A. SUDAN, H. KAWANO, M. OBARA und K. MIDORIKAWA  
*Generation and characterisation of ultrafast white-light continuum in condensed media*  
Appl. Opt. **41** (18), 3735–3742 (2002)
- [166] O. E. MARTÍNEZ  
*Matrix formalism for pulse compressors*  
IEEE J. Quantum Elec. **24** (12), 2530–2536 (1988)
- [167] C. W. HILLEGAS, J. X. HULL, D. GOSWAMI, D. STRICKLAND und W. S. WARREN  
*Femtosecond laser pulse shaping by use of microsecond radio-frequency pulses*  
Opt. Lett. **19**, 737–739 (1994)
- [168] M. A. DUGAN, J. X. TULL und W. S. WARREN  
*High-resolution acousto-optic shaping of unamplified and amplified femtosecond laser pulses*  
J. Opt. Soc. Am. B. **14** (9), 2348–2358 (1997)
- [169] M. HACKER, G. STOBRAWA, R. SAUERBREY, T. BUCKUP, M. MOTZKUS, M. WILDENHAIN und A. GEHNER  
*Micromirror SLM for femtosecond pulse shaping in the ultraviolet*  
Appl. Phys. B **76**, 711–714 (2003)
- [170] C. RADZEWICZ, P. WASYLCHYK, W. WASUKIEWSJU und J. S. KRASIŃSKI  
*Piezo-driven deformable mirror for femtosecond pulse shaping*  
Opt. Lett. **29**, 177–179 (2004)
- [171] K. LI, U. KRISHNAMORTHY, J. P. HERITAGE und O. SOLGAARD  
*Coherent micromirror arrays*  
Opt. Lett. **27**, 366–368 (2002)
- [172] A. SUDA, Y. OISHI, K. NAGASAKA, P. WANG und K. MIDORIKAWA  
*A spatial light modulator based on fused-silica plates for adaptive feedback control of intense femtosecond laser pulses.*  
Opt. Express **9**, 2–6 (2001)



- [173] M. ROTH, M. MEHENDELE, A. BARTELT und H. RABITZ  
*Acousto-optical shaping of ultraviolet femtosecond pulses*  
Appl. Phys. B **80**, 441–444 (2005)
- [174] M. HACKER, R. NETZ, G. STOBRAWA, T. FEURER und R. SAUERBREY  
*Frequency doubling of phase-modulated ultrashort laser pulses*  
Appl. Phys. B **73**, 273–277 (2001)
- [175] M. HACKER, T. FEURER, R. SAUERBREY, T. LUCZA und G. SZABO  
*Programmable femtosecond laser pulses in the ultraviolet*  
J. Opt. Soc. Am. B **18** (6), 866–871 (2001)
- [176] R. TREBINO, K. W. DELONG, D. N. FITTINGHOFF, J. N. S. ABD  
M. A. KRUMBÜGEL und B. A. RICHMAN  
*Measuring ultrashort laser pulses in the time-frequency domain using  
frequency-resolved optical gating*  
Rev. Sci. Inst. **68**, 3277–3295 (1997)
- [177] D. KANE und R. TREBINO  
*Characterization of arbitrary femtosecond pulses using frequency-resolved optical  
gating*  
IEEE J. Quantum Electron. **29**, 571–579 (1993)
- [178] A. BALTUŠKA, M. S. PSHENICHNIKOV und D. O. WIERSMA  
*Second-harmonic generation frequency-resolved optical gating in the single-cycle  
regime*  
IEEE J. Quantum Electron. **35** (4), 459–478 (1999)
- [179] L. LEPETIT, G. CHÉRIAUX und M. JOFFRE  
*Linear techniques of phase measurement by femtosecond spectral interferometry for  
applications in spectroscopy*  
J. Opt. Soc. Am. B **12**, 2467–2474 (1995)
- [180] M. HIRASAWA, N. NAKAGAWA, K. YAMAMOTO, R. MOLITA, H. SHIGEKAWA und  
M. YAMASHITA  
*Sensitivity improvement of spectral phase interferometry for direct electric-field  
reconstruction for the characterisation of low-intensity femtosecond pulses*  
Appl. Phys. B. Suppl. **74**, 225–229 (2002)
- [181] C. DORRER und I. A. WALMSLEY  
*Accuracy criterion for ultrashort pulse characterisation techniques: application to  
spectral phase interferometry for direct electric field reconstruction*  
J. Opt. Soc. Am. B **19** (5), 1019–1029 (2002)
- [182] M. E. ANDERSON, L. E. E. DE ARAUJO, E. M. KOSIK und I. A. WALMSLEY  
*The effects of noise on ultrashort-optical-pulse measurement using SPIDER*  
Appl. Phys. B. Suppl. **70**, 85–93 (2000)

- [183] C. DORRER, B. DE BEAUVOIR, C. L. BLANC, S. RANC, J. P. ROUSSEAU, P. ROUSSEAU, J. P. CHAMBARET und F. SALIN  
*Single-shot real-time characterization of chirped-pulse amplification systems by spectral phase interferometry for direct electric-field reconstruction*  
Opt. Lett. **24** (22), 1644–1646 (1999)
- [184] C. DORRER  
*Implementation of spectral phase interferometry for direct electric-field reconstruction with a simultaneously recorded reference interferogram*  
Opt. Lett. **24** (21), 1432–1434 (1999)
- [185] C. IACONIS und I. A. WALMSLEY  
*Spectral phase interferometry for direct electric-field reconstruction of ultrashort optical pulses*  
Opt. Lett. **23** (10), 1030–1038 (1998)
- [186] L. LI, S. KUSAKA, N. KARASAWA, R. MORITA, H. SHIGEKAWA und M. YAMASHITA  
*Amplitude and phase characterisation of 5.0fs optical pulses using spectral phase interferometry for direct electric-field reconstruction*  
Jap. J. Appl. Phys. **40**, L684–L687 (2001)
- [187] J. K. RHEE, T. S. SOSNOWSKI, A. C. TIEN und T. B. NORRIS  
*Real-time dispersion analyzer of femtosecond laser pulses with use of spectrally and temporally resolved upconversion technique*  
J. Opt. Soc. Am. B **13**, 1780–1785 (1996)
- [188] J. K. RHEE, T. S. SOSNOWSKI, T. B. NORRIS, J. A. ARNS und W. S. COLBURN  
*Chirped-pulse amplification of 85-fs pulses at 250 kHz with third-order dispersion compensation by use of holographic transmission gratings*  
Chem. Phys. Lett. **19** (19), 1550–1552 (1994)
- [189] F. TECHNOLOGIES  
*FROG*  
Oakland, USA (2003/04)
- [190] S. LINDEN, H. GIESSEN und J. KUHL  
*XFROG - a new method for amplitude and phase characterization of weak ultrashort pulses*  
Phys. Stat. Sol. B **206**, 119–124 (1998)
- [191] A. YABUSHITA, T. FUJI und T. KOBAYASHI  
*SHG FROG and XFROG methods for phase/intensity characterization of pulses propagated through an absorptive optical medium*  
Opt. Commun. **198**, 227–232 (2001)
- [192] S. LINDEN, J. KUHL und H. GIESSEN  
*Amplitude and phase characterization of weak blue ultrashort pulses by downconversion*  
Opt. Lett. **24**, 569–571 (1999)

- [193] D. T. REID, P. LOZA-ALVAREZ, C. T. A. BROWN, T. BEDDARD und W. SIBBETT  
*Amplitude and phase measurement of mid-infrared femtosecond pulses by cross-correlation frequency-resolved optical gating*  
Opt. Lett. **25**, 1478–1480 (2000)
- [194] H. KÖPPEL, W. DOMCKE und L. S. CEDERBAUM  
*Multimode molecular dynamics beyond the Born-Oppenheimer approximation*  
Adv. Chem. Phys. **57**, 59–246 (1984)
- [195] R. SCHNEIDER und W. DOMCKE  
 *$S_1$ - $S_2$  conical intersection and ultrafast  $S_2 \rightarrow S_1$  internal conversion in pyrazine*  
Chem. Phys. Lett. **150** (3,4), 235–242 (1988)
- [196] R. SCHNEIDER, W. DOMCKE und H. KÖPPEL  
*Aspects of dissipative electronic and vibrational dynamics of strongly vibronic coupled systems*  
J. Chem. Phys. **92** (2), 1045–1061 (1990)
- [197] C. WOYWOD, W. DOMCKE, A. L. SOBOLEWSKI und H.-J. WERNER  
*Characterization of the  $S_1 - S_2$  conical intersection in pyrazine using *ab initio* multiconfiguration self-consistent-field and multireference configuration-interaction methods*  
J. Chem. Phys. **100** (2), 1400–1413 (1989)
- [198] W. DOMCKE, H. KÖPPEL und L. S. CEDERBAUM  
*Spectroscopic effects of conical intersections of molecular potential energy surfaces*  
Mol. Phys. **43** (4), 851–857 (1981)
- [199] L. SEIDNER und W. DOMCKE  
*Microscopic modelling of photoisomerization and internal-conversion dynamics*  
Chem. Phys. **186**, 27–40 (1994)
- [200] H. KOEPPPEL, L. S. CEDERBAUM und W. DOMCKE  
*Strong nonadiabatic effects and conical intersections in molecular spectroscopy and unimolecular decay:  $C_2H_4^+$*   
J. Chem. Phys. **77** (4), 2014–2022 (1981)
- [201] F. HUND  
*Zur Deutung der Molekelspektren I*  
Z. Physik **40**, 742–764 (1927)
- [202] J. VON NEUMANN und E. WIGNER  
*Über das Verhalten von Eigenwerten bei adiabatischen Prozessen*  
Physik Z. **30**, 467–470 (1929)
- [203] E. TELLER  
*The crossing of potential surfaces*  
J. Phys. Chem. S. 109–116 (1937)

- [204] L. S. CEDERBAUM, W. DOMCKE, H. KÖPPEL und W. VON NIESSEN  
*Strong vibronic coupling effects in ionization spectra: the "mystery band" of butatriene*  
Chem. Phys. **26**, 169–177 (1977)
- [205] S. HAHN und G. STOCK  
*Femtosecond secondary emission arising from the nonadiabatic photoisomerization in rhodopsin*  
Chem. Phys. **259**, 297–312 (2000)
- [206] S. SPÖRLEIN, H. CARSTENS, H. SATZGER, C. RENNER, R. BEHRENDT, L. MORODER, P. TAVAN, W. ZINTH und J. WACHTVEITL  
*Ultrafast spectroscopy reveals subnanosecond peptide conformational dynamics and validates molecular dynamics simulation*  
Proc. Natl. Acad. Sci. **99**, 7998 – 8002 (2002)
- [207] E. N. KALITEEVSKAYA, T. K. RAZUMOVA und A. N. TARNOVSKII  
*Effect of photoisomerization upon the process of lasing in solutions of symmetric and asymmetric cyanine dyes*  
Opt. Spectrosc. **86**, 126–133 (1999)
- [208] M. SPAETH und D. BORTFELD  
*stimulated emission from polymethine dyes*  
Appl. Phys. Lett. **9**, 179–181 (1966)
- [209] W. SIBBETT, J. R. TAYLOR und D. WELFORD  
*Substituent and environmental effects on the picosecond lifetimes of the polymethine cyanine dyes*  
IEEE J. Quant. Electron. **QE-17**, 500–509 (1981)
- [210] N. LANGFORD, K. SMITH und W. SIBBETT  
*Passively mode-locked color-center laser*  
IEEE J. Quant. Electron. **12**, 903–905 (1987)
- [211] A. NABER, U. C. FISCHER, S. KIRCHNER, T. DZIOMBA, G. KOLLAR, L. F. CHI und H. FUCHS  
*Architecture and surface properties of monomolecular films of a cyanine dye and their light-induced*  
J. Phys. Chem. **103**, 2709–2717 (1999)
- [212] A. GRETCHIKHINE, G. SCHWEITZER, M. V. DER AUWERAER, R. D. KEYZER, D. VANDENBROUCKE und F. D. SCHRYVER  
*Femtosecond transient absorption and luminescence decay studies of spectrally sensitized photographic emulsions*  
J. Appl. Phys. **85**, 1283–1293 (1999)
- [213] A. KHAZRAJI, S. HOTCHANDANI, S. DAS und P. KAMAT  
*Controlling dye (Merocyanine-540) aggregation on nanostructured TiO<sub>2</sub> films. An organized assembly approach for enhancing the efficiency of photosensitization*  
J. Phys. Chem. B **103**, 4693–4700 (1999)

- [214] Y. YONEZAWA, N. KOMETANI, T. SAKAUE und A. YANE  
*Photoreduction of silver ions in a colloidal titanium dioxide suspension*  
J. Photochem. Photobiol. A: Chem. **171**, 1–8 (2005)
- [215] J. S. KIM, T. Y. NAM und Y. J. HUH  
*The optical characteristics in the layers of compact disc-recordable*  
Korean J. Chem. Eng. **14**, 88–92 (1997)
- [216] A. MANDAL und M. K. PAL  
*Strong fluorescence emissions by H-aggregates of the dye thiocyanine in the presence of the surfactant aerosol-OT*  
Chem. Phys. **253**, 115–124 (2000)
- [217] C. PEYRATOUT und L. DAEHNE  
*Aggregation of thiocyanine derivatives on polyelectrolytes*  
Phys. Chem. Chem. Phys. **4**, 3032–3039 (2002)
- [218] T. N. TARNOVSKII, T. K. RAZUMOVA, E. P. SHCHELKINA und T. V. VESELOVA  
*Photophysical, photochemical, and lasing characteristics of symmetric and asymmetric di- and tricarbo-cyanine dyes*  
Optics and Spectroscopy **74**, 107–129 (1993)
- [219] T. K. RAZUMOVA und A. N. TARNOVSKII  
*Effect of photoisomerisation upon the process of lasing in solutions of symmetric and asymmetric cyanine dyes*  
Optics and Spectroscopy **86** (1), 139–147 (1999)
- [220] N. J. L. ROTH und A. C. CRAIG  
*Predicted observable fluorescent lifetimes of several cyanines*  
J. Phys. Chem. **78** (12), 1154–1155 (1974)
- [221] P. A. HUNT und M. A. ROBB  
*Systematic control of photochemistry: The dynamics of photoisomerization of a model cyanine dye*  
J. Am. Chem. Soc. **127**, 5720–5726 (2005)
- [222] B. BAGCHI, G. R. FLEMING und D. W. OXTOBY  
*Theory of electronic relaxation in solution in the absence of an activation barrier*  
J. Chem. Phys. **78** (12), 7375–7385 (1983)
- [223] G. VOGT, P. NUERNBERGER, R. IMPROTA, F. SANTORO und G. GERBER  
*Femtosecond study on the isomerization dynamics of NK88: II. Excited state dynamics*  
submitted to J. Chem. Phys. (2006)
- [224] P. NUERNBERGER, G. VOGT, R. IMPROTA, F. SANTORO und G. GERBER  
*Femtosecond study on the isomerization dynamics of NK88: I. Ground state dynamics after photoexcitation*  
submitted to J. Chem. Phys. (2006)

- [225] N. GRIGORIEFF, T. A. CESKA, K. H. DOWNING, J. M. BALDWIN und R. HENDERSON  
*Electron-crystallographic refinement of the structure of bacteriorhodopsin*  
J. Mol. Biol. **259**, 393–421 (1996)
- [226] E. RACKER und W. STOECKENIUS  
*Reconstitution of purple membrane vesicles catalyzing light-driven proton uptake and adenosine triphosphate formation*  
J. Bio. Chem. **249** (2), 662–663 (1974)
- [227] H. ABRAMCZYK  
*Femtosecond primary events in bacteriorhodopsin and its retinal modified analogs: Revision of commonly accepted interpretation of electronic spectra of transient intermediates in the bacteriorhodopsin photocycle*  
J. Chem. Phys. **120**, 11120–11132 (2004)
- [228] Y. OHTSUKI, K. OHARA, M. ABE, K. NAKAGAMI und Y. FUJIMURA  
*New quantum control pathway for a coupled-potential system*  
Chem. Phys. Lett. **369**, 525–533 (2003)
- [229] F. GROSSMANN, L. FENG, G. SCHMIDT, T. KUNERT und R. SCHMIDT  
*Optimal control of a molecular cis-trans isomerization model*  
Europhys. Lett. **60**, 201–206 (2002)
- [230] S. C. FLORES und V. S. BATISTA  
*Model study of coherent-control of the femtosecond primary event of vision*  
J. Phys. Chem. B **108**, 6745–6749 (2004)
- [231] M. V. KOROLKOV, J. MANZ und G. K. PARAMONOV  
*Theory of ultrafast laser control of isomerization reactions in an environment: Picosecond cope rearrangement of substituted semibullvalenes*  
J. Chem. Phys. **105** (24), 10874–10889 (1996)
- [232] J. MANZ, K. SUNDERMANN und R. DE VIVIE-RIEDLE  
*Quantum optimal control strategies for photoisomerization via electronically excited states*  
Chem. Phys. Lett. **290**, 415–422 (1998)
- [233] M. SUGAWARA und Y. FUJIMURA  
*Control of quantum dynamics by a locally optimized laser field. Application to ring puckering isomerization*  
J. Chem. Phys. **100** (8), 5646–5655 (1994)
- [234] L. BAÑARES, T. BAUMERT, M. BERGT, B. KIEFER und G. GERBER  
*The ultrafast photodissociation of Fe(CO)<sub>5</sub> in the gas phase*  
J. Chem. Phys. **108**, 5799–5811 (1998)
- [235] P. O. STOUTLAND, J.-C. LAMBRY, J.-L. MARTIN und W. H. WOODRUFF  
*Femtosecond dynamics of reduced cytochrome oxidase and its CO derivative*  
J. Phys. Chem. **95**, 6406–6408 (1995)

- [236] J. Z. ZHANG, B. J. SCHWARTZ, J. KING und C. B. HARRIS  
*Ultrafast studies of photochromic spiropyrans in solution*  
J. Am. Chem. Soc. **114**, 10921–10927 (1992)
- [237] T. ZHANG, C. CHEN, Q. GONG, W. YAN, S. WANG, H. YANG, H. JIAN und G. XU  
*Time-resolved excited state dynamics of a cyanine dye*  
Chem. Phys. Lett. **298**, 236–240 (1998)
- [238] V. GULBINAS, G. KODIS, S. JURSENAS, L. VALKUNAS, A. GRUODIS, J. C. MIALOCQ, S. POMMERET und T. GUSTAVSSON  
*Charge transfer induced excited state twisting of N,N-Dimethylaminobenzylidene-1,3-indandione in solution*  
J. Phys. Chem. A **103**, 3969–3980 (1999)
- [239] G. HARAN, E. A. MORLINO, J. MATTHES, R. H. CALLENDER und R. M. HOCHSTRASSER  
*Femtosecond polarized pump-probe and stimulated emission spectroscopy of the isomerization reaction of rhodopsin*  
J. Phys. Chem. A **103**, 2202–2207 (1999)
- [240] L. M. YODER, A. G. COLE, L. A. WALKER, II und R. J. SENSION  
*Time-Resolved Spectroscopic Studies of B<sub>12</sub> Coenzymes: Influence of Solvent on the Photolysis of Adenosylcobalamin*  
J. Phys. Chem. B **105**, 12180–12188 (2001)
- [241] D. S. LARSEN, M. VENGRIS, I. H. M. VAN STOKKUM, M. A. VAN DER HORST, F. L. DE WEERD, K. J. HELLINGWERF und R. VAN GRONDELLE  
*Photoisomerization and photoionization of the photoactive yellow protein chromophore in solution*  
Biophys. J. **86**, 2538–2550 (2004)
- [242] C. ADAMO und V. BARONE  
*Toward reliable density functional methods without adjustable parameters: The PBE0 model*  
J. Chem. Phys. **110**, 6158–6170 (1999)
- [243] M. ENZERHOF und G. E. SCUSERIA  
*Assessment of the Perdew-Burke-Ernzerhof exchange-correlation functional*  
J. Chem. Phys. **110**, 5029–5036 (1999)
- [244] C. PENG, P. Y. AYALA, H. B. SCHLEGEL und M. J. FRISCH  
*Using redundant internal coordinates to optimize equilibrium geometries and transition states*  
J. Comp. Chem. **17**, 49–56 (1996)
- [245] T. A. WESOLOWSKI, O. PARISEL, Y. ELLINGER und J. WEBER  
*Comparative study of benzene center dot center dot center dot X (X = O<sub>2</sub>, N<sub>2</sub>, CO) complexes using density functional theory: The importance of an accurate exchange-correlation energy density at high reduced density gradients*  
J. Chem. Phys. **101**, 7818–7825 (1997)

- [246] M. KAMIYA, T. TSUNEDA und K. HIRAO  
*A density functional study of van der Waals interactions*  
J. Chem. Phys. **117**, 6010–6015 (2002)
- [247] S. TSUZUKI und H. P. LÜTHI  
*Interaction energies of van der Waals and hydrogen bonded systems calculated using density functional theory: Assessing the PW91 model*  
J. Chem. Phys. **114**, 3949–3957 (2001)
- [248] R. IMPROTA und V. BARONE  
*Assessing the reliability of density functional methods in the conformational study of polypeptides: The treatment of intraresidue nonbonding interactions*  
J. Comp. Chem. **25**, 1333–1341 (2004)
- [249] M. COSSI, N. REGA, G. SCALMANI und V. BARONE  
*Polarizable dielectric model of solvation with inclusion of charge penetration effects*  
J. Chem. Phys. **114**, 5691–5701 (2001)
- [250] V. BARONE, M. COSSI und J. TOMASI  
*A new definition of cavities for the computation of solvation free energies by the polarizable continuum model*  
J. Chem. Phys. **107**, 3210–3221 (1997)
- [251] M. COSSI und V. BARONE  
*Time-dependent density functional theory for molecules in liquid solutions*  
J. Chem. Phys. **115**, 4708–4717 (2001)
- [252] M. J. FRISCH, G. W. TRUCKS, H. B. SCHLEGEL, G. E. SCUSERIA, M. A. ROBB, J. R. CHEESEMAN, J. A. M. J. AND T. VREVEN, K. N. KUDIN, J. C. BURANT, J. M. MILLAM, S. S. IYENGAR, J. TOMASI, V. BARONE, B. MENNUCCI, M. COSSI, G. SCALMANI, N. REGA, G. A. PETERSSON, H. NAKATSUJI, M. HADA, M. EHARA, K. TOYOTA, R. FUKUDA, J. HASEGAWA, M. ISHIDA, T. NAKAJIMA, Y. HONDA, O. KITAO, H. NAKAI, M. KLENE, X. LI, J. E. KNOX, H. P. HRATCHIAN, J. B. CROSS, C. ADAMO, J. JARAMILLO, R. GOMPERTS, R. E. STRATMANN, O. YAZYEV, A. J. AUSTIN, R. CAMMI, C. POMELLI, J. W. OCHTERSKI, P. Y. AYALA, K. MOROKUMA, G. A. VOTH, P. SALVADOR, J. J. DANNENBERG, V. G. ZAKRZEWSKI, S. DAPPRICH, A. D. DANIELS, M. C. STRAIN, O. FARKAS, D. K. MALICK, A. D. RABUCK, K. RAGHAVACHARI, J. B. FORESMAN, J. V. ORTIZ, Q. CUI, A. G. BABOUL, S. CLIFFORD, J. CIOSLOWSKI, B. B. STEFANOV, G. LIU, A. LIASHENKO, P. PISKORZ, I. KOMAROMI, R. L. MARTIN, D. J. FOX, T. KEITH, M. A. AL-LAHAM, C. Y. PENG, A. NANAYAKKARA, M. CHALLACOMBE, P. M. W. GILL, B. JOHNSON, W. CHEN, M. W. WONG, C. GONZALEZ, und J. A. POPLE  
*Gaussian 03, Revision B.01*  
Gaussian Inc., Pittsburgh PA (2003)
- [253] F. FURCHE und R. AHLRICHS  
*Adiabatic time-dependent density functional methods for excited state properties*  
J. Chem. Phys. **117**, 7433–7447 (2002)



- [254] M. WANKO, M. GARAVELLI, F. BERNARDI, T. A. NIEHAUS, T. FRAUENHEIM und M. ELSTNER  
*A global investigation of excited state surfaces within time-dependent density-functional response theory*  
J. Chem. Phys. **120**, 1674–1692 (2004)
- [255] A. . DREUW, J. L. WEISMAN und M. HEAD-GORDON  
*Long-range charge-transfer excited states in time-dependent density functional theory require non-local exchange*  
J. Chem. Phys. **119**, 2943–2946 (2004)
- [256] A. V. SMIRNOV, K. DAS, D. S. ENGLISH, Z. WAN, G. A. KRAUS und J. W. PETRICH  
*Excited-state intramolecular H atom transfer of hypericin and hypocrellin A investigated by fluorescence upconversion*  
J. Phys. Chem. A **103**, 7949–7957 (1999)
- [257] V. H. VILCHIZ, J. A. KLOEPFER, A. C. GERMAINE, V. A. LENCHENKOV und S. E. BRADFORTH  
*Map for the relaxation dynamics of hot photoelectrons injected into liquid water via anion threshold photodetachment and above threshold solvent ionization*  
J. Phys. Chem. A **105**, 1711–1723 (2001)
- [258] N. H. DAMRAUER, G. CERULLO, A. YEH, T. R. BOUSSIE, C. V. SHANK und J. K. MCCUSKER  
*New quantum control pathway for a coupled-potential system*  
Science **275**, 54–57 (1997)
- [259] N. H. DAMRAUER, T. R. BOUSSIE, M. DEVENNEY und J. K. MCCUSKER  
*Effects of intraligand electron delocalization, steric tuning, and excited-state vibronic coupling on the photophysics of aryl-substituted bipyridyl complexes of Ru(II)*  
J. Am. Chem. Soc. **119**, 8253–8268 (1997)
- [260] G. B. SHAW, D. J. STYERS-BARNETT, E. Z. GANNON, J. C. GRANGER und J. M. PAPANIKOLAS  
*Interligand electron transfer dynamics in  $[Os(bpy)_3]^{2+}$ : Exploring the excited state potential surfaces with femtosecond spectroscopy*  
J. Phys. Chem. A **108**, 4998–5006 (2004)
- [261] L. NIKOWA, D. SCHWARZER und J. TROE  
*Transient hot UV spectra in the collisional deactivation of highly excited trans-stilbene in liquid solvents*  
Chem. Phys. Lett. **233**, 303–308 (1995)
- [262] D. GEPPERT und R. DE VIVIE-RIEDLE  
*Reaction velocity control by manipulating the momentum of a nuclear wavepacket with phase-sensitive optimal control theory*  
Chem. Phys. Lett. **404**, 289–295 (2005)

- [263] T. G. V. SUNDSTRÖM  
*Viscosity-dependent isomerization yields of some cyanine dyes. A picosecond laser spectroscopy study*  
J. Phys. Chem. **86**, 1788–1794 (1982)
- [264] T. HASCHE, S. H. ASHWORTH, E. RIEDLE, M. WOERNER und T. ELSAESSER  
*Vibrational and vibronic dynamics of large molecules in solution studied on a 20fs timescale*  
Chem. Phys. Lett. **244**, 164–170 (1995)
- [265] M. S. CHURIO, K. P. ANGERMUND und S. E. BRASLAVSKY  
*Combination of laser-induced optoacoustic spectroscopy (LIOAS) and semiempirical calculations for the determination of molecular volume changes: the photoisomerization of carbocyanines*  
J. Phys. Chem. **98**, 1776–1782 (1994)
- [266] K. NAKATSU, H. YOSHIOKA und T. AOKI  
*The crystal structure of 3,3'-dieethyl-thiacyanine bromide*  
Chem. Lett. **5**, 339–340 (1972)
- [267] N. KATAYAMA, Y. OZAKI, S. YASUI und K. IRIYAMA  
*Spectroscopic studies of thiatri, penta- and heptamethine cyanine dyes: I. Structure of thiatri, penta- and heptamethine cyanine dyes in solution studied by NMR*  
J. Mol. Struct. **274**, 171–181 (1992)
- [268] S. GHELLI und G. PONTERINI  
*Identification of the photoisomers of two carbocyanines by  $^1\text{H}$  NMR spectroscopy*  
J. Mol. Struct. **355**, 193–200 (1995)
- [269] H. UMEDA, M. TAKAGI, S. YAMADA, S. KOSEKI und Y. FUJIMURA  
*Quantum control of molecular chirality: optical isomerisation of difluorobenzo[*c*]phenanthrene*  
J. Am. Chem. Soc. **124** (31), 9265–9271 (2002)
- [270] M. SHAPIRO, E. FRISHMAN und P. BRUMER  
*Coherently Controlled Asymmetric Synthesis with Achiral Light*  
Phys. Rev. Lett. **84**, 1669–1672 (2000)
- [271] Y. FUJIMURA, L. GONZÁLEZ, K. HOKI, J. MANZ und Y. OHTSUKI  
*Selective preparation of enantiomers by laser pulses: quantum model simulation for  $\text{H}_2\text{POSH}$*   
Chem. Phys. Lett. **306**, 1–8 (1999)
- [272] S. S. BYCHKOV, B. A. GRISHANIN und V. N. ZADKOV  
*Laser synthesis of chiral molecules in isotropic racemic media*  
J. Exp. Theor. Phys. **93**, 24–32 (2001)
- [273] F. BERNARDI, M. OLIVUCCI und M. A. ROBB  
*Potential energy surface crossings in organic photochemistry*  
Chem. Soc. Rev. **25** (5), 321 (1996)

- [274] M. BERGT  
*Photodissoziationsdynamik metallorganischer Moleküle: Beobachtung und Steuerung mit Femtosekunden-Laserpulsen*  
Dissertation, Universität Würzburg, Physikalisches Institut (1999)
- [275] G. CERULLO, C. J. BARDEEN, Q. WANG und C. V. SHANK  
*High-power femtosecond chirped pulse excitation of molecules in solution*  
Chem. Phys. Lett. **262**, 362–368 (1996)
- [276] R. A. MATHIES, C. H. B. CRUZ, W. T. POLLARD und C. V. SHANK  
*Direct observation of the femtosecond excited-state cis-trans isomerization in bacteriorhodopsin*  
Science **240**, 777–779 (1988)
- [277] Y. KOYAMA, K. KUBO, M. KOMORI, H. YASUDA und Y. MUKAI  
*Effect of protonation on the isomerization properties of n-butylamine schiff base of isomeric retinal as revealed by direct HPLC analysis: Selection of isomerization pathways by retinal proteins*  
Photochem. Photobiol. **54** (3), 433–443 (1991)
- [278] Y. SHICHIDA  
*Ultra-fast laser spectroscopy of visual pigments*  
Photochem. Photobiol. **52** (6), 1179–1185 (1990)
- [279] S. RUHMAN, B. HOU, N. FIEDMAN, M. OTTOLENGHI und M. SHEVES  
*Following evolution of bacteriorhodopsin in its reactive excited state via stimulated emission pumping*  
J. Am. Chem. Soc. **124**, 8854–8858 (2002)
- [280] F. GAI, J. C. MCDONALD und P. A. ANFINRUD  
*Pump-Dump-Probe spectroscopy of bacteriorhodopsin: Evidence for a Near-IR excited state absorbance*  
J. Am. Chem. Soc. **119**, 6201–6202 (1997)
- [281] D. ZEIDLER, S. FREY, W. WOHLLEBEN, M. MOTZKUS, F. BUSCH, T. CHEN, W. KIEFER und A. MATERNY  
*Optimal control of ground-state dynamics in polymers*  
J. Chem. Phys. **116**, 5231–5235 (2002)
- [282] D. ORON, N. DUDOVICH, D. YELIN und Y. SILBERBERG  
*Quantum control of coherent anti-Stokes Raman processes*  
Phys. Rev. A **65**, 043408 (2002)
- [283] G. HARAN, K. WYNNE, A. XIE, Q. HE, M. CHANCE und R. M. HOCHSTRASSER  
*Excited state dynamics of bacteriorhodopsin revealed by transient stimulated emission spectra*  
Chem. Phys. Lett. **261**, 389–395 (1996)
- [284] S. L. LOGUNOV, T. M. MASCIANGIOLI, V. F. KAMALOV und M. A. EL-SAYED  
*Low-temperature retinal photoisomerization dynamics in bacteriorhodopsin*  
J. Phys. Chem. B **102** (13), 2303–2306 (1998)

- [285] R. GONZÁLEZ-LUQUE, M. GARAVELLI, F. BERNARDI, M. MERCHÁN, M. A. ROBB und M. OLIVUCCI  
*Computational evidence in favor of a two-state two-mode model of the retinal chromophore photoisomerization*  
Proc. Natl. Acad. Sci. **97** (17), 9379–9384 (2000)
- [286] S. E. WHITMIRE, D. WOLPERT, A. G. MARKELZ, J. R. HILLEBRECHT, J. GALAN und R. R. BIRGE  
*Protein flexibility and conformational state: A comparison of collective vibrational modes of wild-type and D96N bacteriorhodopsin*  
Biophys. J. **85** (2), 1269–1277 (2003)
- [287] T. YE, N. FRIEDMAN, Y. GAT, G. H. ATKINSON, M. SHEVES, M. OTTOLENGHI und S. RUHMAN  
*On the nature of the primary light-induced events in bacteriorhodopsin: Ultrafast spectroscopy of native and C-13=C-14 locked pigments*  
J. Phys. Chem. B. **103**, 5122–5130 (1999)
- [288] S. H. ASHWORTH, T. HASCHE, M. WOERNER, E. RIEDLE und T. ELSAESSER  
*Vibronic excitations of large molecules in solution studied by two-color pump-probe experiments on the 20 fs time scale*  
J. Chem. Phys. **104**, 5761–5769 (1996)
- [289] U. BANIN, A. BARTANA, S. RUHMAN und R. KOSLOFF  
*Impulsive excitation of coherent vibrational motion ground surface dynamics induced by intense short laser pulses*  
J. Chem. Phys. **101** (10), 8461–8481 (1994)
- [290] A. E. JOHNSON und A. B. MYERS  
*A comparison of time- and frequency-domain resonance Raman spectroscopy in triiodide*  
J. Chem. Phys. **104** (7), 2497–2507 (1996)
- [291] T. KÜHNE und P. VÖHRINGER  
*Vibrational relaxation and geminate recombination in the femtosecond-photodissociation of triiodide in solution*  
J. Chem. Phys. **105** (24), 10788–10802 (1996)
- [292] T. KÜHNE, R. KÜSTER und P. VÖHRINGER  
*Femtosecond photodissociation of triiodide in solution: Excitation energy dependence and transition state dynamics*  
Chem. Phys. **233**, 161–178 (1998)
- [293] E. GERSHGORIN, J. VALA, R. KOSLOFF und S. RUHMAN  
*Impulsive control of ground surface dynamics of  $I_3^-$  in solution*  
J. Phys. Chem. A **105**, 5081–5095 (2001)

- [294] A. BARTANA, U. BANIN, S. RUHMAN und R. KOSLOFF  
*Intensity effects on impulsive excitation of ground surface coherent vibrational motion. A 'V' jump simulation*  
Chem. Phys. Lett. **229**, 211–217 (1994)
- [295] S. A. RICE und M. ZHAO  
*Optical control of molecular dynamics*  
Wiley-Interscience (2000)
- [296] P. NUERNBERGER  
*Formung und Charakterisierung von Femtosekunden-Laserimpulsen im Ultravioletten*  
Diploma thesis, Universitaet Wuerzburg, Physikalisches Institut (2004)
- [297] M. J. TAUBER, R. A. MATHIES, X. CHEN und S. E. BRADFORTH  
*Flowing liquid sample jet for resonance Raman and ultrafast optical spectroscopy*  
Rev. Sci. Instrum. **74**, 4958–4960 (2003)
- [298] S. MITAKU, K. IKUTA, H. ITOH, R. KATAOKA, M. NAKA, M. YAMADA und M. SUWA  
*Denaturation of bacteriorhodopsin by organic-solvents*  
Biophys. Chem. **30**, 69–79 (1988)
- [299] P. V. ARGADE und K. J. ROTHSCHILD  
*Kinetic resonance Raman-spectroscopy of purple-membrane using rotating sample*  
Biophys. Chem. **88**, 643–648 (1982)
- [300] R. HUBER, H. SATZGER, W. ZINTH und J. WACHTVEITL  
*Noncollinear optical parametric amplifiers with output parameters improved by the application of a white light continuum generated in CaF<sub>2</sub>*  
Opt. Comm. **194**, 443–448 (2001)
- [301] M. LIM, T. A. JACKSON und P. A. ANFINRUD  
*Nonexponential protein relaxation: Dynamics of conformational change in myoglobin*  
Proc. Natl. Acad. Sci. USA **90**, 5801 (1993)
- [302] F. ROSCA, A. T. N. KUMAR, D. IONASCU, T. SJODIN, A. A. DEMIDOV und P. A. CHAMPION  
*Wavelength selective modulation in femtosecond pump probe spectroscopy and its application to heme proteins*  
J. Chem. Phys. **114**, 10884 (2001)
- [303] D. J. LOUGNOT, P. BRUNERO, J. P. FOUASSIER und J. FAURE  
*Etude physicochimique d'une serie de cyanines; partie IV ridification, photoisomerisation et effet laser*  
J. de chimie physique **79** (4), 343–349 (1982)
- [304] H. GRATZ, A. PENZKOFER, C. ABELS, R. M. SZEIMIES, M. LANDTHALER und B. W  
*Photo-isomerisation, triplet formation, and photo-degeneration dynamics of indocyanine green solutions*  
J. Photobio. Photochem. **128**, 101–109 (1999)

- [305] W. HOLZER, M. MAUERER, A. PENZKOFER, R.-M. SZEIMIES, C. ABELS,  
M. LANDTHALER und W. BÄUMLER  
*Photostability and thermal stability of indocyanine green*  
J. Photochem. Photobiol. B: Biol. **47**, 155–164 (1998)

## Acknowledgements

This work could not have been finished in this form without the interaction and support of many people. A lot of projects in this thesis have only been possible due to excellent team work, even bridging the national borders. I want to thank all people at the different places for having a nice time and especially the members of the group “Experimentelle Physik I” for the very friendly and always helpful atmosphere. Even in times, the conditions for the experiments seemed to be too difficult to finish them successfully, the support and motivation by the whole group always helped to overcome these situations. Although it will not be possible to honor all people here by name, I am very appreciate to everyone. I want to give special thanks to the following people:

- Prof. Dr. Gustav Gerber for his encouragement and advice all over the years and for giving me the possibility to work in this very exciting, new and fast developing research field. For the opportunity to attend many national and international conferences, as well as for the research visit at the University of Sapporo and the institute for Advanced Industrial and Scientific Technology (AIST) in Japan for three months. The experiences I gained have significantly contributed to many aspects of my work. The international atmosphere and the invited guests visiting our institute also enabled the very fruitful cooperation with a research group in Italy.
- Prof. Dr. Roberto Improta and Dr. Fabrizio Santoro for the excellent cooperation in the investigation of isomerization dynamics of the short-chained cyanine dyes. Without their theoretical simulations at the border of the computational potentials, the understanding and the experimental progress in this field would not have been possible.
- Dr. Tobias Brixner for the excellent coordination of the laboratory and the opportunity for discussions of many different topics. His advice and competence concerning many experimental and other questions has supported the progress of many different aspects connected with this thesis. His proposals regarding the formulation of various publications always helped improving the quality of the text.
- Patrick Nürnberger for his endless support in the different night-filling experiments. His expertise that he brought into the group helped in many situations. For the always well-founded discussions concerning the interpretation of various experimental results and his readiness and support, when trying new methods and approaches for the diverse experimental objectives.

- Dr. Gerhard Krampert for his support in the cyanine control experiment, his expertise concerning various mechanical issues and the possibility to always discuss various topics
- Dr. Patrick Niklaus also for his assistance in the cyanine control experiment as well as his competence in the mid infrared transient absorption experiment not shown here.
- In the context of the MIR experiment, I want also especially thank Daniel Wolpert and Mareike Koch for rebuilding the setup after the restructuring of the laser system and Matthias Bräuninger in his assistance for testing the suitability of different substances for the MIR experiments.
- Reimer Selle for the nice teamwork in various experiments concerning the issue of reducing the problem complexity and the experiments in connection with the experimental tests of his neural network approach.
- Frank Dimler, Florian Langhojer, Patrick Nürnberger, Daniel Wolpert and Reimer Selle for the good cooperation while rebuilding and improving the laser system and Prof. Gustav Gerber and Dr. Tobias Brixner for organizing the financial support.
- Thomas Sokollik for the investigations of certain aspects of the molecular dynamics on a 20 fs time scale.
- Thomas Hochrein in his assistance regarding the project for improving the signal-to-noise ratio and Michael Maurer for helping in the design of the moving sample holder.
- Susanne Fechner for her cooperation in the realization of the double-pulse generation part.
- The not yet mentioned coworkers of our laboratory: Christian Dietl, Claudia Treml, Jens König, Evangelos Papastathopoulos, Jesus Tonerro, Eliza-Beth Lerch, Kate Moore and Christian Tutsch enjoyable and helpful discussions and their support regarding various issues.
- Carsten Winterfeldt, Thomas Pfeifer, Dominik Walter and Alexander Paulus from the laboratory A for the friendly atmosphere and the possibility to discuss many different topics.
- Prof. Dr. Christian Spielmann, Prof. Dr. Walter Pfeiffer and their groups and all others for the possibility to have an insight into diverse topics and their helpful support on many different ways.
- The technical assistants Helga Schwark, Monika Seifert and Valentin Baianov as well as our secretary Diep Phan.



- The machine shop for the exact realization of various mechanical parts, which exceed the presented moving sample holder and the electric workshop especially for the improved circuits for suppression of the electronic noise.
- The computer administration team Christian Dietl, Patrick Nicklaus, Sandra Dantscher, Dominik Walter and Robert Spitzenpfeil for maintaining the information network in our group.
- All the people, that have read through earlier versions of this manuscript, especially to Patrick Nürnberger, Frank Dimler, Florian Langhojer, Daniel Wolpert and Christian Tutsch

I want to give extraordinary thanks to Isabell Götz for always taking care of me, to my family for all the things they have done for me and all my friends for the good time.



# Curriculum Vitae - Gerhard Vogt

## personal data

|                 |   |
|-----------------|---|
| private address | Semmelstr. 11<br>97070 Würzburg         |
| birth           | August, 5 <sup>th</sup> 1976 in Cologne |
| nationality     | German                                  |
| family status   | single                                  |

## school

|                   |                                    |
|-------------------|------------------------------------|
| Sep. 83 - Jul. 87 | elementary school, Delhoven        |
| Sep. 87 - Jun. 96 | High school, Knechtsteden (Abitur) |

## university

|                   |   |
|-------------------|---|
| Oct. 97 - Sep. 99 | undergraduate studies in physics (Vordiplom),<br>Heinrich-Heine-Universität Düsseldorf                            |
| Oct. 99 - Dez.02  | graduate studies in physics (Diplom),<br>Julius-Maximilians-Universität Würzburg                                  |
| Sep. 00 - Jul. 02 | Studies of Japanology   |
| Oct. 01 - Jan. 03 | Diplom-thesis in the group of Prof. Dr. G. Gerber<br>"Coherent control of chemical reactions in the liquid phase" |
| Oct. 02 - Nov. 02 | Research stay in the groups of<br>Prof. Dr. M. Yamashita and Dr. M. Kakehata (Japan)                              |
| Since Jan. 03     | Promotion in the group of Prof. Dr. G. Gerber   |

**occupational history**

Jul. 96 - Apr. 97      basic military service, Hemer  
Feb. 98 - Sep. 99      network-assistant: netadministration in the  
                                 mathematical institute of the university Düsseldorf  
Since Jan. 03            Scientific assistant at the University of Würzburg

**further skills**

languages                English, Latin, French, Japanese  
EDV                        Several programming languages  
                                 Programs, relevant for physics (CAD, Mathematika, LabVIEW)

Würzburg, June, 1<sup>st</sup> 2006

---

Gerhard Vogt